Metal-organic frameworks for environmental and energy related applications

Bingbing Chen

To cite this version:

Bingbing Chen. Metal-organic frameworks for environmental and energy related applications. Material chemistry. Université Paris sciences et lettres, 2023. English. ⟨NNT : 2023UPSLE023⟩. ⟨tel-05069722⟩

HAL Id: tel-05069722
https://theses.hal.science/tel-05069722v1
Submitted on 15 May 2025

PSL
UNIVERSITÉ PARIS

THÈSE DE DOCTORAT
DE L'UNIVERSITÉ PSL

Préparée à l' École Normale Supérieure de Paris

Solides poreux hybrides pour des applications dans le domaine de l'environnement et de l'énergie

Metal-organic frameworks for environmental and energy related applications

Soutenue par
Bingbing CHEN
Le 6 Juin 2023

Ecole doctorale n° 397
Physique et Chimie des Matériaux

Spécialité
Chimie des matériaux

Composition du jury :

Caroline MELLOT-DRAZNIEKS
Directrice de recherche CNRS
Collège de France *Président*

Vanessa FIERRO
Directrice de recherche CNRS
Institut Jean Lamour ENSTIB *Rapporteure*

Stéphane BAUDRON
Directeur de recherche CNRS
Institut Le Bel *Rapporteur*

Michael CARBONI
Chargé de recherche CEA
Institut de Chimie Séparative de Marcoule *Examinateur*

Moisés PINTO
Full professor, Instituto Superior Técnico
Universidade de Lisboa *Co-Directeur de thèse*

Georges MOUCHAHAM
Chargé de recherche CNRS
Ecole Normale Supérieure, ESPCI Paris *Co-Encadrant, invité*

Christian SERRE
Directeur de Recherche CNRS
Ecole Normale Supérieure, ESPCI Paris *Directeur de thèse*

ENS | PSL

ESPCI PARIS | PSL

Acknowledgement

These more than four years' period in France pursuing my PhD degree offered a huge change in my life. Saving time, working hard, and doing whatever comes to my mind will continue throughout the rest of my life. Sincerely, I must extend my deep gratitude to those who love me, help me, and support me along this unforgettable path. Particularly, I will thank China Scholarship Council (CSC) with four years funding for my PhD thesis.

With sincere gratitude, I will thank my thesis director **Dr. Christian SERRE and Prof. Dr. Moisés L. PINTO** for their invaluable guidance, support, and encouragement throughout my PhD thesis. With superb scientific literacy and insight into the steps of research, you taught me how to understand deeply from the experimental findings, how to design the experiments to prove the hypothesis. I will express my gratitude to my supervisor **Dr. Georges MOUCHAHAM** for his kind help and supervision, especially, for his patience, understanding, and unwavering support during the entire period. I am grateful to have this opportunity of standing on their shoulders to learn about this field and explore this field in a deeper and more meaningful way.

I would express my gratitude to the members of ED397 committee, **Prof. Claudia ZLOTEA** and **Prof. Fabric MATHEVET** who provided me with many help during the four years of my research.

I would express my gratitude to all the members of my thesis committee, **Prof. Dr. Vanessa FIERRO**, **Prof. Dr. Stéphane BAUDRON**, **Prof. Dr. Caroline MELLOT-DRAZNIEKS**, **Prof. Dr. Michael CARBONI**. Special thanks to Prof. Dr. Vanessa FIERRO and Prof. Dr. Stéphane BAUDRON, who are the rapporteurs of my thesis.

I would express my gratitude to all collaborators: **Marta G. BORDONHOS** from Universidade de Lisboa, **Prof. Dr. Guillaume MAURIN** and **Dr. Dong FAN** from Université Montpellier, **Prof. Dr. Guy DE WEIRELD**, **Dr. Nicolas HEYMANS** from Université de Mons, **Dr. Marco DATURI** from Université de Caen, **Dr. Gilles PATRIARCHE** from Université Paris-Saclay, **Dr. Philippe BOULLAY** from Normandie Université, **Celia Maria RUEDA NAVARRO**, **Prof. Dr. Sergio NAVALÓN OLTRA**, and **Prof. Dr. Hermenegildo GARCIA GOMEZ** from Universitat Politècnica de València. With all of your wonderful support, I was able to comprehend all of the work I did during my PhD.

I would use this chance to express my sincere appreciation to all of the colleagues in IMAP: **Bernard, Antoine, Farid, Iurii, Vanessa, Mathilde L., Mégane, Debanjan, Aysu, Rosana, Arianna, Ahmad, Katrin, Claire, Pierre, etc, and all the previous colleagues Raquel, Ben, Shyama, Asma, Ines, Mathilde R., Nacho, My-an, Ella, Masheer, Xandi, Javier, Angelika,**

Joanna, Sarah, etc. I would express my sincere gratitude to all the members in #**Beer club**#. I would give big thanks to all Chinese members in IMAP: **Sujing, Shan, Heng, Xin, Wenqing, Chenchen, Yuwei, Zhihao, Yutong, Qingfeng, Jiangliang, Shaokang, Meng, Xinrui, Xingze**. All the wonderful moments with you will be the treasure of my life.

I wish to express the deepest gratitude to my teachers: **Guangqian WANG**, **Jianjun TONG**, **Yufa FENG**, **Hui LI**, **Qingjie Ge**, **Dongyan XU**, who taught me be an honest person, pursue the goal in a practical and realistic manner.

I wish to express my gratitude to my friends: **Xiangli**, **Lingchao**, **Qingchao**, **Junteng**, **Xia**, **Jinxia**, **Meishan, Jiayi, Caihong, Dan** thank you for all your help and support.

Very importantly, I will give my deepest love to my family for their invaluable support.

Table of contents

Chapter 3 Post-synthetic functionalization of metal-organic framework for the high pressure separation of C_2 hydrocarbons 117

Chapter 4 An easy scalable, highly robust microporous Al MOF for post-combustion carbon capture 139

Abbreviations

MOFs: Metal-organic frameworks

C_2H_2: Acetylene

C_2H_4: Ethylene

C_2H_6: Ethane

CO_2: Carbon dioxide

VPSA: Vacuum pressure swing adsorption

TSA: Temperature swing adsorption

COFs: Covalent-organic frameworks

HOFs: Hydrogen-boned organic frameworks

POCs: Porous organic cages

IAST: Idea adsorbed solution theory

ZJNU: Zhejiang normal university

1,4-BDC: Benzene-1,4-dicarboxylic acid or terephthalic acid

DABCO: 1,4-diazabicyclo[2.2.2]octane

DOBDC: Dihydroxyl-benzene-1,4-dicarboxylic acid

NPD: Neutron powder diffraction

PyC: 4-Pyrazolecarboxylic acid

Ad: Adenine

JNU: Jinan university

NIIC: Nikolaev institute of inorganic chemistry

Et: Ethylene glycol

Pr: 1,2-Propanediol

Bu: 1,2-Butanediol

Pe: 1,2-Pentanediol

GI: Glycerol

1,4-BDC-2CF$_3$: Diperfluoromethyl terephthalic acid

UiO: University i Oslo

FMOF: Fluorinated metal-organic framework

IPA: Isophthalic acid

MUF: Massey university frameworks

DCiM-Br: 4,5-Dicyanoimidazole-bromine

DCiM-Me: Methyl-4,5-dicyanoimidazole

NKMOF: Nankai metal organic frameworks

Qc: Quinoline-5-carboxylic acid

TBA: 4-(1H-tetrazol-5-yl) benzoic acid

Q_{st}: Heat enthalpy

DBPT: 4′-(3,5-dicarboxyphenyl)-4,2′:6′,4″-terpyridine

SNNU: Shaanxi normal university

PSP: Pore space partition

DSI: Dynamic spacer installations

CPM: Crystalline porous materials

DMBDC: 2,5-Dimethyl-benzene-1,4-dicarboxylic acid

NDC: 1,4-Naphthalenedicarboxylic acid

TPBz: 1,3,5-Tri(4-pyridyl)-benzene

TPPy: 2,4,6-Tris(4-pyridyl)pyridine

TPT: 2,4,6-Tri(4-pyridyl)-1,3,5-triazine

LIFM: Lehn institute of functional materials

Me$_2$-BPDC: Dimethyl-2,2′-dimethylbiphenyl-4,4′-dicarboxylic acid

ZIF: Zeolitic imidazolate framework

DCPN: 5-(3′,5′-Dicarboxylphenyl) nicotinic acid

TJT: Tianjin university of technology

GCMC: Grand canonical monte carlo

Tripp: 2,4,6-Tris(4-pyridyl)pyridine

NPU: Northwestern polytechnical university

SSST: Synergistic sorbent separation technology

ATZ: 3-Amino-1,2,4-triazolate

SIFSIX: SiF_6^{2-}

TIFSIX: TiF_6^{2-}

OSST: One-sorbent separation technology (OSST)

H_2OBA: 4,4-Dicarboxyl diphenyl ether

2,6-NDC: Naphthalene-2,6-dicarboxylic acid

DUT: Dresden university of technology

IPCC: Intergovernmental panel on climate change

CCS & CCUS: Carbon capture & storage & utilization

NGCC: Natural gas combined cycle

DAC: Direct air capture

MEA: Mono-ethanolamine

DEA: Diethanolamine

MIL: Matériaux de l′Institut Lavoisier

OMS: Open metal sites

NOTT: University of Nottingham

BTC: Benzene-1,3,5-tricaroxylic acid

PTEI: 5,5′-((5′-(4-((3,5-Dicarboxyphenyl)ethynyl)phenyl)-[1,1′:3′,1″-terphenyl]-4,4″-diyl)-bis(ethyne-2,1-diyl))diisophthalic acid

DOBPDC: 4,4′-Dioxidobiphenyl-3,3′-dicarboxylic acid

TFA: Trifluoroacetic acid

USTC: University of Science and Technology of China

SBPDC: 4,4′-Dibenzoic acid-2,2′-sulfone

BPY: 4,4′-Bipyridine

EDS:1,2-Ethanedisulfonate

CD-MOFs: Cyclodextrin-based metal organic frameworks

CALF: Calgary framework

TCPP: Tetrakis(4-carboxyphenyl)porphyrin

TBAPy: 1,3,6,8-tetrakis(p-benzoic acid)pyrene

RH: Relative humidity

STY: Space-time yield

IMAP: Institut des matériaux poreux de Paris

PVB: Polyvinyl butyral

PCPs: Porous coordination polymers

BET: Brunauer-Emmett-Teller

K_H: Henry's constant

MAF: Metal azolate framework

PSM: Post-synthetic modification

VdW: Van de Waals

TPA: 3,3,3-Trifluoropropionic acid

NSA: 2-Naphthalene-sulfonic acid

PXRD: Powder X-ray diffraction

TGA: Thermogravimetric analysis

NMR: Nuclear magnetic resonance

SEM: Scanning electron microscopy

AP: Ambient pressure synthesis

IR: Infrared spectroscopy

BTec: Benzene-1,2,4,5-tetracarboxylic acid

DFT: Density functional theory

$Al(NO_3)_3$: Aluminum nitrate

$Al(OH)(CH_3COO)_2$: Aluminum acetate

$NaAlO_2$: Sodium aluminate

SSL: Single-Site Langmuir

DSL: Dual-Site Langmuir

Ti-MOFs: Titanium-based metal organic frameworks

MIP: Materials from institute of porous materials of Paris

cRED: Continuous rotation electron diffraction method

IBUs: Inorganic building units

FT-IR: Fourier transform infrared spectroscopy

XPS: X-ray photoelectron spectroscopy

E^{f}_{υ}: Fermi level

NHE: Normal hydrogen electrode

VB: Valence band

CB: Conduction band

LUCO: Lowest unoccupied crystal orbital

HER: Hydrogen evolution reaction

OWS: Overall water splitting

PDF: Pair distribution function

HRSTEM: High-resolution scanning transmission microscopy images

TEM: Transmission electron microscopy

PSD: Pore size distribution

General introduction

Decreasing the current energy-intensive processes in heavy industries (e.g., petrochemical, cement factory, etc.) and mitigating the environmental issues through the utilization of clean and sustainable energy sources have attracted much more attention due to critical climate change and a number of increased risks for humans, economies, and ecosystems. For instance, separation/purification through cryogenic distillation, one of the most energy-intensive procedures in current petrochemical industrial plants, accounts for 10-15% of the world's energy consumption. Additionally, because of the utilization of fossil fuels, many environmental issues come out such as global warming and air pollution. Therefore, global political, economic, and technological investment in the quick implementation will be necessary to meet these challenges. The community of advanced materials should significantly contribute to these efforts by providing highly performing materials for effective separation/purification processes and/or high selective conversion of sustainable source into clean energy, at lowest energetical costs.

Among the potential material candidates, metal-organic frameworks (MOFs) has started to deliver promising premises. MOFs are porous crystalline hybrid solids, that can be rationally designed through the multi-metallic units called inorganic building units (IBUs) and diverse organic linkers into the two- or three-dimensional frameworks. Their versatile structures, in terms of chemical compositions and geometrical features, empower them with numerous merits, thus, a great potential in diverse applications related to energy, environment and health.

Ethylene (C_2H_4) is one of the essential raw materials for manufacturing plastics such as polyethylene around the world. To date, producing *ca.* 200 million tons of C_2H_4 mainly from ethane (C_2H_6) stream cracking requires around 0.3% of the global energy consumption, which obviously highlights that its separation procedure by conventional cryogenic distillation is energy-intensive although it is a highly heat integrated process in petrochemical industries. Alternative to this energy-intensive distillation, adsorption separation using porous adsorbents under moderate conditions have demonstrated as an efficient procedure from gas mixtures in petrochemical downstream. This adsorption separation has the advantage to be achieved in a relatively short operational time due to rapid regeneration/cycling, as well as the possibility to provide a relatively flexible and scalable technologies. In this regard, the use of MOF-based adsorbents bearing open metal sites (OMS), such as Ag(I), Cu(I) and Fe(II) has shown to be very efficient. The presence of these OMS well arranged in a confined space provides a relatively strong interaction ($Q_{st} > 60$ kJ mol^{-1}) with the π-electron cloud of C_2H_4 molecules to achieve C_2H_4-selective adsorption over C_2H_6 under ambient conditions. However, the relatively high Q_{st} may lead to energy demanding regeneration process in case of strong adsorbent-adsorbate affinity, requiring higher vacuum and/or heating. Therefore, optimal MOF-based adsorbent offering high C_2H_6 selectivity over C_2H_4 with relatively moderate interactions is key parameter to design economically and energetically viable adsorption-based solutions for effective C_2H_6/C_2H_4 separation processes. Additionally, considering the practical industrial pressure range, when the operation is carried out under relatively high pressure, C_2H_4 production with high purity could be enhanced because of larger amount of C_2H_6 could retain in the adsorbent fixed-bed column.

From a broader point of view, the CO_2 is another facet of the global energy production/consumption, since the large majority still depend on fossil resources. Being the predominant cause for the global warming, the CO_2 concentration in the atmosphere has dramatically increased in the past decades, due to the growth of the demand of global electricity and heat, the increased CO_2 emission, reaching up to 36.3 gigatonnes (Gt) CO_2 in 2021. Until significantly reducing our dependency on fossil resources, the only possible solution to decrease the amount of CO_2 in the atmosphere is to capture and store it. So far, aqueous amine solution through a combination of chemical and physical absorption affinity with CO_2 molecule, is the benchmark technology for CO_2 capture in coal-fired power plants. However, the well-established carbon capture process using aqueous amine solution at large scale has been given some environmentally unfriendly issues such as the release of toxic pollutants, oxidation of amine group, and the corrosivity of the equipment. This process also requires a highly energy consumption for the full-regeneration due to the reversible formation of carbamate or bicarbonate species. Consequently, driven by the non-thermal and environmentally friendly technology, the utilization of efficient porous adsorbents for physisorptive CO_2 capture from power plant flue gas (10-15% CO_2) is desperately needed to decrease CO_2 emission, avoid air pollution, and mitigate current global warming phenomenon. MOF-based adsorbents are also potential physisorbent candidates with excellent working capacity and selectivity of CO_2 given their relatively strong affinity of CO_2 over other gases present in the power plant flue gas. A promising zinc-based metal-organic framework, CALF-20, exhibited selectively capture CO_2 under high humid conditions, and its large-scale synthesis reached the industrial application level.

As described above, since the utilization of fossil fuel is at the origin of major CO_2 accumulation, it is imminent to seek sustainable resources with low carbon footprint and impact. Hydrogen energy is considered to be an ideal alternative source owing to its characteristics of wide sources high calorific value of combustion and carbon-free by nature. So far, electrocatalytic processes are the most advanced technologies deployed for the hydrogen production. Besides, producing H_2 from renewable resources such as the sun power, through for instance the photocatalytic hydrogen evolution reaction (HER) and the overall water splitting (OWS) reaction, has been attracting a lot of attention in the last few years. Although not to be in opposition with photo-electrocatalytic processes, relying on the sole sun light source, allow to simplify the process and significantly reduce the cost and the hurdles of heavy infrastructure that electrochemical processes require, thus making of photocatalysis a good alternative to consider for H_2 stations in a remote location for decentralized small to medium-sized energy production. Titanium-based photocatalyst (i.e., TiO_2) is a very eco-friendly technology with water used as the raw material and the endless solar energy as the driving force. When it comes to TiO_2 photocatalyst, the enhancement of its photocatalytic performance is strongly required via efficient exploitation of visible light, high adsorption capacity of reactants, and simplification in separating from the suspension. Construction of long-range order Ti-oxo/hydroxo compounds/clusters into the stable titanium-based MOFs (Ti-MOFs), could achieve not only the improvement of the more accessible active sites and rapid diffusion rate of reactants and products but also the enhancement of photocatalytic reaction conditions under UV and/or visible light via the rational design of inorganic/organic moieties. However, the design and synthesis of Ti-MOFs remain still at the early stage because of the complexity of titanium chemistry in solution rendering any attempt of rational design still challenging, despite recent progresses.

In this regard, my PhD project mainly aimed not only to explore rational strategies to develop MOF-based sorbents for the hydrocarbon separation under high pressure and for the CO_2 capture, but also to discover new MOF-based photocatalyst suitable for the photocatalytic hydrogen production. The work performed in this PhD project is described and argued hereafter throughout five chapters, divided as follow:

Chapter 1 consists of a general introduction on hydrocarbon separation and CO_2 capture using MOF-based sorbents;

Chapter 2 relates on the study of MOF bearing aromatic groups towards the ethane-selective adsorption over ethylene under high pressure;

Chapter 3 focuses on the improvement of C_2 hydrocarbon working capacity under high pressure via grafting fluorinated and aryl-based groups onto zirconium clusters of MOF-808 framework;

Chapter 4 is dedicated to the development and advanced study of an easy scalable and highly robust Al-MOF for post-combustion carbon capture; and

Chapter 5 describes a new titanium terephthalate metal-organic framework where it is structure was characterized by means of highly advanced techniques and their photocatalytic properties were proven for hydrogen production from water.

Finally, a general conclusion is drawn summarizing the work performed along this PhD project as well as the challenges that are still to be tackled.

Summary

As mentioned above, this PhD thesis focuses on the synthesis porous crystalline MOFs in three critical applications related to the energy and the environment fields: (i) the C_2 hydrocarbon separation under high pressure, (ii) the CO_2 capture and (iii) the photocatalytic H_2 production. In detail, this thesis is divided into five chapters.

Chapter 1 aims at giving general overview on the use of MOFs for the separation of short chain hydrocarbons as well as the CO_2 capture. It is composed of two non-exhaustive minireviews illustrating the major examples and the best strategies that have been adopted so far in each case. The first part presents the MOF-based adsorbents exhibit C_2H_6-selective adsorption separation based on different adsorption mechanisms, and discuss several examples about C_2H_6/C_2H_4 adsorption separation under high pressure conditions. The second part briefly introduces four design strategies of MOF-based adsorbent for the enhancement of CO_2 capture performance and explain them carefully through several benchmark examples, respectively.

In **chapter 2**, as a first strategy to obtain C_2H_6-selective adsorbents, porous MOF-based candidates with rich aromatic moieties have been studied under high pressure conditions. Among these structures (Al/Fe/Zr-1,4-NDC (naphthalene-1,4-dicarboxylic acid), Al-2,6-NDC-OP/CP (naphthalene-2,6-dicarboxylic acid, OP = open pore, CP = close pore)), the results revealed that the increased C-H···π interactions between C_2H_6 molecule and these moieties in these frameworks could enhance the C_2H_6-selective separation performance in C_2H_6/C_2H_4 binary mixture. Through pure-component gas adsorption experiments study, the results revealed that the increased C-H···π interactions between C_2H_6 molecules and these moieties enhanced the space confinement of C_2H_6 in C_2H_6/C_2H_4 binary mixture. Among these adsorbent candidates, Al-2,6-NDC-OP exhibited the best C_2H_6-selective performance with high C_2H_6 selectivity and working capacity under high pressure. Unfortunately, the preliminary dynamic column breakthrough experiments didn't confirm, so far, the C_2H_6-selective adsorption as suggested from near-ambient pressure single component isotherms. Additionally, from practical application point of view, Al-2,6-NDC-OP was shaped (i.e., extrusion followed by spheronisation) with 3% PVB binder (PVB stands for polyvinyl butyral) prior to breakthrough measurements. The obtained beads (*ca.* 2 mm diameter) exhibited good mechanical strength (*ca.* 11 N) with preserved porosity. Additional studies are still in progress for further understandings.

Chapter 3 related on the second strategy I have deployed in view of enhancing the Van de Waals (VdW) interaction with C_2H_6 over C_2H_4 molecules. It relies on engineering the organic units or by post-modifying the inorganic building units in MOFs. MOF-808 was selected as backbone framework due to the existence of six terminal formate ligands ($HCOO^-$) on the belt of Zr_6 oxoclusters. This allowed us to replace (some of) these formate groups easily by other acid bearing fluorinated or phenyl functional groups through post-synthetic modification (PSM) strategy. We presented here that MOF-808-R (R = 2,2,2-trifluoroacetic acid (TFA), 3,3,3-trifluoropropionic acid (TPA), 2-naphthalene-sulfonic acid (NSA)), provided a fluorine-rich or phenyl-rich pore environment, reduced the pore size and contributed denser contact sites between fluorine or phenyl and hydrogen from C_2 hydrocarbons. Compared with that of MOF-808, MOF-808-R exhibited the stronger affinity of C_2 hydrocarbons improving the working capacity of C_2 hydrocarbons from ambient to high pressure range. Because of more molecular interactions between C_2 hydrocarbons and MOF-808-TFA/TPA, the increased working capacity (from 1 to 9 bar) of C_2H_6 presented almost 133% and 155% higher than that of MOF-808, respectively.

In **chapter 4**, we have demonstrated the potential of MIL-120(Al)-AP (refers to MIL-120(Al)-AP via ambient pressure synthesis) for CO_2 capture. It exhibited high CO_2 uptake due to the high density of μ_2-OH group and their availabilities for the interactions with CO_2, which was further supported by the GCMC simulations. The CO_2 isosteric heat of adsorption (Q_{st}) MIL-120(Al)-AP (44 kJ mol^{-1}) indicates relatively low energetical cost for adsorbent regeneration. *In situ* PXRD study confirms a phase transition from monoclinic to triclinic due to partial removal of the guest water molecules. Compared with the slow H_2O adsorption, rapid kinetic adsorption of CO_2 molecules was observed through *in situ* infrared spectroscopy (IR) studies, which indirectly indicated that this MOF displays more favorable kinetics for CO_2 sorption compared to water, and, hence, can be an ideal process for CO_2/N_2 separation in the presence of H_2O. The synthesis of MIL-120(Al)-AP, under environmentally friendly (i.e., in water at ambient pressure), using inexpensive starting materials was first optimized at the g-scale and successfully scaled up to the kg-scale. The efficient adsorptive separation of CO_2/N_2 of the structured MIL-120(Al)-AP was validated by breakthrough experiments. The ongoing research in collaboration with Prof. G De WEIRELD aims to investigate the kinetics effects in real separation conditions on a VPSA unit, requiring 3 kg of shaped material.

In **chapter 5**, we presented a new series of microporous Ti-MOFs, labeled MIP-209(Ti) (MIP stands for Materials from Institute of Porous Materials of Paris) constructed by terephthalate derivatives ligands and $Ti_{12}O_{15}$ oxo-cluster with the formula $Ti_{12}O_{15}(NO_2\text{-}1,4\text{-}BDC)_6(acetate)_3$ as revealed by continuous rotation electron diffraction method (cRED), crystalized in a hexagonal space group $P6_3/mmc$ with unit cell parameters of a = 22.3854 Å, c = 16.5906 Å and V= 7199.83 Å^3. Indeed, MIP-209(Ti) could be obtained using various terephthalate (1,4-BDC) derivatives such as NO_2- and 2Cl-1.4-BDC, in an eco-friendly solvent (i.e., acetic acid). Alternatively, it was also possible to tune the composition of its Ti oxocluster, similarly to MIP-177(Ti)_LT. For instance, 5% Cr^{3+} doping could favorably enhance the water stability, and maintained good crystallinity after soaking in water for at least 7 days. Motivated by the enhanced water stability and unique Ti-MOFs properties, photocatalytic hydrogen evolution from water splitting reaction have been measured. MIP-209(Ti-Cr)-NO_2 displayed a very high hydrogen production rate with good reusability and stability in presence of methanol as scavenger under simulated sunlight irradiation, which exhibited fourfold enhanced hydrogen production, in comparison with the benchmark IEF-11 framework.

Finally, the general conclusion and perspectives are discussed about the performance of several robust MOFs on hydrocarbon separation, CO_2 capture and photocatalytic hydrogen production, and the further work that we should investigate further.

Chapter 1

Introduction

This chapter contains two parts, namely “Recent progress of ethane selective adsorption in C_2 hydrocarbons using metal-organic frameworks” and “Metal-organic frameworks for carbon dioxide capture”.

Table of Contents

1.1 Recent progress of ethane selective adsorption in C_2 hydrocarbons using metal-organic frameworks

Abstract

C_2 hydrocarbon separation and purification via cryogenic distillation is one of the most energy demanding processes in petrochemical industry. Compared with cryogenic distillation, adsorption separation through the relatively weak affinity between guest molecules and adsorbent needs much less energy input and produces higher purity of ethylene during the adsorption/desorption cycles. Meanwhile, favoring ethane-selective adsorption over ethylene will allow to achieve more direct production of polymer-grade ethylene and, thus, to reach even lower energy penalty processes. In this regard, metal-organic frameworks (MOFs) are a class of hybrid adsorbents that have shown high promises in C_2 hydrocarbon separation, with increasing efforts on ethane/ethylene separation, including one-step ethylene purification from multiple components mixture (acetylene/ethylene/ethane or acetylene/ethylene/ethane/carbon dioxide). This review mainly focuses on MOF sorbents, showing ethane-selective adsorption separation based on five different adsorption mechanisms. Moreover, from a practical industrial applications point of view, several examples about C_2 hydrocarbon separation under high pressure will be discussed here.

1.1.1 Introduction

The separation of C_2 hydrocarbon mixture in petrochemical industry is an indispensable procedure to obtain 99.5% purity of ethylene for polymerization reaction and for many other critical processes for the chemical industry value chain.[1,2] For example, with exceeding 180 trays and high reflux ratio, cryogenic distillation is required for ethane/ethylene separation due to their close boiling points (184 K and 169 K for ethane and ethylene, respectively), resulting in one of the highest energy consumption separation in the industrial processes.[3,4] So far, producing *ca.* 200 million tons of ethylene around the world requires around 0.3% of the global energy consumption, which obviously highlights that this separation is energy intensive although it is a highly heat integrated process. Achieving cost- and energy-efficient C_2 hydrocarbon separation is highly desired and has been recently highlighted as one of the most important industrial separation tasks for future energy efficient utilization.[5]

Compared to cryogenic distillation, adsorption or membrane separation has emerged as serious alternatives for the separation of light hydrocarbons since the 1990s due to their higher selectivity and energy-efficiency, while showing lower carbon footprint.[6,7] By contrast of membrane separation with lower productivity and gas permeability in small-scale operation, adsorption separations (i.e., vacuum pressure swing adsorption (VPSA) or temperature swing adsorption (TSA)) could offer much higher working capacity and throughput in large-scale industrial platform.[8-10] In addition, C_2 hydrocarbon separation has the advantage to be achieved in a relatively short operational time due to rapid regeneration/cycling, as well as the possibility to provide a relatively flexible and scalable technologies. Nevertheless, it may suffer from energy demanding regeneration process in case of strong adsorbent-adsorbate affinity, requiring higher vacuum and/or heating. Therefore, an optimal balance offering suitable adsorbents showing high selectively together with relatively moderate interactions should be the key parameter to design economically and energetically viable adsorption-based solutions for effective separation processes.[11]

To date adsorbents such as porous activated carbons, porous alumina/silica and zeolites have been applied as commercially available adsorbents on variable separations or purifications procedures.[12,13] However, porous activated carbons suffer from low selectivity and slow diffusion rate in the separation of C_2 hydrocarbon, while porous alumina/silica and zeolites (pristine or chemically modified) exhibit, in general, limited working capacities because of their limited pore volume. Moreover, these adsorbents may be limited by their lack of possibilities to chemical and geometrical design and limited structural tunability.[14] For other crystalline solids such as covalent organic frameworks (COFs), hydrogen-boned organic frameworks (HOFs) or porous organic cages (POCs), only a few of them showed the behavior of ethane-selective adsorption. How to further improve their ethane uptakes and ethane/ethylene selectivity remains challenging as discussed in detail in recent reviews.[15]

MOFs, a relatively recent class of hybrid and crystalline porous materials, have emerged as promising multifunctional materials in gas capture, separation and storage, among other applications, owing to the versatile and tunable design in terms of chemical composition and pore engineering.[16-19] Bülow and his co-workers firstly reported the separation of hydrocarbons by using MOFs materials.[20] Up to now, unremitting efforts are still devoted to exploring the promising MOFs candidate for hydrocarbons separation.[7,21-25] By analogy with zeolites, MOFs exhibit usually a better selectivity and a higher working capacity in hydrocarbons separation.[26,27] Several MOFs have shown a better separation ability than that of conventional adsorbents, indicating a strong potential towards practical industrial application. Generally, from the coordination chemistry point of view, this sometimes relatively strong affinity for ethylene is caused by the π-complexation interactions between ethylene molecules and transition metal ions (mostly Ag^+ and Cu^+) or alternatively open metal sites.[28,29] Looking at the kinetics of separation and due to the rapid diffusion rate and smaller molecular size of ethylene, it usually goes through the adsorbent firstly, achieving ethylene preferential adsorption. Nevertheless, ethane as ethylene's corresponding counterpart, disturbs the production of high purity ethylene during the adsorption separation procedure. To achieve the purity limit required ($\geq$99.95%) for polymerization reactor, at least four adsorption-desorption cycles are essential to purify the product further by inert gas or a vacuum pump which are quite energy intensive.

Imagining that if ethane is preferential adsorbed in the adsorption cycle, ethylene with high purity could be firstly produced at the outlet of adsorption column. For instance, compared with ethylene-selective adsorbent, this approach using ethane-selective adsorbent would save approximately 40% of energy consumption (0.4 to 0.6 GJ ton^{-1} of ethylene) on PSA technology for the ethane/ethylene separation.[3] However, only limited MOFs candidates have shown to perform a preferential adsorption behavior for ethane over ethylene with quite low separation selectivity and working capacity. Through there are many reviews in the hydrocarbons separation and purification field,[7,30-32] and several reviews involve the alkanes selective adsorption separation overviewing from ethane uptakes, ethane/ethylene selectivity, stability, cost, scale-up synthesis, regeneration performance and shaping of ethane-selective MOFs.[15,33,34] But there is still a need to summarize the recent ethane-selective MOFs-based adsorbents viewing from the fundamental adsorption separation mechanisms that also address the demanding practical industrial conditions such as the gas flow with multiple components, or the operation under high pressure, and not only under ambient or sub ambient pressure.

1.1.2 Molecular interactions in ethane-selective MOFs

Taking benefit from the easily structural tunability and functionalization, MOFs adsorbents are promising candidates to meet the requirements of optimal adsorption mechanism. To have ethane being trapped first in the pores of the MOFs, relatively stronger molecular interactions are required between ethane molecules and MOFs, in comparison with ethylene molecules. Here in this part, various dispersion forces such as weak hydrogen bonding (C-H···O/N/F), C-H···π interactions and their combinations will be separately described and illustrated. In addition, several reviews focusing on the relevant adsorption parameters have been reported, due to a large number of ethane-selective MOFs investigated so far.

1.1.2.1 Van der Waals forces

As the simplest, weakest affinity among inter-molecular interactions, Van der Waals forces can commonly play an important role in adsorption separation, particularly, achieving an efficient C_2 hydrocarbons separation in ethane-selective MOFs adsorbents. Whilst, MOFs could precisely provide more molecular interactions due to their diverse hybrid structures and relatively easy tunability. For instance, Li et al. investigated A520 (Al(OH)(Fumarate)), the commercial version of MIL-53(Al)-FA (MIL stands for Materials from Institut Lavoisier), shown in Fig. 1a.[35] Single component isotherms shows that this MOF exhibits a higher ethane capacity than that of ethylene, with ethane working capacity of 0.8 $mmol{\cdot}g^{-1}$ from 0.3 bar to 1 bar at 298 K. Ethane preferential adsorption behaviour has been conformed through binary gas breakthrough experiments. Selectivity of ethane over ethylene was estimated as 1.9 under 1 bar using Idea Adsorbed Solution Theory (IAST) calculation for an equimolar ethane/ethylene mixture. Derived from the Clausius-Clapeyron equation, the isosteric heat of ethane and ethylene was estimated close to zero coverage to be *ca.* 34 and 30 kJ mol^{-1}, respectively, with gradual decrease upon the loading of gas molecules. The moderate adsorption heat suggests that mainly dispersive interactions occur between the framework and adsorbate. Moreover, simulated interaction energy and adsorption density distribution showed that, the average energies between the gases and the adsorbent are -41.84 kJ mol^{-1} and -33.47 kJ mol^{-1} for ethane and ethylene, respectively. When considering the mixture adsorption distribution, ethane molecules were shown to be more closely compacted in the pores compared to ethylene molecules.

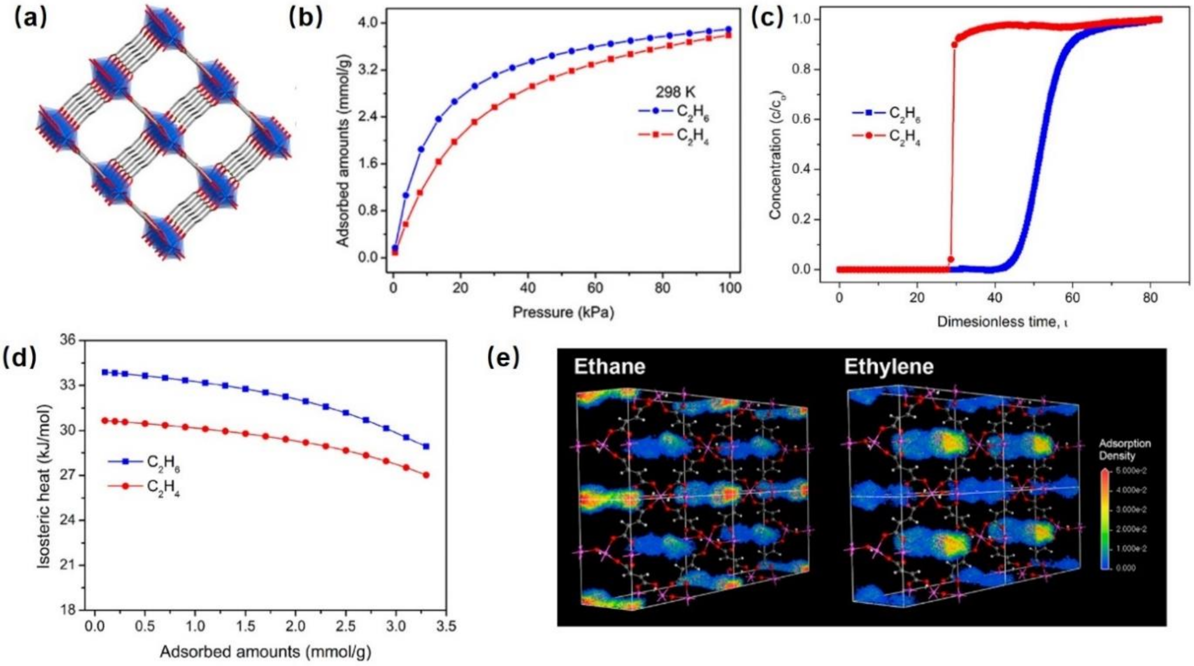

Figure 1: Structure and C$_2$ hydrocarbon adsorption performance of A520.[35] (a) Crystal structure and channels. (b) Ethylene and ethane single component adsorption isotherms of A520 at 298 K. (c) Breakthrough curves of the cracked gas (ethane/ethylene = 1/15) through the A520 column at 308 K and 1 bar. (d) Isosteric heat of ethane and ethylene on A520. (e) Simulated density distribution of ethane (left) and ethylene (right). This figure has been reproduced from ref. 35 with permission from American Chemical Society, copyright 2019.

Enhancing the selectivity/capacity of ethane adsorption through the functionalization of the linkers using more aromatic or aliphatic groups, the load of guest molecules, such as naphthalene or the incorporation/installation of parent MOFs backbone is another well explored strategy, in order to increase the dispersion force between guest molecules and non-polar group. Due to the larger polarizability of ethane compared to ethylene (44.4-44.7×10^{-25} vs 42.52×10^{-25} cm^3), one could expect that the inner surface of the desired MOFs decorated with aromatic or aliphatic groups will significantly enhance the interaction with ethane. Indeed, He and co-workers found recently that endowing MOFs with non-polar or low-polar surfaces generate ethane-favorable induction/dispersion forces, well correlated with the adsorbate polarizability. In that work, methyl, methoxy, and chloro functional groups as nonpolar or weakly polarized substituents in ZJNU-21/ZJNU-22/ZJNU-23 (Cu(L)·DMF·CH_3OH, L21 = 5-(5-methylpyridin-3-yl) isophthalate), L22 = 5-(5-methoxypyridin-3-yl)-1,3-benzenedicarboxylate, L23 = 5-(5-chloropyridin-3-yl)-1,3-benzenedicarboxylate, ZJNU stands for Zhejiang Normal University), might enhance the ethane uptake and selectivity caused by the more C-H···π and C-H···O multiple interactions.[36] It was found indeed that the heterofunctional ligands exhibit dissimilar torsional angles between the pyridine and benzenedicarboxylate moieties, spanning from -50.2 to 44.7°. Additionally, the organic functionality is oriented toward the pore center of the parallelepiped unit, thus offering the finely tuned pore size and higher dispersion force for ethane-selective adsorption. For instance, ZJNU-21 provided high uptake capacity of ethane over ethylene (2.36 mmol g^{-1} for ethane and 1.92 mmol g^{-1} at 0.1 bar) at the low-pressure region and its Q_{st} values for ethane and ethylene molecules were 37.36 and 34.22 kJ mol^{-1}, respectively, indicating a possible lower energy consumption for regeneration procedure. Similarly, Ma et al. pointed out that replacing 1,4-BDC (terephthalic acid) by different ratio of TMBDC (tetramethyl-terephthalic acid) in the microporous $Ni(BDC)(DABCO)_{0.5}$, (DABCO, 1,4-diazabicyclo[2.2.2]octane) MOF could lead to an enhanced ethane-selective adsorption performance over ethylene due to the increasing dispersive interactions between ethane molecules and methyl groups.[37] This was confirmed experimentally with the full replacement of BDC by TMBDC leading to the best ethane/ethylene selectivity of 1.985 at 298 K, 1 bar, in line with IAST calculations. Whilst, this microporous $Ni(TMBDC)_{0.5}(DABCO)_{0.5}$ led to an effective separation performance of ethane/ethylene (v/v=1/15) as well as a good regenerability upon five consecutive adsorption-desorption cycles. Additionally, one summarizes the ethane-selective MOFs built on dispersive interactions in Table 1.

Table 1: list of ethane-selective MOFs with dispersion force

MOFs	Molecular formula	S_{BET} [m^2 g^{-1}]	Pore [Å]	C_2H_4 uptake [mmol g^{-1}]	C_2H_6 uptake [mmol g^{-1}]	IAST selectivity C_2H_6 over C_2H_4 at 1 bar		Q_{st} [kJ mol^{-1}]		Ref.
				0.3/1 bar	0.3/1 bar	v/v=1/15	v/v=1/1	C_2H_4	C_2H_6	
$Ni(bdc)(ted)_{0.5}$	-	1905	1D channel (5.8)	3.29/8.8 (1-10 bar) at 298 K	4.8/8.6 (1-10 bar) at 298 K	-	1.85	25.3	29	38
$Zn(bdc)(ted)_{0.5}$	-	1781	1D channel (5.8)	3.16/8.5 (1-10 bar) at 298 K	4.45/8.1 (1-10 bar) at 298 K	-	1.73	25.5	34	
$Co(bdc)(ted)_{0.5}$	-	1708	1D channel	2.77/7.9 (1-10 bar) at	4.13/7.7 (1-10 bar) at	-	1.83	24.2	28.6	

			(5.8)	298 K	298 K					
Cu(bdc)(ted)$_{0.5}$	-	1631	1D channel (5.9)	2.53/7 (1-10 bar) at 298 K	3.68/6.9 (1-10 bar) at 298 K	-	1.82	24.4	29.4	
Ni(tmbdc)(dabco)$_{0.5}$	-	894	1D channel (5.9)	1/2.9 at 298 K	1.5/4.2 at 298 K	1.985	-	32	39	37
A520	Al(OH)(Fumate)	1160	1D channel (5.7x6.0)	2.5/3.8 at 298 K	3.1/3.9 at 298 K	-	1.9	30.5	34	35
UiO-66-adc	$Zr_6O_4(OH)_4(adc)_6$	556	Aperture (4.4)	1.25/1.7 at 298 K	1.3/1.6 at 298 K	-	1.8	36	36	39
In-soc-MOF-1	$In_3((\mu_3\text{-}O)(\mu_2\text{-}O)_3)(abtc)_3$	1223	Channel (6.8/8.1)	1.9/3.72 at 298 K	2.4/4.04 at 298 K	1.4	-	25.2	28.4	40

1.1.2.2 Hydrogen bonding

Similarly, to dispersive interactions, weak hydrogen-bonding interactions have been also proven to be more favorable to ethane than ethylene because of two additional C-H groups in ethane. Indeed, interactions such as C-H···N/O/F molecules can be considered as weak hydrogen bonding since they are relatively weaker than O/N-H···N/O/F hydrogen bonding but relatively stronger than the dispersion force discussed above. Due to two extra C-H bonds, several MOFs adsorbents have demonstrated selective adsorption of ethane over ethylene. For example, Chen and co-workers studied the microporous peroxo-MOF-74-Fe ($Fe_2(O_2)$(DOBDC), DOBDC = dihydroxyl-1,4-benzene-dicarboxylic acid), which displayed ethane preferential adsorption over ethylene in binary mixture owing to the present of peroxo sites on incomplete coordinated iron atoms, as shown in Fig. 2.[41] This phenomenon would be elucidated by high resolution neutron powder diffraction (NPD) studies at 7 K, that C_2D_6 molecules exhibited preferential binding with the peroxo sites through C-D···O hydrogen bonding (D···O, 2.17 to 2.22 Å) as. The D···O distance was found to be much shorter than the sum of Van der Waals radii of oxygen (1.52 Å) and hydrogen (1.20 Å), indicating a relatively strong interaction between ethane and oxygen atoms. This is consistent with the high heat of ethane adsorption (66.8 kJ mol^{-1}) for peroxo-MOF-74-Fe. Besides, IAST calculation proved that peroxo-MOF-74-Fe would be a new benchmark adsorbent for ethane-selective adsorption over ethylene at 298 K below 1 bar, with a superior selectivity of 4.4 compared to the previously reported best-performing MOF, Cu(Qc)$_2$, (Qc-5-Cu-sql, HQc = quinoline- 5-carboxylic acid) (3.4).[42] From gas breakthrough experiments of peroxo-MOF-74-Fe, ethane preferential adsorption from $C_2H_6/C_2H_4/C_2H_2/CH_4/H_2$ (10/87/1/1/1) mixtures was realized definitely, further high-purity ethylene (≥ 99.99% pure) was readily produced during the first breakthrough cycle with high productivity and low energy consumption. While conceptually, this MOF represents a breakthrough in the field, unfortunately, from a practical point of view, the low to moderate ethane/ethylene working capacity added to the very high air/moisture sensitivity of this material strongly hampers its deployment in practical conditions.

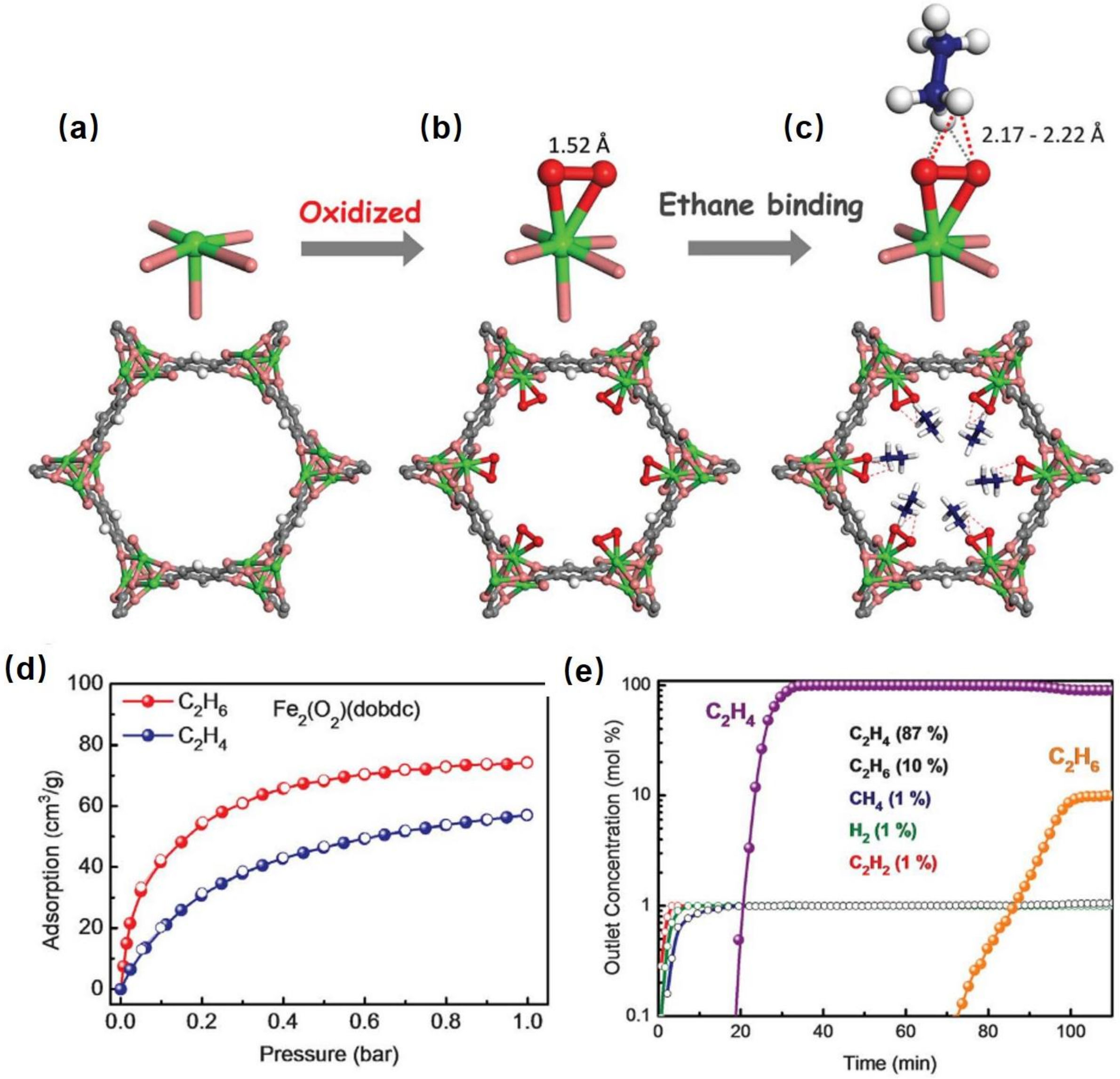

Figure 2: Structure determined from NPD studies and C_2 hydrocarbon adsorption performance of peroxo-MOF-74-Fe.[41] (a) Fe$_2$(dobdc). (b) Fe$_2$(O$_2$)(dobdc). (c)Fe$_2$(O$_2$)(dobdc)·C_2D_6 at 7 K deteremined by NPD studies (d) Ethylene and ethane single component adsorption isotherms at 298 K.(e) Experimental column breakthrough curves for $C_2H_6/C_2H_4/C_2H_2/CH_4/H_2$ (10/87/1/1/1) mixtures in an adsorbent bed at 298 K and 1.01 bar. This figure has been

reproduced from ref. 41 with permission from American Association for the Advancement of Science, copyright 2018.

Minimizing the impact of humidity on separation capacity, another ethane-selective MOF, JNU-2 ($Zn_2Cu(PyC)_2(Ad)$, PyC = 4-pyrazolecarboxylic acid, Ad = adenine, JNU stands for Jinan University), was reported recently.[43] Li et al. constructed this microporous MOF that is built of cage-like cavities interconnected through their apertures, (Fig. 3). The pore environment is rich in electronegative nitrogen and oxygen atoms, paving the way for host-guest interactions between ethane/ethylene molecules and the pores thanks to C-H···N/O interactions. As expected, it was found, through structural analysis and energy decomposition analysis of the interaction energy between gas molecules and channel model, that ethane molecule might better interact with the framework due to the additional hydrogen bonding of ethane compared to ethylene. According to single component adsorption isotherms, JNU-2 exhibited a higher working capacity (1.76 mmol g^{-1} for ethane) in the range of 0.3 to 1 bar, than almost all ethane-selective MOFs, such as In-soc-MOF-1[40] (1.64 mmol g^{-1}), TJT-100[44] (1.06 mmol g^{-1}), $Cu(Qc)_2$[42] (1.05 mmol g^{-1}; as shown in Fig. 6), A520[35] (0.8 mmol g^{-1}), and $Fe_2(O_2)(DOBDC)$[41] (0.65 mmol g^{-1}) under similar conditions. To assess the performance under humid condition, gas breakthrough tests were carried out in an equimolar ethane/ethylene mixture under 10% RH condition. It showed that JNU-2 could achieve ethane preferential adsorption over ethylene as well as a good room-temperature regeneration under vacuum along three cycles of gas breakthrough tests, in agreement with the relatively weak interactions between guest molecules and host framework.

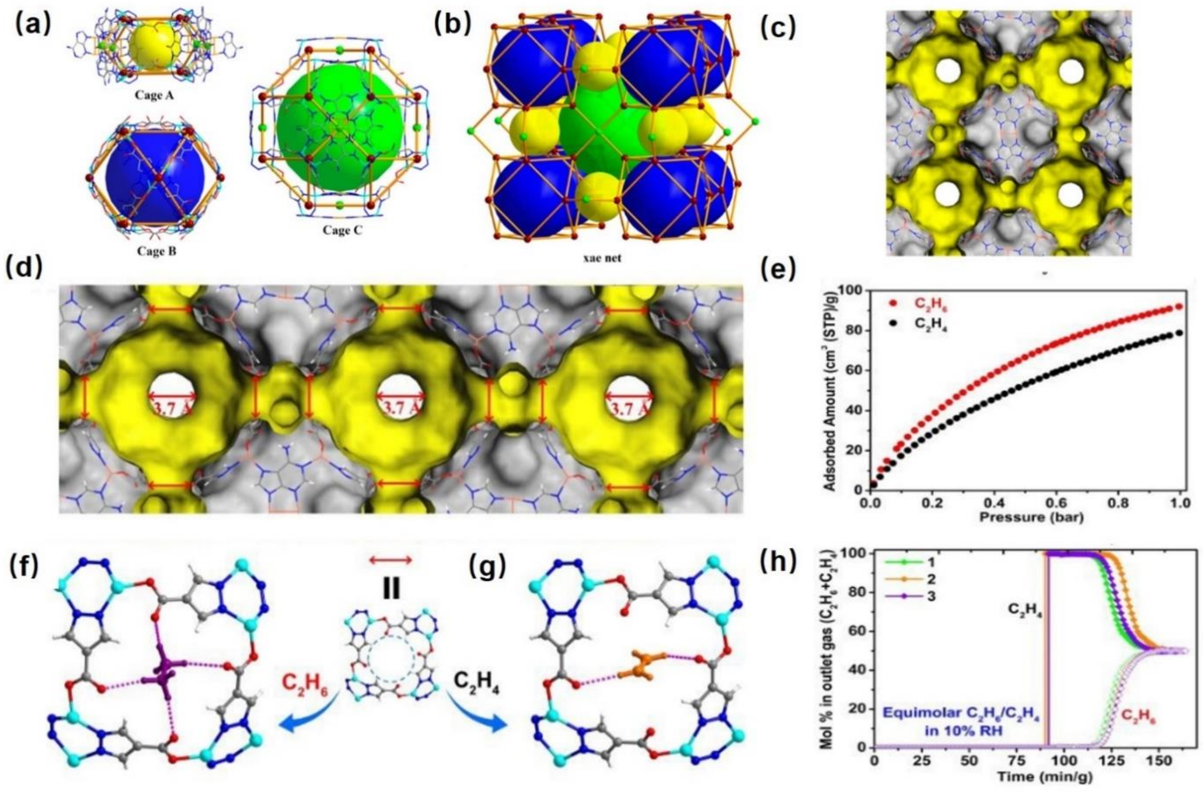

Figure 3: Structure, DFT calculation results and C_2 hydrocarbon adsorption performance of JNU-2.[43] (a, b, c) Three different cages and connolly surface representation (yellow/gray curved surface). (d, f, g) Schematic illustration of the multistage apertures (connolly surface), and comparison of the host-guest interactions of ethane and ethylene with JNU-2 at the aperture by DFT calculations; weak hydrogen bonding (2.3 to 2.8 Å) is displayed in pink. (e) Ethane and ethylene single-component adsorption isotherms at 298 K. (h) Three cycles of dynamic column breakthrough curves for an ethane/ethylene (10/90) mixture through a packed bed of JNU-2 under dry condition. This figure has been reproduced from ref. 43 with permission from American Chemical Society, copyright 2019.

Microporous materials are usually the main candidates for the separation of small gas molecules. Recently, Fedin and co-workers however proposed the use of a series of mesoporous MOFs, denoted NIIC-20 (NIIC stands for Nikolaev Institute of Inorganic Chemistry), that exhibit remarkable ethane selective adsorption over ethylene under ambient conditions.[45] NIIC-20 materials are built from zinc dodecanuclear wheel-shaped carboxylate building blocks, delimiting one nanocage (25 Å) and tunable aperture sizes depending on the selected alcohol: ethylene glycol (Et), 1,2-propanediol (Pr), 1,2-butanediol (Bu), 1,2-pentanediol (Pe) or glycerol (Gl), as shown in Fig. 4. Among NIIC-20 candidates, NIIC-20-Bu exhibited the highest ethane/ethylene adsorption selectivity (15.4 for an equimolar ethane/ethylene mixture under ambient condition) because the ethyl pending group leads to an ideal combination of adequate window geometry and sufficient hydrophobicity for optimized ethane-ethane intermolecular interactions. Three adsorption sites located within nanocage (site A and C) and inside smaller pores connecting nanocages (site B) were identified through computational approach based on the dispersion-corrected density functional theory method, as show in Fig.4. The electrostatic potential calculation demonstrated that the values of ethane molecules on site B and C were lower than that of ethane, only higher on site A. Authors also noticed there existed the 4:1:2 ratio of the numbers of site A, B and C, respectively in the NIIC-20-Bu framework, indicating the ethane-selective performance was mainly caused by its more numerous stronger C-H···O hydrogen bonding at site A.

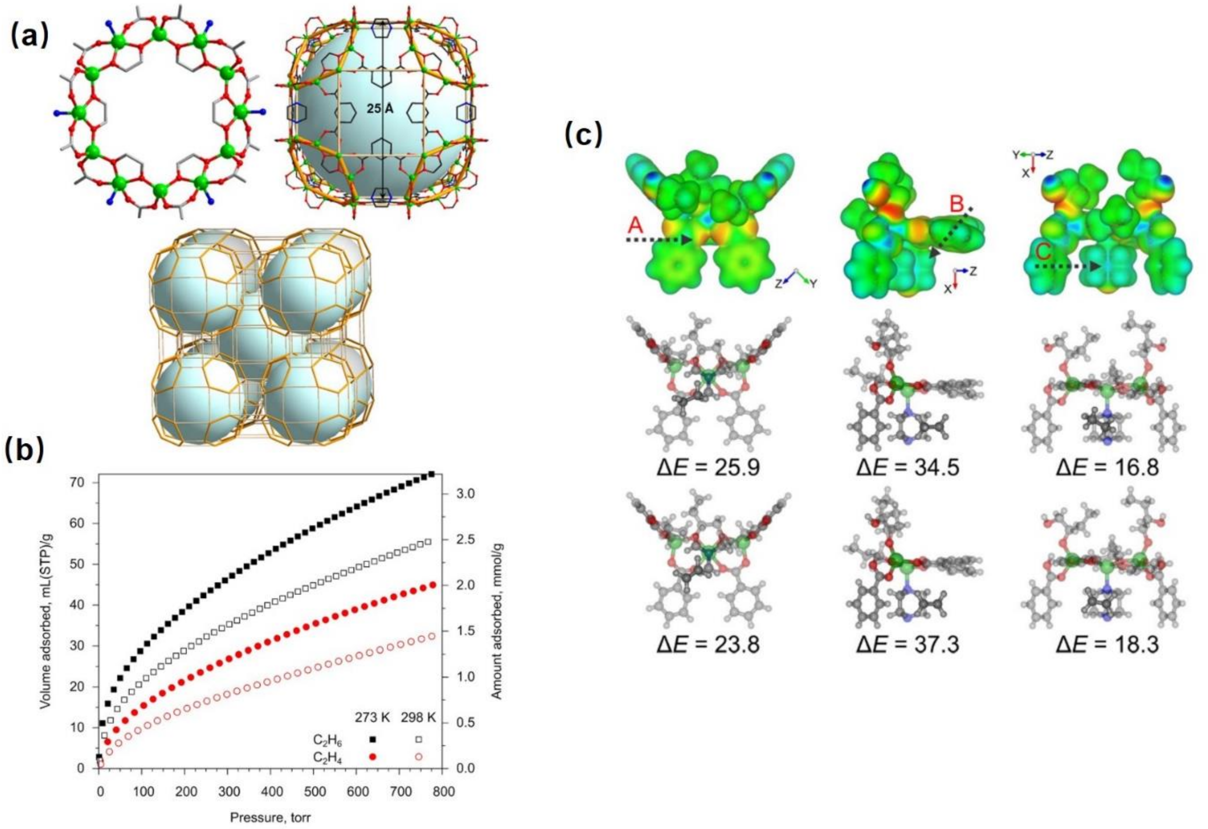

Figure 4: Structure, gases isotherm curves and simulations of NIIC-20.[45] (a) Zn_{12} carboxylate wheel in NIIC-20-Et, the topology of the MOF and the connectivity of nanocages of NIIC-20-Et. (b) The adsorption isotherms of ethane and ethylene at 273 K (filled symbols) and 298 K (empty symbols) for NIIC-20-Bu. (c) Calculated molecular electrostatic potential of NIIC-20-Bu model. This figure has been reproduced from ref. 45 with permission from Angewandte Chemie International Edition, copyright 2020.

Besides hetero-elements (N/O) containing MOFs, fluorinated based MOFs have been also designed for ethane/ethylene adsorption separation to promote hydrogen bonding between ethane and fluorine group into the frameworks. Pinto et al. investigated the benchmark microporous Zr-MOF UiO-66(Zr) decorated with two CF_3 functional groups per organic spacer ($Zr_6O_4(OH)_4(BDC\text{-}2CF_3)_6$, 1,4-BDC-2$CF_3$ = diperfluoromethyl terephthalic acid, UiO stands for University i Oslo) for ethane/ethylene adsorption separation, especially under high pressures, which section will be discussed later.[46] They found that UiO-66-2CF_3 revealed a unique combination of selectivity (value of 2.5 up to 10 bar) for ethane/ethylene and working capacity when two perfluoro groups were present on the aromatic ring (UiO-66-2CF_3), in comparison with the bare UiO-66 material. Considering the working capacity of an adsorbent as the difference between adsorbed amounts at the highest and lowest pressures in a cyclic process, UiO-66-2CF_3 reached an interesting value of about 1 mmol g^{-1} between the atmospheric pressure (1 bar) and 10 bar. Besides, recently Chang and his co-workers discovered another fluorinated MOFs, named as FMOF-2 ($Zn_4O(L)_2$, L=2,2-bis(4-carboxyphenyl) hexafluoropropane, FMOF stands for fluorinated metal-organic framework) which exhibited preferential adsorption of ethane over ethylene at pressures in the range of 0.04 bar with calculated IAST selectivity of 3.3.[47] These examples illustrate the beneficial role of perfluorinated functional groups possess a great potential to provide a good trade-off balance between ethane selectivity and ethane working capacity via more numerous hydrogen bonding interactions for ethane molecules. In addition, all ethane-selective MOFs with relatively weak hydrogen bonding are listed in below detailed Table 2.

Table 2: list of ethane-selective MOFs with relatively weak hydrogen bonding

MOFs	Molecular formula	S_{BET} [m^2 g^{-1}]	Pore [Å]	C_2H_4 uptake [mmol g^{-1}]	C_2H_6 uptake [mmol g^{-1}]	IAST selectivity C_2H_6 over C_2H_4 at 1 bar		Q_{st} [kJ mol^{-1}]		Ref.
				0.3/1 bar	0.3/1 bar	v/v=1/15	v/v=1/1	C_2H_4	C_2H_6	
MAF-49	Zn(batz)	-	1D channel (3.3x3.0)	1.60/1.62 at 316 K	1.62/1.68 at 316 K	-	9	45.5	56.7	48
Peroxo-MOF-74-Fe	$Fe(O)_2$(dobdc)	1073	1D channel (< 11)	1.23/1.79 at 298 K	1.85/2.34 at 298 K	-	4.4	36.5	66.8	42
JNU-2	CuZn(4-pyc)(adenine)	1219	Connected cages (aperture 3.7)	1.17/2.46 at 298 K	1.48/2.8 at 298 K	-	-	26	29	43
Zn-atz-ipa	-	650	-	-/1.24 at 298 K	-/1.25 at 298 K	-	1.7	40	45.8	49
UiO-66-CF_3	$Zr_6O_4(OH)_4$(bcd-CF_3)$_6$	467	Cages (7.5 and 10)	0.5/1.5 (1-10 bar) at 298 K	0.85/1.75 (1-10 bar) at 298 K	-	2.5	-	14	46
TJT-100	(Me_2NH_2) [Co_3(DCPN)$_2$ (μ_3 -OH) (H_2	890	1D channel (8.7 x	1.88/3.11 at 298 K	2.30/3.36 at 298 K		1.2	25	29	44

	O)]·11H_2O		11.6)							
Mn-PNMI	Mn(PNMI)	818	1D channel (9.1 x 13.3)	0.61/1.84 at 298 K	0.82/2.54 at 298 K	1.35		16.9	23.5	
Zn-PNMI	Zn(PNMI)	305	1D channel (8.3 x 11.8)	0.66/1.27 at 298 K	0.9/1.47 at 298 K	1.48		23.8	24.5	50
Cd-PNMI	Cd(PNMI)	264	1D channel (8.5 x 12.6)	0.45/1.27 at 298 K	0.57/1.68 at 298 K	1.4		13.8	19.4	
BUT-10	$Zr_6O_4(OH)_4(FDC)_6$	1726	octahedral cages and tetrahedral cages	1.05/3.25 at 298 K	1.91/4.40 at 298 K					51
FMOF-2	$Zn_4O(L)_2$, (L=2,2-bis(4-carboxyphenyl)hexafluoropropane)	390	6.5	1 at 0.3 bar 303 K	1.15 at 0.3 bar 303 K		3.3 at 0.04 bar, 303 K		37	47
MOF-545/PCN-222	$Zr_6(\mu_3\text{-}O)_4(\mu_3\text{-}OH)_4(OH)_4(H_2O)_4(FeTCPPCl)_2$	2265	Micropores (13) and mesopores (33)	0.8/2.57 at 298 K	1.05/3.12 at 298 k	1.31	1.31	23.6	27.4	52
ZJU-HOF-1	TMBTI (2,4,6-trimethylbenzene-1,3,5-triylisophthalate)	1465	Hexagonal channel (4.6)	2.04/3.67 at 298 K	2.86/4.45 at 298 K		2.25	29	31.5	53
Zn-atz-ipa	$Zn_2(atz)_2(ipa)$	650	1D triangular channel (2.8)	1.5/1.76 at 298 K	1.67/1.76 at 298 K		2	40	45.8	49
Zn-atz-oba	Zn-atz-oba	710	Ultramicropore (3.2 and	1.1/2.05 at 298 K	1.25/2.05 at 298 K		1.27	27		54

Cr-BTC(O_2)	$Cr_3(btc)_2(O_2)_3$	1135	4.4) large square shaped pore	1.75/2.9 at 298 K	2/ 3.25 at 298 K		1.48	23.5	37.2	55
MAF-123-Zn	$Zn_3(vtz)_6$,	871	5.1	1.17 at 298 K	1.39 at 298 K		2	23.2	24.8	56
MAF-123-Mn	$Mn_3(vtz)_6$,	458	6.1	1.17 at 298 K	1.45 at 298 K		1.73	21.2	23	
MAF-123-Cu	$Cu_3(vtz)_6$,	385	4.9	1.35 at 298 K	1.5 at 298 K		1.85	25.7	27.5	
HOF-76a	hexakis(4-carboxyphenylethynyl)-benzene	1100	1D triangular channel (7)	0.55/1.67 at 296 K	1.25/2.95 at 296 K		2	20.5	22.8	57
NIIC-20	$Zn_{12}(iph)_6(1,2\text{-butane-diol})_6(dabco)_3$	1033	Nanocage (25)	0.76/1.4 at 298 K	1.55/2.5 at 298 K		15.4	22.9	24.1	45

1.1.2.3 C-H···π interactions

The π-based interactions benefit from the partial negative charge above and below the plane of the aromatic ring, where the hydrogen atoms in C_2 hydrocarbon molecules can interact favorably with the aromatic or heterocyclic plane in MOFs where long-range ordered aromatic organic part exists in the structures. Due to two extra C-H bonds in ethane, ethane selective adsorption behavior based on C-H···π interactions have been proven in several studies. As the first sample, the investigation of IRMOF-8 by Pinto's group demonstrated the beneficial effect of aromaticity over ethane-selective separation though the naphthalene ring of the framework. In a follow-up work, the ethane-selectivity was demonstrated to be enhanced by the interpenetration of the IRMOF-8 framework.[58,59] Recently Telfer et al. synthesized the robust MUF-15 ($Co_3(\mu_3\text{-}OH)(IPA)_2 \cdot 5(H_2O)$, IPA = isophthalic acid, MUF stands for Massey University Framework) built from inexpensive aromatic ligand and relatively small pores, as shown in Fig. 5.[60] MUF-15 is endowed by zig-zag channels decorated by numerous phenyl groups prone to generate close contacts between guest molecules and MUF-15 efficient gas separation. Based on single component isotherm curves, MUF-15 displayed good working capacity of 1.4 mmol g^{-1} for ethane at range of 0.3 to 1 bar under 293 K. Due to the stronger ethane affinity, dynamic gas breakthrough test under an equimolar ethane/ethylene mixture confirmed the ethane-selective behaviour. Furthermore, DFT calculation illustrated that the bulky size of ethane enables C-H···π interactions between all six hydrogen atoms of ethane and three adjacent phenyl rings, while four hydrogen atoms of ethylene process short contacts only with two parallel edges of the cavity. From an industrial application point of view, MUF-15 exhibited no noticeable loss in the ethane adsorption and separation capacity over 12 cycles. Meanwhile the cost of this adsorbent based on commercial prices, is estimated to be less than \$20 per kg which would be beneficial to the scale up synthesis in the future although the use of cobalt is highly questionable due to environmental and toxicity issues.

Directly observing the adsorption sites of ethane or ethylene molecules will be an efficient way to explain the multiple interactions between guest-host molecules. Zhang and his co-workers synthesized two new ethane-selective NKMOF-8-Br and -Me (Cu(I)(DCiM-X)$_2$, DCiM-Br = 4,5-dicyanoimidazole-bromine, DCiM-Me = methyl-4,5-dicyanoimidazole, NKMOF stands for Nankai MOFs) materials for the separation of C_2 mixtures.[61] Built up from Cu(I) atom and 4,5-dicyanoimidazolate derivatives, NKMOF-8-Br and -Me exhibit narrow square channels along the *a* direction with pore apertures of 6.15 Å x 7.11 Å and 6.21 Å x 6.96 Å, respectively. Both frameworks showed ethane selectivity of 2.7 for NKMOF-8-Br and 1.9 for NKMOF-8-Me in initial ethane/ethylene (v/v=1/1) adsorption test at 298 K under ambient condition. According to the direct observation in the crystal structure of ethane@NKMOF-8-Br, two binding sites were formed by C-H···π interactions (a distance of 3.53 Å) between hydrogen atoms of ethane and C=N double bonds from imidazole groups, which slightly differs in the case of ethylene (a distance of 3.90 Å). Similar interactions (a distance of 3.66 Å for ethane and 3.94 Å for ethylene) were also observed in the case of NKMOF-8-Me.

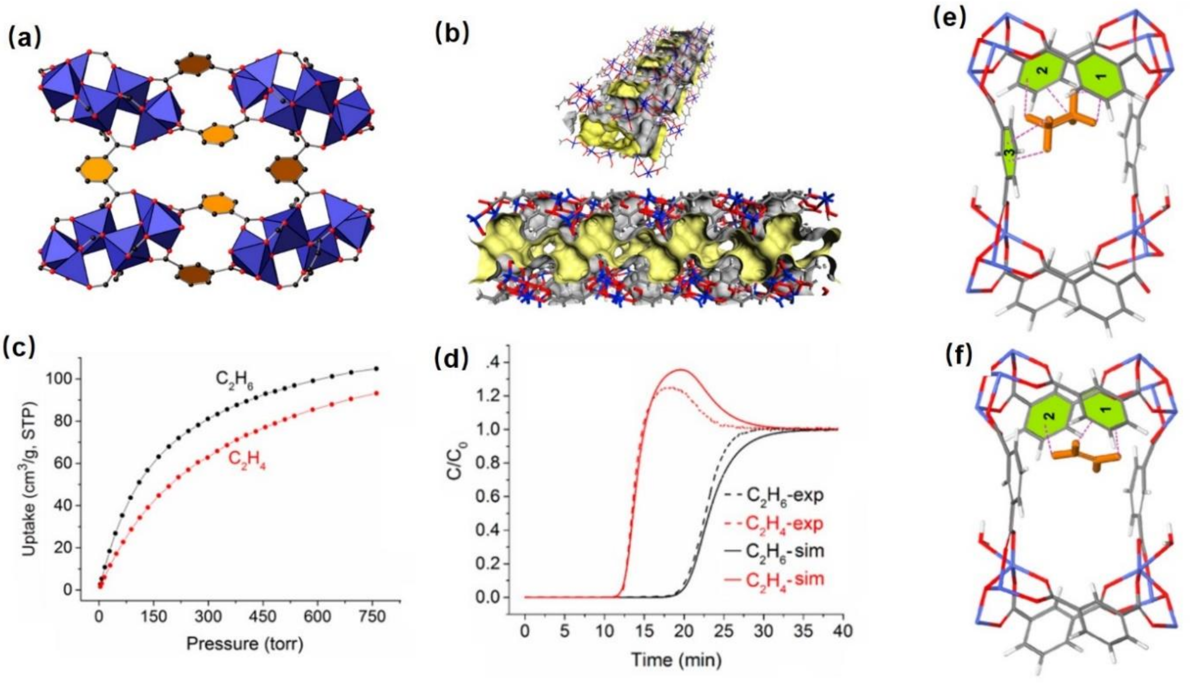

Figure 5: Structure, gases isotherm curves, simulations, C_2 hydrocarbon adsorption performance of MUF-15.[60] (a) 3D channels. (b) Internal structure of the network of pores (c)

Ethane and ethylene single component adsorption isotherms of MUF-15 at 293 K.(d) Simulated and experimental breakthrough curves for an ethane/ethylene (50/50) mixture at 293 K and 1.1 bar in an adsorption column packed with MUF-15. (e) ethane and (f) ethylene adsorption sites (Co, blue; O, red; C, dark gray; H, white) observed by DFT-D_3 calculations. This figure has been reproduced from ref. 60 with permission from American Chemical Society, copyright 2019.

MOFs adsorbents built from aromatic or heterocyclic ligands possess an inert or weakly polar pore surface, generally bringing better structural stability under humid conditions. Changing the ligand from terephthalic acid to naphthalic acid in the 3D microporous UiO-66, rather than in the 1D channels MIL-140, might favor the ethane-selective performance, because of the possibility of the molecules to interact with more than one ligand at a time, which was still reported by Pinto et al.[46] Recently, Chen and his co-workers designed precisely one ultra-microporous Cu-MOF ($Cu(Qc)_2$, Qc = Quinoline-5-carboxylic acid) with heterocyclic ligand, as depicted in Fig. 6.[42] This adsorbent enabled ethane-selective adsorption over ethylene with enhanced ethane/ethylene selectivity (3.4) at 298 K, 1 bar. Multiple C-D···π interactions sites for ethane and ethylene molecule have been identified through high-resolution NPD analysis, depicted in Fig. 6d and e. For instance, the preferential bonding sites could be observed between C_2D_6 molecule and three heterocyclic rings within the rhombic cavity. Low pressure ethane and ethylene adsorption and gas breakthrough tests proved that the inert pore surface and suitable pore size of $Cu(Qc)_2$ could be one potential candidate for ethane/ethylene separation. Very recently, Li et al. optimized the previous synthesis $Cu(Qc)_2$ and proposed a facile and efficient room-temperature synthesis approach with better selectivity (3.7) of ethane over ethylene than before. RT-$Cu(Qc)_2$ would be worth to further exploiting towards practical industrial tests of ethane/ethylene separation, however one shall also consider the question of the long term stability as well as the production at industrial scale of such MOFs based on somehow expensive ligands because C_2 separation is a very large scale application.[62]

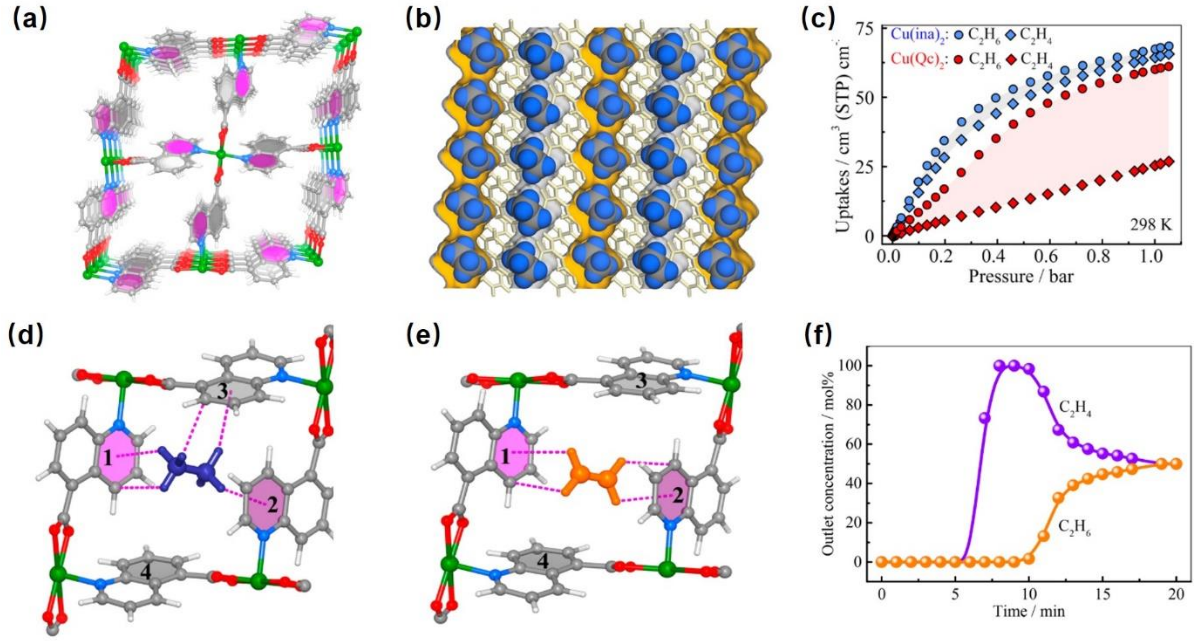

Figure 6: Structure, gases isotherm curves, simulations, C_2 hydrocarbon adsorption performance of $Cu(Qc)_2$.[42] (a) 1D channels. (b) Internal structure of the network of pores. (c) Ethane and ethylene single component adsorption isotherms of $Cu(Qc)_2$ at 298 K. Neutron diffraction crystal structures of $[Cu(Qc)_2]\cdot$ 0.41 C_2D_6 (d) and $[Cu(Qc)_2]\cdot$ 0.16 C_2D_4 (e). (f) Experimental column breakthrough curves for equimolar ethane/ethylene mixture (298 K, 1 bar) in an absorber bed packed with $Cu(Qc)_2$. This figure has been reproduced from ref. 42 with permission from American Chemical Society, copyright 2018.

Recently, Chen et al. designed successfully a UiO-66 type structure via solvothermal reaction of $Th(NO_3)_4$ and 4-(1H-tetrazol-5-yl) benzoic acid (TBA), as shown in Fig. 7.[63] This actinide framework, Azole-Th-1, is the first Th-MOF showing such abnormal adsorption behaviour (selectivity of 1.46 for ethane over ethylene). Based on gas isotherms, the adsorption amount of ethane at 298 K (100.2 cm^3 g^{-1}) was higher than the corresponding ethylene (80.7 cm^3 g^{-1}). This result is in good agreement with their Q_{st} values of ethane and ethylene, giving 28.6 kJ mol^{-1} for ethane, 26.1 kJ mol^{-1} for ethylene at zero coverage. Authors observed there were three main adsorbed areas in Azole-Th-1, including benzene region (I-region), the tetrazol heterocycle region (II-region), and carboxylate region (III-region), relying of the density distribution of ethane at 298 K and 1 bar. The four pairs of C-H···π interactions with region M2 was stronger than that with region M1 (Fig. 7d). In addition, Azole-Th-1 was able to be regenerated five times without any noticeable decrease in performances and relatively high working capacity. In addition, all ethane-selective MOFs with C-H···π interactions were listed in below detailed Table 3. These results are nice from the conceptual point of view but using an actinide MOF for such an application is clearly not relevant.

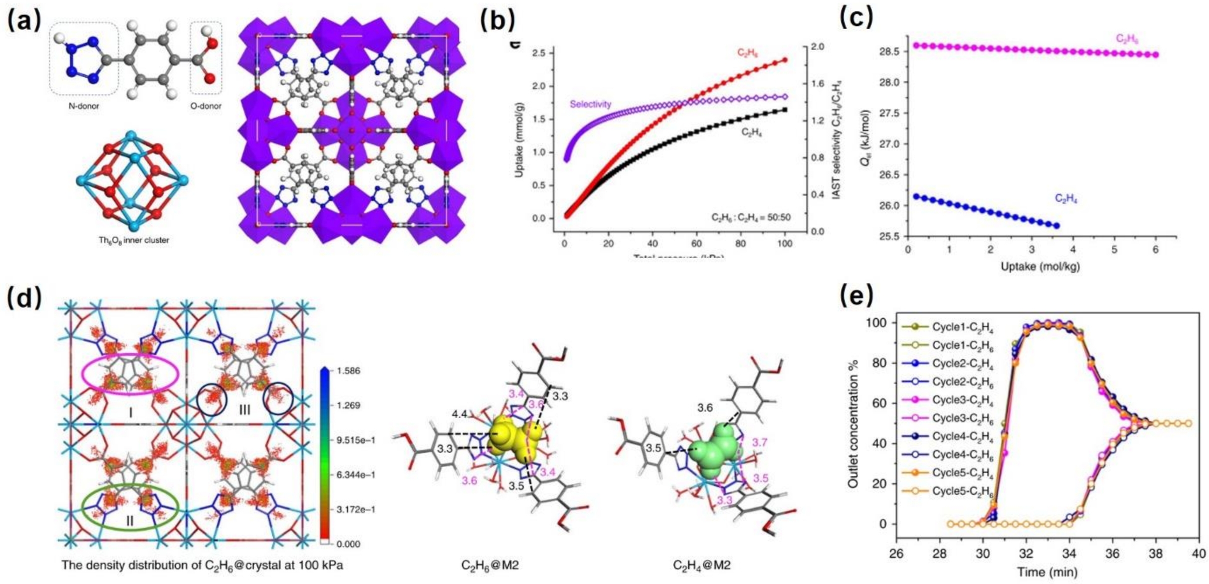

Figure 7: Structure, gases isotherm and analysis, simulations, C_2 hydrocarbon breakthrough test of Azole-Th-1.[63] (a) Ligand TBA, including carboxylic acid donor (O-donor) and tetrazole donor (N-donor), inner core Th_6-cluster drawn alone for clarity (Th_6O_8), unit cell structure in crystal. (b) Predicted mixture adsorption isotherms and selectivity by IAST method for a 50/50 ethane/ethylene mixture at 298 K. (c) The adsorption heat enthalpy of ethane and ethylene, calculated from the single component adsorption data at 298 and 273 K. (d) The density distribution of ethane at 1 bar and 298 K, and the structures of adsorptions for ethane and ethylene at M2 model. (e) Experimental breakthrough curves for ethane/ethylene (50/50, v/v) binary mixture for five cycles at 298 K and 1 bar.

Table 3: list of ethane-selective MOFs with C-H···π interactions

MOFs	Molecular formula	S_{BET} [m^2 g^{-1}]	Pore [Å]	C_2H_4 uptake [mmol g^{-1}]	C_2H_6 uptake [mmol g^{-1}]	IAST selectivity C_2H_6 over C_2H_4 at 1 bar		Q_{st} [kJ mol^{-1}]		Ref.
				0.3/1 bar	0.3/1 bar	v/v=1/15	v/v=1/1	C_2H_4	C_2H_6	
RT-Cu(Qc)$_2$	Cu(Qc)$_2$	251	1D channel (3.3)	0.30/0.56 at 298 K	0.60/2.04 at 298 K	-	3.7	30	35	63
PAF-301	$C_{104}H_{64}$	1880	Diamond cage (5.2)	-/2 at 298 K	-/3 at 298 K	-	3.2	-	-	64
PAF-302(PAF-1)	C200H128	7100	Diamond cage (7.4)	1.5/31.8 (1-10 bar) at 298 K	2/28/2021 (1-10 bar) at 298 K	-	1.5	33.86	33.86	
MUF-15	$Co_3(\mu_3$-OH)(ipa)$_2$	1130	Orthogonal	1.6/2.86 at 293 K	2.16/3.23 at 293 K	-	1.95	28.2	29.2	60

			channels							
PCN-245	$Fe_3(\mu_3\text{-}O)(\mu_2\text{-}O)_3(bpdc)_3$	1743	Two type cages (13.4/10.7)	0.75/2.25 at 298 K	1.15/3.25 at 298 K	-	1.8	20.5	23	65
ZJU-30	$Cu_2(bptc)(H_2O)_2$	228	Intersecting channels (4.0 x 4.0, 5.6 x 5.6, 5.0 x 5.0)	0.86/1.36 at 298 K	1.01/1.47 at 298 K	-	1.7	28.1	29.7	66
IRMOF-8	$Zn_4O(2,6\text{-}ndc)_3$	1360	1D channel 12.6	3.1/7.2 (1-10 bar) at 298 K	4.3/7.2 (1-10 bar) at 298 K	-	1.6	49	54	58
MIL-142A	$Fe_3O(H_2O)_2(bdc)(btb)_{4/3}$	1580	7	1.1/2.8 at 298 K	1.5/3.8 at 298 K	-	1.5	26.2	27.3	67
USTA-30	Yb(5,5’5”-Benzene-1,3,5-triyl-1,1’,1”-trinaphthoicate)-3DMA	592	1D tetragonal channel	1.23/1.89 at 296 K	1.36/1.89 at 296 K		3.8	30	30	68
Azole-Th-1	$Th_6O_4(OH)_4(H_2O)_6(tba)_6$	983	Two Cages (diameter: 11, 12)	1.55/3.29 at 298 K	2.04/4.09 at 298 K	1.44	1.46	26.1	28.6	63
CPOC-301	RC4ACHO (p-phenylenediamine)$_2$	670	1D channel (7)	3.06 at 293 K	3.55 at 293 K		1.4 at 293 K	24.2	32.4	69
DUT-52-Hf	$Hf_6O_4(OH)_4(2,6\text{-}NDC)_6$	1505	Tetrahedral and octahedral cages (8.4 and 10.5)	1.25/3.2 at 296 K	1.9/4.02 at 296 K		1.9 at 296 K	24.1	25.6	70

DUT-8-Cu	Cu_2 (2,6-ndc)$_2$ (dbco)	2370	1D channel	1.92/9.63 (1-10 bar) at 303 K	3.45/10.12 (1-10 bar) at 303 K		1.43 at 303 K	18.3	25.5	71
DUT-8-Ni	Ni_2 (2,6-ndc)$_2$ (dbco)	2440	1D channel	2.27/9.79 (1-10 bar) at 303 K	3.96/10.23 (1-10 bar) at 303 K		1.65 at 303 K	24.1	25.8	
MIL-53-NDC	AlO(2,6-ndc)	1590	1D channel	1/3.15 at 298 K	1.5/4.2 at 298 K		1.53	17	24.2	72
NUM-9a	$Mg_2(tcpe)(\mu_2\text{-}OH_2)(dma)_2$	330	1D channel (4.5 x 4.5)	1.31/2.08 at 298 K	1.59/2.26 at 298 K		1.61	32	36.2	73
Sc-BPDC	ScBPDC	1777.7	Cage (8)	0.9/2.41 at 298 K	1.2/3.42 at 298 K		1.7 at 283 K	15.4	16.4	74
UPC-613	[$(H_4TCPCBCPC)$ $(H_4L\text{-}S)$]	853	Cage (7 and 12)	1.02/2.11 at 298 K	1.33/2.33 at 298 K		1.38	28.51	31.83	75
ZJU-120	$Ni(2,6\text{-}ndc)(ted)_{0.5}$	389	1D channel (4.4)	2.37/3.59 at 296 K	3.22/4.49 at 296 K		2.74 at 296 K	25.5	27.6	76
MIL-125	$Ti_8O_8(OH)_4(bdc)_6$	1435	Octahedral (12) and tetrahedral (6)	1.31/3.67	1.84/4.69		1.5	17	24	77
ZSTU-2	$Ti_6(m_3\text{-}O)_6(m_2\text{-}OH)_6(btb)_2(dmf)_2$	862	1D hexagonal channel (8.5 x 4.6)	1.22/2.12	1.58/2.49		1.7	33	33	
Co(AIN)$_2$	$Co(AIN)_2$	450	1D channel (4.72 x 4.72)	2.86/2.86 at 298 K	2.86/2.86 at 298 K	2.98		34.1	34.7	78
CAU-3-NDCA	$Al_2(OCH_3)_4(2,6\text{-}ndc)$	2350	Distorted tetra hedral and	8.7 (15 bar) at 293 K	9.2 (15 bar) at 293 K		1.54-1.9 (1-15 bar) at	13.6	17.2	79

			octahedral cavities (14 and 15)				293 K			
CPM-35	$Ni_3(OH)(bpdc)_3(tpt)$	724	Two type cages (trigonal bipyrimidal and cylinder shaped)	1.02/2.37	1.35/3.26		1.51	21.4	23,3	80
CPM-81-Co	$Co_3(OH)(fdc)(ina)_3$	1015	Three types of 1D triangle channels	3.1/4.61 at 298 K	4.02/5.02 at 298 K		1.8	24.1	24.2	81
ZJNU-7	$[Cu_4L_3Cl]Cl\cdot 2.7\ DMF$	1180	Four types of cages: 5.0, 6.0, 7.0 and 8.3	1.92/3.88 at 298 K	2.37/3,71 at 298 K	1.58	1.56	36.5	38.3	82
ZJNU-115	$[In_2L]\cdot 2Me_2NH_2\cdot 5DMF\cdot H_2O$	1291	1D channel	3.43 at 298 K	3.84 at 298 K		1.56	27.7	28.2	83
Dia-4-Ni	$Ni(pba)_2$	260	Rectangular 1D channel (7.8 x 9.9)	1.71/3.67 at 298 K	2.44/4.08 at 298 K		1.76	23.59	24.85	84
Dia-4-Co	$Co(pba)_2$		Rectangular 1D channel (7.8 x 9.9)	1.63/3.67 at 298 K	2.40/4.16 at 298 K		2.03	23.37	24.56	
$Fe_2(BDP)_3$		1097	Triangular channel (4.9)	1.4/2.1 at 298 K	1.7/2.25 at 298 K		2.1	19.8	23.9	85

ZJU-HOF-10(sc)	H_4TCHB	1169	1D rhombic-like pore channel (14.07 × 16.73)	1/1.88 at 296 K	1.3/2.19 at 296 K		1.9	21.4	25.4	86
JXNU-9	$Co_8(OH)_4(tca)_4(H_2O)_4$	1952	Small cage (6.3 x10) and 1D channel (12)	0.8/2.4	1.25/3.5		1.7	21.4	23,6	87
NKMOF-8-Br	CuI(L), L=2-bromoimidazole-4, 5-dicarbonitrile	352	1D channel (6.6)	2.77/3.67 at 298 K	3.51/4.22 at 298 K		2.65	33.6	40.8	61
NKMOF-8-Me	CuI(L), L=2-methyl-4, 5-dicarbonitrile	655	1D channel (5.9)	3.26/4.67 at 298 K	3.67/4.82 at 298 K		1.88	37.6	38.4	

1.1.2.4 Multiple weak interactions

Synergistic interactions of several intermolecular interactions, might lead to even better ethane preferential adsorption over ethylene in C_2 hydrocarbons separation. As shown in Fig. 8, Xia et al. reported a Ni-4PyC (4-PyC = 4-pyridylcarboxylic acid) framework exhibited good ethane-selective adsorption over ethylene with selectivity of 1.7 for ethane/ethylene at 298 K, 1 bar and high capacity (3.84 mmol g^{-1}) for ethane in ethane/ethylene(v/v=1/15) mixture through the efficient synergy of hydrogen bonding and C-H···π interactions between ethane molecules and the frameworks.[88] Furthermore, the isosteric heat of adsorption for both molecules (29.07 kJ mol^{-1} for ethane and 27.32 kJ mol^{-1} for ethylene at zero coverage) demonstrated Ni-4PyC had much stronger interactions with ethane molecules. From molecular simulation, authors found that ethane-selective phenomenon was mainly ascribed to multiple weak C-H···π interactions and stronger C-H···N hydrogen bonding with two perpendicular pyridine rings owing to its larger molecular size and higher polarizability compared with these of ethylene. Similarly, a single-walled nickel MOF SNNU-40 (Ni(DBPT), DBPT = 4’-(3,5-dicarboxyphenyl)-4,2’:6’,4’’-terpyridine, SNNU stands for Shaanxi Normal University) reported by Zhai and his co-workers, performed the recorded ethane and ethylene uptake capacities (6.9 and 4.49 mmol g^{-1} at 298 K, 1 bar, respectively) via these multiple molecular interactions.[89]

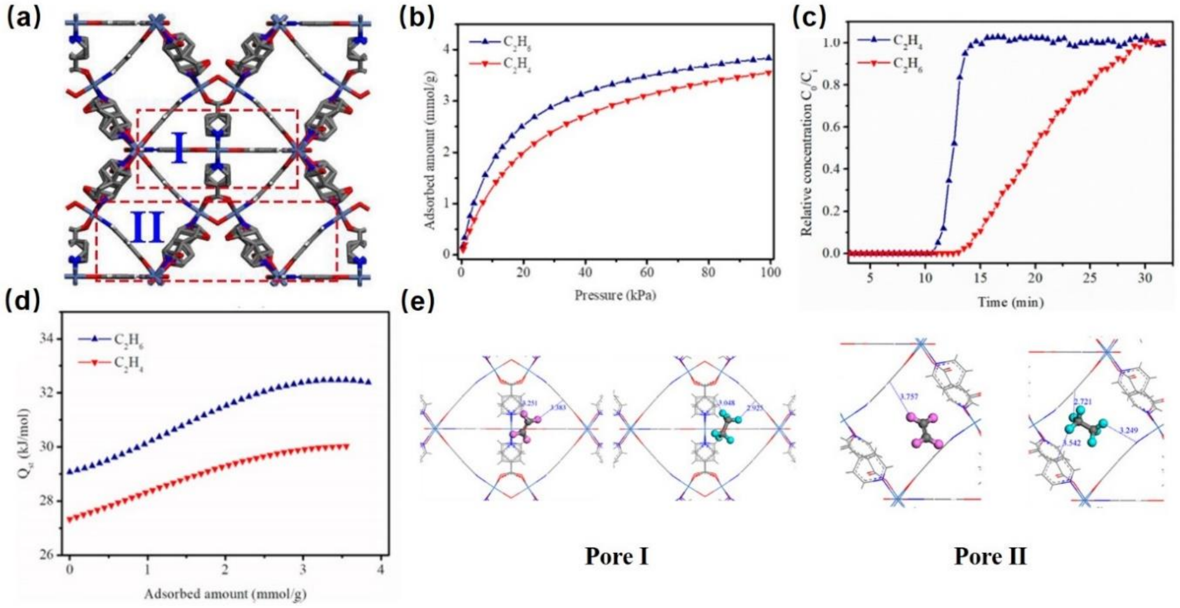

Figure 8: Structure, C_2 hydrocarbon separation and molecular simulations of Ni-4PyC framework.[88] (a) Pore I and Pore II. (b) Ethane and ethylene isotherm curves at 298 K, 1 bar. (c) Breakthrough curves for ethane/ethylene (1:15, v/v) mixtures at 298 K. (d) Q_{st} values calculated from three ethane/ethylene isotherm curves under three different temperatures. (e) Preferential binding sites between a single adsorbed molecule (ethylene and ethane) and the framework: ethylene and ethane in Pore I (left); ethylene and ethane in Pore II (right). This figure has been reproduced from ref. 88 with permission from American Chemical Society, copyright 2019.

By playing on pore engineering such as pore space partition (also called PSP), dynamic spacer installations (also called DSI), etc., this might lead to multi-functional MOFs where the pore space can be rationally partitioned, leading to dense small pore size, high pore volume, and functionalized pore surface, thus opening up a new road for achieving highly efficient C_2 hydrocarbons separation. For example, Feng et al. reported a series of heterometallic crystalline porous materials (CPMs) by their PSP strategy for ethane/ethylene adsorption separation. Nine CPMs structures with a general framework formula $[(M1_2M2)(O/OH)L1_3]L2$, where M1 and M2 are the metals in the trimer (i.e. Co_2V, Co_2Ti, Mg_2V, and Mg_2Ti), L1 is the dicarboxylate ligand for the formation of the acs framework (i.e. bdc, dmbdc, and ndc), and L2 is the pore-partitioning agent (i.e. tpbz, tppy, and tpt), as shown in Fig. 9.[90] All performed ethane preferential adsorption over ethylene in the binary gas mixtures. The high ethane uptakes were accomplished with low adsorption enthalpies ranging from 21.9 to 30.4 kJ mol^{-1} at zero coverage which were caused by widespread weak Van der Waals intermolecular interactions. Besides, ethane molecules dispersed quite well in all the pore space under different pressures as suggested by GCMC simulations. The values of ethane uptake and ethylene recovered in

CPMs were lower than that of Fe_2O_2(DOBDC) (1.93), but higher than those of other prominent ethane-selective MOFs. This looks like a promising strategy but once again the question of the cost and scalability of these more complex MOF materials is on the table.

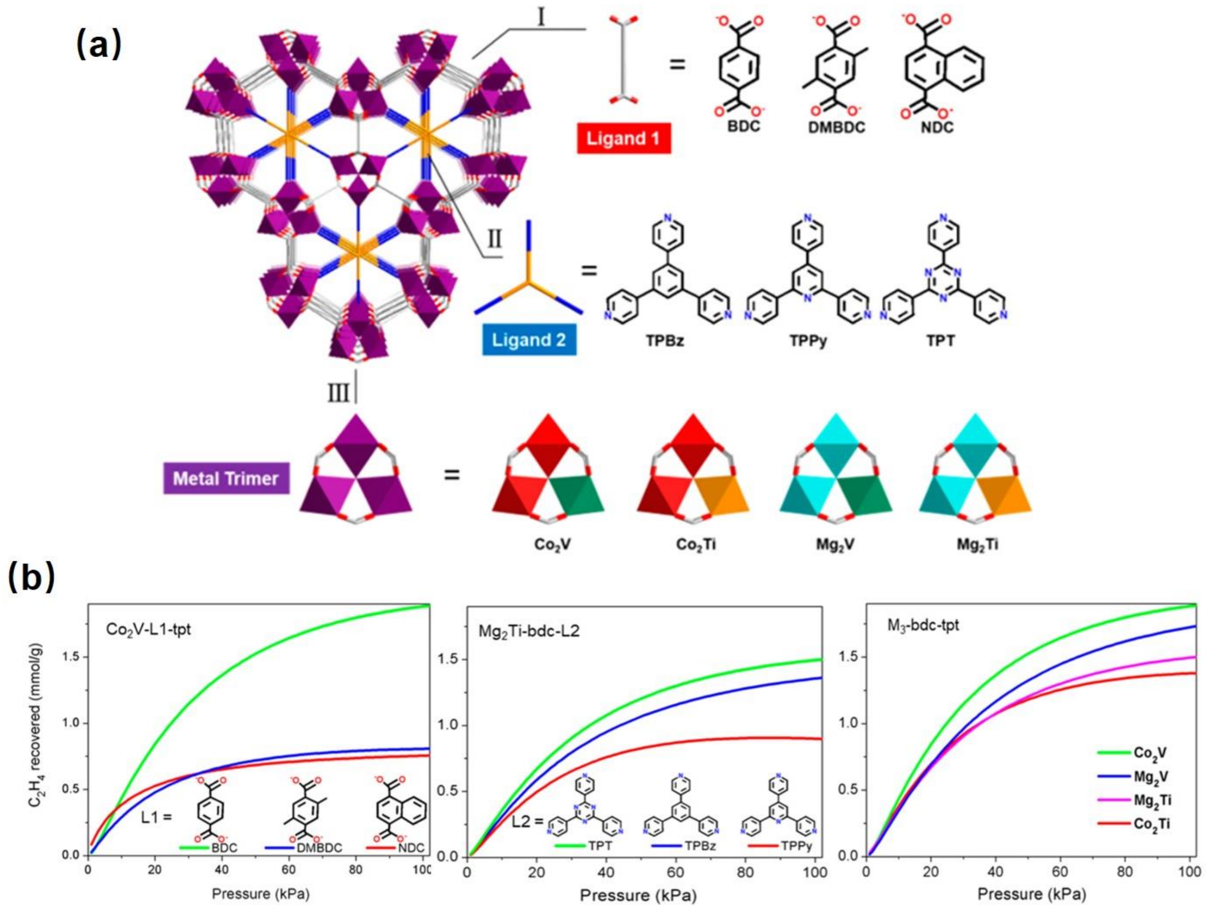

Figure 9: Pore space partition strategy of CPMs and these results of ethylene recovery.[90] (a) Three modules of pacs MOFs studied. Three kinds of Ligand Type 1, three kinds of Ligand Type 2 and four kinds of metal trimers are used (1,4-BDC; DMBDC = 2,5-dimethylterephthalate; NDC = 1,4-naphthalenedicarboxylate; TPBz = 1,3,5-tri(4-pyridyl)-benzene, TPPy = 2,4,6-tris(4-pyridyl)pyridine, TPT = 2,4,6-tri(4-pyridyl)-1,3,5-triazine). (b) Comparisons of separation potential for ethane/ethylene (50/50) mixture: Co_2V-L1-tpt with different dicarboxylate ligands (left); Mg_2Ti-bdc-L2 with different pore-partitioning agents (middle); M_3-bdc-tpt with different metal trimers (right). This figure has been reproduced from ref. 90 with permission from American Chemical Society, copyright 2020.

Recently, Ma et al. constructed under solvothermal conditions a series of multifunctional LIFMs (LIFM stands for Lehn Institute of Functional Materials) through DSI strategy based on prototype LIFM-28 ($Zr_6O_8(OH)_8(Me_2\text{-}BPDC)_4$, Me_2-BPDC = Dimethyl-2,2'-dimethylbiphenyl-4,4'-dicarboxylic acid). For example, through DSI strategy, LIFM-63 exhibited significant reduced pore size (5.6 and 8.6 Å), increased pore volume (0.62 cm^3 g^{-1}) and functional pore surface from proto-LIFM-28 (6.8 and 11.8 Å for pore size and 0.41 cm^3 g^{-1} for pore volume), leading to potentially enhanced confinement effects, multi-site adsorption and higher hydrogen bonding acceptors, especially for ethane with higher polarizability and.[91] From ethane/ethylene isotherm experiments, LIFM-63 (4.8 mmol g^{-1}) presented nearly three times higher ethane capacity compared to its prototypical counterpart, LIFM-28 (1.7 mmol g^{-1}), and much higher than ethylene (3.7 mmol g^{-1}). This illustrated the higher binding affinity of LIFM-63 for ethane over ethylene. Besides, Q_{st} values at high ethane/ethylene coverage for LIFM-63, suggest stronger intermolecular interactions between ethane molecules and the framework which could be ascribed to the crystallographically small pore size and more hydrogen atoms of ethane. Compared with ethylene molecules in LIFM-63, authors found that ethane molecules possessed stronger C-H···F (2.70, 3.36, 3.74 and 3.82 Å), C-H···π interactions (2.86 and 3.56 Å), and Van der Waals force (C-H···O distance ranges from 3.24 to 3.50 Å) between ethane and the framework through theoretical calculations. MOF adsorbents bearing an appropriate pore space and more ethane contact sites have been obtained through pore engineering strategy, however, the poor repeatability and the complex synthesis at small scale cannot let these adsorbents be applied for practical applications. All ethane-selective MOFs with multiple weak interactions were listed in below detailed Table 4.

Table 4: list of ethane-selective MOFs with multiple weak interactions

MOFs	Molecular formula	S_{BET} [m^2 g^{-1}]	Pore [Å]	C_2H_4 uptake [mmol g^{-1}]	C_2H_6 uptake [mmol g^{-1}]	IAST selectivity C_2H_6 over C_2H_4 at 1 bar		Q_{st} [kJ mol^{-1}]		Ref.
				0.3/1 bar	0.3/1 bar	v/v=1/15	v/v=1/1	C_2H_4	C_2H_6	
Ni-4PyC	$Ni_9(\mu\text{-}H_2O)_4(H_2O)_2(C_6NH_4O_2)_{18}$	943	Two types of channels (1D: 6.7 x 6.7 2D: 7.8 x 7.8; 7.5 x 7.5	2.55/3.55 at 298 K	3/3.84 at 298 K	1.7	-	27.32	29.07	88
SBMOF-2	Ca(tcpb)	195	diamond shaped channel (7 x 7)	1.32/1.85 at 298 K	1.51/1.91 at 298 K	1.4	-	29.2	32.3	92

NUM-7A	Mn_2(tcpe)	345	1D channel (4.7 x 7.8)	1.3/1.63 at 298 K	1.66/2 at 298 K	-	1.76	30	35.8	93
CPM-733	Co_2V-bdc-tpt	1328.5	1D channel (7.3)	3.2/5.85 at 298 K	4.8/6.54 at 298 K		1.75	22.5	23.4	
CPM-736	Co_2V-1,4-ndc-tpt	472.5	1D channel (5.9)	2.46/3.56 at 298 K	2.79/3.70 at 298 K		1.48	30.1	30.4	
CPM-738	Co_2V-dmbdc-tpt	1161.5	1D channel (5.9)	2.7/4.18 at 298 K	3.11/4.29 at 298 K		1.42	26.5	27.9	
CPM-723	Co_2Ti-bdc-tpt	1369.8	1D channel (6.8)	3.28/6.12 at 298 K	4.18/6.34 at 298 K		1.5	20	21.7	90
CPM-223	Mg_2Ti-bdc-tpt	1460.6	1D channel (6.8)	2.95/5.82 at 298 K	4.09/6.48 at 298 K		1.57	25	25.4	
CPM-223-tppy	Mg_2Ti-bdc-tppy	1599.1	1D channel (6.8)	3.52/6.74 at 298 K	4.18/6.58 at 298 K		1.28	22.6	25	
CPM-223-tpbz	Mg_2Ti-bdc-tpbz	1661.7	1D channel (6.8)	2.86/5.74 at 298 K	3.89/6.32 at 298 K		1.51	23.3	21.9	

CPM-233	Mg_2V-bdc-tpt	1597.9	1D channel (6.8)	3.2/5.99 at 298 K	4.8/6.84 at 298 K		1.64	26.7	27.3	
CPM-238	Mg_2V-dmbdc-tpt	1444.4	1D channel (5.9)	2.87/4.82 at 298 K	3.44/5.1 at 298 K		1.43	24.4	24.7	
LIFM-63	$Zr_6O_8(OH)_8(Me_2$-bpdc$)_4(H_2$bpdc)	1486	Channel (5.6 x 5.6) and tetrahedral cages (*ca.* 5)	0.75/2.1 at 298 K	1.05/2.86 at 298 K		1.56	27.5	26.9	91
IISERP-MOF2	[Ni-$(4PyC)_2$]·dmf	496	1D channel (4.6)	3.26/3.26 at 298 K	3.27/3.27 at 298 K		-	50	56.7	94
NPU-1	$Mn_5^{II}Mn^{III}(\mu_3$-$O)_{2}$-$(CH_3COO)_3$(Tripp$)_2(L)_3$ (L = BDC^{2-}),	1396	Cage (7.4)	2/4.2 at 298 K	2.8/4.5 at 298 K		1.32	23.95	29.1	95
PCN-250	$Fe_3(\mu_3$-$O)(\mu_2$-$O)_3$(abtc$)_3$	1470	Two type cages (5.5 x 9.6)	2.2/4.22 at 298 K	3.4/5.21 at 298 K	-	1.9	21.1	23.6	96
SNNU-40	Ni(dbpt)	2233.8	1D channel (7.8 x 7.8)	1.02/4.49 at 298 K	1.63/6.9 at 298 K		1.58	18.1	18	89

1.1.2.5 Gate-opening effect

Gate-opening effect occurs when the framework is stimulated through host guest interactions for a given molecule at a certain pressure. Such behavior was observed two decades ago by

Kaneko. In general, the gate opening pressure of each molecule shows a guest dependency. This effect majorly happens in ZIFs (ZIFs stand for zeolitic imidazolate frameworks), a subclass of MOFs, bearing quite rigid positions of the metal centers and flexible of imidazolate ligands. The ligands can rotate (flip) around the M-M axis, thereby precisely modifying the size of the pore aperture, leading to molecular sieving separations of light hydrocarbons. In 2010, ZIF-7 ($Zn(PhIm)_2$, PhIm = benzimidazolate) was the first reported MOF achieving ethane-selective adsorption over ethylene using gate-opening effect between ethane molecule and the framework.[97] The specific threshold pressures control the uptake and release of individual molecules selectively, which could be obviously observed from the hysteresis isotherms of ethane and ethylene. Gascon et al. speculated that because of the three-fold symmetry of the methyl groups, ethane molecules fitted best in the largest opening of the ZIF-7 cage (a three-lobe structure formed by three benzene rings); hence, they could penetrate at lower pressure than ethylene. Compared to ZIF-7, ZIF-9 ($Co(PhIm)_2$) based on cobalt metal nodes was investigated by Keil and his co-workers this framework exhibited better ethane preferential adsorption over ethylene at special gate-opening pressure.[98] The conformational change of ZIF-9 for ethane adsorption happened at 0.1 bar which is little higher than that of ZIF-7 (below 0.1 bar). More important factor is that the gate-opening pressure of ZIF-9 for ethylene is close to 0.4 bar which is higher than that of ZIF-7 (0.2 bar). Unfortunately, authors didn’t provide any breakthrough results, to further assess the potential to ethane/ethylene separation. For C_2 hydrocarbons separation using ZIFs, the gate-opening effect comes from the guest-host interactions and the external stimulus (such as pressures, temperatures) which could achieve the precise control of guest diffusion rates and the apertures/window size of channels/cages. However, the main disadvantage is ethylene molecule can also enter into the pore after the gate open is triggered by ethane molecules in the mixed C_2 adsorption measurements under realistic conditions, which can decrease the ethane selectivity. Despite the exceptional thermal and chemical stability, ZIFs tend to exhibit poor mechanical stability, which is also another barrier for its practical application, because the crystallinity can be lost irreversibly at high pressures, manual packing or ball milling. The ethane-selective MOFs with gate-opening effect were listed in below detailed Table 5.

Table 5: list of ethane-selective MOFs with gate-opening effect

MOFs	Molecular formula	S_{BET} [m^2 g^{-1}]	Pore [Å]	C_2H_4 uptake [mmol g^{-1}]	C_2H_6 uptake [mmol g^{-1}]	IAST selectivity C_2H_6 over C_2H_4 at 1 bar		Q_{st} [kJ mol^{-1}]		Ref.
				0.3/1 bar	0.3/1 bar	v/v=1/15	v/v=1/1	C_2H_4	C_2H_6	
ZIF-7	$Zn(PhIM)_2$	362	Cage (aperture 2.9)	0.2/1.8 at 298 K	1.7/1.9 at 298 K		2.2	24	27	97

ZIF-4	Zn(Im)$_2$	300	Cage (aperture 2)	1.8/2.1 at 293 K	2.1/2.25 at 293 K	2 (12bar) at 293 K	-	-	99
ZIF-318	Zn(Mim)(TFMlm)	835	Cage (aperture 3.4)	0.25/1 at 303 K	0.5/1.5 at 303 K	1.43	-	-	100
ZIF-8	Zn(Mlm)$_2$	1900	Cage (aperture 3.4)	2.6/7 (1-8 bar) at 298 K	4.2/7.6 (1-8 bar) at 298 K	1.85			101
ZIF-69	Zn(NO$_2$-IM)(ClBzIM)	890	Cage (aperture 4.4)	0.87/1.75 at 298 K	1.2/2.1 at 298 K	1.65	23.5	26	102
ZIF-9	Co(PhIM)$_2$	500	Cage (aperture 2.9)	0.2/2.4 at 293 K	2.25/2.45 at 293 K	-	-	-	98

1.1.3 Separation from multicomponent systems

Apart from the above assessment of the MOF adsorbent using only C$_2$ hydrocarbon mixture under ambient pressure, it is essential to evaluate the purity of ethylene, capacity of impurities and renderability of the adsorbents under real conditions, such as multicomponent gas mixtures, high pressures. For instance, in the downstream products of the practical steam pyrolysis process, several other gas contaminants such as carbon dioxide, acetylene, propylene, propane, etc., lead to heavily competitive adsorption behaviour with ethylene, decreasing the purity and capacity of the adsorbents. In current industrial platform, ethylene is generated by stepwise removal: carbon dioxide is removed using caustic soda which is a corrosive, non-environmentally friendly chemical. Acetylene is eliminated via catalytic hydrogenation with noble-metal catalysts at high temperature and pressure which is a high risk and high-cost operation. Cryogenic distillation is typically employed to remove ethane under high pressure and low temperature which leads large energy penalty. To mitigate the high energy footprint of ethylene production, so far, only relatively few studies have been reported on strategies that integrate physisorbents for enhanced ethylene purification in the ternary or even quaternary components systems. The promise of these adsorbents lies on their relatively low energy consumption and operational cost compared to the present processes thanks to facile regeneration/recycling. From an applications perspective, only few successful studies have shown significantly high working capacity of impurities for adsorbents when operated under high pressures, to allow regeneration of the MOF at pressures close to ambient, i.e., 100 kPa or moderate vacuum in PSA process. Hence, this part will be dedicated to discuss examples displaying how to solve the C_2 hydrocarbons separations from practical conditions of view. We believe that they will open a new horizon to explore more promising adsorbent candidates for practical ethylene purification in the next future.

1.1.3.1 C_2 hydrocarbons separation from multicomponent systems

In general, after carbon dioxide and water removal (that are easier to remove) the two main impurities are acetylene and ethane in stream cracking of naphtha, and simultaneous removal of these from ethylene streams has been investigated using MOFs adsorbent since 2018. As the first ethylene purification MOF adsorbent from ternary gas mixture, TJT-100 ($(Me_2NH_2)[Co_3(DCPN)_2(\mu_3\text{-}OH)(H_2O)]\cdot 11H_2O$, DCPN = 5-(3',5'-dicarboxylphenyl) nicotinic acid, TJT stands for Tianjin university of Technology) reported by Lu et al., exhibited a three-dimensional porous architecture with a high density of carboxylates on the surface of 1D pores.[44] It is worth noticing that there were Me_2NH^{2+}cations to balance the negative charge of the host framework, as shown in Fig. 10. Authors calculated the Q_{st} values of 31, 29 and 25 kJ mol^{-1} for acetylene, ethane and ethylene through single-component adsorption isotherms measured at 273, 298 and 318 K. To investigate the real separation potential, ternary (acetylene/ethane/ethylene = 0.5/0.5/99 v/v/v) breakthrough test was carried out. Only a single adsorption-desorption cycle was required to achieve an ethylene purity of greater than 99.997%. Because single crystals of TJT-100 were hard to obtain, the nature of gas adsorption sites within the frameworks was investigated through Grand Canonical Monte Carlo (GCMC) simulations. GCMC calculations revealed that acetylene molecules are bound to two uncoordinated carboxyl oxygen atoms, $C\text{-}H\cdots O_9$ and $C\text{-}H\cdots O_{11}$ through hydrogen-bonding interactions. Also, acetylene molecules are close to Me_2NH^{2+}cations and linkers in the framework of TJT-100. In addition, the high uptake of ethane in activated TJT-100 could be attributed to the existence of a large number of weak interactions between the anionic oxygen atoms and the slightly polarizable C-H bonds of ethane. But, for ethylene molecules, only weak Van der Waals interactions were shown between ethylene molecules and Me_2NH^{2+} cations as concluded from GCMC simulations. Because the structure was composed of Me_2NH^{2+} cations, the usage of toxic solvent and solvothermal synthesis for this adsorbent lead to the potential environmental issue and the difficulty of large-scale application. In terms of real conditions, another losing assessment of this adsorbent is the regenerability and the separation performance under high pressures.

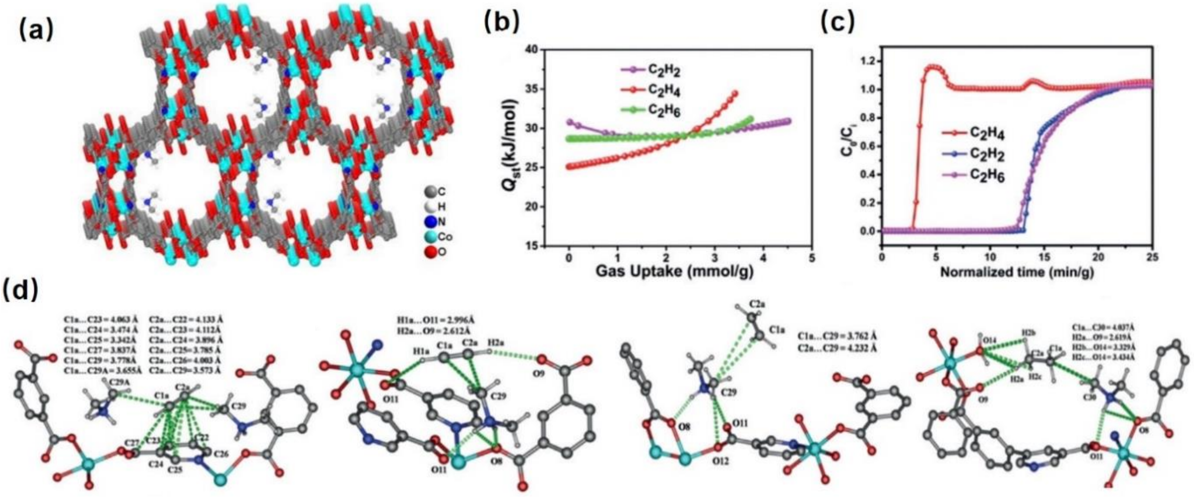

Figure 10: Structure, Q_{st} and breakthrough result for ternary components, GCMC simulations of TJT-100.[44] (a) The structure viewed along the b axis. (b) The calculated Q_{st} values of activated sample for ethane, ethylene and acetylene. (c) Breakthrough curves of activated sample for acetylene/ethane/ethylene = 0.5/0.5/99, v/v/v measured at 298 K and 1 bar. (d) Results of the GCMC simulations, showing the preferential adsorption sites for acetylene (left and middle left), ethylene (middle right) and ethane(right) in activated sample. This figure has been reproduced from ref. 44 with permission from Angewandte Chemie International Edition, copyright 2018.

As mentioned above for Azole-Th-1, authors observed that ethylene purification could be realized not only from a binary ethane/ethylene (1/9 v/v) mixture but also using a ternary mixture of ethane/acetylene/ethylene (9/1/90 v/v/v) at 298 K, 1 bar. However, the acetylene adsorption mechanism in Azole-Th-1 wasn't elucidated. Later, Zaworotko's group introduced a new hexanuclear Mn cluster as a building block and terephthalate group for the isostructural 9-connected (9-c) NPU-1 ($Mn_5(II)Mn(III)(\mu_3\text{-}O)_2\text{-}(CH_3COO)_3(Tripp)_2(BDC)_3$, Tripp = 2,4,6-tris(4-pyridyl)pyridine, NPU stands for Northwestern Polytechnical University), which can effectively capture acetylene and ethane from the 1/1/1 gas mixture and afforded polymer-grade ethylene in the effluent stream.[95] From Q_{st} calculations for acetylene, ethane, and ethylene, NPU-1 possessed the values of 27.88, 29.10 and 23.95 kJ mol^{-1} at low loading, respectively. Through molecular simulations, authors found that there existed more stronger C-H···O from carboxylate group and C-H···π interactions between acetylene/ethane molecules and NPU-1 framework, compared with that of ethylene. Almost at the same time, Sun et al. reported that two new ftw-type MOFs, UPC-612, 613 ($Zr_6O_8(L)_3$, L612 = (Tetrakis(4-carboxybiphenyl)cyclobutadiene)cyclopentadienylcobalt, L613 = (Tetrakis(4-carboxyphenyl)cyclobutadiene)cyclopentadienylcobalt) could be obtained with introduction of a cyclopentadiene cobalt functional group in MOF-525.[75] These two MOFs also performed acetylene and ethane selective adsorption over ethylene at room temperature through stronger van der Waals force exerted by the modified cyclopentadiene ring on acetylene and ethane. Furthermore, as the first case of a single adsorbent for one-step ethylene purification, large proportion (1/1/1) of acetylene, ethylene and ethane has been applied in recyclable breakthrough tests. Because the adsorbents for acetylene/ethylene separation usually are appropriate for ethylene selective adsorption over ethane, thus they are unable to adsorb ethane preferentially any more, thus realizing one-step ethylene purification in acetylene/ethylene/ethane mixture. Recently, Chen and his co-workers reported another strategy to design one efficient adsorbent UiO-67-$(NH_2)_2$ (Zr_6O_8(BPDC-$(NH_2)_2$)) based on ethane-selective MOF (UiO-67) through immobilization of some acetylene-affinity sites.[103] As shown in Fig. 11, GCMC simulations and *in situ* infra-red spectroscopic studies illustrated that after incorporating -NH_2 functional groups, the large tetrahedral pore could be partitioned to form small pore pockets at each corner site (Fig. 11b), which provides more suitable pore confinement and additional binding sites for this C_2 hydrocarbons adsorption. To elucidate the changes observed on acetylene uptake and binding energy before and after amino functionalization, authors carried out in situ infra-red spectroscopy measurements of acetylene adsorption in UiO-67-$(NH_2)_2$. The results demonstrated that the adsorbed acetylene molecules exhibit interactions with the carboxylates and -NH_2 groups. The feed gases in the industrial production of high-purity ethylene typically contain a small amount of water and acidic gases. Authors investigated that the separation capacity of UiO-67-$(NH_2)_2$ had almost unchanged after six cycles of dynamic column breakthrough experiments with 60% humidity. From the industrial applications, high pressure (5-15 bar) usually is required for the adsorption operation to increase the working capacity of ethane and acetylene. UiO-67-$(NH_2)_2$ still exhibited the high selectivity and working capacity for acetylene and ethane over ethylene when carried out the breakthrough test under 5 bar.

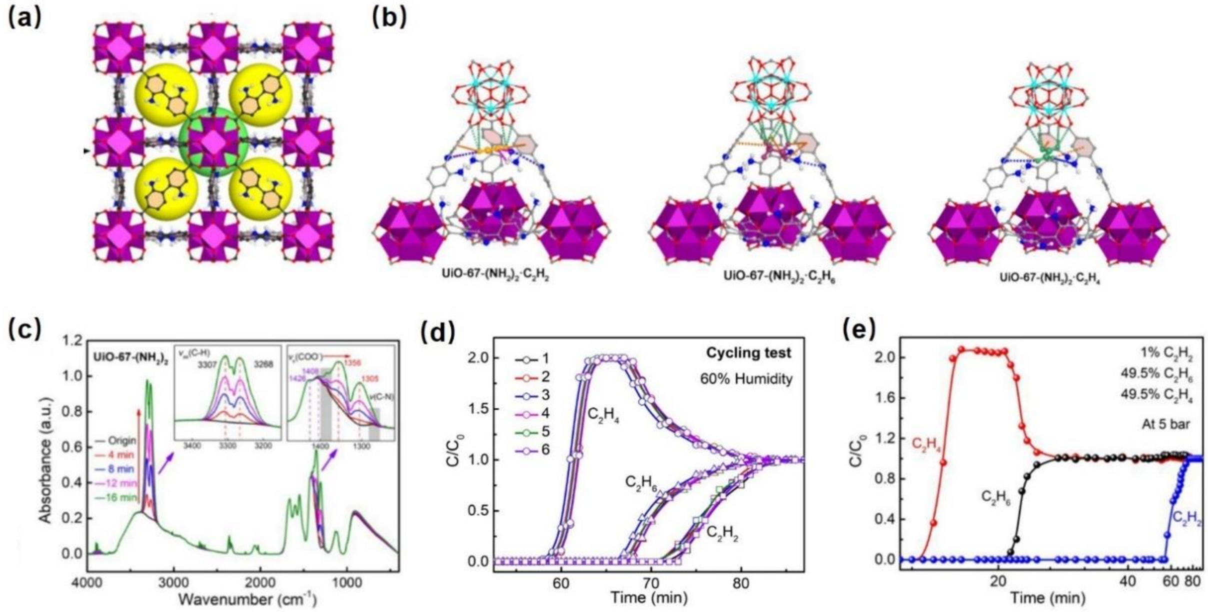

Figure 11: Structure, theoretical and experimental results of UiO-67-$(NH_2)_2$.[103] (a) The isostructural UiO-67 with tetrahedral (yellow) and octahedral (green) cages. (b) Adsorption binding sites for acetylene (left), ethane (middle) and ethylene (right) molecule binding sites

by theoretical calculations. (c) *In situ* FT-IR spectra of the activated sample exposed to acetylene gas at room temperature. (d) The cycling tests of 1/49.5/49.5 acetylene/ethane/ethylene mixture with a flow rate of 1.25 mL min^{-1} in an absorber bed packed with activated sample for a wet ternary mixture under 60% humidity. (e) Experimental breakthrough curve for 1/49.5/49.5 acetylene/ethane/ethylene mixture at 298 K and 5 bar. This figure has been reproduced from ref. 103 with permission from American Chemical Society, copyright 2021.

As mentioned above, it is an inevitable issue that there exists several kinds of impurities or by-products in naphtha cracking steams. So far, there are only two cases which could realize one-step ethylene purification from quaternary mixtures (acetylene/ethylene/ethane/carbon dioxide) through physisorbents. It's worth noting both came from Zaworotko's group. They developed firstly synergistic sorbent separation technology (SSST) concept which could achieve one-step ethylene purification from quaternary components.[49] Three porous sorbents (Zn-atz-ipa, atz = 3-amino-1,2,4-triazolate, SIFSIX-3-Ni, SIFSIX = SiF_6^{2-}, 3 = pyrazine, and TIFSIX-2-Cu-i, TIFSIX = TiF_6^{2-}, 2 = 4,4'-dipyridylacetylene, i = interpenetrated) were tandemly-packed in a single column to sequentially remove ethane, carbon dioxide, and acetylene, respectively. However, the interplay of packing sequence and gas mass transfer in SSST could make industrial-scale processes infeasible. For example, a column with looser packing offered much-reduced performance of ethylene purification. After SSST, he and his co-workers reported a completely new strategy was called as one-sorbent separation technology (OSST).[54] A ultra-microporous sorbent Zn-atz-oba (H_2oba = 4,4-dicarboxyl diphenyl ether; Hatz = 3-amino-1,2,4-triazole), enables to co-adsorb acetylene, ethane, and carbon dioxide from quaternary components. The pcu topology framework of Zn-atz-oba was built from oba^{2-} ligands and 2D undulating layers which formed by dinulear Zn cluster and atz- anions, as shown in Fig. 12. From gas isotherm curves, this framework performed higher uptake of acetylene, ethane, and carbon dioxide at 298 K across the entire pressure range tested, 0-1 bar, especially in the low-pressure region, 0-0.02 bar. Based on the isotherm curves at 273, 298 K, the values of adsorption enthalpy were 30.0 kJ mol^{-1} for ethane, 29.0 kJ mol^{-1} for carbon dioxide, 27.5 kJ mol^{-1} for acetylene and 27.0 kJ mol^{-1} for ethylene, in agreement with a one-step ethylene purification from quaternary components and a relatively low energy footprint for regeneration. For instance, the regeneration of this adsorbent was achieved with 140 min under Helium flow of 20 cm^3 min^{-1} under ambient conditions (298 K and 100 KPa) Through the quaternary components' breakthrough experiment test, polymer grade purity ethylene could be collected at the outlet of one-adsorbent packed column at 298 K, 1 bar. Authors observed there was no loss of ethane retention time after ten cycles of breakthrough experiments, indicating Zn-atz-oba possess good recyclable on ethylene purification. Unfortunately, the working capacity of this framework reduced under a relative humidity (52%) during breakthrough experiment due to the competitive sorption of water molecules with other four gases. Nevertheless, ethylene with effluent purity >99.95% was collected at the column outlet in the presence of water vapor.

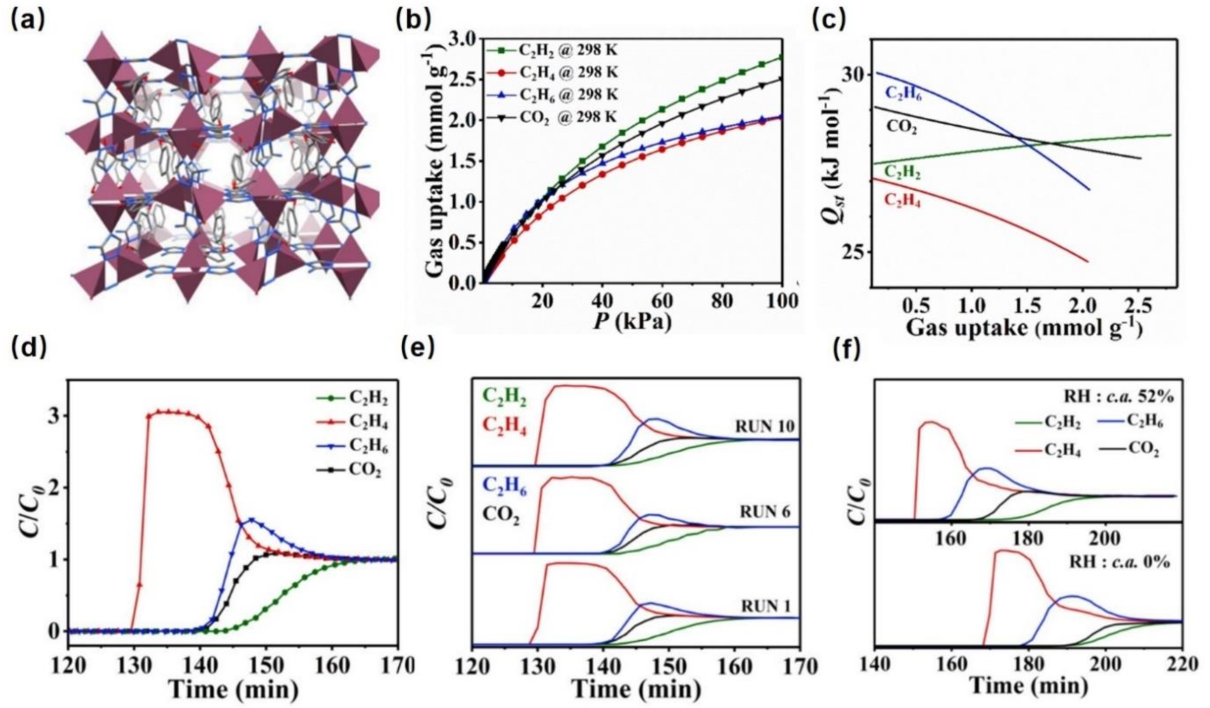

Figure 12: Structure and gas sorption properties of Zn-atz-oba.[54] (a) The pore structure. (b) Gas sorption isotherms at 298 K (c) Adsorption enthalpy profiles (Q_{st}). (d) Acetylene/ethylene/ethane/carbon dioxide (1/1/1/1) separations equimolar mixtures; total gas pressure 1bar; total gas flow 1.4, 2.1 and 2.8 cm^3 min^{-1}, respectively based on 6.3 g sample packed column (C: Outlet gas concentration, C_0: Inlet gas concentration). (e) Dynamic breakthrough data obtained with the fixed-bed in 1st, 5th, and 10th cycle when subjected to four-component equimolar mixtures. (f) Equimolar mixtures breakthrough experiment in the presence of water vapor at 288 K and 1 bar based on 7.0 g sample packed column (total gas flow of 2.8 cm^3 min^{-1}).

1.1.3.2 High pressure separation

In general, for gas separation or storage, adsorption at temperatures much lower than ambient is efficient but expensive, because to reach cryogenic temperature needs to use extra refrigeration systems. This is why, when possible, adsorption at room temperature is preferred in industry. The loss of efficiency due to a higher adsorption temperature must then be balanced by the use of higher pressures, essentially in the 5-50 bar range. These conditions also correspond to higher densities of the gas and adsorbed phases and then to more compact equipment for the same operating capacity. In research work, the range is sometimes extended up to 150 bar and even above. Additionally, the adsorption process under high pressure would provide several advantages: 1) increasing the working capacity for ethane/acetylene adsorption; 2) producing the poly-grade ethylene in one cycle step; 3) reducing the energy consumption when the regeneration could operate close to ambient pressure. Unfortunately, scarce MOFs as ethane-selective adsorbent have been tested under high pressures conditions. For that, as the first one, IRMOF-8 ($Zn_4O(2,6\text{-}NDC)_2$, 2,6-NDC = 2,6-naphthalene-dicarboxylic acid) tested by Pinto and co-workers in 2014, exhibited a high working capacity of ethane and ethane selectivity over ethylene in a wide range of pressures (until 10 bar) at near ambient temperature.[58] The authors concluded that high density of the aromatic groups in IRMOF-8 possessed the potential of the ethane-selective adsorption over ethylene via multiple C-H···π interactions. Chang and co-workers investigated the C_2 hydrocarbons adsorption performance using the microporous DUT-8 (M) (MO(2,6-NDC), M = Cu, Ni, Co and Zn, DUT stands for Dresden University of Technology) whose ligand was the same as IRMOF-8, as shown in Fig. 13.[71] Among them, the best material for ethane-selective adsorption was DUT-8 (Cu) which exhibited a higher working capacity of ethane and similar Q_{st} values of ethane/ethylene compared with these of IRMOF-8. Besides, the retention time of ethane molecule was extended at 5 bar by contrast of that at 1 bar, which agrees with the improvement of ethane working capacity when operating under high pressure. Also, the same adsorption performance behaviour could be observed directly showing longer retention of ethane/acetylene compared with that of ethylene at 5 bar.

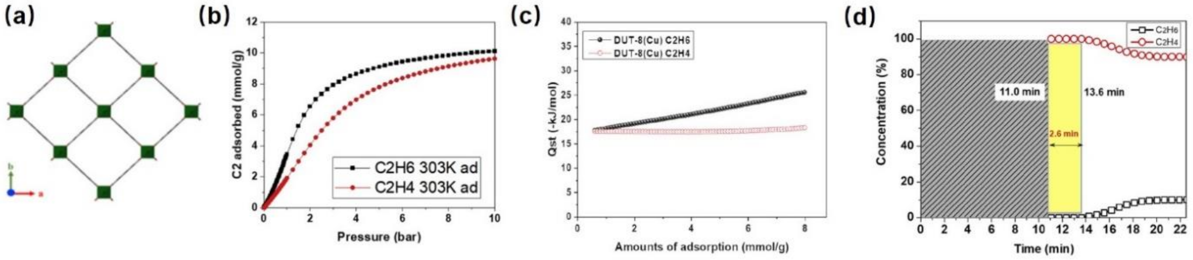

Figure 13: Structure, C_2 hydrocarbon adsorption properties, Q_{st} values and breakthrough test of DUT-8-Cu.[71] (a) The structure with 1D channel calculated from crystallography information. (b) Ethane and ethylene adsorption isotherm curves, at 303 K. (c) Isosteric heats of adsorption calculated from the adsorption isotherms. (d) Experimental breakthrough curves for ethane/ethylene (0.1/0.9) binary mixture at 283 K and pressure of 5 bar. A volume of adsorbent bed is 5.2 mL and total gas flow is 25 mL min^{-1}. The outlet concentration was recorded as a function of time on stream. This figure has been reproduced from ref. 71 with permission from Microporous and Mesoporous Materials, copyright 2020.

Except for the aromatic groups, Pinto et al. also noticed multiple hydrogen bonding interactions could give the same potential to achieve ethane-selective adsorption behaviour under high pressure. To elucidate this hypothesis, they investigated the C_2 hydrocarbon adsorption separation using the perfluorinated microporous UiO-66-2CF_3 which possesses a high density of perfluorinated groups, as shown in Fig.14.[46] According to the single gas isotherm curves, UiO-66-2CF_3 exhibited a stronger affinity with ethane molecules, and the selectivity value of ethane over ethylene could keep at above 2 over a larger pressure range according to IAST calculations. The adsorbed gases could be easily removed by vacuum or inert gas purging due to its low Q_{st} values. Besides, -CF_3 groups could be beneficial due to the hydrophobicity of UiO-66, this would let this adsorbent maintain good adsorption properties after being exposed to water vapor.

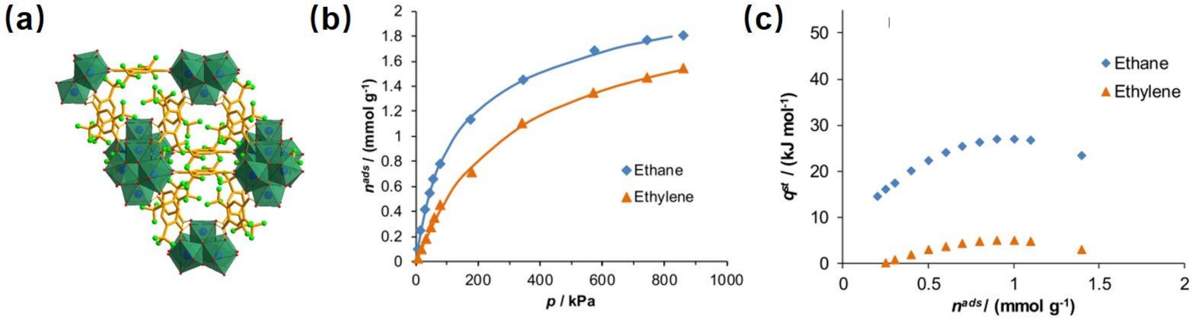

Figure 14: Structure. C_2 hydrocarbon adsorption properties and Q_{st} values of UiO-66-2CF_3.[46] (a) The UiO-66 topology structure with 2CF_3 groups, Zirconium, fluorine and oxygen atoms are blue, green and red spheres, respectively. (b) Ethane and ethylene adsorption isotherms curves at 298 K. The lines represent the virial isotherm fits to the experimental data. (c) Isosteric heats of adsorption calculated from the adsorption isotherms at 298 and 318 K. This figure has been reproduced from ref. 46 with permission from American Chemical Society, copyright 2019.

1.1.4 Conclusion and discussion

The search of efficient MOFs for gas phase separation has been utmostly active during the past decade. MOFs for the separation of C_2 hydrocarbons have been demonstrated to be very promising due to their functionalized pore surfaces and tailored structures that allows different strategies to introduce stronger molecular interactions with the guest molecules. Compared with the ethylene-selective ones, ethane-selective MOFs can achieve the ethylene breakthrough first at the end of the fixed bed column which could obtain poly-grade purity of ethylene in one adsorption-desorption cycle step. In this progress review, recent advances in exploiting MOF materials have been summarized for efficient ethylene purification. The design of the ethane-selective MOFs stems from more ethane affinity sites or non-polar/inert pore surfaces providing stronger interactions between ethane molecules and the wall of the frameworks. Five types of separation mechanism on C_2 hydrocarbon separation have been discussed, and commonly, these ethane-selective MOFs exhibit good selectivity (4.4) and working capacity (2.3 mmol g^{-1} for ethane) in binary mixture under the ambient condition. Whilst, to get closer to practical applications, novel strategies such as the ternary/quaternary components separation, the separation operation under high pressures, have been reported more recently which is a prerequisite to get closer to more efficient procedures on the purification of ethylene. However, it is still far away from the application under the real conditions. For instance, using the shaping/structured MOFs-based materials for the large-scale pilot tests is still missing. The usage of expensive, toxic precursor should be avoided in the synthesis procedure, because that will lead to a very high cost with environmental issues. And it is almost impossible to obtain a kg or ton-scale MOFs-based adsorbent synthesized from poorly scalable, complex precursors.

Besides, very few researchers are seeking for the collaboration with chemical engineers to make real laboratory pilot tests. Meanwhile combining with the modeling to identify valuable materials for this separation. Besides, the energy estimation of the adsorbent regeneration still requires more attention during the whole separation procedure, nevertheless, it was ignored generally by the research community. This is particularly critical for MOFs that require high vacuum for regeneration, which corresponds to a significant energy consumption. We hope this review can provide some insights into the future directions of the design of adsorbents and the different types of measurements of gas adsorption separation used to characterize their adsorption properties.

1.1.5 References

(1) Ruthven, D. M.; Reyes, S. C. Adsorptive separation of light olefins from paraffins. *Microporous and Mesoporous Materials* **2007**, *104*, 59-66.

(2) Eldridge, R. B. Olefin/paraffin separation technology: a review. *Industrial & engineering chemistry research* **1993**, *32*, 2208-2212.

(3) Mersmann, A.; Fill, B.; Hartmann, R.; Maurer, S. The Potential of Energy Saving by Gas-Phase Adsorption Processes. *Chemical Engineering & Technology: Industrial Chemistry-Plant Equipment-Process Engineering-Biotechnology* **2000**, *23*, 937-944.

(4) Sholl, D. S.; Lively, R. P. Seven chemical separations to change the world. *Nature* **2016**, *532*, 435-437.

(5) Wu, Y.; Weckhuysen, B. M. Separation and purification of hydrocarbons with porous materials. *Angewandte Chemie International Edition* **2021**, *60*, 18930-18949.

(6) Baker, R. W. Future directions of membrane gas separation technology. *Industrial & engineering chemistry research* **2002**, *41*, 1393-1411.

(7) Yang, L.; Qian, S.; Wang, X.; Cui, X.; Chen, B.; Xing, H. Energy-efficient separation alternatives: metal–organic frameworks and membranes for hydrocarbon separation. *Chemical Society Reviews* **2020**, *49*, 5359-5406.

(8) Kosinov, N.; Gascon, J.; Kapteijn, F.; Hensen, E. J. M. Recent developments in zeolite membranes for gas separation. *Journal of Membrane Science* **2016**, *499*, 65-79.

(9) Wiessner, F. G. Basics and industrial applications of pressure swing adsorption (PSA), the modern way to separate gas. *Gas Separation & Purification* **1988**, *2*, 115-119.

(10) Sircar, S. Pressure Swing Adsorption. *Industrial & Engineering Chemistry Research* **2002**, *41*, 1389-1392.

(11) Sircar, S.; Cao, D. V. Heat of Adsorption. *Chemical Engineering & Technology* **2002**, *25*, 945-948.

(12) Flanigen, E. M.: Chapter 2 Zeolites and molecular sieves: An historical perspective. In *Studies in Surface Science and Catalysis*; van Bekkum, H., Flanigen, E. M., Jacobs, P. A.,

Jansen, J. C., Eds.; Elsevier, 2001; Vol. 137; pp 11-35.

(13) Flanigen, E.; Mumpton, F. Commercial properties of natural zeolites. *Mineralogy and geology of natural zeolites, Reviews in Mineralogy. MINER. SOC. AMER* **1981**, *4*, 165-175.

(14) Tsapatsis, M. Toward High-Throughput Zeolite Membranes. *Science* **2011**, *334*, 767.

(15) Lv, D.; Zhou, P.; Xu, J.; Tu, S.; Xu, F.; Yan, J.; Xi, H.; Yuan, W.; Fu, Q.; Chen, X. Recent advances in adsorptive separation of ethane and ethylene by C2H6-selective MOFs and other adsorbents. *Chemical Engineering Journal* **2021**, 133208.

(16) Zhou, H.-C.; Long, J. R.; Yaghi, O. M.: Introduction to metal–organic frameworks. ACS Publications, 2012; Vol. 112; pp 673-674.

(17) Kitagawa, S. Metal–organic frameworks (MOFs). *Chemical Society Reviews* **2014**, *43*, 5415-5418.

(18) Kaskel, S.: *The Chemistry of metal-organic frameworks, 2 volume set: synthesis, characterization, and applications*; John Wiley & Sons, 2016; Vol. 1.

(19) Maurin, G.; Serre, C.; Cooper, A.; Férey, G. The new age of MOFs and of their porous-related solids. *Chemical Society Reviews* **2017**, *46*, 3104-3107.

(20) Min Wang, Q.; Shen, D.; Bülow, M.; Ling Lau, M.; Deng, S.; Fitch, F. R.; Lemcoff, N. O.; Semanscin, J. Metallo-organic molecular sieve for gas separation and purification. *Microporous and Mesoporous Materials* **2002**, *55*, 217-230.

(21) Barnett, B. R.; Gonzalez, M. I.; Long, J. R. Recent progress towards light hydrocarbon separations using metal–organic frameworks. *Trends in Chemistry* **2019**, *1*, 159-171.

(22) Cui, W. G.; Hu, T. L.; Bu, X. H. Metal–organic framework materials for the separation and purification of light hydrocarbons. *Advanced Materials* **2020**, *32*, 1806445.

(23) Wang, Y.; Peh, S. B.; Zhao, D. Alternatives to cryogenic distillation: advanced porous materials in adsorptive light olefin/paraffin separations. *Small* **2019**, *15*, 1900058.

(24) Saha, D.; Kim, M.-B.; Robinson, A. J.; Babarao, R.; Thallapally, P. K. Elucidating the mechanisms of Paraffin-Olefin separations using nanoporous adsorbents: An overview. *Iscience* **2021**, *24*, 103042.

(25) Lin, R.-B.; Zhang, Z.; Chen, B. Achieving high performance metal–organic framework materials through pore engineering. *Accounts of Chemical Research* **2021**, *54*, 3362-3376.

(26) Bloch, E. D.; Queen, W. L.; Krishna, R.; Zadrozny, J. M.; Brown, C. M.; Long, J. R. Hydrocarbon separations in a metal-organic framework with open iron (II) coordination sites. *science* **2012**, *335*, 1606-1610.

(27) Lin, R.-B.; Li, L.; Zhou, H.-L.; Wu, H.; He, C.; Li, S.; Krishna, R.; Li, J.; Zhou, W.; Chen, B. Molecular sieving of ethylene from ethane using a rigid metal–organic framework. *Nature materials* **2018**, *17*, 1128-1133.

(28) Safarik, D. J.; Eldridge, R. B. Olefin/paraffin separations by reactive absorption: a review. *Industrial & engineering chemistry research* **1998**, *37*, 2571-2581.

(29) Li, B.; Zhang, Y.; Krishna, R.; Yao, K.; Han, Y.; Wu, Z.; Ma, D.; Shi, Z.; Pham, T.;

Space, B. Introduction of π-complexation into porous aromatic framework for highly selective adsorption of ethylene over ethane. *Journal of the American Chemical Society* **2014**, *136*, 8654-8660.

(30) Mukherjee, S.; Sensharma, D.; Chen, K.-J.; Zaworotko, M. J. Crystal engineering of porous coordination networks to enable separation of C2 hydrocarbons. *Chemical Communications* **2020**, *56*, 10419-10441.

(31) Wang, H.; Liu, Y.; Li, J. Designer Metal–Organic Frameworks for Size-Exclusion-Based Hydrocarbon Separations: Progress and Challenges. *Advanced Materials* **2020**, *32*, 2002603.

(32) Wang, T.; Lin, E.; Peng, Y.-L.; Chen, Y.; Cheng, P.; Zhang, Z. Rational design and synthesis of ultramicroporous metal-organic frameworks for gas separation. *Coordination Chemistry Reviews* **2020**, *423*, 213485.

(33) Xiang, H.; Fan, X.; Siperstein, F. R. Understanding ethane/ethylene adsorption selectivity in ethane-selective microporous materials. *Separation and Purification Technology* **2020**, *241*, 116635.

(34) Yang, S.-Q.; Hu, T.-L. Reverse-selective metal–organic framework materials for the efficient separation and purification of light hydrocarbons. *Coordination Chemistry Reviews* **2022**, *468*, 214628.

(35) Peng, J.; Sun, Y.; Wu, Y.; Lv, Z.; Li, Z. Selectively trapping ethane from ethylene on metal–organic framework MIL-53 (Al)-FA. *Industrial & Engineering Chemistry Research* **2019**, *58*, 8290-8295.

(36) Zhou, P.; Yue, L.; Wang, X.; Fan, L.; Chen, D.-L.; He, Y. Improving ethane/ethylene separation performance of isoreticular metal–organic frameworks via substituent engineering. *ACS applied materials & interfaces* **2021**, *13*, 54059-54068.

(37) Wang, X.; Niu, Z.; Al-Enizi, A. M.; Nafady, A.; Wu, Y.; Aguila, B.; Verma, G.; Wojtas, L.; Chen, Y.-S.; Li, Z. Pore environment engineering in metal–organic frameworks for efficient ethane/ethylene separation. *Journal of Materials Chemistry A* **2019**, *7*, 13585-13590.

(38) Xiang, H.; Ameen, A.; Gorgojo, P.; Siperstein, F. R.; Holmes, S. M.; Fan, X. Selective adsorption of ethane over ethylene on M (bdc)(ted) 0.5 (M= Co, Cu, Ni, Zn) metal-organic frameworks (MOFs). *Microporous and Mesoporous Materials* **2020**, *292*, 109724.

(39) Wang, Y.; Yuan, S.; Hu, Z.; Kundu, T.; Zhang, J.; Peh, S. B.; Cheng, Y.; Dong, J.; Yuan, D.; Zhou, H.-C. Pore size reduction in zirconium metal–organic frameworks for ethylene/ethane separation. *ACS Sustainable Chemistry & Engineering* **2019**, *7*, 7118-7126.

(40) Wu, H.; Chen, Y.; Lv, D.; Shi, R.; Chen, Y.; Li, Z.; Xia, Q. An indium-based ethane-trapping MOF for efficient selective separation of C2H6/C2H4 mixture. *Separation and Purification Technology* **2019**, *212*, 51-56.

(41) Li, L.; Lin, R.-B.; Krishna, R.; Li, H.; Xiang, S.; Wu, H.; Li, J.; Zhou, W.; Chen, B. Ethane/ethylene separation in a metal-organic framework with iron-peroxo sites. *Science* **2018**, *362*, 443-446.

(42) Lin, R.-B.; Wu, H.; Li, L.; Tang, X.-L.; Li, Z.; Gao, J.; Cui, H.; Zhou, W.; Chen, B. Boosting ethane/ethylene separation within isoreticular ultramicroporous metal–organic frameworks. *Journal of the American Chemical Society* **2018**, *140*, 12940-12946.

(43) Zeng, H.; Xie, X.-J.; Xie, M.; Huang, Y.-L.; Luo, D.; Wang, T.; Zhao, Y.; Lu, W.; Li, D. Cage-interconnected metal–organic framework with tailored apertures for efficient C2H6/C2H4 separation under humid conditions. *Journal of the American Chemical Society* **2019**, *141*, 20390-20396.

(44) Hao, H. G.; Zhao, Y. F.; Chen, D. M.; Yu, J. M.; Tan, K.; Ma, S.; Chabal, Y.; Zhang, Z. M.; Dou, J. M.; Xiao, Z. H. Simultaneous Trapping of C2H2 and C2H6 from a Ternary Mixture of C2H2/C2H4/C2H6 in a Robust Metal–Organic Framework for the Purification of C2H4. *Angewandte Chemie* **2018**, *130*, 16299-16303.

(45) Lysova, A. A.; Samsonenko, D. G.; Kovalenko, K. A.; Nizovtsev, A. S.; Dybtsev, D. N.; Fedin, V. P. A series of mesoporous metal-organic frameworks with tunable windows sizes and exceptionally high ethane over ethylene adsorption selectivity. *Angewandte Chemie International Edition* **2020**, *59*, 20561-20567.

(46) Pires, J. o.; Fernandes, J.; Dedecker, K.; Gomes, J. R.; Perez-Sanchez, G.; Nouar, F.; Serre, C.; Pinto, M. s. L. Enhancement of ethane selectivity in ethane–ethylene mixtures by perfluoro groups in Zr-based metal-organic frameworks. *ACS applied materials & interfaces* **2019**, *11*, 27410-27421.

(47) Lee, S. K.; Lee, Y. J.; Cho, K.; Lee, U. H.; Chang, J. S. A Fluorinated Metal-Organic Framework, FMOF-2, for Preferential Adsorption of Ethane over Ethylene. *Bulletin of the Korean Chemical Society* **2021**, *42*, 286-289.

(48) Liao, P.-Q.; Zhang, W.-X.; Zhang, J.-P.; Chen, X.-M. Efficient purification of ethene by an ethane-trapping metal-organic framework. *Nature communications* **2015**, *6*, 1-9.

(49) Chen, K.-J.; Madden, D. G.; Mukherjee, S.; Pham, T.; Forrest, K. A.; Kumar, A.; Space, B.; Kong, J.; Zhang, Q.-Y.; Zaworotko, M. J. Synergistic sorbent separation for one-step ethylene purification from a four-component mixture. *Science* **2019**, *366*, 241-246.

(50) Yang, L.; Wang, Y.; Chen, Y.; Yang, J.; Wang, X.; Li, L.; Li, J. Microporous metal-organic framework with specific functional sites for efficient removal of ethane from ethane/ethylene mixtures. *Chemical Engineering Journal* **2020**, *387*, 124137.

(51) He, C.; Wang, Y.; Chen, Y.; Wang, X.; Yang, J.; Li, L.; Li, J. An ethane-favored metal-organic framework with tailored pore environment used for efficient ethylene separation. *Microporous and Mesoporous Materials* **2021**, *320*, 111096.

(52) Zhang, Y.; Lv, D.; Chen, J.; Liu, Z.; Duan, C.; Chen, X.; Yuan, W.; Xi, H.; Xia, Q. Preferential adsorption of ethane over ethylene on a Zr-based metal–organic framework: impacts of C–H··· N hydrogen bonding. *New Journal of Chemistry* **2021**, *45*, 8045-8053.

(53) Zhang, X.; Wang, J. X.; Li, L.; Pei, J.; Krishna, R.; Wu, H.; Zhou, W.; Qian, G.; Chen, B.; Li, B. A Rod-Packing Hydrogen-Bonded Organic Framework with Suitable Pore Confinement for Benchmark Ethane/Ethylene Separation. *Angewandte Chemie International*

Edition **2021**, *60*, 10304-10310.

(54) Cao, J.-W.; Mukherjee, S.; Pham, T.; Wang, Y.; Wang, T.; Zhang, T.; Jiang, X.; Tang, H.-J.; Forrest, K. A.; Space, B. One-step ethylene production from a four-component gas mixture by a single physisorbent. *Nature Communications* **2021**, *12*, 1-8.

(55) Yang, L.; Zhou, W.; Li, H.; Alsalme, A.; Jia, L.; Yang, J.; Li, J.; Li, L.; Chen, B. Reversed ethane/ethylene adsorption in a metal–organic framework via introduction of oxygen. *Chinese journal of chemical engineering* **2020**, *28*, 593-597.

(56) Jiang, X.; Zhang, T.; Cao, J.-W.; Zhao, C.-K.; Yang, R.; Zhang, Q.-Y.; Chen, K.-J. Effect of pore size on the separation of ethylene from ethane in three isostructural metal azolate frameworks. *Inorganic chemistry* **2020**, *59*, 13019-13023.

(57) Zhang, X.; Li, L.; Wang, J.-X.; Wen, H.-M.; Krishna, R.; Wu, H.; Zhou, W.; Chen, Z.-N.; Li, B.; Qian, G. Selective ethane/ethylene separation in a robust microporous hydrogen-bonded organic framework. *Journal of the American Chemical Society* **2019**, *142*, 633-640.

(58) Pires, J.; Pinto, M. L.; Saini, V. K. Ethane selective IRMOF-8 and its significance in ethane–ethylene separation by adsorption. *ACS applied materials & interfaces* **2014**, *6*, 12093-12099.

(59) Pillai, R. S.; Pinto, M. L.; Pires, J.; Jorge, M.; Gomes, J. R. Understanding gas adsorption selectivity in IRMOF-8 using molecular simulation. *ACS applied materials & interfaces* **2015**, *7*, 624-637.

(60) Qazvini, O. T.; Babarao, R.; Shi, Z.-L.; Zhang, Y.-B.; Telfer, S. G. A robust ethane-trapping metal–organic framework with a high capacity for ethylene purification. *Journal of the American Chemical Society* **2019**, *141*, 5014-5020.

(61) Geng, S.; Lin, E.; Li, X.; Liu, W.; Wang, T.; Wang, Z.; Sensharma, D.; Darwish, S.; Andaloussi, Y. H.; Pham, T. Scalable room-temperature synthesis of highly robust ethane-selective metal–organic frameworks for efficient ethylene purification. *Journal of the American Chemical Society* **2021**, *143*, 8654-8660.

(62) Tang, Y.; Wang, S.; Zhou, X.; Wu, Y.; Xian, S.; Li, Z. Room temperature synthesis of Cu(Qc)2 and its application for ethane capture from light hydrocarbons. *Chemical Engineering Science* **2020**, *213*, 115355.

(63) Xu, Z.; Xiong, X.; Xiong, J.; Krishna, R.; Li, L.; Fan, Y.; Luo, F.; Chen, B. A robust Th-azole framework for highly efficient purification of C2H4 from a C2H4/C2H2/C2H6 mixture. *Nature communications* **2020**, *11*, 1-9.

(64) Huang, L.; Cao, D. Selective adsorption of olefin–paraffin on diamond-like frameworks: diamondyne and PAF-302. *Journal of Materials Chemistry A* **2013**, *1*, 9433-9439.

(65) Lv, D.; Shi, R.; Chen, Y.; Wu, Y.; Wu, H.; Xi, H.; Xia, Q.; Li, Z. Selective adsorption of ethane over ethylene in PCN-245: impacts of interpenetrated adsorbent. *ACS applied materials & interfaces* **2018**, *10*, 8366-8373.

(66) Cai, J.; Yu, J.; Xu, H.; He, Y.; Duan, X.; Cui, Y.; Wu, C.; Chen, B.; Qian, G. A Doubly Interpenetrated Metal–Organic Framework with Open Metal Sites and Suitable Pore Sizes for

Highly Selective Separation of Small Hydrocarbons at Room Temperature. *Crystal Growth & Design* **2013**, *13*, 2094-2097.

(67) Chen, Y.; Wu, H.; Lv, D.; Shi, R.; Chen, Y.; Xia, Q.; Li, Z. Highly adsorptive separation of ethane/ethylene by an ethane-selective MOF MIL-142A. *Industrial & Engineering Chemistry Research* **2018**, *57*, 4063-4069.

(68) He, Y.; Xiang, S.; Zhang, Z.; Xiong, S.; Fronczek, F. R.; Krishna, R.; O'Keeffe, M.; Chen, B. A microporous lanthanide-tricarboxylate framework with the potential for purification of natural gas. *Chemical Communications* **2012**, *48*, 10856-10858.

(69) Su, K.; Wang, W.; Du, S.; Ji, C.; Yuan, D. Efficient ethylene purification by a robust ethane-trapping porous organic cage. *Nature Communications* **2021**, *12*, 1-7.

(70) Gu, X.-W.; Pei, J.; Shao, K.; Wen, H.-M.; Li, B.; Qian, G. Chemically stable hafnium-based metal–organic framework for highly efficient C2H6/C2H4 separation under humid conditions. *ACS applied materials & interfaces* **2021**, *13*, 18792-18799.

(71) Cho, K. H.; Yoon, J. W.; Lee, J. H.; Kim, J. C.; Kim, K.; Lee, U.-H.; Kwak, S. K.; Chang, J.-S. Effect of framework rigidity in metal-organic frameworks for adsorptive separation of ethane/ethylene. *Microporous and Mesoporous Materials* **2020**, *307*, 110473.

(72) Cho, K. H.; Yoon, J. W.; Lee, J. H.; Kim, J. C.; Kim, K.; Lee, U.-H.; Choi, M.; Kwak, S. K.; Chang, J.-S. Pore control of Al-based MIL-53 isomorphs for the preferential capture of ethane in an ethane/ethylene mixture. *Journal of Materials Chemistry A* **2021**, *9*, 14593-14600.

(73) Yang, S.-Q.; Sun, F.-Z.; Liu, P.; Li, L.; Krishna, R.; Zhang, Y.-H.; Li, Q.; Zhou, L.; Hu, T.-L. Efficient purification of ethylene from C2 hydrocarbons with an C2H6/C2H2-selective metal–organic framework. *ACS applied materials & interfaces* **2020**, *13*, 962-969.

(74) Jiang, S.; Li, L.; Guo, L.; Song, C.; Yang, Q.; Zhang, Z.; Yang, Y.; Ren, Q.; Bao, Z. A robust ethane-trapping metal-organic framework for efficient purification of ethylene. *Science China Chemistry* **2021**, *64*, 666-672.

(75) Wang, Y.; Hao, C.; Fan, W.; Fu, M.; Wang, X.; Wang, Z.; Zhu, L.; Li, Y.; Lu, X.; Dai, F. One-step Ethylene Purification from an Acetylene/Ethylene/Ethane Ternary Mixture by Cyclopentadiene Cobalt-Functionalized Metal–Organic Frameworks. *Angewandte Chemie* **2021**, *133*, 11451-11459.

(76) Pei, J.; Wang, J.-X.; Shao, K.; Yang, Y.; Cui, Y.; Wu, H.; Zhou, W.; Li, B.; Qian, G. Engineering microporous ethane-trapping metal–organic frameworks for boosting ethane/ethylene separation. *Journal of Materials Chemistry A* **2020**, *8*, 3613-3620.

(77) Liu, P.; Wang, Y.; Chen, Y.; Yang, J.; Wang, X.; Li, L.; Li, J. Construction of saturated coordination titanium-based metal–organic framework for one-step C2H2/C2H6/C2H4 separation. *Separation and Purification Technology* **2021**, *276*, 119284.

(78) Kang, M.; Kang, D. W.; Choe, J. H.; Kim, H.; Kim, D. W.; Park, H.; Hong, C. S. A Robust Hydrogen-Bonded Metal–Organic Framework with Enhanced Ethane Uptake and Selectivity. *Chemistry of Materials* **2021**, *33*, 6193-6199.

(79) Cho, K. H.; Yoon, J. W.; Lee, J. H.; Kim, J. C.; Kim, K.; Chang, J.-S.; Kwak, S. K.;

Lee, U.-H. Separation of ethane/ethylene gas mixture by ethane-selective CAU-3-NDCA adsorbent. *Microporous and Mesoporous Materials* **2022**, *330*, 111572.

(80) Lu, N.; Gao, Q.; Zhang, Y.-M.; Gao, Y.; Wu, L.-Y.; Zhao, Y.-A.; Chen, L.-Z. Ethane/ethylene separation in a metal-organic framework with shape-matching ethane traps. *Journal of Solid State Chemistry* **2021**, *304*, 122594.

(81) Lei, X.-W.; Yang, H.; Wang, Y.; Wang, Y.; Chen, X.; Xiao, Y.; Bu, X.; Feng, P. Tunable Metal–Organic Frameworks Based on 8-Connected Metal Trimers for High Ethane Uptake. *Small* **2021**, *17*, 2003167.

(82) Jiang, Z.; Fan, L.; Zhou, P.; Xu, T.; Hu, S.; Chen, J.; Chen, D.-L.; He, Y. An aromatic-rich cage-based MOF with inorganic chloride ions decorating the pore surface displaying the preferential adsorption of C 2 H 2 and C 2 H 6 over C 2 H 4. *Inorganic Chemistry Frontiers* **2021**, *8*, 1243-1252.

(83) Fan, L.; Zhou, P.; Wang, X.; Yue, L.; Li, L.; He, Y. Rational Construction and Performance Regulation of an In(III)–Tetraisophthalate Framework for One-Step Adsorption-Phase Purification of C2H4 from C2 Hydrocarbons. *Inorganic chemistry* **2021**, *60*, 10819-10829.

(84) Wang, S.-M.; Wang, F.; Dong, Y.-L.; Shivanna, M.; Dong, Q.; Mu, X.-T.; Duan, J.; Yang, Q.; Zaworotko, M. J.; Yang, Q.-Y. Reversed C2H6/C2H4 separation in interpenetrated diamondoid coordination networks with enhanced host–guest interaction. *Separation and Purification Technology* **2021**, *276*, 119385.

(85) Gao, Q.; Li, A.-L.; Chen, X.; Lu, N.; Zhang, Y.-M.; Chen, L.-Z. A microporous metal–organic framework with triangular channels for C2H6/C2H4 adsorption separation. *Separation and Purification Technology* **2021**, *276*, 119424.

(86) Wang, J.-X.; Gu, X.-W.; Lin, Y.-X.; Li, B.; Qian, G. A Novel Hydrogen-Bonded Organic Framework with Highly Permanent Porosity for Boosting Ethane/Ethylene Separation. *ACS Materials Letters* **2021**, *3*, 497-503.

(87) Wang, Z.-Q.; Luo, H.-Q.; Wang, Y.-L.; Xu, M.-Y.; He, C.-T.; Liu, Q.-Y. Octanuclear Cobalt(II) Cluster-Based Metal–Organic Framework with Caged Structure Exhibiting the Selective Adsorption of Ethane over Ethylene. *Inorganic chemistry* **2021**, *60*, 10596-10602.

(88) Wu, H.; Chen, Y.; Yang, W.; Lv, D.; Yuan, Y.; Qiao, Z.; Liang, H.; Li, Z.; Xia, Q. Ethane-Selective Behavior Achieved on a Nickel-Based Metal–Organic Framework: Impact of Pore Effect and Hydrogen Bonds. *Industrial & Engineering Chemistry Research* **2019**, *58*, 10516-10523.

(89) Li, Y. P.; Zhao, Y. N.; Li, S. N.; Yuan, D. Q.; Jiang, Y. C.; Bu, X.; Hu, M. C.; Zhai, Q. G. Ultrahigh-Uptake Capacity-Enabled Gas Separation and Fruit Preservation by a New Single-Walled Nickel–Organic Framework. *Advanced science* **2021**, *8*, 2003141.

(90) Yang, H.; Wang, Y.; Krishna, R.; Jia, X.; Wang, Y.; Hong, A. N.; Dang, C.; Castillo, H. E.; Bu, X.; Feng, P. Pore-space-partition-enabled exceptional ethane uptake and ethane-selective ethane–ethylene separation. *Journal of the American Chemical Society* **2020**, *142*,

2222-2227.

(91) Chen, C. X.; Wei, Z. W.; Pham, T.; Lan, P. C.; Zhang, L.; Forrest, K. A.; Chen, S.; Al-Enizi, A. M.; Nafady, A.; Su, C. Y. Nanospace engineering of metal–organic frameworks through dynamic spacer installation of multifunctionalities for efficient separation of ethane from ethane/ethylene mixtures. *Angewandte Chemie International Edition* **2021**, *60*, 9680-9685.

(92) Plonka, A. M.; Chen, X.; Wang, H.; Krishna, R.; Dong, X.; Banerjee, D.; Woerner, W. R.; Han, Y.; Li, J.; Parise, J. B. Light hydrocarbon adsorption mechanisms in two calcium-based microporous metal organic frameworks. *Chemistry of Materials* **2016**, *28*, 1636-1646.

(93) Sun, F.-Z.; Yang, S.-Q.; Krishna, R.; Zhang, Y.-H.; Xia, Y.-P.; Hu, T.-L. Microporous metal–organic framework with a completely reversed adsorption relationship for C2 hydrocarbons at room temperature. *ACS applied materials & interfaces* **2020**, *12*, 6105-6111.

(94) Jiang, X.; Wang, Y.; Cao, J. W.; Ye, Z. M.; Zhang, T.; Liu, D. X.; Li, K. L.; Yang, R.; Wang, T.; Zhang, Q. Y. Low-Concentration C2H6 Capture Enabled by Size Matching in the Ultramicropore. *Chemistry–A European Journal* **2021**, *27*, 12753-12757.

(95) Zhu, B.; Cao, J.-W.; Mukherjee, S.; Pham, T.; Zhang, T.; Wang, T.; Jiang, X.; Forrest, K. A.; Zaworotko, M. J.; Chen, K.-J. Pore engineering for one-step ethylene purification from a three-component hydrocarbon mixture. *Journal of the American Chemical Society* **2021**, *143*, 1485-1492.

(96) Chen, Y.; Qiao, Z.; Wu, H.; Lv, D.; Shi, R.; Xia, Q.; Zhou, J.; Li, Z. An ethane-trapping MOF PCN-250 for highly selective adsorption of ethane over ethylene. *Chemical Engineering Science* **2018**, *175*, 110-117.

(97) Gucuyener, C.; van den Bergh, J.; Gascon, J.; Kapteijn, F. Ethane/ethene separation turned on its head: selective ethane adsorption on the metal− organic framework ZIF-7 through a gate-opening mechanism. *Journal of the American Chemical Society* **2010**, *132*, 17704-17706.

(98) Bendt, S.; Hovestadt, M.; Böhme, U.; Paula, C.; Döpken, M.; Hartmann, M.; Keil, F. J. Olefin/Paraffin Separation Potential of ZIF-9 and ZIF-71: A Combined Experimental and Theoretical Study. *European Journal of Inorganic Chemistry* **2016**, *2016*, 4440-4449.

(99) Hartmann, M.; Böhme, U.; Hovestadt, M.; Paula, C. Adsorptive Separation of Olefin/Paraffin Mixtures with ZIF-4. *Langmuir : the ACS journal of surfaces and colloids* **2015**, *31*, 12382-12389.

(100) Mondal, S. S.; Hovestadt, M.; Dey, S.; Paula, C.; Glomb, S.; Kelling, A.; Schilde, U.; Janiak, C.; Hartmann, M.; Holdt, H.-J. Synthesis of a partially fluorinated ZIF-8 analog for ethane/ethene separation. *CrystEngComm* **2017**, *19*, 5882-5891.

(101) Martins, V. F.; Ribeiro, A. M.; Kortunov, P.; Ferreira, A.; Rodrigues, A. E. High purity ethane/ethylene separation by gas phase simulated moving bed using ZIF-8 adsorbent. *AIChE Journal* **2019**, *65*, e16619.

(102) Yuan, W.; Zhang, X.; Li, L. Synthesis of zeolitic imidazolate framework-69 for adsorption separation of ethane and ethylene. *Journal of Solid State Chemistry* **2017**, *251*, 198-

203.

(103) Gu, X.-W.; Wang, J.-X.; Wu, E.; Wu, H.; Zhou, W.; Qian, G.; Chen, B.; Li, B. Immobilization of lewis basic sites into a stable ethane-selective MOF enabling one-step separation of ethylene from a ternary mixture. *Journal of the American Chemical Society* **2022**, *144*, 2614-2623.

1.2 Metal-organic frameworks for carbon dioxide capture

Abstract

Carbon dioxide (CO_2) capture from large point-source emitters and ambient air has drawn a considerable attention during the last few years to slow down the global warming issue. Among different technologies, CO_2 adsorption-based processes have shown to be among the most promising capture strategies due to their low energy requirements when compared to benchmark amine-solution-based (absorption) process. Over the past decades, the development of metal-organic frameworks (MOFs) as CO_2 adsorbents have received considerable attention thanks to their highly tunable CO_2-binding functionalities and modular porous crystalline structures, for enhanced sorption capacities and selectivity with optimal regeneration energy. In this minireview, first, the downstream gas in different combustion processes, including air atmosphere, will be introduced. Then, the main strategies for the enhancement of CO_2 selective adsorption on MOF-based adsorbents will be discussed: i) utilization of unsaturated open metal sites as Lewis acid sites; ii) alkylamine incorporation as Lewis basic sites; iii) introduction of polar functional groups; iv) pore size and charge density. A particular highlight of the new benchmark MOF-based adsorbent for CO_2 capture, CALF-20, will be given, encompassing the structural analysis to the large-scale gas separation in cement industrial settings.

1.2.1 Introduction

As the predominant cause for the global warming, the CO_2 concentration in the atmosphere has increased dramatically in the past decades.[1,2] The Intergovernmental Panel on Climate Change (IPCC) anticipates that reaching 1.5ºC would cause unavoidable increases in numerous risks to nature and human being including sea-level rise, extreme weather events, species extinction, and threats to human health, security, food and water.[3] Unfortunately, meeting the growth of global electricity and heat demand, the CO_2 emission from the world's power plants in 2021 hasn't stopped increasing and reached its highest ever annual level, where a 6% increase from 2020 pushed emissions to more than 36 gigatons (Gt).[4] For example, coal-fired power plants as the largest contributor to global CO_2 emissions rose to a record 10.5 Gt which was 800 Mt above their 2020 level and more than 200 Mt above their previous peak in 2018.[5] Equivalently, natural gas-fired power plants are poised to surpass coal-fired power plants in their contribution to global primary energy by 2030 due to increasingly available reserves and their lower CO_2 emissions footprint among fossil fuels.[6] Additionally, some key industrial sectors including cement industry, petroleum refining, iron and steel manufacturing generate the large fraction of industrial CO_2 emissions. Consequently, it is critical to decrease the CO_2 emission of current power sectors via, for instance, the utilization of renewable energy sources and mitigate atmospheric CO_2 concentration through carbon capture & storage (CCS) & utilization (CCUS) technology, which need political, economic and technological investment at a global scale.[7,8]

Because the current insufficient renewable energy sources could not stop the increasing CO_2 emission, CCS technology would provide a great potential to target the emissions of large point-source emitters, such as coal- or natural gas-fired power plants and support the production of renewable or low-carbon fuels. However, the physical properties, composition and gas volume flows are different for each industrial process, therefore the suitability and selection of a CCS technology would depend on the corresponding stream properties, e.g., CO_2 concentration, moisture content, residual acid gas traces, and other impurities.[7,9-11] For instance, a typical coal-fired power plant emits a flue gas stream at ambient pressure that can be cooled to ~40-60°C and contains 70-75% N_2, 10-15% CO_2, 8-10% H_2O, 3-4% O_2, and traces of SOx, NOx and other impurities, while in the flue gas of natural gas combined cycle (NGCC) power, it contains ~4% CO_2, ~12% O_2, ~8% water concentrations, lower levels of SOx, particulate matter and Hg.

Generally, based on the fundamental chemical process involved in the combustion carbon capture can be adopted: 1) pre-combustion; 2) oxy-fuel combustion; 3) post-combustion and finally 4) direct air capture (DAC).

1.2.2 CO_2 capture processes

In pre-combustion process, it involves the gasification of fossil fuels, such as coal or natural gas, to produce a mixture of CO_2 and H_2. The CO_2 is then captured and stored meanwhile the hydrogen is used as a fuel. In oxy-fuel combustion process, pure oxygen is employed instead of air, resulting in a flue gas containing CO_2 and H_2O during the burning of hydrocarbon fuel. Post-combustion capture is the most commonly used CCS strategy, where CO_2 is captured after the fuel is burned, involving the use of solvents or other technologies to capture CO_2 from flue gas emissions. Direct air capture also is an important option for CO_2 capture, which is differentiated from other method for CO_2 removal through its use of abiogenic means of extracting CO_2 from the atmosphere. These four carbon capture processes will be discussed in the following part.

1.2.2.1 Pre-combustion

A primary fuel reacts with oxygen or air, producing synthesis gas (syngas), mainly composed of CO and H_2. Then CO passes through a shift converter and reacts with steam to produce CO_2 (25%-35%) and additional H_2 (30%-50%) at high pressure (5-40 bar) in the catalytic reactor. Therefore, the target is to obtain high-concentrated H_2 for fuel and CO_2 for subsequent compression and sequestration in pre-combustion carbon capture. The capture usually operates at elevated pressures and/or temperatures with an adsorbent bed, and the pressure or temperature drop is later applied to regenerate those adsorbents. In pre-combustion carbon capture, several drawbacks still exist: (a) high cost; (b) insufficient technical know-how for good operability; (c) absence of single concise process for overall operational performance; and (d) lack of development work for industrial application.[12]

1.2.2.2 Oxy-fuel combustion

In oxy-fuel combustion technology, pure oxygen is mixed with a fuel and combusted in a furnace or boiler, producing a flame with a higher temperature and greater heat output than traditional combustion with air. The high temperatures produced by oxy-fuel combustion can also be useful in some industrial processes, such as glass manufacturing and cement production. The downstream flue gas in a conventional oxy-fuel combustion setup contains CO_2 (55%-65%) and easy condensable H_2O (25%-35%). After condensation and water removal, nearly pure CO_2 can be directly subjected to sequestration. One significant advantage of oxy-fuel combustion is that flue gas is almost entirely composed of CO_2, which greatly benefits the following separation process. Most existing power plants can be readily retrofitted with an oxy-fuel combustion system. However, several disadvantages are still needed to consider: (a) high energy consumption for supply of pure oxygen; (b) the lack of full readiness for this technology with very little experience on a commercial scale; (c) the equipment used to handle pure oxygen must be carefully designed and maintained to prevent safety hazards. Additionally, some fuels may not be suitable for use with oxy-fuel combustion, therefore modifications to existing combustion systems may be necessary to accommodate this process.[13] Unlike in pre/post-combustion carbon capture, the CO_2 adsorbent in this case is made of high density redox active metals.

1.2.2.3 Post-combustion

Post-combustion technologies are important for reducing the environmental impact of fossil fuel combustion, as they help to reduce the emission of harmful pollutants into the atmosphere. However, these technologies can also add to the cost of electricity generation and may reduce the overall efficiency of the power plant. Post-combustion carbon capture involves capturing CO_2 from the exhaust gases produced during combustion and storing it underground or using it for other purposes, such as enhanced oil recovery. It is an important technology used in power generation and industrial processes to reduce greenhouse gas emissions from fossil fuel combustion, but it also requires significant energy and can add to the cost of electricity generation. The basic process of post-combustion carbon capture involves using an amine-based solvent to selectively absorb CO_2 from flue gas streams. The absorbed CO_2 can then be separated from the solvent and compressed for storage or other uses. However, there are also some drawbacks associated with their use: a) large energy consumption from the regeneration of the amine solvent to release the captured CO_2; b) corrosion issue could damage the equipment and infrastructure; c) environmental concerns come from the release of amine solution; d) solvent loss because of the thermal and chemical degradation of amines. Compared with absorption, there are two classes of adsorption are being considered to achieve efficient post-combustion carbon capture which could hugely decreased the energy consumption. The first one is amine-grafted materials based on chemisorption. Although these materials exhibit high CO_2 capture capacity, low energy consumption, low corrosion, and reusability, the improvement of the limited stability and cost-effectiveness of these materials is still needed. Another is that the selective CO_2 adsorption behaviour of adsorbent is based on physisorption mechanism. These materials provide a relatively high selectivity of CO_2 over other gases, low energy consumption, and the ongoing research and development efforts are focused on improving the CO_2 capture capacity and stability of these materials for large-scale CO_2 capture applications.

1.2.2.4 Direct air capture

Direct air capture (DAC) is a process by which CO_2 is removed from the atmosphere using specialized technology. The process involves pulling air into a capture system, where CO_2 is selectively separated from the other gases present in the air, such as nitrogen and oxygen. DAC has attracted growing attention in recent years as a potential negative carbon emission technology. The most challenging target is to adsorb from the quite low concentration of CO_2 in air (around 410 ppm) which is over 100 times more dilute than the exhaust streams of fossil fuel-fired power plants (4-15%). DAC technology typically uses a combination of chemical and physical processes to capture CO_2 from the air. The most commonly used method is called absorption, which involves passing air through a liquid or solid material that selectively absorbs CO_2 molecules. The captured CO_2 can then be released from the absorbent material and stored or used. Another method used in DAC is adsorption, which involves using a porous solid material to adsorb CO_2 from the air. Once the material is saturated with CO_2, it can be regenerated by heating or changing the pressure, allowing the captured CO_2 to be released and stored or used. While cost estimates for DAC vary over orders of magnitude, scaling the average cost of CO_2 captured from a coal-fired power plant (roughly US$100 per tCO_2) by the minimum work suggests a cost of US$300 per tCO_2 for DAC. Until now, relatively few adsorbents have demonstrated effective abilities to remove CO_2 through direct sequestration because of the relative low affinity to CO_2 molecules, the effect of other gases in the air, especially H_2O. Additionally, the oxidative stability and kinetics of CO_2 capture are critical to consider for dilute streams.[9,14]

1.2.2.5 CO_2 sorbents

Post-combustion carbon capture technology is expected to be more relevant for addressing CO_2 emission into the atmosphere due to the huge amount of CO_2 emission from power plant sector around the whole world. The conventional amine-based absorption technology has been implemented on a large commercial scale. However, amine solutions such as mono-ethanolamine (MEA) and diethanolamine (DEA) suffer from volatilization and oxidation as well as corrosivity, which necessitates dilute solutions that require energy-intensive regeneration due to the large volume of inert water that must be thermally cycled.[15] Compared with amine-based capture relying on chemical absorption with high energy penalties (2.3-2.4 $GJ\cdot ton(CO_2)^{-1}$), physical adsorption using porous adsorbents have attracted growing attention as another alternative due to their potential to achieve intrinsically relatively low energy consumption in the CO_2 capture process.[16] Physical adsorbents offer a number of potential advantages in CO_2 capture processes: pore size and shape act as additional handles to fine-tune capture chemistry in the solid state; adsorbents and cycling configurations can be varied to target a wide range of thermodynamic conditions; toxic or corrosive volatiles emitted from amine absorption units can be avoided. In the past decades, several classes of micro and meso-porous materials, including MOFs,[3,17-19] and their sub-class zeolitic imidazole frameworks (ZIFs),[20] zeolites,[21-24] covalent-organic frameworks (COFs),[25] porous activated bioderived activated carbons,[26] porous polymers,[27] and mesoporous carbon nitrides,[28] have been proposed for CO_2 capture. Here a particular focus will be given for MOF-based adsorbents (Fig. 15) Indeed, compared to traditional porous solids, MOFs possess numerous merits, as above mentioned, providing great potential to be among the most promising materials for CO_2 capture in combustion or even DAC processes.[3,29,30]

This part of chapter I aims at providing the different design strategies of MOF-based CO_2 adsorbents with some representative examples for each strategy, where the required criteria to select "realistic" scalable and sustainable MOF-based CO_2 adsorbents suitable for practical application will be also discussed. Besides, the current existing challenges and future directions to the development of MOF-based CO_2 adsorbents will be outlined.

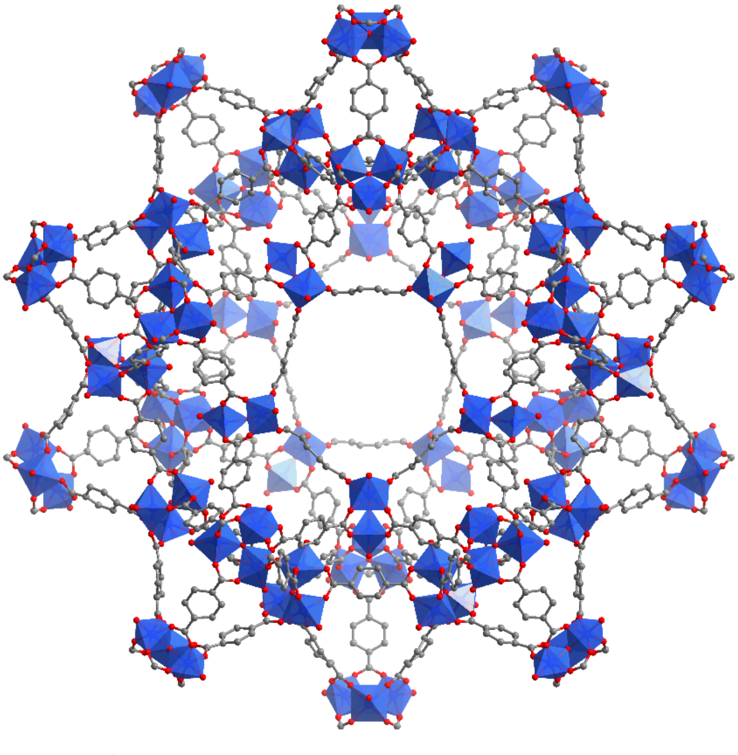

Figure 15: Metal-organic frameworks. Here the representative MIL-101(Cr) MOF structure ($Cr_3O(BDC)_3F$; MIL, Material from Institut Lavoisier; BDC^{2-}, 1,4-benzenedicarboxylate). Color code: blue, red, and grey spheres represent Cr, O, and C atoms, respectively.[31]

1.2.3 Design strategies on MOF-based CO_2 adsorbents

The main purpose for the design of MOF-based adsorbents is to reduce the very high interaction (covalent bonds) between CO_2 and adsorbents, like CO_2 in amine-based solution, leading to a lower energy consumption for adsorbent regeneration, and a faster adsorption-desorption process. In general, the relatively strong molecular interaction(s) between the MOFs and CO_2 molecules, similar to C_2 hydrocarbon adsorption separation (cf. Chapter 1-part A), would play a critical role in the enhancement of CO_2 adsorption performance under different conditions, especially at low loading pressure. Four strategies for the enhancement of CO_2 selective adsorption, which could be separated or concomitant in a given MOF, will be discussed: i) the utilization of unsaturated open metal sites (OMS) as Lewis acid sites that could coordinate CO_2 molecules efficiently; ii) the incorporation of alkylamine as Lewis basic sites which was motivated/inspired by the remarkable CO_2 absorption abilities of aqueous amine solutions; iii) the introduction of polar functional groups prone to enhanced interactions between the CO_2 quadrupole and the dipole of the polar functional group; and iv) the design of 'ultra-suitable' pore size and charge density via the tunability of MOFs. Each strategy will be illustrated by benchmark examples, while inherent limitations will be also discussed.

1.2.3.1 Open metal sites

Compared with that of N_2 molecules (polarizability: 1.76×10^{-24} cm^3, quadrupole moment: 4.7 x 10^{-40} C m^2), CO_2 molecules possess higher polarizability (2.63×10^{-24} cm^3) and quadrupole moment (13.4 x 10^{-40} C m^2) which leads to an increased polarization and binding energy between CO_2 molecules and Lewis acid sites. Therefore, as relatively strong Lewis acid sites, unsaturated OMS in certain MOFs generated by heating or vacuuming of the metal atoms, offer a perfect platform for efficient CO_2/N_2 adsorption separation under different conditions. Since the development of OMS reported in 1998, it was discovered in 2005 that HKUST-1 ($Cu_3(BTC)_2$) with Cu^{2+} OMS performed high CO_2 uptake (around 10 mmol g^{-1}) at room temperature and 42 bar.[32] Also, the typical type I isotherm of the CO_2 adsorption in HKUST-1 indicated that this MOF possesses a relatively strong affinity for CO_2 at low partial pressure. Albeit being far from the ideal MOF for the CO_2 capture because of limited hydrolytic stability in real conditions, it highlights the potential of OMS for high interactions with CO_2. Following this pioneer study, several MOFs bearing OMS have been investigated for CO_2 adsorption including MOF-74 (Mg_2(dobdc), H_4dobdc = 2,5-dihydroxy-terephthalic acid, OMS: open Mg^{2+} sites),[33,34] MIL-88A ($Fe^{III}_3O(CH_3OH)_3(O_2C\text{-}(CH)_2\text{-}CO_2)_3$, OMS: isolated Fe trimer),[35] MIL-96 ($Al_{12}O(OH)_{18}(H_2O)_3(Al_2(OH)_4)(btc)_6 \cdot 24H_2O$, btc = benzene-1,3,5-tricaroxylic acid, OMS: $AlO_2(OH)_4$ octahedra),[36] MIL-100 ($Cr_3F(H_2O)_3O(C_6H_3\text{-}(CO_2)_3)_2 \cdot n\,H_2O$ (n~28), OMS: isolated Cr trimer),[37] Mg doped MIL-101 ($Cr_3F(H_2O)_3O(C_6H_4\text{-}(CO_2)_2)_3$ with different quantity of Mg, OMS: isolated Cr trimer and open Mg^{2+} sites),[38] MIL-102 ($Cr^{III}_3O(H_2O)_2F(C_{10}H_4(CO_2)_4)_{1.5} \cdot 6H_2O$, OMS: isolated Cr trimer),[39] MIL-127 ($Fe_3O(OH)(H_2O)_3(C_{16}O_8N_2H_6)_2$, OMS: isolated Fe trimer),[35] NOTT-140 ($Cu_4(C_{57}H_{36}O_{16})(H_2O)_4$, OMS: open Cu^{2+} sites, NOTT stands for University of Nottingham),[40] PCN-68 ($Cu_3(H_2O)_3$(ptei)·13 H_2O, ptei = 5,5'-((5'-(4-((3,5-dicarboxyphenyl)ethynyl)phenyl)-[1,1':3',1''-terphenyl]-4,4''-diyl)-bis(ethyne-2,1-diyl))diisophthalic acid, OMS: open Cu^{2+} sites, PCN stands for porous coordination network)[41] etc. Due to their exceptional CO_2 uptake capabilities at low pressure, the M-MOF-74 (M_2(dobdc), M = Mg^{2+}, Ni^{2+}, Co^{2+}, Zn^{2+}) isoreticular series has emerged as one of the most studied MOFs for CO_2 capture, as depicted in Fig. 16.[42,43] It is made up of a variety of one-dimensional nm size hexagonal channels decorated with OMS at the inorganic building units (IBUs). More significantly, depending on the nature of the metal from which the MOF is constructed, the CO_2 adsorption of this series can be tuned. In similar conditions, the CO_2 uptake of Mg-MOF-74 (5.4 mmol g^{-1} at 0.1 bar) was 2-4 times higher than those of the other isoreticular M-MOF-74. Through the analysis of zero-coverage isosteric heats of CO_2 adsorption (Q_{st}), Mg-MOF-74 exhibited the highest CO_2 affinity (47 kJ mol^{-1}), whereas Zn-/Ni-/Co-MOF-74 had initial affinities of 26, 37, and 41 kJ mol^{-1}, respectively. This was ascribed to the enhanced ionic character of the Mg-O bond, leads to higher charge-quadrupole interactions between the Mg OMS and CO_2. However, the ongoing research on how the MOFs perform under humid conditions poses a significant challenge in this field. Indeed, these highly energetic sites are also very good coordination sites for other polar molecules, in particular water, which is the main competitor in real conditions. For instance, the regeneration and recyclability of Mg-MOF-74 for CO_2 adsorption in the presence of water is poor mainly due to the competitive adsorption between water and CO_2 molecules on the Mg sites. Additionally, the presence of OMS can be a source of weakness/hydrolysis of certain MOFs (in particular, M^{II}-carboxylate MOFs) because the sites could be attacked easily by corrosive or acid gases; consequently, the only MOF-74 material that exhibits a reasonable stability in the presence of water is the Ni-form; all other analogues suffer from a more or less rapid degradation when exposed to air moisture.[44]

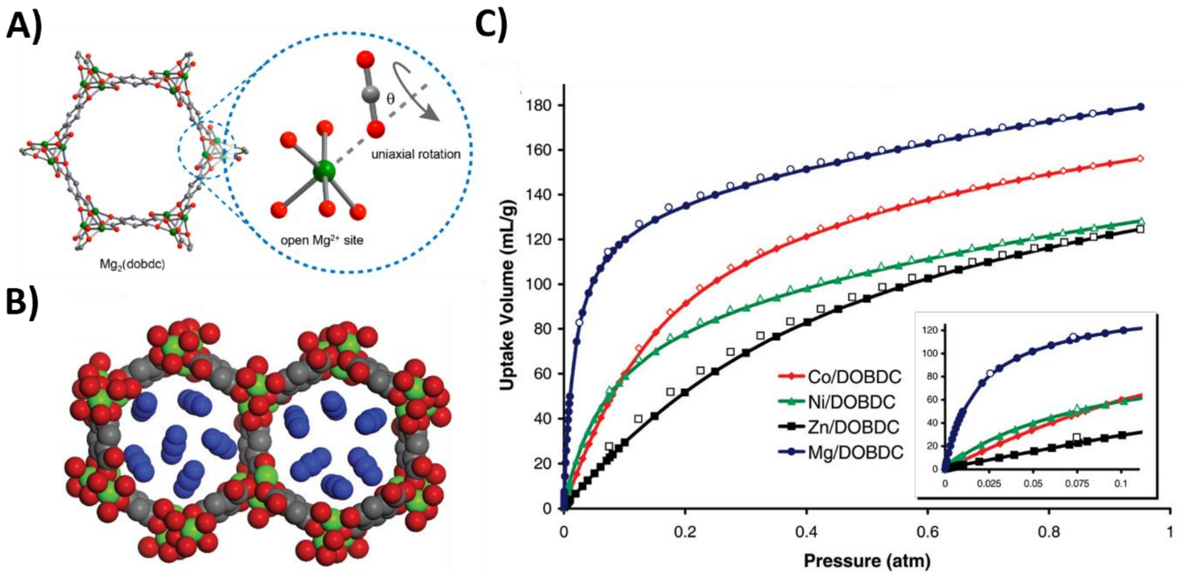

Figure 16: The general structure of M-MOF-74 and their CO_2 uptakes. (A) Schematic illustration of CO_2 uniaxial rotation at the open Mg^{2+} site in Mg_2(dobdc). Note that the rotation

axis is arbitrarily drawn in the picture.[43] (B) Space-filling model of the pore structure of 1 unit cell of Mg-MOF-74 occupied by 12 molecules of CO_2 (blue) which represents the sorption at 0.1 bar and 296 K. Gray, red, and green spheres represent C, O, and Mg atoms, respectively; H atoms are omitted for clarity. (C) CO_2 sorption isotherm (296 K, 0 to 1 bar) comparing M-MOF-74 series, along with an inset of the low-pressure region from 0 to 0.1 bar (filled markers represent adsorption points; open markers represent desorption points).[42]

1.2.3.2 Amine appended groups

While SBU-based OMS have shown impressive performance for CO_2 capture (dry conditions) in terms of adsorption capacity and selectivity, another crucial strategy on MOF-based adsorbents, could enhance the CO_2 binding affinities through the incorporation of alkylamine groups as Lewis basic sites in the frameworks. This strategy was motivated by combining the exceptional CO_2 absorption capabilities of aqueous amine solutions, like industrial MEA solutions,[45] with the confinement effect promoted by the porous sorbent, while at the same time avoiding the use of liquids. In this strategy, the introduction of these amine groups is usually achieved by grafting the corresponding molecules on the OMS of the frameworks. Among the first examples one can cite the example of the alkyl amine-modified Cr-MIL-101 exhibiting highly efficient CO_2 uptake (4.21 mmol g^{-1} at 0.15 bar, 298 K - post-combustion conditions) due to high amine group density and adequate pore space, which allow CO_2 molecules to easily chemisorb to these amine groups.[46,47] Moreover, the material also displayed remarkably different breakthrough time for CO_2 and N_2, and was capable to capture 4.35 mmol g^{-1} CO_2 at 298 K or 4.22 mmol g^{-1} CO_2 at 313 K in the dynamic breakthrough experiments with a gas mixture of 15:85 CO_2/N_2 (v/v). The Long group devoted much effect to understanding the effect of amine-appended MOFs for CO_2 capture under dry and humid conditions. An extended version of MOF-74-Mg, Mg_2(dobpdc) (dobpdc = 4,4′-dioxidobiphenyl-3,3′-dicarboxylate) grafting ethylene diamines by post-synthetic modification, exhibited amine tethering provided protection for electrophilic open Mg^{2+} sites, leading to less competitive adsorption of water in CO_2 adsorption (Fig. 17A-B). In the latest benchmark adsorbent reported by Long's group, Mg_2(dobpdc) with the grafting of tetraamines chains (Fig. 17C), displayed the potential for exceptional efficiency in capturing CO_2 under the harsh conditions relevant to natural gas flue emissions.[48] Depending on the length difference, each tetraamine chain coordinates with one or two Mg^{2+} sites to further modify the pore's inner wall. When CO_2 molecules enter the pores, they individually interact with two amino sites to generate ammonium carbamate by creating the Mg-N bond. The CO_2 capture performance can be further adjusted by altering the length of the tetraamine chains (Fig. 17D). By single-crystal X-ray diffraction (XRD) data the highly ordered manner of tetraamines groups were coordinated in the isostructural framework Zn_2(dobpdc), as depicted in Fig. 17E-F. All of the Mg_2(dobpdc)(tetraamine) variants exhibited sharp step-shaped CO_2 adsorption profiles consistent with cooperative adsorption and ammonium carbamate chain formation (Fig. 17G-H). Authors proposed that initial chemisorption of CO_2 took place at one amine group of tetraamine-appended Mg_2(dobpdc), resulting in ammonium carbamates that ran down one vertex of the hexagonal pore. The second set of amine carbamate chains were created by reorienting the bound, unreacted amines. Two-steps adsorption isotherms were observed in the case of Mg_2(dobpdc) attached with the somewhat bigger 3-4-3, which they ascribed to this tetraamine possibly spanning two metals at a greater distance than 3-3-3 and the other smaller tetraamines. Through single-component isotherms between 90°C and 120°C, Mg_2(dobpdc)(3-4-3) possessed the highest reported heat of CO_2 adsorption ΔH_{ads} (99±3 kJ mol^{-1} at a loading of 1 mmol CO_2 g^{-1}) for amine-functionalized materials.

Therefore, an adsorption process with such high enthalpy of adsorption should be able to absorb CO_2 at high temperatures allowing less energy consumption in a temperature-swing adsorption process by reducing the required temperature swing (for the adsorption step). From practical flue gas steam with saturated water, the CO_2 capture rate of Mg_2(dobpdc) (3-4-3) was as high as 90% at 100°C and ~2.6% H_2O, exhibited excellent cycle stability. With the use of this benchmark material, it was demonstrated that the post-synthesis grafting of small basic amine molecules can increase the host-guest interactions, and concomitantly reduce the channel size, hence enhancing the CO_2 capture ability. However, from a practical point of view, further investigations still need to be carried out, such as the stability after the recyclability tests, the large-scale synthesis potential difficulties (control the homogeneity, materials cost and avaibility which is critical for such a large-scale application involving thousands of tons of adsorbent, quality, etc.).

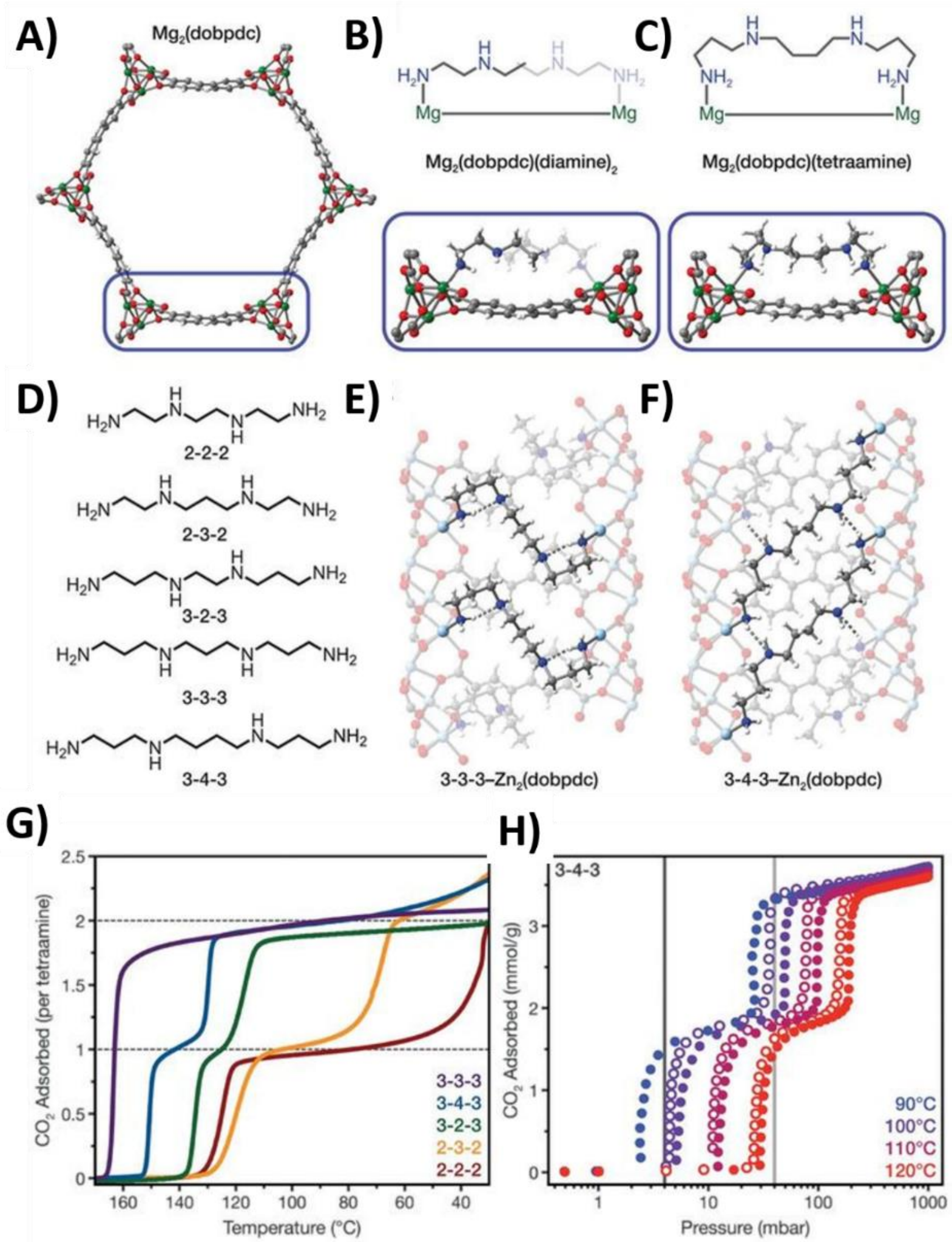

Figure 17: Diamine versus tetraamine coordination in M_2(dobpdc) and their CO_2 uptakes. (A) Illustration of a hexagonal channel of Mg_2(dobpdc) viewed in the ab-plane. (B and C) Diamine-functionalized material features coordination of one diamine to each Mg^{2+} site (B), whereas tetraamines can coordinate to two Mg^{2+} sites (C). (D) Tetraamines explored in this work and their abbreviations. (E and F) Single-crystal XRD structures (100 K) of Zn_2(dobpdc) functionalized with 3-3-3 and 3-4-3 tetraamines, respectively. The tetraamines span metal centers across the pore that are 10.4637(11) Å apart (3-3-3) and 16.8312(19) Å apart (3-4-3). Green, light blue, gray, red, blue, and white spheres represent Mg, Zn, C, O, N, and H, respectively. (G) Adsorption isobars obtained through thermogravimetric analysis of

Mg_2(dobpdc)(tetraamine) under pure CO_2 at atmospheric pressure. Dashed lines indicate the theoretical capacities for binding of one and two CO_2 molecules per tetraamine. (H) Adsorption (filled circles) and desorption (open circles) isotherms for CO_2 uptake in Mg_2(dobpdc)(3-4-3) at 90°, 100°, 110°, and 120°C. The CO_2 pressures in an untreated NGCC flue emission stream (40 mbar) and after 90% capture (4 mbar) are indicated with light gray and dark gray lines, respectively.[48]

1.2.3.3 Polar functional groups

A first alternative strategy is to rely on MOFs without Lewis basic sites through the introduction of polar functional groups such as -F, -Br, -Cl, -OH, -COOH, $-NO_2$, and $-SO_3$ on the organic linkers of MOFs enhancing CO_2 capacity due to the interactions between the quadrupole of CO_2 molecule and dipole of these polar functional groups. For instance, trifluoroacetic acid (TFA) has been utilized in MOF-808 ($Zr_6O_4(OH)_4(BTC)_3(formate)_6$) and USTC-253 (USTC = University of Science and Technology of China, Al(OH)(sbpdc), sbpdc = 4,4'-dibenzoic acid-2,2'-sulfone); both MOFs exhibited high CO_2 adsorption capacity and very little N_2 under the same conditions, yielding a high CO_2/N_2 selectivity.[49,50] And a sulfonate-based MOF (TMOF-1, $Cu(bpy)_2(EDS)$, bpy = 4,4′-bipyridine, EDS = 1,2-ethanedisulfonate) where the free oxygen atoms from the sulfonate groups were charged and highly polar.[51] Through dispersion-corrected DFT calculations, each CO_2 molecule was surrounded by four sulfonate groups from the two adjacent ligands, indicating the strong binding between CO_2 molecule and organosulfonate functionalities. From the natural products point of view, crystalline porous cyclodextrin-based MOFs (CD-MOFs), although not considered as robust highly water stable MOFs, have been proposed for carbon capture due to the high free hydroxyl groups density into the framework.[52] As depicted in Fig. 18 A and B, a cyclic oligosaccharide (CD-MOF-1) was composed of eight α-D-glucopyranosyl residues connected to each other. Alkali metal cations are linked into porous cubic or hexagonal frameworks with charge-balancing anions in the pores. The description by Milner et al. was that the CO_2 chemisorption occurred via HCO_3^- formation at nucleophilic hydroxyl sites within the framework pores in combination with ^{13}C SSNMR analysis and DFT calculations.[53] With respect to CD-MOFs bearing nucleophilic counter anions, the inexpensive $KHCO_3$ CD-MOF is the most promising framework (Fig. 18C and D) due to the high CO_2 working uptake (2.09 mmol g^{-1} at 30°C) and rapid adsorption kinetic (less than 2 mins). From the components of flue gas from power plant, $KHCO_3$ CD-MOF performed rapid CO_2 uptake from a 15% CO_2 in N_2 stream with a high capacity (1.43 mmol g^{-1}).Whilst the incorporation of hydroxyl sites within porous frameworks represents a potentially general strategy for design of new oxidation-resistant adsorbents for carbon capture that are potentially competitive with amine-based technologies.[54,55]

To reduce the water influence on CO_2 adsorption, MOFs with hydrophobic character can be constructed from the various ligands bearing hydrophobic moieties.[56-58] For instance, one can give the example copper(II) MOF, CALF-33-Et_3 ($Cu_3(L1\text{-}Et3)_2$, (where, L1-Et_3 = 1,3,5-Tris(4-phenyl)benzene-$(PO_3H)_3$-Et_3, CALF stands for Calgary Framework), reported by Shimizu's group.[59] An isomorphous MOF of CALF-33-Et_3, CALF-33-Et_2H, was also obtained by controlling the reaction conditions, where one of the ligand's phosphonate monoesters was *in situ* hydrolyzed to hydrogen phosphonate. The 3D frameworks CALF-33-Et_3 and CALF-33-Et_2H are both built up from the same 1D copper-phosphonate chains crosslinked by the Et_3 and it is hydrolyzed analogue H-Et_2 ligands, and endowed with 1D channels with a size of 7.2 x 16.1 Å running along the inorganic chains. The low heat of CO_2 adsorption (16.8-20.8 kJ mol^{-1}) was taken as indirect evidence that the pore of the more hydrophobic character of CALF-33-Et_3 due to the ethyl ester groups decorating the pore surface. When one of the phosphonate monoesters' pore surfaces get hydrolyzed into hydrogen phosphonate to form CALF-33-Et_2H, the heat of CO_2 adsorption becomes significantly higher (20.8-29.6 kJ mol^{-1}). With low heat of adsorption and hydrophobicity, this adsorbent can be easily regenerated and still can adsorb CO_2 in the presence of vapour; however, the rather complex poorly scalable synthesis of ligand precursor might hugely hinder its practical use. It is noteworthy that there exist other strategies (not discussed in this chapter) to introduce hydrophobic character to the sorbent such as the case of composites where an external coating of hydrophobic polymer could prevent/limit water sorption without altering the targeted application.[60]

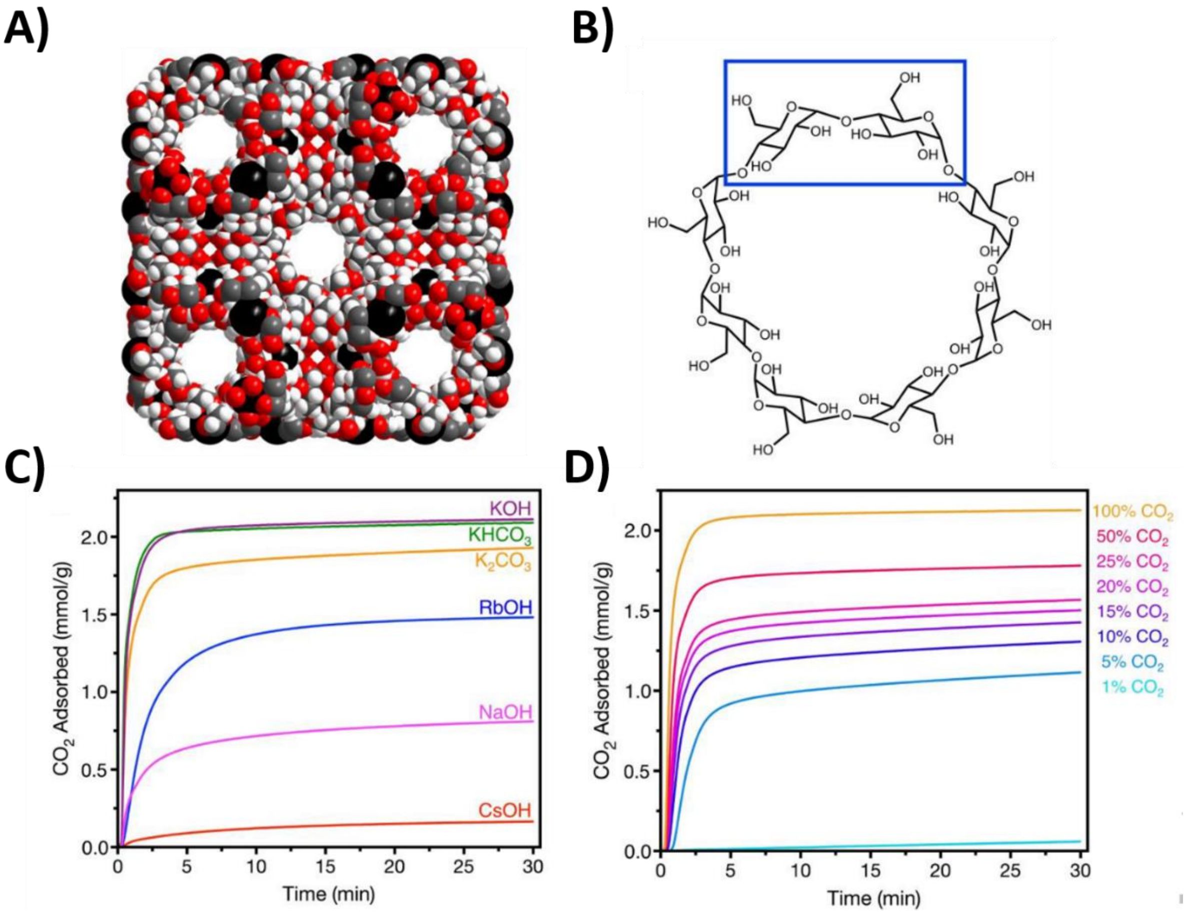

Figure 18: Structure and CO_2 adsorption properties of $K_2(OH)_2(\gamma\text{-CD})$ or CD-MOF-1. A) Space-filling model of the unit cell. B) Molecular structure of γ-CD. C) Pure CO_2 adsorption isotherms at 30°C as measured by TGA for CD-MOFs after exposure to a flow of dry N_2 for 30 min at the optimal activation temperature for each CD-MOF (70°C for KOH; 80°C for $KHCO_3$; 110°C for K_2CO_3; 120°C for RbOH; 30°C for NaOH; 30°C for CsOH). D) Adsorption isotherms at different percentages of CO_2 in N_2 at 30°C as measured by TGA for $KHCO_3$ CD-MOF. The sample was (re-)activated with dry N_2 at 80°C for 30 min between measurements.[53]

1.2.3.4 Pore size and charge density

Still, the practical implementation for CO_2 capture is hindered by the high energy cost and low oxidation-resistance associated with activation, regeneration, and recycling of the adsorbent containing Lewis acid or basic sites. Therefore, a desirable sorbent providing favourable CO_2 sorption kinetics and thermodynamics over a wide range of CO_2 loading would permit efficient CO_2 capture with minimal regeneration costs. To address this, hybrid ultra-microporous materials exhibit new benchmarks for CO_2 selectivity vs. important gases such as N_2 and CH_4 with physical reversible adsorption (45-52 kJ mol^{-1}).[61] The construction of this material is usually based on different pillar anions such as MFSIX, (M = Ti, Si), MOFFIVE, (M = Nb, Al), or MOFOUR, (M = Cr, W, Mo) and diverse two-dimensional square grids formed by the coordination of metal or metal clusters with multi-functional organic ligands, into three-dimensional nets with primitive cubic topology. These frameworks exhibit uniform one-dimensional channels with different sizes (< 0.7 nm) and strong, homogeneous charge density which are important factors to ensure high CO_2 affinity (determining the CO_2 selectivity) over a wide range of CO_2 concentrations, including low concentrations in air. As a remarkable illustration, SiFSIX-based frameworks (SIFSIX-3-Zn and SIFSIX-3-Cu), particularly the isostructural analogues constructed using pyrazine ligand reported by Eddaoudi's and Zaworotko's groups, displayed unprecedented selectivity for CO_2, as shown in Fig. 19.[62] As expected, SIFSIX-3-Cu displayed a smaller unit cell than its Zn analogue and based on the outstanding CO_2 adsorption under low pressure, the authors enabled to target the direct air capture. Compared with the CO_2 uptake of SIFSIX-3-Zn (0.13 mmol g^{-1} at 400 ppm CO_2), SIFSIX-3-Cu performed much higher CO_2 uptake (1.24 mmol g^{-1} at 400 ppm CO_2) due to the pore contraction from SIFSIX-3-Zn (3.84 Å) to SIFSIX-3-Cu (3.5 Å). Moreover, the breakthrough experiments for SIFSIX-3-Cu were conducted at dry and humid circumstances (relative humidity of 74%) with 1000 ppm of diluted CO_2 in N_2, where the latter did not influence the CO_2 adsorption behavior. Once an adsorbent belongs to the saturated metal site-type material, it will possess the benefit of not being deactivated by the complexation of the water molecule on the open metal site, as was the case with MOF-74-Mg and HKUST-1. Significantly, a 50% enhancement of CO_2 selectivity for SIFSIX-3-Cu over SIFSIX-3-Zn was achieved under breakthrough conditions. Smaller pores in SIFSIX-3-Cu resulted in a higher charge density, which in turn allowed for stronger interactions between the fluorine atoms and the guest molecule, giving the extreme CO_2-philic behavior of the copper homologue. Additionally, compared to the N_2 molecule, the adsorption kinetics were in favor of a rapid CO_2 adsorption. Finally, the SIFSIX structure's alteration of Cu for Zn also resulted in an increase in the isosteric heat of adsorption of 20%, from 45 kJ mol^{-1} to 54 kJ mol^{-1}, which did not interfere with the full regeneration of the adsorbent up to 4 cycles after evacuation or under a N_2 flow. Although SIFSIX-3-Cu has excellent CO_2 uptake even at atmospheric concentration (400 ppm), this MOF was found not to be stable to humidity and water while its scalability was not established; hence, it could not be used for practical applications. To avert the issue of water stability, Eddaoudi and co-workers used $(NbOF_5)^{2-}$, a stronger nucleophile than $(SiF_6)^{2-}$, as a pillar to construct a stable isostructural framework.[63] The resultant framework, NbOFFIVE-1-Ni (also known as KAUST-7), has excellent water stability. The relatively larger size of Nb compared to Si resulted in longer Nb-F distance than Si-F distance, making $(NbOF_5)^{2-}$ bulkier pillar compared to $(SiF_6)^{2-}$. As a result, although the square grid of NbOFFIVE-1-Ni and its $(SiF_6)^{2-}$ analog SIFSIX-3-Ni have almost identical dimensions (7.030 and 7.015 Å, respectively), pendent F···F distance decreases to 3.210(1) Å for NbOFFIVE-1-Ni compared to 3.691(1) Å for SIFSIX-3-Ni. The decreased F···F distance within the channel resulted in a drastic increase in CO_2 affinity for NbOFFIVE1-Ni, making it one of the best physisorbents for CO_2 capture at the atmospheric concentration (400 ppm). In the presence of dry 1% CO_2/N_2, the CO_2 uptake was 1.86 mmol g^{-1}; however, at 75% RH, although water capacity was 10 mmol g^{-1}, the CO_2 uptake was reduced only to 1.27 mmol g^{-1}. Nonetheless, Thanks to the synergetic relationship between suitable pore size and high charge density, the design of novel hybrid ultra-microporous materials family will be extremely important for usage in trace CO_2, low and high concentration CO_2 removal. However, for these fluorinated family materials, there still exist several limitations on the synthesis, stability in practical applications. For instance, the synthesis relying on the use of DMF and HF solvents raises severe environmental issues that will strongly hamper their large-scale production at reasonable cost that are required for industrial applications such as CO_2 capture.

Recently, Boyd et al. employed the Henry constant for water adsorption as a key factor in choosing and designing the best MOFs for wet flue gas CO_2 absorption.[64] A binding pocket for CO_2, consisting of aromatic rings 6.5-7.0 Å apart, was identified by selecting MOFs from a library of 325000 hypothetical candidates. These materials bearing parallel aromatic rings with interatomic spacings of approximately 7 Å, provides a near optimum interaction with all three atoms of CO_2, with lower affinity toward N_2 and H_2O. Based on these results, the authors synthesized two water-frustrating MOFs, Al-PMOF and Al-PyrMOF,[65] which include one-dimensional rods of Al^{III} connected by TCPP (tetrakis(4-carboxyphenyl)porphyrin) and TBAPy (1,3,6,8-tetrakis(p-benzoic acid)pyrene), respectively. Not only both materials were found to be reasonably water-stable, but their high CO_2 uptake was hardly affected by moisture. In the presence of 85% relative humidity in the flue gases, the capacity of Al-PMOF got only a minimal influence, whereas for Al-PyrMOF the capture capacity was in fact enhanced. From this work, computational techniques could be considered as one potent screening tool for designing efficient CO_2 adsorbents, even if here the two MOFs are not 'realistic' adsorbents due to the very high cost of the ligands as well as non-sustainable synthesis conditions.

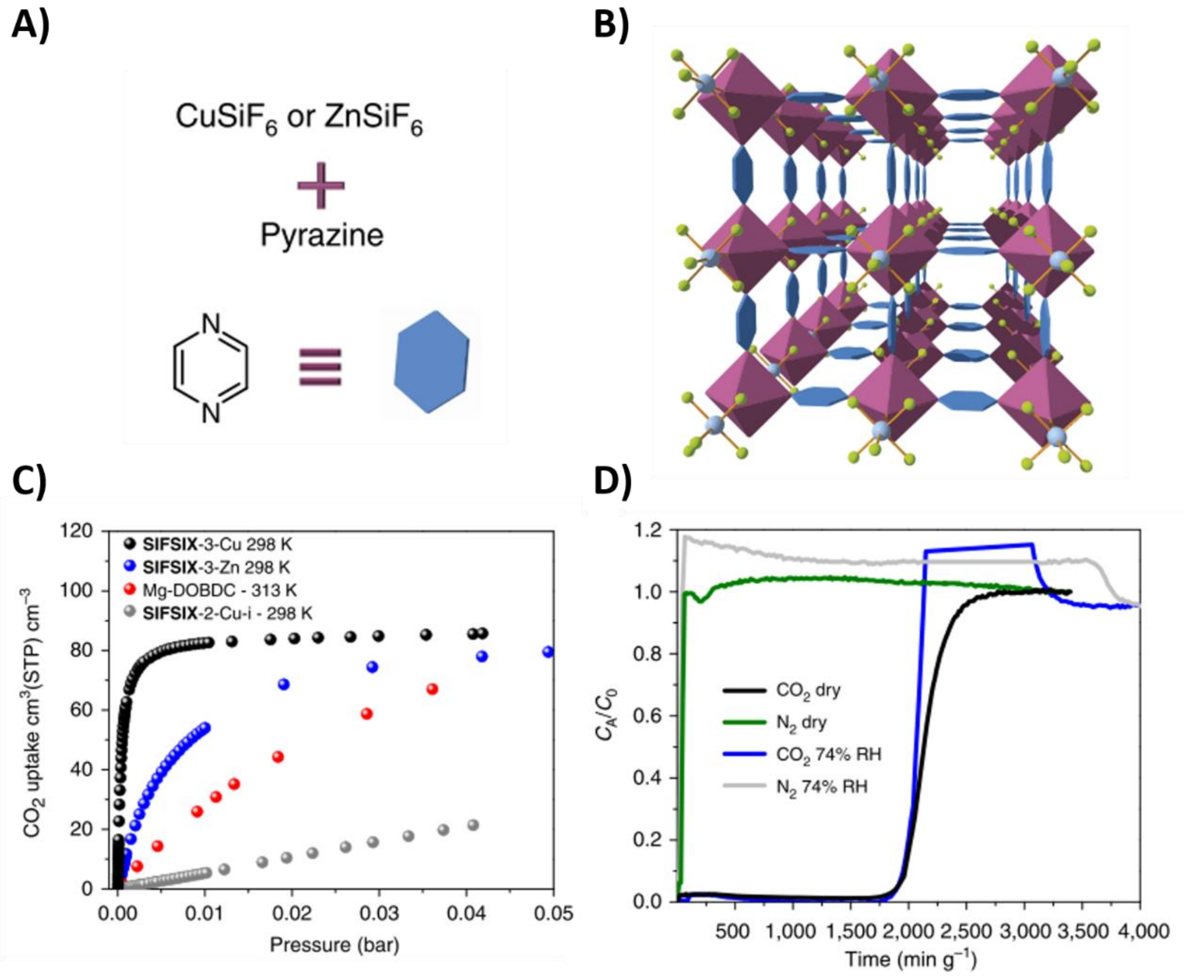

Figure 19: Pore size tuning, CO_2 volumetric uptake, and column breakthrough experiments of SIFSIX-3-Zn or/and SIFSIX-3-Cu. (A and B) SIFSIX-3-Zn or/and SIFSIX-3-Cu. Color code: Pyrazine (pyz, blue polygon), Zn, Cu (purple polyhedra), Si (light blue spheres), F (light green spheres). All guest molecules are omitted for clarity. (C) CO_2 volumetric uptake for SIFSIX-3-Cu at 298 K compared with SIFSIX-3-Zn, SIFSIX-2-Cu-i and Mg-MOF-74. The adsorption results at very low pressure (400 ppm-5%) for the SIFSIX-3-Cu showed that the Cu analogue exhibits steeper adsorption isotherms at very low CO_2 concentration in comparison with other materials. At 7.6 torr (0.01 bar), SIFSIX-3-Cu uptakes 82.6 cm^3(STP) cm^{-3} versus 55 and 28 cm^3(STP) cm^{-3} for SIFSIX-3-Zn and Mg-MOF-74, respectively. (D) Column breakthrough test of CO_2/N_2:1,000 ppm./99.9% for SIFSIX-3-Cu in dry as well as at 74% RH.[62]

1.2.4 Criteria in practical applications

With respect of CO_2 capture under different conditions, an ideal MOF-based CO_2 adsorbent designed by aforementioned strategies, should be evaluated by several key factors: 1) selective adsorption performance of CO_2 from a mixture of gases in the flue stream as the utmost criteria; 2) comparable or higher working capacity with MEA (1.5 mmol g^{-1}) under similar conditions from the industrial-scale applications; 3) the low energy required to cycle or regenerate the adsorbent; 4) high thermal, chemical and water stability of adsorbents over thousand cycles; 5) faster processability in the adsorption-desorption cycle; 6) low cost and high environmentally friendly in a cradle-to-grave lifecycle assessment; 7) the high resistance to steam and contaminants; 8) easy scalability in large-scale synthesis using green solvent and cheap precursors (e.g. ligand). Beyond, final evaluation of an ideal MOF-based CO_2 adsorbent requires adsorption analysis of a structured/shaping materials (i.e., pellets, fibres, monoliths, laminates) with a pilot or full-scale process, with a number of possible cycling configurations (for example, temperature swing, pressure or vacuum swing, concentration swing) and adsorption unit configurations (for example, fixed bed, fluidized bed, rotating bed). One of the examples that illustrates what can be a benchmark material, one can undoubtedly mention CALF-20, (Zn_2(1,2,4-triazolate)$_2$(oxalate), constructed of oxalate ions pillared by layers of 1,2,4-triazolate-bridged zinc (II) ions to form a three-dimensional (3D) lattice and 3D micropore structure (2.7 Å x 3.0 Å factroing VDW radii), has lately been demonstrated by Shimizu's group to be a milestone CO_2 adsorbent post-combustion candidate due to its unique pore structure confinement for CO_2 molecule, as depicted in Fig. 20A and B.[66,67] The CO_2 and N_2 gas adsorption measurements at different conditions revealed that CALF-20 exhibits high CO_2 uptake (4.07 mmol g^{-1} at 1.2 bar, 293 K), especially at low pressure, and negligible N_2 uptake (< 0.5 mmol g^{-1} at 1.2 bar, 293 K). The calculated selectivity of CO_2/N_2 using ideal adsorbed solution theory was 230 for a 10:90 CO_2/N_2 mixture, and the zero-loading heat of adsorption for CO_2 by the Clausius-Clapeyron equation was 39 kJ mol^{-1} indicating this adsorbent only requires relatively low energy consumption for cycle operation and regeneration. In the commercialized zeolite 13X, trace water impurity will compete with CO_2 for adsorption, drastically reducing the CO_2 uptake of adsorbent (98% under 74.4% relative humidity).[68] Designing a slightly hydrophobic adsorbent is crucial to avoiding the decrease of CO_2 adsorption in the presence of water. As shown in Fig. 20C and D, water isotherms and competitive CO_2 breakthrough curves measured at various relative humidity (RH) values remarkably show a negligible effect of water on the CO_2 selective adsorption of CALF-20, compared with zeolite 13X, and two other water-resistant MOFs (CAU-10 and Al-fumarate). It is noteworthy that CALF-20 with NH_2 group reported by Shimizu's group in 2009, shows also a slightly higher CO_2 uptake than bare CALF-20, however the presence of NH_2 group leads to a detrimental effect of moisture on the CO_2 capacity.[66] Strongly motivated by the outstanding performance, stability assessments of CALF-20 have been conducted to date by multiple academic, governmental, and industrial partners. The thermal gravimetric analysis (Fig. 20E) demonstrated the remarkable stability of CALF-20 in the retention of CO_2 capacity after being heated to dry air at 150°C repeatedly. Due to the residual O_2 in the flue gas as well as during conditioning of the bed, where air can oxidize reactive groups, this feature is essential for long-term durability. A large-scale CO_2 capture facility from a cement plant has been built (Svante) on the basis of rotating beds and fast cycles (~1 min) at 0.1 ton per day CO_2 capacity using CALF-20. With the anticipated key performance indicators, and no appreciable performance loss, the process was evaluated for more than 2000 hours. Additionally, the process enabled to reach the 95% CO_2 purity goal set by the US department of Energy. It is crucial that the scale-up be feasible from an economic and technological perspective for large-scale applications.[69] CALF-20 can obtain an exceptional high solid content (total quantity of dried MOF per total amount of solvents utilized) of >35% during large-batch synthesis. For the precipitation step, a high space-time yield (STY) of 550 kg m^{-3} day was achieved as a result of the high yield of >90%, reasonably short reaction time, and the extremely high solid content. Zeolites, in comparison, exhibit typically STYs in the range of 50 to 150 kg m^{-3} per day. Significantly, the CO_2 uptake of CALF-20 was maintained in a variety of scaling and structuring conditions, Fig. 20F showed a 3-million-fold variation in scale with matched CO_2 isotherms. This is considered as a unique illustration of a MOF-based CO_2 adsorbent that has been carried from the laboratory to the industrial scale while fulfilling almost all criteria for a practical and feasible sorbent. This work represents a major de-risking demonstration beyond the CO_2 capture application, where it was established that MOFs can be produced at the industrial level with a possible industrial scale application.

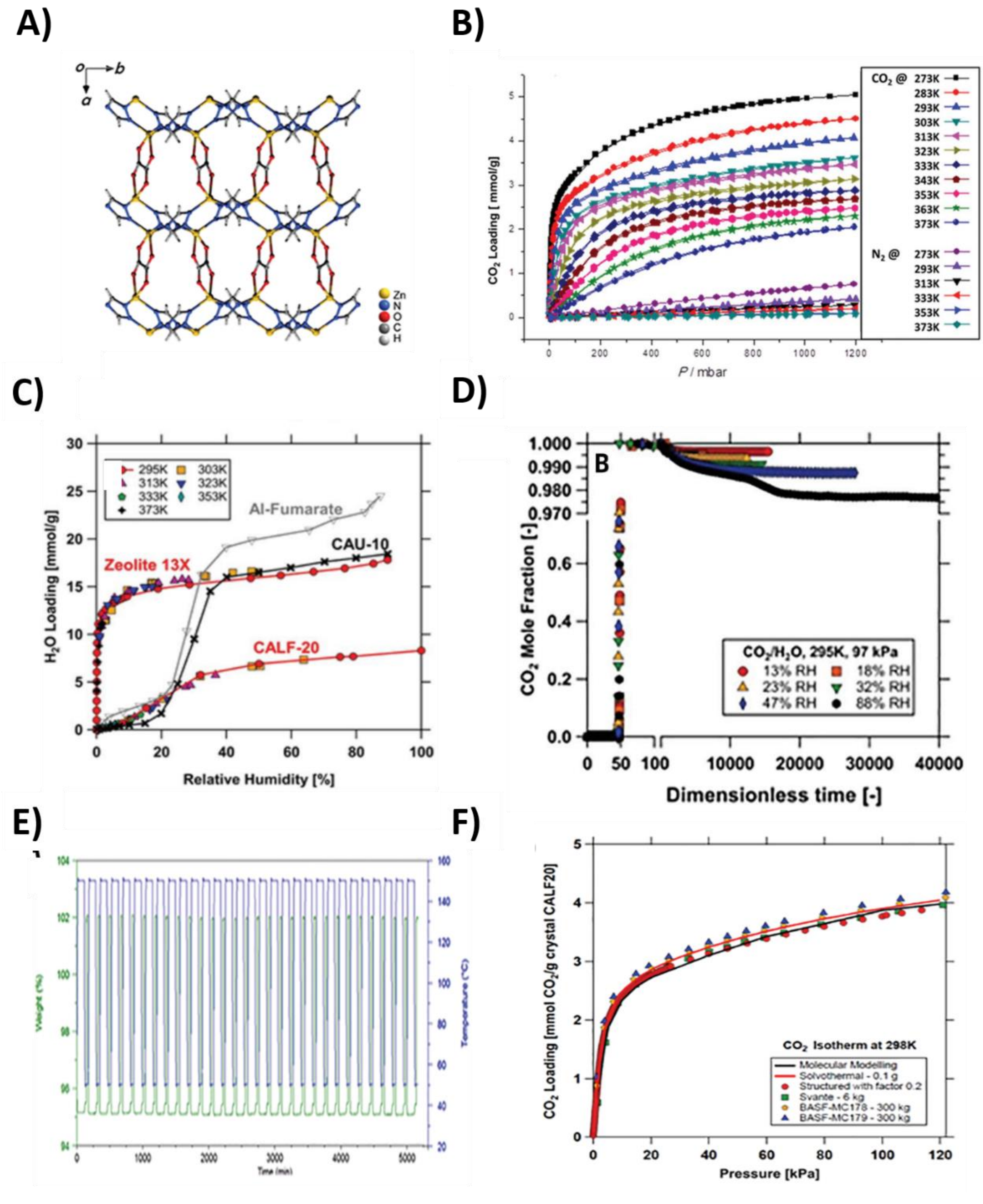

Figure 20: CALF-20 structure, gas adsorption, stability, and scalability. A) Single-crystal structure, the pillaring of the zinc triazolate layers by oxalate anions. B) CO_2 and N_2 isotherms from 273 to 373 K on pure CALF-20. The isotherms of CO_2 and N_2 were measured by volumetry. C) A comparison of H_2O isotherm on zeolite 13X, CAU-10, Al fumarate and structured CALF-20 at 295 K. The isotherms of H_2O were measured by gravimetry. D) Competitive CO_2 breakthrough curves measured at various RH values. The breakthrough curves are plotted in dimensionless time, which is the ratio of the actual time to the average retention time taken of a nonadsorbed component. Also, there is a break in the abscissa of breakthrough curves. E) Cycling of heating and introduction of CO_2 showing 30 cycles heated

to 150°C. The left y axis is truncated to show the CO_2 mass gain on each cycle. F) CO_2 isotherms on 3-million-fold different scale batch preparations of CALF-20, showing retention of the CO_2 capacity. Comparisons with simulated uptake from the crystal structure and the structured CALF-20 scaled by a factor of 0.2 to account for 20% polysulfone are also shown.[67]

1.2.5 Conclusion

MOF-based adsorbents provide a new horizon leading to a new class of promising adsorbents for CO_2 capture. This minireview listed briefly four favorable strategies: i) utilization of unsaturated open metal sites as Lewis acid sites; ii) alkylamine incorporation as Lewis basic sites; iii) introduction of polar functional groups; iv) pore size and charge density, which have been applied for several benchmark MOF-based adsorbents in view of the CO_2 capture from large point-source emitters or ambient air. Although water vapour or acidic gases conditions are unavoidable to consider in practical CO_2 capture process, rare MOF-based CO_2 adsorbent investigated the effect of water vapour or acidic gases in dynamic column breakthrough experiment. Other issues such as cost, long-term stability, sustainable scalability, etc., still remain for large-scale application of MOFs to CO_2 capture, despite CALF-20 showed excellent capabilities for the CO_2 capture in real operating conditions. Even if CALF-20 has demonstrated to be "ideal" sorbent for the VPSA capture process developed by Svante (rotary bed), other promising capture processes are still yet to be developed for which adequate sorbents will be required. Amine-appended Mg_2(dobpdc) series materials have been applied for CO_2 capture in Mosaic Materials startup. Nuada from MOF Technologies is a next-generation carbon capture technology that provides energy-efficient and cost-effective CO_2 capture. Also, several other startups such as Atomis, MOFapp, novoMOF, NuMat Technologies, Framergy, etc. are pushing MOF-based adsorbents to real applications. Thus, it is up to academic researchers and industrial partners to work hand by hand in to seek for a suitable MOF-based CO_2 adsorbent meeting the practical desired performance, for the CO_2 capture and beyond. Finally, an equivalent important part with the reduction of energy consumption by physisorption is develop new adsorption separation processes to save energy using directly or indirectly renewable electricity, magnetic, electric or microwave assisted swing adsorption.

1.2.6 References

(1) Bui, M.; Adjiman, C. S.; Bardow, A.; Anthony, E. J.; Boston, A.; Brown, S.; Fennell, P. S.; Fuss, S.; Galindo, A.; Hackett, L. A. *Energy & Environmental Science* **2018**, *11*, 1062.

(2) Lenssen, N. J. L.; Schmidt, G. A.; Hansen, J. E.; Menne, M. J.; Persin, A.; Ruedy, R.; Zyss, D. *Journal of Geophysical Research: Atmospheres* **2019**, *124*, 6307.

(3) Siegelman, R. L.; Kim, E. J.; Long, J. R. *Nature Materials* **2021**, *20*, 1060.

(4) Arakawa, J.; Okuno, S.; Takano, K.; Yamanaka, Y.; Matsuyama, T.; Feron, P.; Cottrell,

A.; Cousins, A.; Huang, S.; Davies, R.; Sertori, P. *Energy Procedia* **2017**, *114*, 1061.

(5) Agency, I. E. *World Energy Outlook 2018*, 2018.

(6) Lai, J. Y.; Ngu, L. H.; Hashim, S. S. *Greenhouse Gases: Science and Technology* **2021**, *11*, 1076.

(7) Siegelman, R. L.; Milner, P. J.; Kim, E. J.; Weston, S. C.; Long, J. R. *Energy & environmental science* **2019**, *12*, 2161.

(8) Zhu, X.; Xie, W.; Wu, J.; Miao, Y.; Xiang, C.; Chen, C.; Ge, B.; Gan, Z.; Yang, F.; Zhang, M. *Chemical Society Reviews* **2022**.

(9) Kolle, J. M.; Fayaz, M.; Sayari, A. *Chemical Reviews* **2021**, *121*, 7280.

(10) Wang, X.; Song, C. *Frontiers in Energy Research* **2020**, *8*, 560849.

(11) Chen, Z. In *2022 7th International Conference on Social Sciences and Economic Development (ICSSED 2022)*; Atlantis Press: 2022, p 524.

(12) Li, X.; Peng, Z.; Pei, Y.; Ajmal, T.; Rana, K. J.; Aitouche, A.; Mobasheri, R. *International Journal of Energy Research* **2022**, *46*, 505.

(13) Chao, C.; Deng, Y.; Dewil, R.; Baeyens, J.; Fan, X. *Renewable and Sustainable Energy Reviews* **2021**, *138*, 110490.

(14) Shi, X.; Xiao, H.; Azarabadi, H.; Song, J.; Wu, X.; Chen, X.; Lackner, K. S. *Angewandte Chemie International Edition* **2020**, *59*, 6984.

(15) Dutcher, B.; Fan, M.; Russell, A. G. *ACS applied materials & interfaces* **2015**, *7*, 2137.

(16) Hu, Z.; Wang, Y.; Shah, B. B.; Zhao, D. *Advanced Sustainable Systems* **2019**, *3*, 1800080.

(17) Ding, M.; Flaig, R. W.; Jiang, H.-L.; Yaghi, O. M. *Chemical Society Reviews* **2019**, *48*, 2783.

(18) Singh, G.; Lee, J.; Karakoti, A.; Bahadur, R.; Yi, J.; Zhao, D.; AlBahily, K.; Vinu, A. *Chemical Society Reviews* **2020**, *49*, 4360.

(19) Bollini, P.; Didas, S. A.; Jones, C. W. *Journal of Materials Chemistry* **2011**, *21*, 15100.

(20) Su, F.; Lu, C. *Energy & Environmental Science* **2012**, *5*, 9021.

(21) Kumar, S.; Srivastava, R.; Koh, J. *Journal of CO2 Utilization* **2020**, *41*, 101251.

(22) Bae, T.-H.; Hudson, M. R.; Mason, J. A.; Queen, W. L.; Dutton, J. J.; Sumida, K.; Micklash, K. J.; Kaye, S. S.; Brown, C. M.; Long, J. R. *Energy & Environmental Science* **2013**, *6*, 128.

(23) Guan, W.; Dai, Y.; Dong, C.; Yang, X.; Xi, Y. *Journal of Applied Polymer Science* **2020**, *137*, 48968.

(24) Zeng, Y.; Zou, R.; Zhao, Y. *Advanced Materials* **2016**, *28*, 2855.

(25) Singh, G.; Lakhi, K. S.; Sil, S.; Bhosale, S. V.; Kim, I.; Albahily, K.; Vinu, A. *Carbon* **2019**, *148*, 164.

(26) Zou, L.; Sun, Y.; Che, S.; Yang, X.; Wang, X.; Bosch, M.; Wang, Q.; Li, H.; Smith, M.; Yuan, S.; Perry, Z.; Zhou, H.-C. *Advanced Materials* **2017**, *29*, 1700229.

(27) Lakhi, K. S.; Park, D.-H.; Al-Bahily, K.; Cha, W.; Viswanathan, B.; Choy, J.-H.; Vinu,

A. *Chemical Society Reviews* **2017**, *46*, 72.

(28) Furukawa, H.; Cordova, K. E.; O'Keeffe, M.; Yaghi, O. M. *Science* **2013**, *341*, 1230444.

(29) Zhao, X.; Wang, Y.; Li, D.-S.; Bu, X.; Feng, P. *Advanced Materials* **2018**, *30*, 1705189.

(30) Slater, A. G.; Cooper, A. I. *Science* **2015**, *348*, aaa8075.

(31) Férey, G.; Mellot-Draznieks, C.; Serre, C.; Millange, F.; Dutour, J.; Surblé, S.; Margiolaki, I. *Science* **2005**, *309*, 2040.

(32) Millward, A. R.; Yaghi, O. M. *Journal of the American Chemical Society* **2005**, *127*, 17998.

(33) Choe, J. H.; Kim, H.; Hong, C. S. *Materials Chemistry Frontiers* **2021**, *5*, 5172.

(34) Britt, D.; Furukawa, H.; Wang, B.; Glover, T. G.; Yaghi, O. M. *Proceedings of the National Academy of Sciences* **2009**, *106*, 20637.

(35) Wongsakulphasatch, S.; Kiatkittipong, W.; Saupsor, J.; Chaiwiseshphol, J.; Piroonlerkgul, P.; Parasuk, V.; Assabumrungrat, S. *Greenhouse Gases: Science and Technology* **2017**, *7*, 383.

(36) Loiseau, T.; Lecroq, L.; Volkringer, C.; Marrot, J.; Férey, G.; Haouas, M.; Taulelle, F.; Bourrelly, S.; Llewellyn, P. L.; Latroche, M. *Journal of the American Chemical Society* **2006**, *128*, 10223.

(37) Llewellyn, P. L.; Bourrelly, S.; Serre, C.; Vimont, A.; Daturi, M.; Hamon, L.; De Weireld, G.; Chang, J.-S.; Hong, D.-Y.; Kyu Hwang, Y. *Langmuir : the ACS journal of surfaces and colloids* **2008**, *24*, 7245.

(38) Zhou, Z.; Mei, L.; Ma, C.; Xu, F.; Xiao, J.; Xia, Q.; Li, Z. *Chemical Engineering Science* **2016**, *147*, 109.

(39) Surblé, S.; Millange, F.; Serre, C.; Düren, T.; Latroche, M.; Bourrelly, S.; Llewellyn, P. L.; Férey, G. *Journal of the American Chemical Society* **2006**, *128*, 14889.

(40) Tan, C.; Yang, S.; Champness, N. R.; Lin, X.; Blake, A. J.; Lewis, W.; Schröder, M. *Chemical Communications* **2011**, *47*, 4487.

(41) Yuan, D.; Zhao, D.; Sun, D.; Zhou, H. C. *Angewandte Chemie* **2010**, *122*, 5485.

(42) Caskey, S. R.; Wong-Foy, A. G.; Matzger, A. J. *Journal of the American Chemical Society* **2008**, *130*, 10870.

(43) Lashaki, M. J.; Khiavi, S.; Sayari, A. *Chemical Society Reviews* **2019**, *48*, 3320.

(44) Li, H.; Wang, K.; Hu, Z.; Chen, Y.-P.; Verdegaal, W.; Zhao, D.; Zhou, H.-C. *Journal of Materials Chemistry A* **2019**, *7*, 7867.

(45) Khutia, A.; Janiak, C. *Dalton transactions* **2014**, *43*, 1338.

(46) Kim, E. J.; Siegelman, R. L.; Jiang, H. Z.; Forse, A. C.; Lee, J.-H.; Martell, J. D.; Milner, P. J.; Falkowski, J. M.; Neaton, J. B.; Reimer, J. A. *Science* **2020**, *369*, 392.

(47) Mao, H.; Tang, J.; Day, G. S.; Peng, Y.; Wang, H.; Xiao, X.; Yang, Y.; Jiang, Y.; Chen, S.; Halat, D. M. *Science advances* **2022**, *8*, eabo6849.

(48) Thür, R.; Van Velthoven, N.; Lemmens, V.; Bastin, M.; Smolders, S.; De Vos, D.;

Vankelecom, I. F. *ACS applied materials & interfaces* **2019**, *11*, 44792.

(49) Jiang, Z. R.; Wang, H.; Hu, Y.; Lu, J.; Jiang, H. L. *ChemSusChem* **2015**, *8*, 878.

(50) Zhang, G.; Wei, G.; Liu, Z.; Oliver, S. R.; Fei, H. *Chemistry of Materials* **2016**, *28*, 6276.

(51) Gassensmith, J. J.; Kim, J. Y.; Holcroft, J. M.; Farha, O. K.; Stoddart, J. F.; Hupp, J. T.; Jeong, N. C. *Journal of the American Chemical Society* **2014**, *136*, 8277.

(52) Zick, M. E.; Pugh, S. M.; Lee, J.-H.; Forse, A. C.; Milner, P. *Angewandte Chemie* **2022**.

(53) Evans, H. A.; Mullangi, D.; Deng, Z.; Wang, Y.; Peh, S. B.; Wei, F.; Wang, J.; Brown, C. M.; Zhao, D.; Canepa, P. *Science Advances* **2022**, *8*, eade1473.

(54) Khraisheh, M.; Mukherjee, S.; Kumar, A.; Al Momani, F.; Walker, G.; Zaworotko, M. J. *Journal of environmental management* **2020**, *255*, 109874.

(55) Shekhah, O.; Belmabkhout, Y.; Chen, Z.; Guillerm, V.; Cairns, A.; Adil, K.; Eddaoudi, M. *Nature communications* **2014**, *5*, 1.

(56) Vaidhyanathan, R.; Iremonger, S. S.; Dawson, K. W.; Shimizu, G. K. *Chemical communications* **2009**, 5230.

(57) Lin, J.-B.; Nguyen, T. T.; Vaidhyanathan, R.; Burner, J.; Taylor, J. M.; Durekova, H.; Akhtar, F.; Mah, R. K.; Ghaffari-Nik, O.; Marx, S. *Science* **2021**, *374*, 1464.

(58) Rubio-Martinez, M.; Avci-Camur, C.; Thornton, A. W.; Imaz, I.; Maspoch, D.; Hill, M. R. *Chemical Society Reviews* **2017**, *46*, 3453.

Chapter 2

Ethane-selective adsorption over ethylene under high pressure using microporous naphthalene spacers-based metal-organic frameworks

Table of Contents

Contributions to this work

In this work, I studied the synthesis of several Al-, Fe- and Zr-based MOF candidates. I characterized the material using many different techniques, such as PXRD, FT-IR, TGA in O_2, N_2 adsorption at 77 K, CO_2 adsorption at 298 K, SEM/EDX, ^{1}H liquid phase NMR. Vapour and ethanol adsorption at 298 K have been measured by Dr. Shyamapada NANDI. Dr. Debanjan CHAKRABORTY shaped the materials by extrusion, wet granulation. Marta BORDONHOS, Prof. Moises L. PINTO pelletized Al-2,6-NDC-OP powder, then measured the pure component adsorption isotherms and dynamic breakthrough experiments with the results analysis.

Abstract

Compared to cryogenic distillation, efficient adsorption separation of ethane/ethylene (C_2H_6/C_2H_4) has a great potential to minimize the energy consumption in the current petrochemical industrial plants. Porous crystalline metal-organic frameworks have attracted much attention as one class of advanced adsorbents due to their rational tunability and functionalization. By contrast with the C_2H_4-selective adsorbents that require additional adsorption-desorption cycles, C_2H_6-selective metal-organic frameworks could obtain high purity of C_2H_4 in a single separation stage which would simplify the operation procedure and achieve energy-efficient utilization. Here different metal-organic frameworks adsorbents bearing rich aromatic Naphthalene Di-Carboxylate (NDC) based moieties (Al-2,6-NDC, Open or Closed Pores (OP/CP), Al/Fe/Zr-1,4-NDC) have been investigated for C_2H_6/C_2H_4 separation under high pressure. Through pure-component gas adsorption experiments, the results revealed that the increased C-H···π interactions between C_2H_6 molecules and these moieties enhanced the space confinement of C_2H_6 in C_2H_6/C_2H_4 binary mixture. Among these MOF candidates, Al-2,6-NDC-OP exhibited the best C_2H_6-selective performance with high C_2H_6 selectivity and working capacity under high pressure. Unfortunately, the preliminary dynamic column breakthrough experiments didn't confirm the C_2H_6-selective adsorption as suggested from near-ambient pressure single component isotherms due to the large decrease of pore volume after pelletization. Additionally, from practical application point of view, Al-2,6-NDC-OP was shaped (i.e., extrusion followed by spheronisation) with 3% PVB binder (PVB stands for PolyVinyl Butyral) prior to breakthrough measurements. The obtained beads (*ca.* 2 mm diameter) exhibited good mechanical strength (*ca.* 11 N) with preserved porosity. Additional studies are still in progress for further understandings.

2.1 Introduction

Ethylene (C_2H_4) is one of the essential feedstocks and widely used for the production of polymers and other useful chemicals.[1] The relatively low purity (60-80%) of C_2H_4 is generally obtained through ethane (C_2H_6) steam cracking in the petroleum refining process under high temperature and pressure, and insufficient for the downstream polymerization reaction because the required purity C_2H_4 should be exceeded 99.95%.[2] Here the main impurity in C_2H_4 flow, C_2H_6, originates from the uncompleted conversion of C_2H_6 steam cracking. Because of similar physical properties (i.e., boiling points (184.55 K for C_2H_6 and 169.42 K for C_2H_4) and kinetic diameters (4.443 Å for C_2H_6 and 4.163 Å for C_2H_4)), the industrial separation of C_2H_4/C_2H_6 typically relies on high pressure cryogenic distillation operated at a low temperature (183-258 K) and high pressure (7-28 bar) using a distillation column consisting of more than 120 trays with a high reflux ratio, which is one of the most energy intensive processes corresponding to 85% of the total energy required for C_2H_4 production and 0.3% of the global energy consumption.[3-5] Compared to conventional cryogenic distillation, adsorption separation due to their energy-efficiency could be a better alternative process for the separation of

C_2H_4/C_2H_6 to enable the C_2H_4 further utilization.[5,6]

In this technology, the development of advanced porous adsorbents with high gas adsorption capacity and selectivity is critical to minimize the energy consumption required for separation procedures. In traditional adsorbents (i.e., porous carbon materials and zeolites), the trade-off between working capacity and selectivity is still a long-term issue to solve, due to the difficult functionalization in the structures.[7] Therefore, the development of highly efficient physical adsorbents is urgently required. The introduction of metal-organic frameworks (MOFs), also known as porous coordination polymers (PCPs), enriches the possibilities in the field of porous materials for designing efficient C_2H_4/C_2H_6 separation adsorbents due to its easy tunable property and long-range ordered porous crystallinity.[8-12] Until now, the common strategy relies mainly on the use of MOFs bearing open metal sites (OMS), such as Ag(I), Cu(I) and Fe(II), that provide a relatively strong interaction ($Q_{st} > 50$ kJ mol^{-1}) with the π-electron cloud of C_2H_4 molecules to achieve C_2H_4-selective adsorption over C_2H_6 under ambient conditions.[13] For instance, Bloch et al. investigated that the redox-active Fe_2(dobdc) (MOF-74-Fe or CPO-27-Fe; dobdc^{4-} = 2,5-dioxido-1,4-benzenedicarboxylate) exhibited high C_2H_4 selectivity (13 to 18) for the separation of C_2H_4/C_2H_6 at 318 K owing to the high dense Fe^{2+} sites in the hexagonal channel.[14] However, to reach the purity requirement (⩾99.95%) for polymerization reactor, at least four adsorption-desorption cycles are essential to purify the product further by inert gas or a vacuum pump which is still quite energy intensive.[15]

Compared with C_2H_4-selective adsorbents, C_2H_6-selective adsorbents could obtain pure C_2H_4 directly in one adsorption-desorption cycle in the fixed-bed column, which would save approximately 40% of energy consumption (0.4 to 0.6 GJ ton^{-1} of C_2H_4) on pressure swing adsorption (PSA) technology for the C_2H_6/C_2H_4 separation. Additionally, considering the practical industrial pressure range, when the operation is carried out under relatively high pressure, not only the C_2H_4 production with high purity can be enhanced because of larger amount of C_2H_6 retains in the adsorbent fixed-bed column, but reducing the pressure from the gas source can be largely avoided. Li et al. investigated $Fe_2(O_2)$(dobdc) which was an isostructural MOF-74-Fe with iron-peroxo sites, provided dense Fe-peroxo sites for the preferential binding with C_2H_6 over C_2H_4 molecule due to the multiple C-H···O interactions, and exhibited the highest C_2H_6-selective separation (4.4) over C_2H_4 under ambient condition.[16] But $Fe_2(O_2)$(dobdc), unstable under air atmosphere, possessed quite low working capacity considering the pressure range from 1 to 10 bar, which is the most attractive conditions for application at industry due to technical and economic reasons (mainly, because of the HC mixture at the outlet is slightly pressurized.[17] Unfortunately, only few studies have been reported on MOFs adsorbents to show high C_2H_6 selectivity and working capacity when operated under high pressures (i.e. with a regeneration pressure above ambient pressure). Some of us reported that UiO-66 functionalised with two CF_3 functional groups possessed relatively high C_2H_6 preferential adsorption over C_2H_4 (2.5 at $V_{ethane}/V_{ethylene} = 1$) and working capacity (1 mmol g^{-1} for C_2H_6, 0.9 mmol g^{-1} for C_2H_4 at 298 K, from 1-10 bar) under high pressure, due to relatively strong C-H···F interactions between C_2H_6 molecule and UiO-66-2CF_3.[18] Similarly, another type of dispersive interactions could also lead to similar effect C_2H_6-selective adsorption behavior, such as for instance, C-H···π interactions. Indeed, the recent work from

Chang's group demonstrated that DUT-8(Cu) provided favorable C-H···π interactions with C_2H_6 molecule due to naphthalene moieties in the framework, leading to C_2H_6-selective adsorption with a relatively high C_2H_6 working capacity as demonstrated from experimental breakthrough test for C_2H_4/C_2H_6 (0.9/0.1) binary mixture at 283 K and pressure of 5 bar.[19]

In this regard, we have sought to study several porous MOFs with rich aromatic moieties, namely, Al/Fe/Zr-1,4-NDC (H_2-1,4-NDC stands for naphthalene-1,4-dicarboxylic acid) and Al-2,6-NDC-OP/CP (H_2-2,6-NDC stands for naphthalene-2,6-dicarboxylic acid, OP = open pore, CP = close pore). The results revealed that the increased C-H···π interactions between C_2H_6 molecule and these moieties in the frameworks could enhance the C_2H_6-selective separation performance in C_2H_6/C_2H_4 binary mixture. Whilst the C_2H_6/C_2H_4 separation performance was carefully carried out by single-component gas thermodynamic adsorption under high pressure (up to 10 bar). Through ideal adsorbed solution theory (IAST) calculation, apart from Al-2,6-NDC-CP, other MOFs samples exhibited C_2H_6-selective adsorption in the whole pressure range (0-10 bar). The best C_2H_6-selective adsorbent candidate with relatively high C_2H_6 selectivity and working capacity was further studied by binary gas breakthrough experiments under different conditions. Unfortunately, the preliminary dynamic column breakthrough experiments didn't confirm well the C_2H_6-selective adsorption as suggested from near-ambient pressure single component isotherms because the large decrease of pore volume after pelletization. Additionally, in order to meet the conditions required for practical application, Al-2,6-NDC-OP was shaped (i.e., extrusion followed by spheronisation) with 3% PVB binder (PVB stands for PolyVinyl Butyral) prior to breakthrough measurements. The obtained beads (*ca.* 2 mm diameter) exhibited good mechanical strength (*ca.* 11 N) with preserved porosity. Additional studies are still in progress for further understandings.

2.2 Results and discussion

2.2.1 Structures and basic characterizations

Several MOFs bearing naphthalene dicarboxylate ligands which can provide relatively stronger C-H···π molecular interactions with C_2 hydrocarbons have been selected because of their aromatic and electron-rich organic spacers. We only focused on naphthalene, not higher numbers of aromatic groups, to avoid the limitations related to cost and solubility of the ligands. As shown in Fig. 1, Al-2,6-NDC-OP, namely MIL-69-OP or DUT-4 with one-dimensional lozenge-shaped channels (8.4 Å), is built with the coordination bonds between corner-sharing chains of $AlO_4(OH)_2$ octahedra and naphthalene-2,6-dicarboxylate groups.[20,21] Similarly to 2,6-NDC ligand, 1,4-NDC ligand can be also a good candidate to provide more C-H···π molecular interactions between C_2H_6 molecules and benzene moieties in MOFs adsorbents. As a case study, here Al-, Fe-, or Zr-1,4-NDC MOFs were identified. Al- and Fe-1,4-NDC are isostructural and both composed from corner-sharing $M^{III}O_4(OH)_2$ octahedra. In Al-1,4-NDC framework, there existed two types of channels with squared-shape cross-section, as shown in Fig. 1C, with the different pore sizes (large channel: 7.7 x 7.7 $Å^2$, small channel: 3.0 x 3.0 $Å^2$). Zr-1,4-NDC exhibit the same fcu topology as UiO-66 framework based on a 12-connected Zr_6 oxo-cluster.[22,23] This type of MOFs is endowed by interconnected tetrahedral or octahedral cages, in contract to the above Al/Fe-MOFs endowed with 1D lozenge shaped channels.

The Al-2,6-NDC-OP, Al-2,6-NDC-CP, Al-1,4-NDC, Fe-1,4-NDC, and Zr-1,4-NDC solids were synthesized as detailed in the supporting information following either known protocols or home-made optimized conditions. The powder X-ray diffraction (PXRD) patterns, depicted in Fig. 2A, revealed that the obtained samples are of very good crystallinity. According to their N_2 adsorption isotherms at 77 K, Fig. 2B, as expected, Al-2,6-NDC-OP shows the highest Brunauer-Emmett-Teller (BET) surface area (1682 m^2 g^{-1}) and pore volume (0.64 cm^3 g^{-1}), consistent with the reported results. According to our investigation (through PXRD and N_2 at 77 K isotherms measurements) about the flexibility on Al-2,6-NDC-OP, Fig. S1, the open pore phase could be mainly kept when washed by more than 50% DMF in the solvent. Once more water was incorporated in the washing solvent, from previous report, hydrogen bond interactions among water molecules, the bridging hydroxyl groups, and the oxygen atoms of carboxylic acids, contribute to the shrinkage of the channels along the b axis, leading the formation of the closed pore phase, Al-2,6-NDC-CP.[20] The transformation from open to closed form (CP to OP, respectively) seems to be irreversible, at least in the conditions experienced in this work (up to 10 bar of C_2H_6 or C_2H_4), mainly due to the strong π···π interactions between adjacent naphthalene moieties once in the compact form. This phase transition phenomenon leads to a significant loss of BET surface area (202 m^2 g^{-1}) and pore volume (0.08 cm^3 g^{-1}) in Al-2,6-NDC-CP, as attested by the N_2 adsorption isotherms measured at 77 K.

According to the PXRD patterns and N_2 adsorption isotherms of Al/Fe-1,4-NDC, the isostructural Al and Fe-1,4-NDC samples have been synthesized. Fe-1,4-NDC possessed relatively higher BET surface area and pore volume than Al-1,4-NDC sample due to larger size of octahedral $Fe^{III}O_4(OH)_2$ chains in the frameworks. Using 1,4-NDC and Zr metal precursor obtained the powder sample with the same PXRD pattern as UiO-66, strongly indicated that this Zr-1,4-NDC framework was built by Zr_6 oxocluster, not the Zr oxide chains in MIL-140.[24-26] Whilst the extra benzene ring from the ligand in Zr-1,4-NDC led the lower BET surface area (628 m^2 g^{-1}) and pore volume (0.25 cm^3 g^{-1}) compared to the bare UiO-66.[24] Besides, FT-IR, thermogravimetric analysis, and CO_2 adsorption experiments performed already and have been discussed in the supporting information (Fig. S2-4).

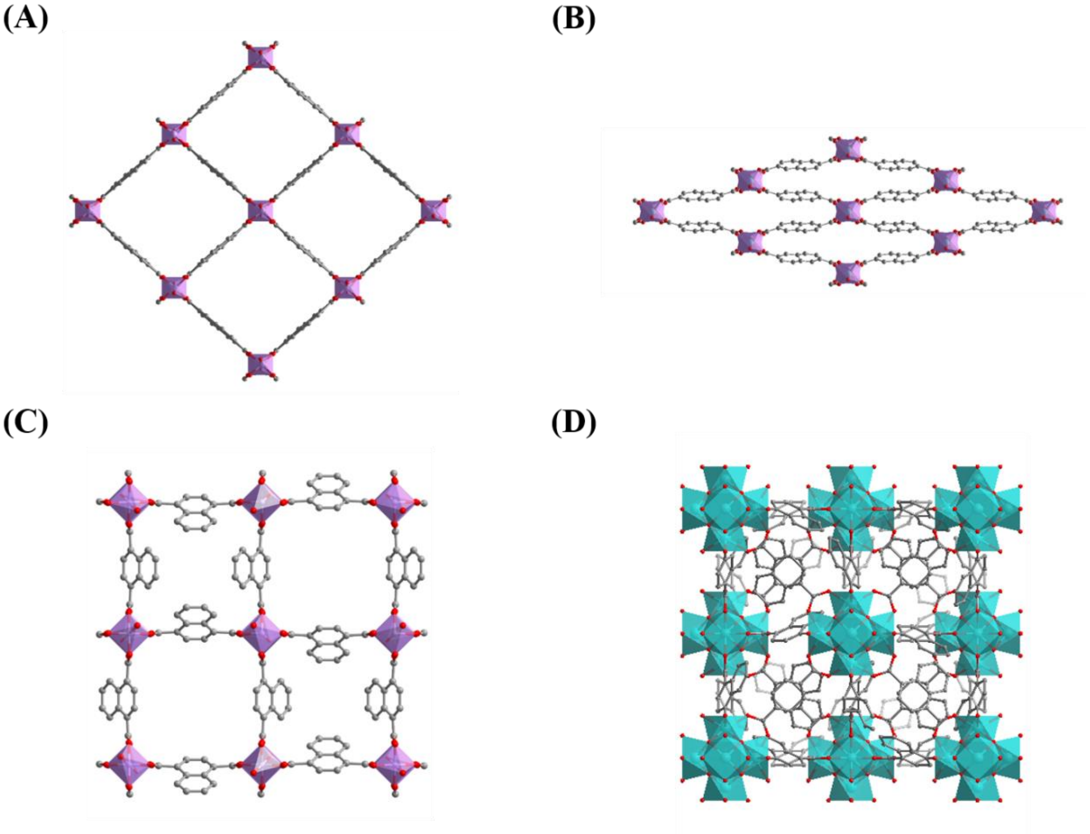

Figure 1: The structures of different MOF candidates. (A) Al-2,6-NDC-OP with octahedral chains of $[Al^{III}O_4(OH)_2]$; (B) Al-2,6-NDC-CP with octahedral chains of $[Al^{III}O_4(OH)_2]$; (C) Al-1,4-NDC and its isostructural Fe-based structure with octahedral chains of $[M^{III}O_4(OH)_2]$ (Al or Fe); (D) Zr-1,4-NDC with 12-connected $Zr_6O_4(OH)_4$ oxoclusters. Color code: carbon atoms, grey; oxygen atoms, red; $[AlO_4(OH)_2]$, purple octahedra; $[Zr_6O_4(OH)_4]$, light green.

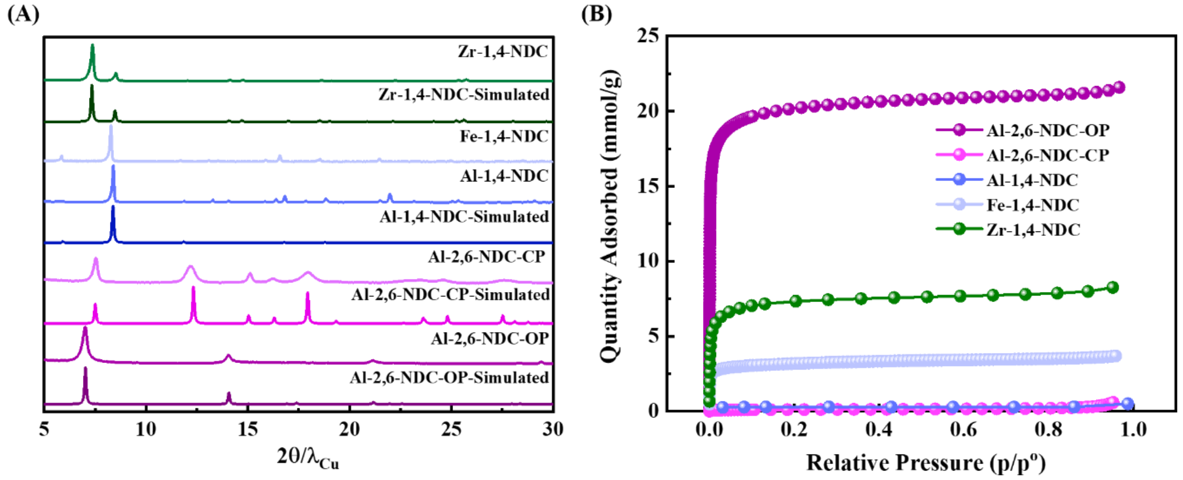

Figure 2: (A) Experimental and simulated PXRD using filtered Cu Kα radiation (λ = 1.5418 Å) (from bottom to up: Al-2,6-NDC-OP, Al-2,6-NDC-CP, Al-1,4-NDC, Fe-1,4-NDC, Zr-1,4-NDC); (B) N_2 adsorption isotherms at 77 K (P_0=1 bar). Color code: purple, Al-2,6-NDC-OP; magenta, Al-2,6-NDC-CP; blue, Al-1,4-NDC; light blue, Fe-1,4-NDC, green, Zr-1,4-NDC.

2.2.2 High pressure single gas adsorption isotherms

To explore gas adsorption and separation performance of different MOF samples, we measured first their pure-component equilibrium adsorption isotherms for C_2H_6 and C_2H_4 at 298 K up to 10 bar, as shown in Fig. 3A. Al-2,6-NDC-OP exhibited C_2H_6-selective adsorption over C_2H_4 with the highest C_2H_6 and C_2H_4 uptake among all MOFs samples probably due to the relatively strong C-H···π molecular interactions between C_2H_6 and benzene moieties in the large 1D channel of the framework. Whilst, Henry's constant (K_H), calculated from the experimental data by fitting the virial equation, reflects the affinity of the materials at low pressures for the adsorption of each gas. The ratio of $K_{ethane}/K_{ethylene}$ was 1.25 in Al-2,6-NDC-OP framework which proved that the aromatic moieties provided relatively stronger infinity with C_2H_6 over C_2H_4 at low pressures, as depicted in Fig. 3B. Its C_2H_6 uptake reaches 4.31 mmol g^{-1} at 298 K at around 1 bar which have been studied in recent paper, higher than most of the benchmark C_2H_6-selective adsorbents for C_2H_6/C_2H_4 separation, such as JNU-2 (4.19 mmol g^{-1})[27], $Fe_2(O_2)$(dobdc) (3.32 mmol g^{-1})[16], TJT-100 (3.84 mmol g^{-1})[28], $Cu(Qc)_2$ (1.85 mmol g^{-1})[29], ZIF-7 (1.85 mmol g^{-1})[30], and MAF-49 (1.73 mmol g^{-1})[31], comparable to MUF-15 (4.69 mmol g^{-1})[32] under similar conditions. More interestingly, the C_2H_6 and C_2H_4 uptake of Al-2,6-NDC-OP increased continuously until 5.8 mmol g^{-1} and 5.26 mmol g^{-1} at 2 bar, respectively, which is really important to obtain high productivity of pure C_2H_4 through the practical PSA technology under relatively high pressure. Compared to C_2H_6-selective Al-2,6-NDC-OP, Al-2,6-NDC-CP preferred to adsorb C_2H_4. This reversible result is possibly caused by the molecular sieving effect, because C_2H_4 (3.28 Å x 4.18 Å x 4.84 Å) possesses slightly more flattened shape than C_2H_6 (3.81 Å x 4.08 Å x 4.82 Å) which might be associated to a C_2H_6 blocking behavior in the one-dimensional tunnel of Al-2,6-NDC-CP (2.7 Å x 19.4 Å with one water molecule trapped in the channel, the pore probably occurs an expansion by heat or pressurization).

Another promising C_2H_6-selective candidate, Al-1,4-NDC, performed C_2H_6-selective adsorption from 0.5 to 9 bar at 298 K. Additionally, this MOF exhibited the highest $K_{ethane}/K_{ethylene}$ ratio value (7.02), which obviously demonstrated that the stronger C_2H_6-affinity existed in Al-1,4-NDC over C_2H_4 at low pressures. In comparison with Al-2,6-NDC-OP where the rigid linear 2,6-NDC lies in the framework between the chains, the benzene ring of NDC in the channel of Al-1,4-NDC is clearly pointing at the center of the pores, and provides a bit more possible flexibility due to its rotation, leading to the strong differences in host-guest interactions between these two frameworks. Due to limited pore volume of Al-1,4-NDC, this framework displayed relatively limited C_2H_6 and C_2H_4 uptake (1.87 mmol g^{-1} for C_2H_6, 1.75 mmol g^{-1} for C_2H_4 at 2 bar) than Al-2,6-NDC-OP. For other samples, Fe-1,4-NDC and Zr-1,4-NDC, the C_2H_6 and C_2H_4 adsorption isotherm curves overlapped a lot, which demonstrated that only little (or no) difference of molecular interactions of C_2H_6 and C_2H_4 with the benzene ring groups in the frameworks. This could be accounted to the relatively lower density of naphthalene groups in the cage-like porosity compared to the other Al-MOFs where they are all endowed by 1D channels with naphthalene arrays alongside. Additionally, the small channels where the benzene rings packed, are not really accessible to the C_2 molecules, while the large channels allow entry, but with less possibilities to get high density of NDC spacers.

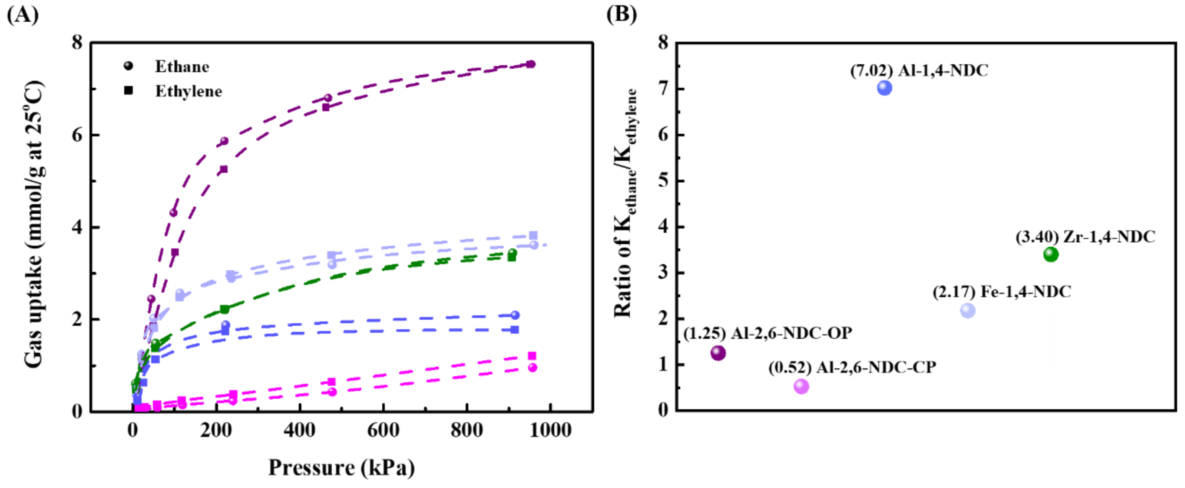

Figure 3: (A) Single-component equilibrium C_2H_6 and C_2H_4 adsorption isotherms at 298 K; (B) The ratio of $K_{ethane}/K_{ethylene}$. The dash lines represented the virial isotherm fits to the experimental data (dots in figure A). Color code: purple, Al-2,6-NDC-OP; magenta, Al-2,6-NDC-CP; blue, Al-1,4-NDC; light blue, Fe-1,4-NDC, green, Zr-1,4-NDC.

2.2.2 IAST separation selectivity at high pressure

Motivated by the selective adsorption and higher Henry's constants of C_2H_6/C_2H_4, the average adsorption selectivity values of C_2H_6/C_2H_4 mixtures with pressures obtained from the experimental data with IAST calculations. As depicted in Fig. 4, apart from Al-2,6-NDC-CP, other MOFs samples exhibited C_2H_6-selective adsorption (i.e., selectivity above 1) in the whole pressure range (0-10 bar), which obviously implied that extra benzene moieties groups in the channel could provide slightly stronger molecular interactions with C_2H_6 molecule instead of

C_2H_4 molecule. Al-1,4-NDC presented the highest C_2H_6-selectivity at 298 K under high pressure, which probably indicated the suitable pore size and relatively strong C-H···π molecular interactions between C_2H_6 molecule and the 1D channels, where could offer the high density of C_2H_6 molecules in the pore space, compared to Al-2,6-NDC-OP and Fe-1,4-NDC with larger pore size. But due to the low surface area and pore volume in Al-1,4-NDC, achieving this combination of good selectivity and high capacity still remains very challenging, especially under high pressure. Herein, Al-2,6-NDC-OP performed the preferential adsorption of C_2H_6 over C_2H_4 with high C_2H_6 uptake under high pressure. Although the dynamic breakthrough experiments under 1 bar have been recently reported for Al-2,6-NDC-OP showing it can adsorb C_2H_6 preferentially over C_2H_4 with high working capacity (4.24 mmol g^{-1})[33], the higher C_2H_6 uptake with good selectivity of C_2H_6/C_2H_4 at high pressure haven't been studied yet. Thus, this motivated us to evaluate the kinetic adsorption through dynamic breakthrough experiments under high pressure conditions.

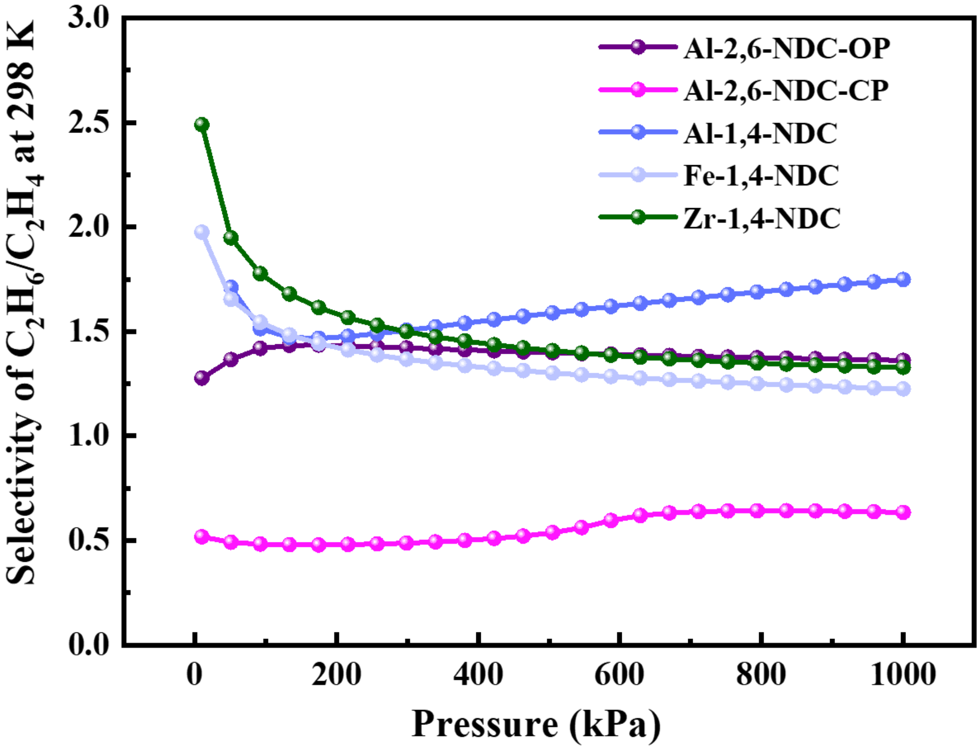

Figure 4: Qualitative comparison of IAST adsorption selectivity of different MOFs for an equimolar C_2H_6/C_2H_4 mixture at 298 K with pressure. Color code: purple, Al-2,6-NDC-OP; magenta, Al-2,6-NDC-CP; blue, Al-1,4-NDC; light blue, Fe-1,4-NDC, green, Zr-1,4-NDC.

2.2.3 Breakthrough dynamic column adsorption tests of shaped Al-2,6-NDC-OP

Before breakthrough experiments of Al-2,6-NDC-OP, the powder material was compressed into several self-supporting discs, which were then shattered into pieces to fill the adsorption column (the pellet preparation was given in the supporting information). The pelletized material exhibited no visible roll-up in the experimental breakthrough curve (Fig. S5), indicating this pelletized material was hard to achieve the efficient adsorption separation of C_2H_4 and C_2H_6 from the gas mixture. To get a better understanding, PXRD and N_2 adsorption at 77 K have been measured for the pelletized material after breakthrough experiments. As depicted in Fig. S6, although its crystallinity remained well, the porosity of the pelletized Al-2,6-NDC-OP sample decreased a lot, which was probably caused by the partial collapse of the structure during pelletization, leading to the negligible adsorption separation behaviour of C_2H_6 and C_2H_4. Therefore, we designed a new column for the powder material. Four experimental breakthrough tests (BTx-pwd, x = 1~4, number of experiment) were performed at near-ambient pressure. These experimental breakthrough results (Fig. S7-10), were not in agreement with expected adsorbed amounts from IAST, even though lower gas mix flows and different conditions have been tested, to account for the lower mass of sample used. However, in some cases, the expected adsorbed phase compositions and corresponding selectivity calculated from BTx-pwd experiments were in agreement with those expected from IAST. When decreasing the total gas mix flow in BT2-pwd experiment, the different retention time for C_2H_6 and C_2H_4 was observed clearly, which demonstrated that C_2H_4 molecule went through the powder column firstly, C_2H_6 followed, achieving one-step C_2H_4 purification but with relatively low production.

From a real application of view, the solid needs however to be shaped to avoid too much operational pressure drop during the measurement under high pressure conditions. To avoid the degradation observed previously by palletization, we selected a ‘softer’ shaping technique that has been extensively studied previously for gas phase separation and MOFs: extrusion followed by spheronisation.[34] Different binders were tried and the best compromise in terms of mechanical stability and minimal pore blocking, was achieved using 3% PVB. The basic characterizations of the shaped Al-2,6-NDC-OP have been included in Fig. S11 and Table S1. The beads we obtained with a diameter of around 2 mm, exhibited a good mechanical strength of *ca.* 11 N, which could enhance their cyclability throughout the ads/desorption process. From the N_2 adsorption isotherm at 77 K, the BET surface area and pore volume of Al-2,6-NDC-OP with 3% PVB exhibited slightly decreased (9%) in the comparison with pure Al-2,6-NDC-OP because of the addition of non-porous PVB binder and a partial pore blocking. The breakthrough experiments of Al-2,6-NDC-OP with 3% PVB is in progress with our collaborator in Lisbon.

2.3 Conclusion

Through this strategy, different metal (Al, Fe, Zr) dicarboxylate microporous MOFs-based adsorbents with rich aromatic moieties, have been investigated carefully for C_2H_6/C_2H_4 separation under high pressure conditions mimicking the conditions of the real application (1-10 bar). Porous MOFs with 2,6 or 1,4 naphthalene dicarboxylate moieties displayed C_2H_6-selective adsorption over C_2H_4 due to the stronger infinity between C_2H_6 molecules and the wall of MOFs, reflecting by single-component equilibrium adsorption isotherms and the

Henry's constants. In particular, the Al-2,6-NDC-OP exhibited higher C_2H_6 uptake than most of the benchmark C_2H_6-selective adsorbents in our conditions (high pressure) due to a compromise between accessible porosity and a high density of naphthalene groups able to interact preferentially with the C_2H_6 molecules. This is the first time that one observes such a high uptake of C_2H_6 over C_2H_4 and a good selectivity under high pressure in the field of MOFs, which makes it very promising for future pressure swing cyclic separation. Al-1.4-NDC showed the highest $K_{ethane}/K_{ethylene}$ ratio value of Henry's constants under low pressure conditions with however a limited adsorption capacity due to the too narrow pores. Unfortunately, the preliminary dynamic column breakthrough experiments didn't confirm well the C_2H_6-selective adsorption as expected from near-ambient pressure single component isotherms. From practical application point of view, prior to breakthrough measurements, Al-2,6-NDC-OP was shaped by extrusion using 3% PVB binder resulting in mm size beds with a good mechanical strength and preserved porosity. Additional studies are still in progress including a computational study to be conducted in collaboration (Prof. PINTO or Prof. MAURIN) to shed light on the interaction laying behind for the most promising candidates. Overall, our findings suggest that C-H···π affinity in the framework is a key parameter to obtain on C_2H_6 preferential adsorption in C_2 hydrocarbon adsorption separation under industrially relevant high pressure conditions.

2.4 References

(1) Koottungal, L. *Oil and Gas Journal* **2012**, *110*, 85.

(2) Sadrameli, S. *Fuel* **2015**, *140*, 102.

(3) Sholl, D. S.; Lively, R. P. *Nature* **2016**, *532*, 435.

(4) Worrell, E.; Phylipsen, D.; Einstein, D.; Martin, N. *Energy use and energy intensity of the US chemical industry*, Lawrence Berkeley National Lab.(LBNL), Berkeley, CA (United States), 2000.

(5) Martins, V. F.; Ribeiro, A. M.; Santos, J. C.; Loureiro, J. M.; Gleichmann, K.; Ferreira, A.; Rodrigues, A. E. *AIChE Journal* **2016**, *62*, 2490.

(6) Wang, Y.; Peh, S. B.; Zhao, D. *Small* **2019**, *15*, 1900058.

(7) Wu, Y.; Weckhuysen, B. M. *Angewandte Chemie International Edition* **2021**, *60*, 18930.

(8) Yang, L.; Qian, S.; Wang, X.; Cui, X.; Chen, B.; Xing, H. *Chemical Society Reviews* **2020**, *49*, 5359.

(9) Cui, W. G.; Hu, T. L.; Bu, X. H. *Advanced Materials* **2020**, *32*, 1806445.

(10) Mukherjee, S.; Sensharma, D.; Chen, K.-J.; Zaworotko, M. J. *Chemical Communications* **2020**, *56*, 10419.

(11) Wang, H.; Liu, Y.; Li, J. *Advanced Materials* **2020**, *32*, 2002603.

(12) Wang, T.; Lin, E.; Peng, Y.-L.; Chen, Y.; Cheng, P.; Zhang, Z. *Coordination Chemistry Reviews* **2020**, *423*, 213485.

(13) Li, B.; Zhang, Y.; Krishna, R.; Yao, K.; Han, Y.; Wu, Z.; Ma, D.; Shi, Z.; Pham, T.; Space, B. *Journal of the American Chemical Society* **2014**, *136*, 8654.

(14) Bloch, E. D.; Queen, W. L.; Krishna, R.; Zadrozny, J. M.; Brown, C. M.; Long, J. R. *science* **2012**, *335*, 1606.

(15) Barnett, B. R.; Gonzalez, M. I.; Long, J. R. *Trends in Chemistry* **2019**, *1*, 159.

(16) Li, L.; Lin, R.-B.; Krishna, R.; Li, H.; Xiang, S.; Wu, H.; Li, J.; Zhou, W.; Chen, B. *Science* **2018**, *362*, 443.

(17) Yang, R. T. *Gas separation by adsorption processes*; World Scientific, 1997; Vol. 1.

(18) Pires, J. o.; Fernandes, J.; Dedecker, K.; Gomes, J. R.; Perez-Sanchez, G.; Nouar, F.; Serre, C.; Pinto, M. s. L. *ACS applied materials & interfaces* **2019**, *11*, 27410.

(19) Cho, K. H.; Yoon, J. W.; Lee, J. H.; Kim, J. C.; Kim, K.; Lee, U.-H.; Kwak, S. K.; Chang, J.-S. *Microporous and Mesoporous Materials* **2020**, *307*, 110473.

(20) Loiseau, T.; Mellot-Draznieks, C.; Muguerra, H.; Férey, G.; Haouas, M.; Taulelle, F. *Comptes Rendus Chimie* **2005**, *8*, 765.

(21) Senkovska, I.; Hoffmann, F.; Fröba, M.; Getzschmann, J.; Böhlmann, W.; Kaskel, S. *Microporous and Mesoporous Materials* **2009**, *122*, 93.

(22) Comotti, A.; Bracco, S.; Sozzani, P.; Horike, S.; Matsuda, R.; Chen, J.; Takata, M.; Kubota, Y.; Kitagawa, S. *Journal of the American Chemical Society* **2008**, *130*, 13664.

(23) Garibay, S. J.; Cohen, S. M. *Chemical Communications* **2010**, *46*, 7700.

(24) Cavka, J. H.; Jakobsen, S.; Olsbye, U.; Guillou, N.; Lamberti, C.; Bordiga, S.; Lillerud, K. P. *Journal of the American Chemical Society* **2008**, *130*, 13850.

(25) Guillerm, V.; Ragon, F.; Dan-Hardi, M.; Devic, T.; Vishnuvarthan, M.; Campo, B.; Vimont, A.; Clet, G.; Yang, Q.; Maurin, G. *Angewandte Chemie* **2012**, *124*, 9401.

(26) Han, G.; Wang, K.; Peng, Y.; Zhang, Y.; Huang, H.; Zhong, C. *Industrial & Engineering Chemistry Research* **2017**, *56*, 14633.

(27) Zeng, H.; Xie, X.-J.; Xie, M.; Huang, Y.-L.; Luo, D.; Wang, T.; Zhao, Y.; Lu, W.; Li, D. *Journal of the American Chemical Society* **2019**, *141*, 20390.

(28) Hao, H. G.; Zhao, Y. F.; Chen, D. M.; Yu, J. M.; Tan, K.; Ma, S.; Chabal, Y.; Zhang, Z. M.; Dou, J. M.; Xiao, Z. H. *Angewandte Chemie* **2018**, *130*, 16299.

(29) Lin, R.-B.; Wu, H.; Li, L.; Tang, X.-L.; Li, Z.; Gao, J.; Cui, H.; Zhou, W.; Chen, B. *Journal of the American Chemical Society* **2018**.

(30) Gucuyener, C.; van den Bergh, J.; Gascon, J.; Kapteijn, F. *Journal of the American Chemical Society* **2010**, *132*, 17704.

(31) Liao, P.-Q.; Zhang, W.-X.; Zhang, J.-P.; Chen, X.-M. *Nature Communications* **2015**, *6*, 8697.

(32) Qazvini, O. T.; Babarao, R.; Shi, Z.-L.; Zhang, Y.-B.; Telfer, S. G. *Journal of the American Chemical Society* **2019**, *141*, 5014.

(33) Cho, K. H.; Yoon, J. W.; Lee, J. H.; Kim, J. C.; Kim, K.; Lee, U.-H.; Choi, M.; Kwak, S. K.; Chang, J.-S. *Journal of Materials Chemistry A* **2021**, *9*, 14593.

(34) Brântuas, P. F.; Henrique, A.; Wahiduzzaman, M.; von Wedelstedt, A.; Maity, T.; Rodrigues, A. E.; Nouar, F.; Lee, U.-H.; Cho, K.-H.; Maurin, G.; Silva, J. A. C.; Serre, C. *Advanced science* **2022**, *9*, 2201494.

Supporting information

Chemicals and instruments

Chemicals

Naphthalene-2,6-dicarboxylic acid (Alfa Aesar), naphthalene-1,4-dicarboxylic acid (Tokyo Chemical Industry, TCI), aluminum chloride hexahydrate (Acros Organics B.V.B.A.), aluminum nitrate nonahydrate (Acros Organics B.V.B.A.), iron nitrate nonahydrate (Alfa Aesar), zirconium chloride (Alfa Aesar), zirconyl chloride octahydrate (Alfa Aesar), saturated hydrochloride (37% HCl) (Fisher), N, N-dimethylformamide (Alfa Aesar), ethanol (Fisher)

Instruments

1) Powder X-ray Diffraction (PXRD)

High-throughput Bruker D8 Advance diffractometer working on transmission mode and equipped with a focusing Göbel mirror producing CuKα radiation (λ = 1.5418 Å) and a LynxEye detector.

2) Nitrogen porosimetry

Micromeritics Tristar/Triflex instrument at 77 K (pre-activating samples at 150°C under vacuum, 8 hours).

3) Thermogravimetric analyses (TGA)

Mettler Toledo TGA/DSC 2, STAR System apparatus with a heating rate of 5°C min^{-1} under the oxygen flow. Mettler Toledo FiveEasyTM Plus pH/mV bench meter.

4) Infrared spectra

Nicolet iS5 FTIR ThermoFisher spectrometer.

5) Scanning transmission microscopy (SEM) and energy dispersive X-ray spectroscopy

FEI Magellan 400 scanning electron microscope, the energy-dispersive X-ray spectroscopy (EDX) analysis allows performing chemical mapping using the "Super-X" systems for EDX analysis that equipped the microscope.

Synthesis procedure

Al-2,6-NDC-OP

Naphthalene-2,6-dicarboxylic acid (0.9 g, 4.16 mmol) was dissolved into 70 mL N,N-dimethylformamide (DMF), aluminum chloride hexahydrate ($AlCl_3 \cdot 6H_2O$) (1 g, 4.12 mmol) was slowly added into above suspension with stirring. The solution was transferred into 250 mL round bottom flask, then heated it under stirring (600 rpm) at 433 K for 9 hours. Then stopped the reaction and removed the solvent by centrifugation. The white slurry was suspended into 300 mL ethanol under stirring at 313 K for 8 hours. The white solid was recovered by centrifugation. Then the solid would be dried under vacuum condition overnight. 1.36 g white powder (yield: 97% based on aluminum metal precursor) was obtained after drying in air condition.

Al-2,6-NDC-CP

Naphthalene-2,6-dicarboxylic acid (0.645 g, 3 mmol) was dissolved into 15 mL DMF and 15 mL DI water, then sodium hydroxide (0.285 g, 7.125 mmol) was added into above suspension solution. Aluminum nitrate nonahydrate ($Al(NO_3)_3 \cdot 9H_2O$) (2.25 g, 6 mmol) was added into above solution with stirring. The solution was transferred into 100 mL round bottom flask, then heated it under stirring (600 rpm) at 393 K for 5 hours. Then white suspension solution would be recovered by centrifugation. The obtained solid was suspended into 100 mL DMF by sonication. Then the obtained solid was transferred into 50 mL DI water, heating at 393 K overnight. The white solid was recovered by centrifugation and dried under vacuum condition overnight.

Al-1,4-NDC

The synthesis procedure was totally followed the previous report from S. Kitagawa. Naphthalene-1,4-dicarboxylic acid (0.108 g, 0.5 mmol 1,4-NDC) was mixed with aluminum nitrate nonahydrate (0.375 g, 1 mmol $Al(NO_3)_3 \cdot 9H_2O$) into 10 mL DI water, then the reaction took place in a 22 mL Teflon autoclave at 453 K for 24 hours. After the reaction, solvent was removed by centrifugation, light yellow powder (ca. 250 mg with 73.7% yield based on aluminum metal precursor) was obtained. By reflux washing in distilled water and centrifugation, the powder was obtained drying in air.

Fe-1,4-NDC

Naphthalene-1,4-dicarboxylic acid (0.216 g, 1 mmol 1,4-NDC) was mixed with iron nitrate nonahydrate (0.404 g, 1 mmol $Fe(NO_3)_3 \cdot 9H_2O$) into 15 mL DI water, then the reaction was run at 393 K under ambient pressure for 24 hours. After the reaction, solvent was removed by centrifugation, light orange powder was obtained. By washing in distilled water and centrifugation, the powder was then dried in air.

Zr-1,4-NDC

Naphthalene-1,4-dicarboxylic acid (0.32 g, 1.48 mmol 1,4-NDC) was firstly added into DMF/H_2O mixture solution (30 mL DMF/80 µL H_2O), then zirconium chloride (0.34 g, 1.46 mmol $ZrCl_4$) was slowly added into above suspension with stirring. Kept stirring at 393 K under ambient pressure for 40 hours, white suspension was obtained. By centrifugation, and washing in ethanol at 333 K, the white powder was obtained after drying in air.

Pure-component gas isotherm test

All the samples were activated under high vacuum (below 10^{-2} Pa) at 473 K overnight, followed by in-situ activation in the high-pressure adsorption line at 473 K for 30 minutes to account for exposure to ambient air during transfer from overnight activation setup to adsorption cell. All adsorption equilibrium isotherms were measured at 298 K, in increasing pressures up to 1000 kPa (10 bar).

Breakthrough dynamic column adsorption tests

1) For the BT1 measurement (denoted as the first breakthrough experiment).

A set of blank experiments with C_2H_4 and C_2H_6 diluted in helium in different quantities, proportions and column pressures were run to determine the dead volume of system. This dead volume is then subtracted from the total breakthrough estimated adsorbed volume to obtain the real adsorbed volume (and quantity) of C_2H_4 and C_2H_6 for each breakthrough test.

The powdered material was very fine and to avoid system contamination, around 583.2 mg of powder was compressed at *ca.* 0.5 ton into several self-supporting discs of d: *ca.* 1 cm, which were then shattered into pieces to fill the adsorption column (stainless steel, dext = ¼”, L: *ca.* 15 cm). The same sample and column were used in all breakthrough runs. The material was activated in-situ in the dynamic column line under He flow at 150°C for 2h before the first breakthrough run to account for exposure to ambient air during column preparation. For the following breakthrough runs, as the column was not removed from the line the material was activated under He flow at 150°C for 30 min before each breakthrough run.

2) For BTx-pwd measurement (denoted as BTx, x = number of experiments, pwd = powder material):

A new column was prepared with the powdered material (BTx-pwd sample, used = 460.4 mg). In both cases the adsorption column had dext = ¼ “, L: *ca.* 15 cm. The material was left under vacuum in the dynamic column line overnight, followed by activation *in situ* in the line under He flow at 150°C for 2h (4h in BT2-pwd) before the breakthrough runs.

All experiments were carried out at 25°C (gas mixture = $C_2H_4 + C_2H_6$).

He was used to dilute the gas mixture going into the MS via a bypass line, with %He > 2.3 x%(C_2H_6+C_2H_4).

C_2H_6 and C_2H_4 concentrations were calibrated from the ion current of the MW=30 and MW=24 ion fragments, respectively, on the MS equipment software, using He (MW=4) as an internal standard for the calibration.

Ion fragment MW = 28 gave the overall best results in the quantification of experimental data. The proportion of C_2H_6 ion fragment MW = 28 was calculated according to the relative intensity of the peak relative to the MW = 30 ion fragment for C_2H_6, Eq. (1) (C_2H_6 MS spectrum from software library shown below). The proportion of C_2H_4 in ion fragment MW = 28 was calculated by subtraction, also considering N_2, (which was < 0.05% of the total signal for ion fragment MW = 28 at column saturation), Eqs. (2) and (3):

$$I_{\text{ethane,MW=28}} = \frac{I_{\text{ethane,MW=30}} \times 100\%}{26\%} \quad (1)$$

$$I_{\text{ethylene,MW=28}} = I_{\text{total,MW=28}} - I_{\text{ethane,MW=28}} - I_{\text{nitrogen,MW=28}} \quad (2)$$

$$I_{\text{nitrogen,MW=28}} = \frac{I_{\text{oxygen,MW=32}} \times 79\%}{21\%} \quad (3)$$

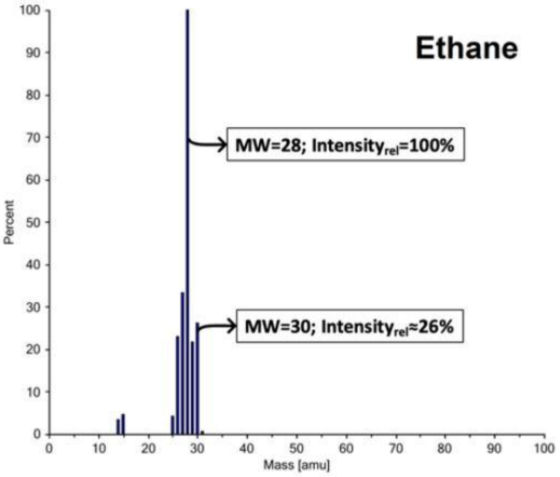

Supporting figures

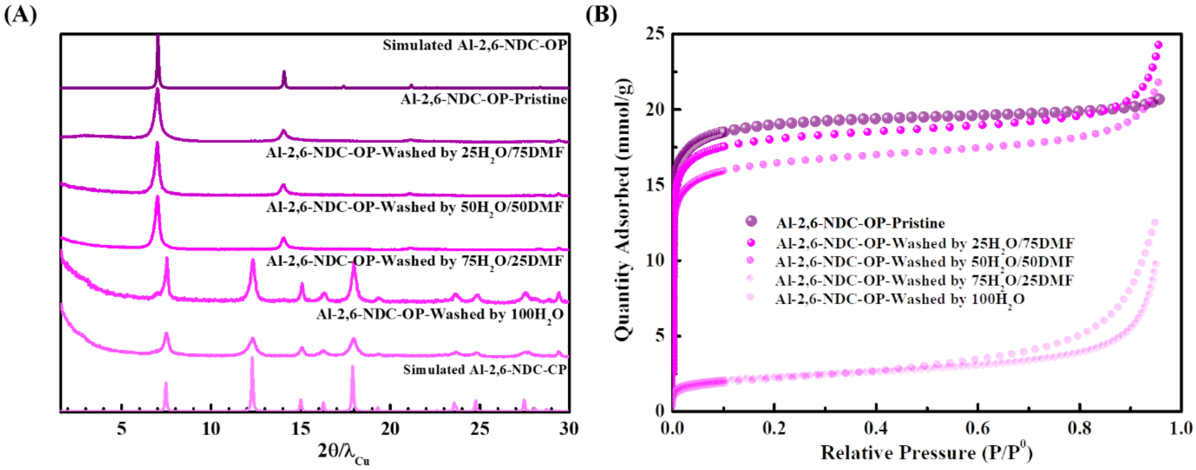

Figure S1: The phase transition between Al-2,6-NDC-OP and Al-2,6-NDC-CP. Once obtained Al-2,6-NDC-OP, pxrd patterns (A) and N_2 adsorption isotherms at 77 K (B) of the samples after different washing conditions (V_{H_2O}/V_{DMF} = 0/100, 25/75, 50/50, 75/25, and 100/0 percentage). This result indicated that the occurrence of phase transition relied on the washing step: big molecule such as DMF, the structure could keep its open pore phase, and vice versa.

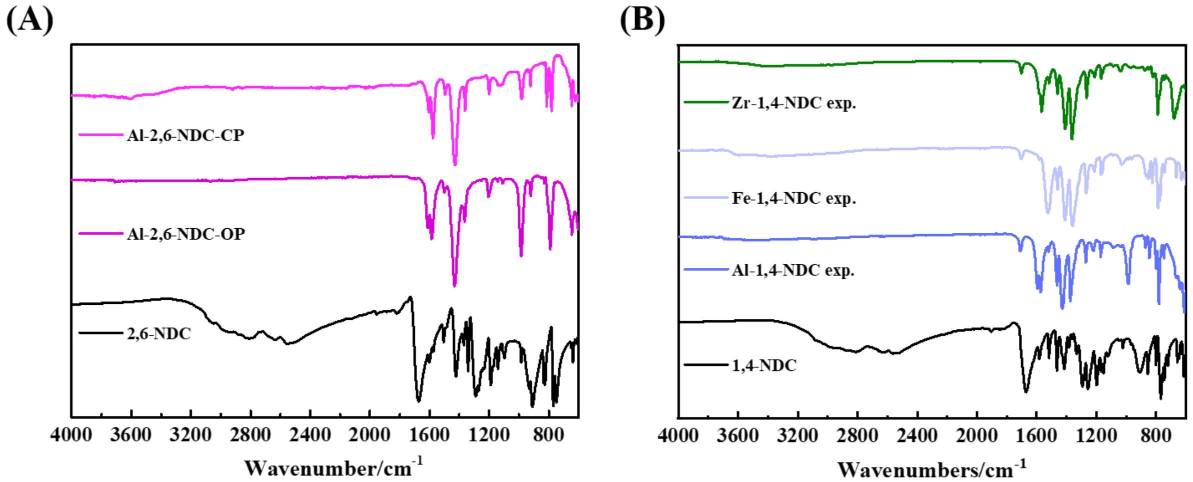

Figure S2: FT-IR data of five samples. (A) the comparison of 2,6-NDC, Al-2,6-NDC-OP, and Al-2,6-NDC-CP; (B) the comparison of 1,4-NDC, Al-1,4-NDC, Fe-1,4-NDC, and Zr-1,4-NDC.

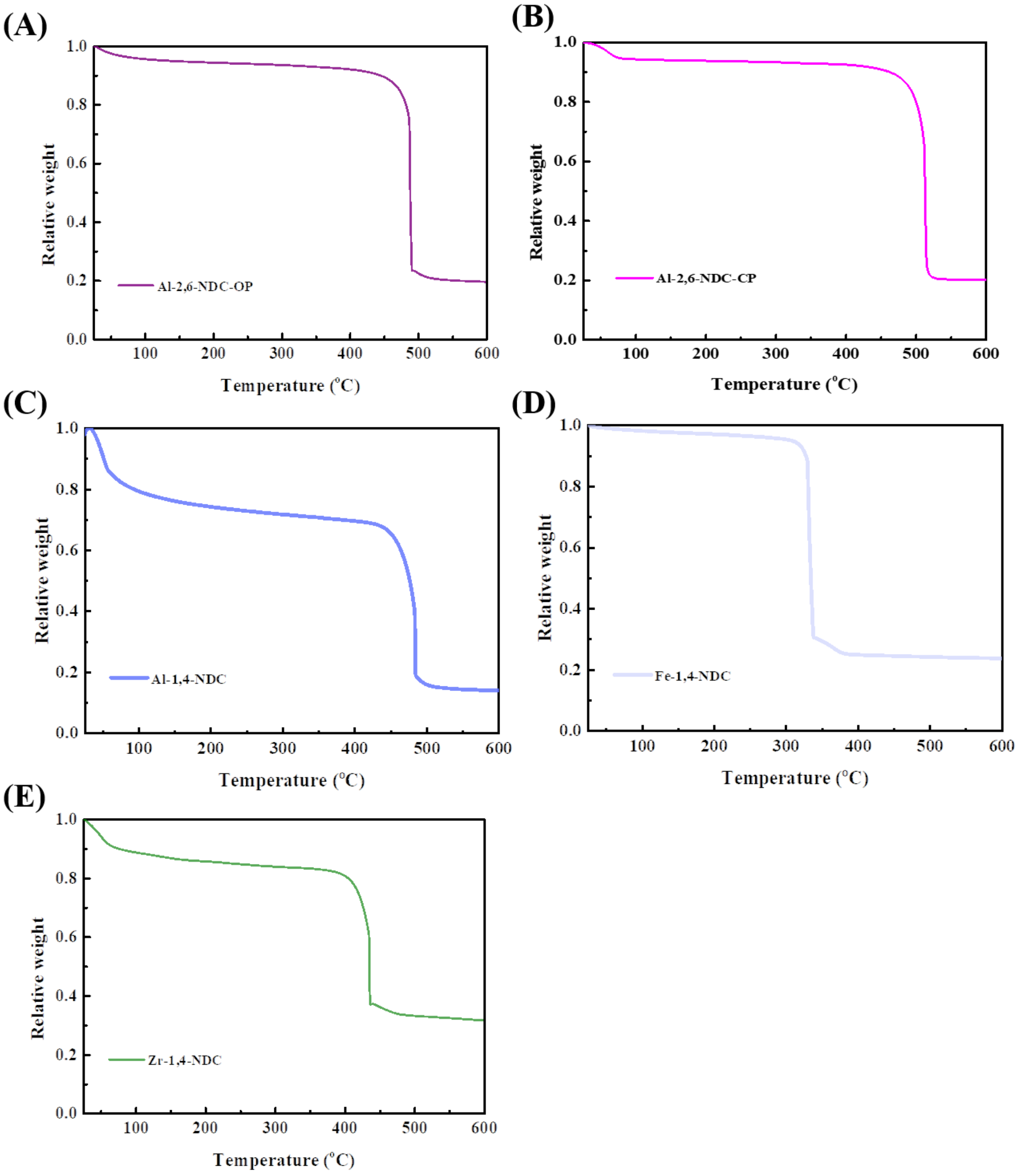

Figure S3: The TGA curves of (A) Al-2,6-NDC-OP; (B) Al-2,6-NDC-CP; (C) Al-1,4-NDC; (D) Fe-1,4-NDC; (E) Zr-1,4-NDC (The ratio of Zr:1,4-NDC is equal to 1:0.92). Measurements under O_2 atmosphere, scan rate = 5°C min^{-1}.

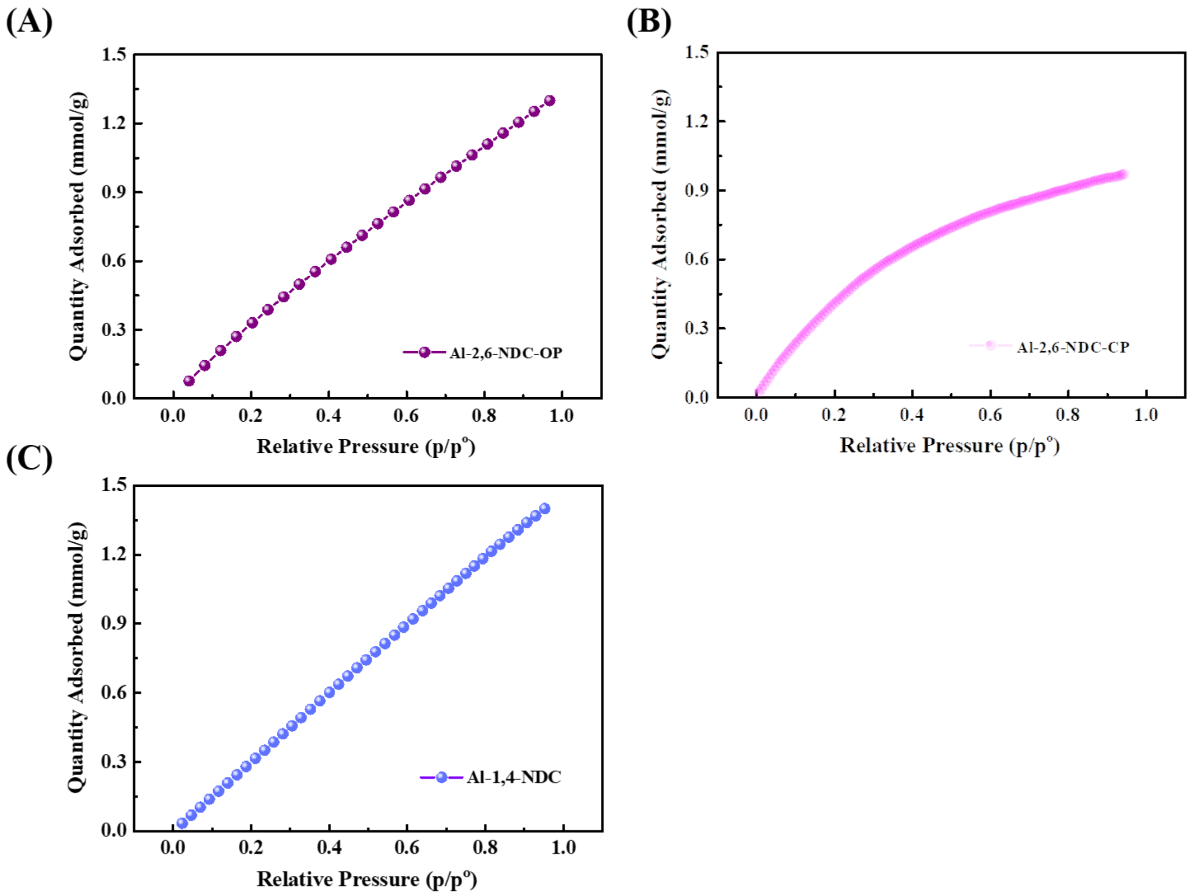

Figure S4: CO_2 adsorption isotherms at 298 K. (A) Al-2,6-NDC-OP; (B) Al-2,6-NDC-CP; and (C) Al-1,4-NDC.

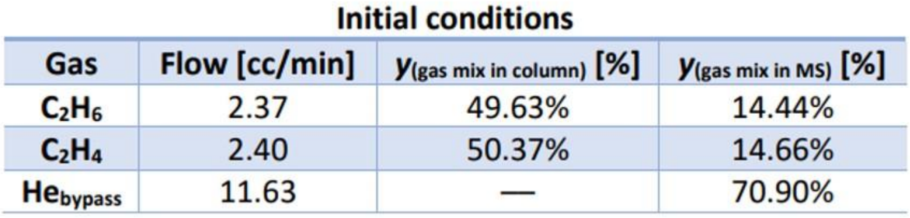

Initial conditions

Gas	Flow [cc/min]	$y_{(\text{gas mix in column})}$ [%]	$y_{(\text{gas mix in MS})}$ [%]
C_2H_6	2.37	49.63%	14.44%
C_2H_4	2.40	50.37%	14.66%
He_{bypass}	11.63	—	70.90%

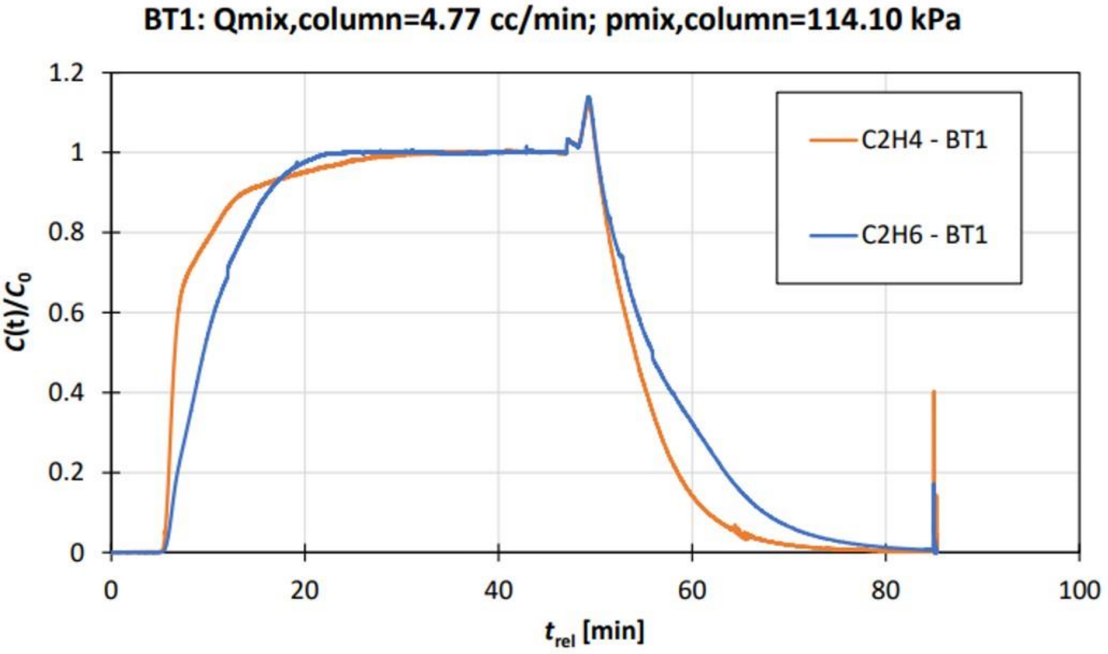

Figure S5: Experimental breakthrough curve for BT1 (pellets).

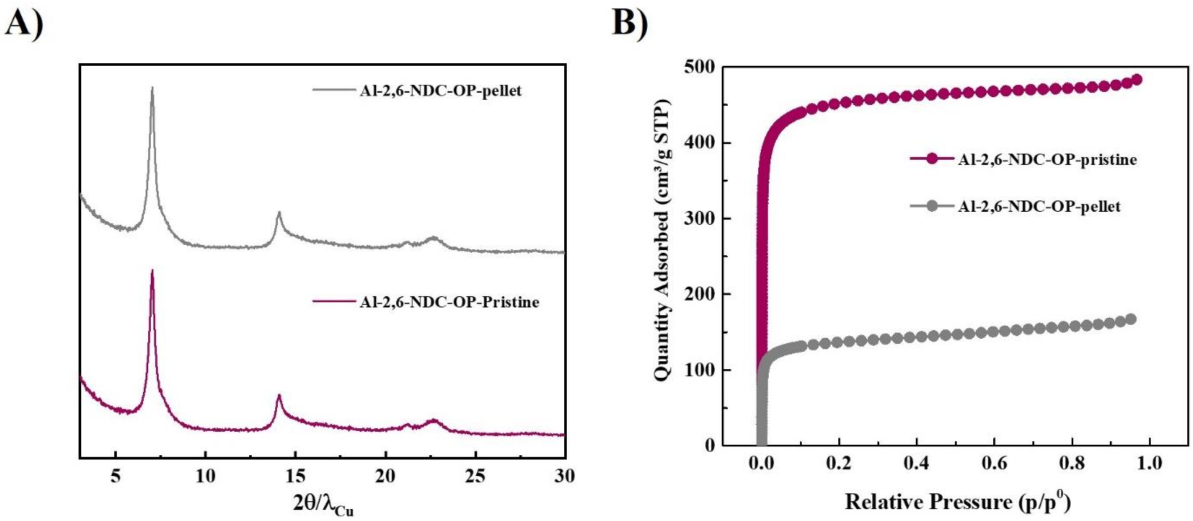

Figure S6: Characteristic comparison Al-2,6-NDC-OP before and after pelletization. (A) PXRD patterns; (B) N_2 adsorption at 77 K.

Initial conditions

Gas	Flow [cc/min]	$y_{\text{(gas mix in column)}}$ [%]	$y_{\text{(gas mix in MS)}}$ [%]
C_2H_6	2.33	49.94%	13.43%
C_2H_4	2.34	50.06%	13.47%
He_{bypass}	12.69	—	73.10%

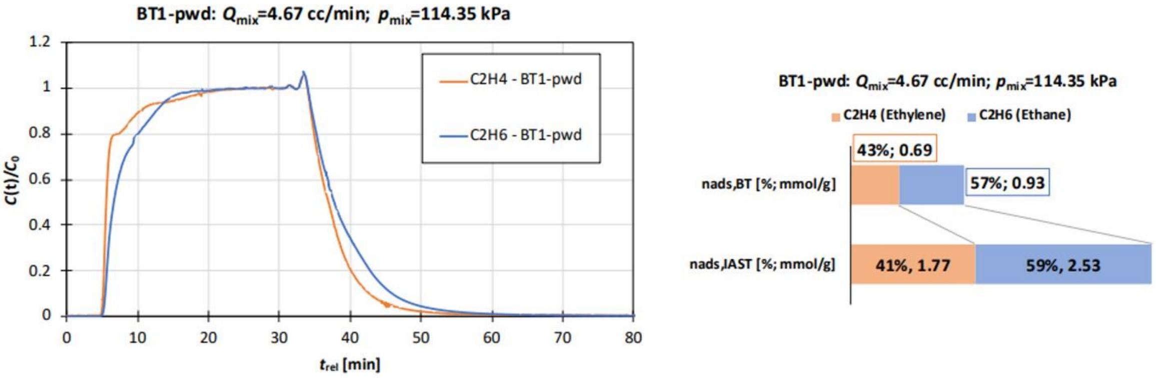

Figure S7: Left: Experimental breakthrough curve for BT1-pwd; Right: Comparison between adsorbed fractions and quantities estimated from BT experiment (nads, BT) and expected from IAST model (nads, IAST) for BT1-pwd.

Initial conditions

Gas	Flow [cc/min]	$y_{\text{(gas mix in column)}}$ [%]	$y_{\text{(gas mix in MS)}}$ [%]
C_2H_6	1.12	50.78%	11.52%
C_2H_4	1.09	49.22%	11.17%
He_{bypass}	7.52	—	77.31%

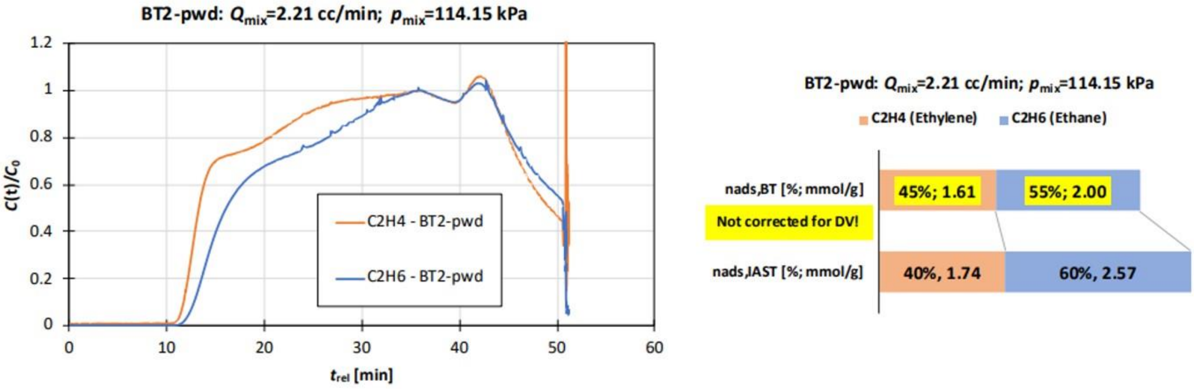

Figure S8: Left: Experimental breakthrough curve for BT2-pwd; Right: Comparison between adsorbed fractions and quantities estimated from BT experiment (nads, BT) and expected from IAST model (nads, IAST) for BT2-pwd.

Initial conditions

Gas	Flow [cc/min]	$y_{(\text{gas mix in column})}$ [%]	$y_{(\text{gas mix in MS})}$ [%]
C_2H_6	2.41	50.01%	13.51%
C_2H_4	2.40	49.99%	13.50%
He_{bypass}	13.00	—	73.91%

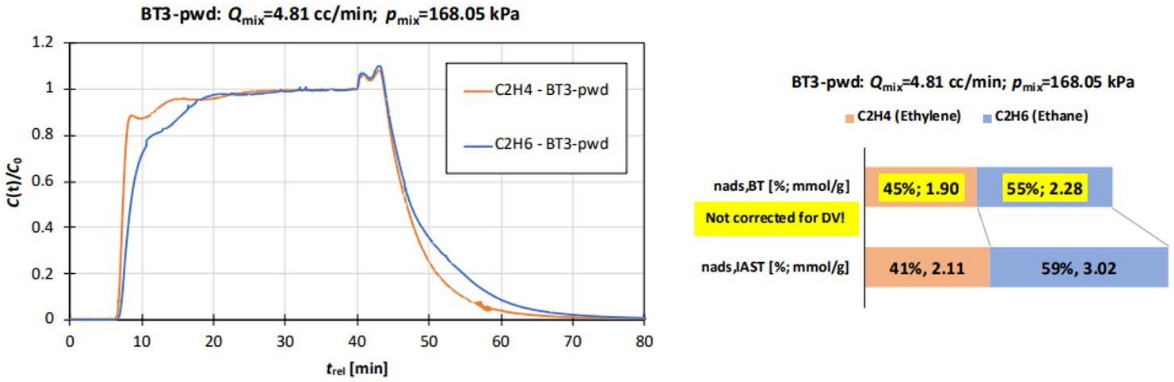

Figure S9: Left: Experimental breakthrough curve for BT3-pwd; Right: Comparison between adsorbed fractions and quantities estimated from BT experiment (nads, BT) and expected from IAST model (nads, IAST) for BT3-pwd.

Initial conditions

Gas	Flow [cc/min]	$y_{(\text{gas mix in column})}$ [%]	$y_{(\text{gas mix in MS})}$ [%]
C_2H_6	1.18	23.69%	6.18%
C_2H_4	3.79	76.31%	19.91%
He_{bypass}	14.06	—	73.91%

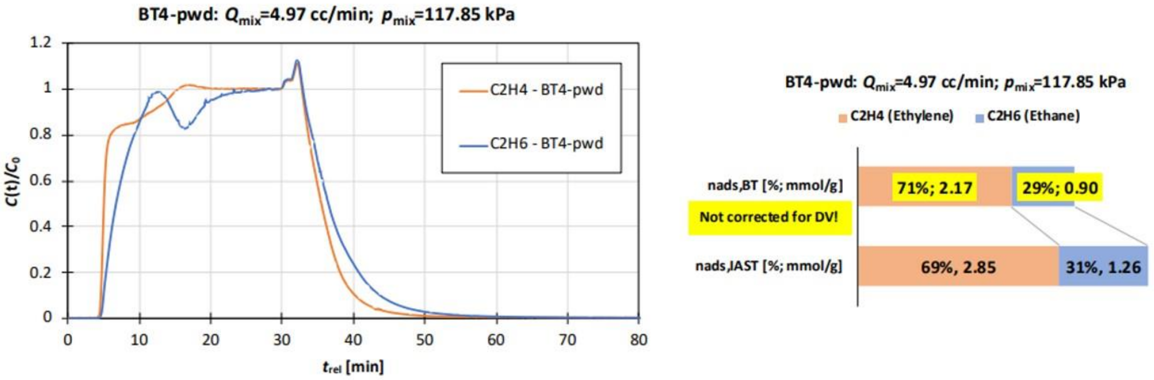

Figure S10: Left: Experimental breakthrough curve for BT4-pwd; Right: Comparison between adsorbed fractions and quantities estimated from BT experiment (nads, BT) and expected from IAST model (nads, IAST) for BT4-pwd.

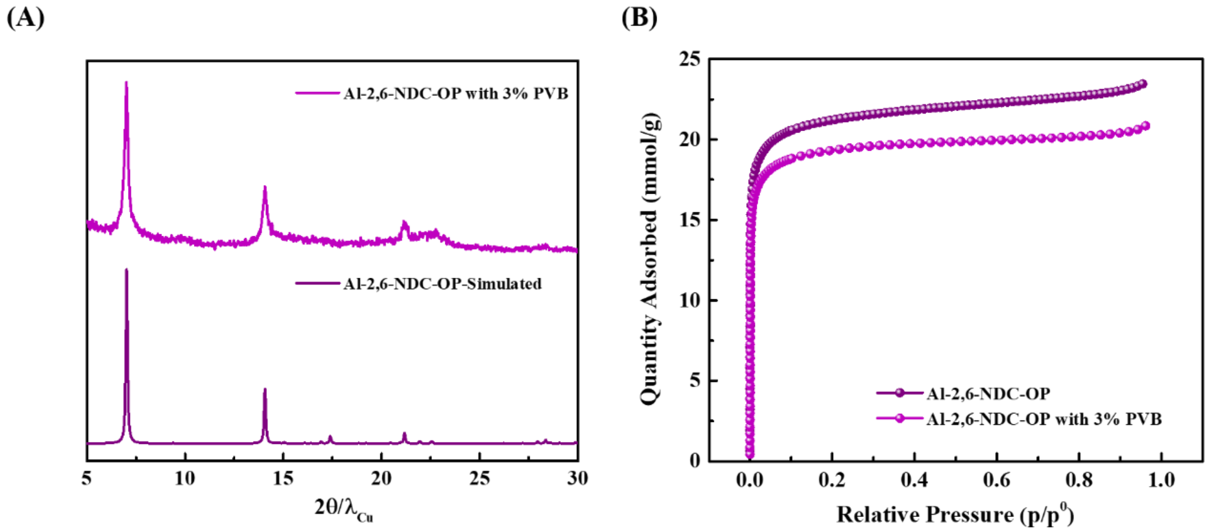

Figure S11: The characterizations of Al-2,6-NDC-OP with 3% PVB. (A) the comparison of PXRD patterns; (B) the comparison of N_2 adsorption isotherms at 77 K, here depicted that Al-2,6-NDC-OP with 3% PVB slightly decreased (9%) the porosity of Al-2,6-NC-OP, due to the PVB binder addition and partial blocking the pore.

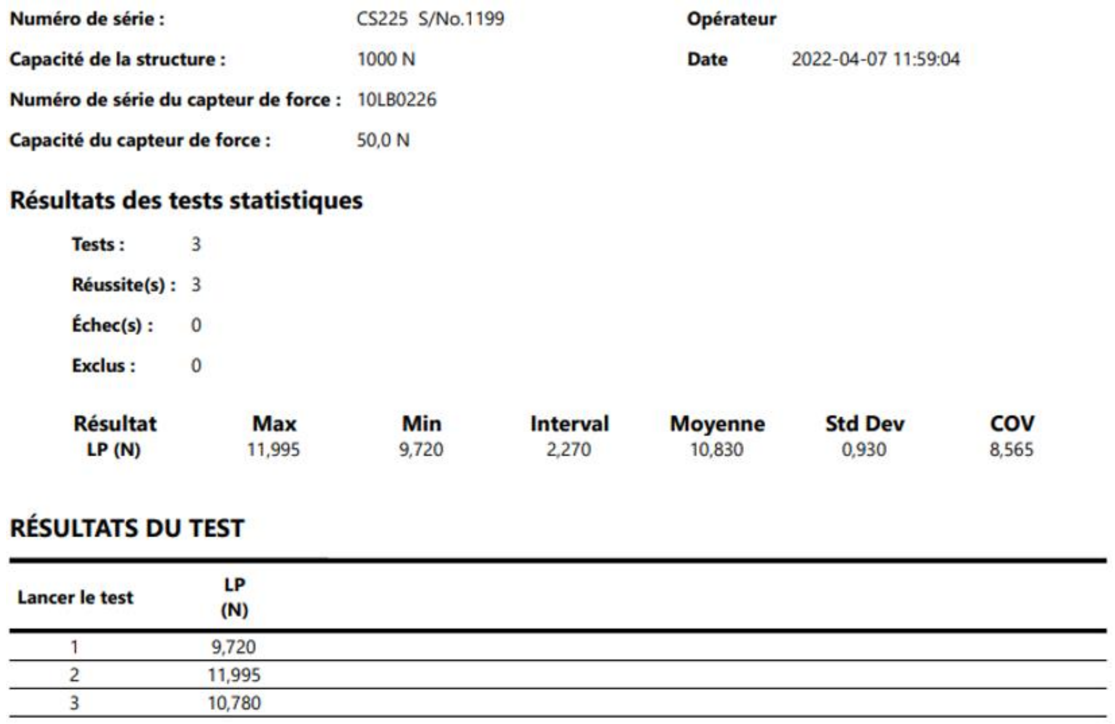

Numéro de série :	CS225 S/No.1199	**Opérateur**	
Capacité de la structure :	1000 N	**Date**	2022-04-07 11:59:04
Numéro de série du capteur de force :	10LB0226		
Capacité du capteur de force :	50,0 N		

Résultats des tests statistiques

Tests :	3
Réussite(s) :	3
Échec(s) :	0
Exclus :	0

Résultat	**Max**	**Min**	**Interval**	**Moyenne**	**Std Dev**	**COV**
LP (N)	11,995	9,720	2,270	10,830	0,930	8,565

RÉSULTATS DU TEST

Lancer le test	**LP (N)**
1	9,720
2	11,995
3	10,780

Table S1: The mechanical result of Al-2,6-NDC-OP with 3% PVB.

Chapter 3

Post-synthetic functionalization of metal-organic framework for the high pressure separation of C_2 hydrocarbons

Table of Contents

Contributions to this work

In this work, robust MOF-808 as a backbone framework has been synthesized and its post-synthetic modification strategy has been applied. Several characterizations such as PXRD, TGA, FT-IR, ^{1}H liquid phase NMR, N_2 adsorption at 77 K, CO_2 adsorption at 298 K, SEM/EDX have been measured. C_2H_6 and C_2H_4 isotherm adsorption under high pressure have been measured and analyzed by Marta BORDONHOS and Prof. Dr. Moisés L. PINTO.

Abstract

Ethane/ethylene (C_2H_6/C_2H_4) separation section using cryogenic distillation is one of the most energy-consuming procedures in the whole petrochemical plants. As one energy-efficient alternative, adsorption separation could be involved in the optimization of energy utilization and the simplification of separation operations. Although adsorption high selectivity has been long term pursued, relying on benchmark adsorbents, the investigation about the enhancement of working capacity of C_2 hydrocarbons is still scarce. Here, we propose a general post-synthetic modification (PSM) strategy on metal-organic frameworks (MOFs) to improve C_2 working capacity above industrially relevant conditions, e.g., above atmospheric pressure. MOF-808, a benchmark Zr tricarboxylate MOF, constituted by a backbone framework with Zr_6 oxoclusters, has been investigated because of its six available sites that can easily be exchanged with groups of interest. As a proof of concept, grafting fluorine-rich (Tri-FluoroAcetic acid or TFA, 3,3,3-TrifluoroPropionic acid or TPA) or phenyl-rich functional groups (Naphthalene-2-sulfonic acid or NSA) on Zr_6 cluster could increase the VdW interactions with C_2H_6 over C_2H_4, leading to a higher working capacity at high pressure. Through pure component gas isotherm adsorption, in comparison with the bare MOF-808, MOF-808-TFA and MOF-808-TPA exhibited a 133% or 155% increase in C_2H_6 working capacity at 298 K, within the 1-9 bar pressure range, respectively.

3.1 Introduction

C_2H_4, as one of the most important source materials in the petrochemical industry, its production is approaching 200 million tons per year.[1] The major procedure to product C_2H_4 in Europe and Asia is now C_2H_6 steam cracking which converts C_2H_6 and introduces unsaturation. However, C_2H_6 is the major impurity in downstream products decreasing the purity of C_2H_4 production, subsequently limiting the diverse applications of C_2H_4, such as polymerization, oxidation, alkylation, hydration, or the halogenation.[2] Due to the similar physical properties between C_2H_6 and C_2H_4, over 120 trays and high reflux ratio on cryogenic distillation columns are used for the separation, leading to the highest energy consumption in a simple separation preformed in chemical plants.[3-6] Compared with cryogenic distillation, adsorption separation (pressure swing adsorption (PSA) or temperature swing adsorption (TSA) could be considered as one of the potential alternatives due to its high selectivity, energy-efficiency, and easy regeneration.[7,8] Generally, the industrial adsorption separation operates technically above ambient pressure, i.e. up to 10-15 bar for adsorption and ambient pressure for desorption to minimize energy consumption. To achieve these merits, the first key point is to seek for robust porous materials with preferential C_2H_6 adsorption over C_2H_4, could be exploited in the fixed-bed column under high pressure.

In the field of porous solids, metal-organic frameworks (MOFs) have been emerging as promising multifunctional materials in gas separation and storage due to their highly versatile and tunable pore engineering.[9,10] Recently, industrial production of the zinc-based MOF (CALF-20) has been applied successfully for cement carbon capture industrial project as a consequence of its high capacity and selectivity for CO_2 in wet gas.[11] Encouraged by this landmark work, it is of interest to seek for a suitable MOF-based adsorbent in a view of the industrial C_2 hydrocarbon adsorption separation. In 2006, Cu(hfipbb)(H_2hfipbb)$_{0.5}$ was proposed for C_2, C_3, and n-C_4 olefins and alkanes separation by Li and her co-workers, which led to a bloom in the study of MOFs for various hydrocarbons separations.[12] From these studies it appears that MOFs bearing a high density of open metal sites and/or highly polar groups such as MIL-101,[13] Fe-MOF-74,[14] NOTT-300,[15] PAF-1-SO_3Ag[16] etc., exhibit a stronger affinity for the alkene, C_2H_4, due to the larger quadrupole moments and more π electrons in C_2H_4 molecules. Consequently, this leads to a C_2H_4-selective adsorption over C_2H_6 with however the need of an additional energy demanding desorption step through inert gas or vacuum to produce polymer-grade C_2H_4 (≥99.95%). To overcome this unwanted desorption step, a few studies have reported the use of C_2H_6-selective MOFs via host-guest interactions favorable to the higher polarizability of C_2H_6 over C_2H_4, such as peroxo-Fe-MOF-74,[17] Cu-(Qc)$_2$,[18,19] UiO-67-(NH_2)$_2$[20] etc. In 2010, ZIF-7 was shown to be ethane-selective based on a gate-opening effect between ethane molecule and the framework. However, due to the strong interactions in these C_2H_6/C_2H_4 selective MOFs, the preferential adsorption behavior occurred only below 0.3 bar implying their saturated adsorption step will be done rapidly. Such a relatively high working capacity below 30 kPa is not suitable for practical industrial applications due to the very costly regeneration of the adsorbents using vacuum pump.

The strategy in the present work is to enhance the Van de Waals (VdW) interaction with C_2H_6 over C_2H_4, via grafting of fluorine-rich or phenyl-rich functional groups on Zr_6 oxoclusters of MOFs through a post-synthetic modification (PSM) strategy to improve the C_2 hydrocarbons working capacity under high pressure. As the framework backbone, MOF-808 has been selected due to its large pores decorated with accessible 6-connected $Zr_6O_4(OH)_4$ clusters, as well as its very good thermal, chemical, and mechanical stability. The as-synthesized MOF-808 comprises six terminal formate ligands ($HCOO^-$) per oxocluster, that is highly favorable for PSM strategy. For instance, a series of fluorinated carboxylic acids as a modulator have been used during MOF-808 synthesis to functionalize MOF-808 structure in a straightforward way. The creation of mixed-matrix membranes with functionalized MOF-808, led to an enhancement of the CO_2/CH_4 separation efficiency.[21] Recently a series of amino acids were introduced into MOF-808 through PSM strategy leading to an amine-rich pore environment and an improvement of the CO_2 capture in the presence of water.[22] This inspired us to design a series of MOF-808-R materials through a PSM with R = 2,2,2-TriFluoroacetic acid (TFA), 3,3,3-TrifluoroPropionic acid (TPA), Naphthalene-2-Sulfonic acid (NSA)); we suspected that either a fluorine-rich or phenyl-rich pore environment, as shown in scheme 1, would lead to a preferential interaction with C_2H_6 over C_2H_4 at high pressure. Indeed, due to the configuration of the Zr_6 oxoclusters decorating the large cages of MOF-808, one expected the grafted TFA/TPA/NSA molecules and their fluorinated or phenyl groups to point at the center of the pores leading to a favorable environment for VdW interactions as well as a more confined space, in order to enable denser contact sites between fluorine or phenyl and hydrogen from C_2 hydrocarbons. Consequently, the stronger affinity of C_2 hydrocarbons of MOF-808-TFA/TPA led to a 133 % and 155 % of enhanced between 1 and 9 bar, in comparison with the bare MOF-808.

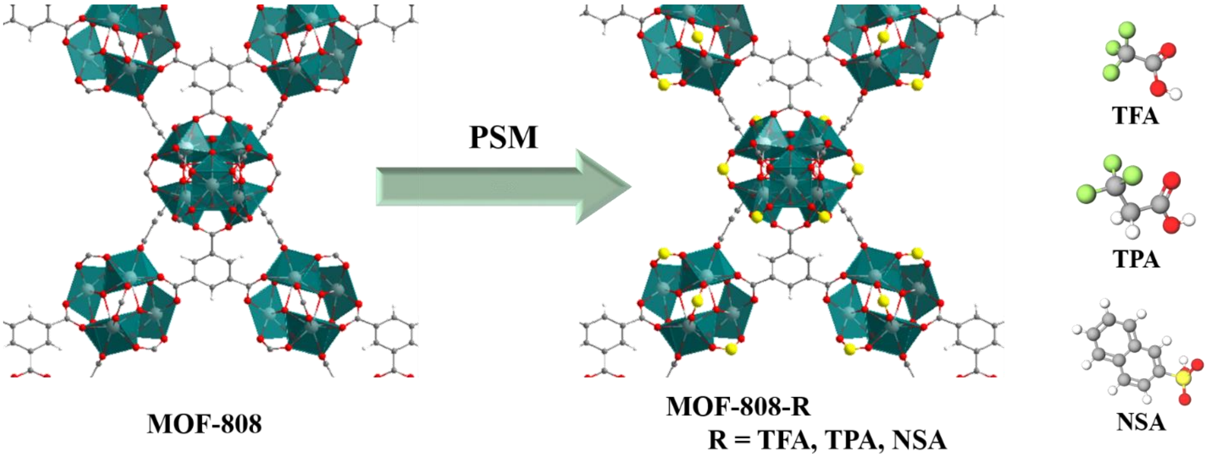

Scheme 1: PSM strategy on Zr_6 oxoclusters of MOF-808 for the denser molecular interactions between fluorine or phenyl groups and C_2H_6 molecules.

3.2 Results and Discussion

3.2.1 Characterization of MOF-808-R

The crystallinity of the MOFs has been checked first by powder X-ray diffraction (PXRD). As shown in Fig. 1A and Fig. S1-3, all samples are highly crystalline, even after PSM. To validate the presence of different functional molecules in MOF-808-TFA/TPA/NSA, these samples were then characterized by FT-IR spectroscopy, as shown in Fig. S4-6. Characteristic bands for MOF-808-TFA were recorded at 1155 and 1194 cm^{-1}, attributed to $-CF_3$ symmetrical and anti-symmetrical stretch of TFA molecules, respectively. Similarly, bands at 1245, 1275 cm^{-1} were assigned to the $-CF_3$ stretches of TPA molecules. Compared with the absorbance bands of S-O in NSA molecule (1024, 1080 cm^{-1}), a little blue shift (1028, 1093 cm^{-1} in MOF-808-NSA) was observed, related to the sulfonic groups grafted on the Zr_6 oxoclusters. Besides, absorbance band of C=O between 1715-1750 cm^{-1} was not observed indicating there were no free carboxylic groups in the pores of MOF-808-R frameworks. Furthermore, the experimental formula of MOF-808-Blank-exp ($Zr_6O_4(OH)_4(BTC)_{1.6}(HCOO)_{2.2}$), was confirmed by TGA and ^1H liquid phase NMR (Fig. S7-8, Table S1), indicating our initial MOF-808 solid became defective after the treatment in pure water. Here MOF-808-Blank exp was considered as a control experiment. The experimental formula of MOF-808-R were deduced from ^1H liquid phase NMR (Table S1). The % of formates on each Zr_6 oxocluster to be replaced by the grafted molecules was estimated of 14.5% for R=TFA, 25% for R=TPA, and 36% for R=NSA.

To clarify the pore environment changes after PSM synthesis, all the activated samples were prepared via heating at 393 K for 8 hours under a dynamic vacuum, then N_2 physisorption isotherms were measured at 77 K (Fig. 1B and C, Fig. S9-10). Compared with that of MOF-

808-Blank-exp (1850 $m^2\ g^{-1}$), all Brunauer-Emmett-Teller (BET) surface areas of MOF-808-TFA (1560 $m^2\ g^{-1}$)/TPA (1480 $m^2\ g^{-1}$)/NSA (737 $m^2\ g^{-1}$) have decreased at variable levels due to the different size/shape and content of PSM molecules. Also, the inflection points of MOF-808-TFA/TPA moved to the direction of lower pressure in agreement with a significant decrease of pore size and/or partial pore blocking due to these functional groups, as shown in Fig. 1D, Table S2. Firstly, there existed two types of pores (11.6 and 18.4 Å) in MOF-808-Blank exp. sample through DFT pore size simulation. As a comparison, the pore size of MOF-808-TFA and TPA showed the large pore decreased to 16.8 and 15.8 Å after PSM, respectively. The pore size distribution agreed well with the hypothesis that the TFA and TPA molecules point to the center of the pores. For the N_2 adsorption isotherm of MOF-808-NSA, the isotherm curve totally changed into microporous Langmuir adsorption (major pore size distribution at 11.1 and 13.6 Å). We hypothesized that the microporosity left after the occupation of the naphthalene moieties in the larger cages, that superposed in the isotherm with the initial microporosity of MOF-808. From scanning electron microscopy (SEM) analysis (Fig. 2), relatively homogeneous shape distributions in all samples were obtained implying that the frameworks did not get macroscopic damage after water/acid treatment.

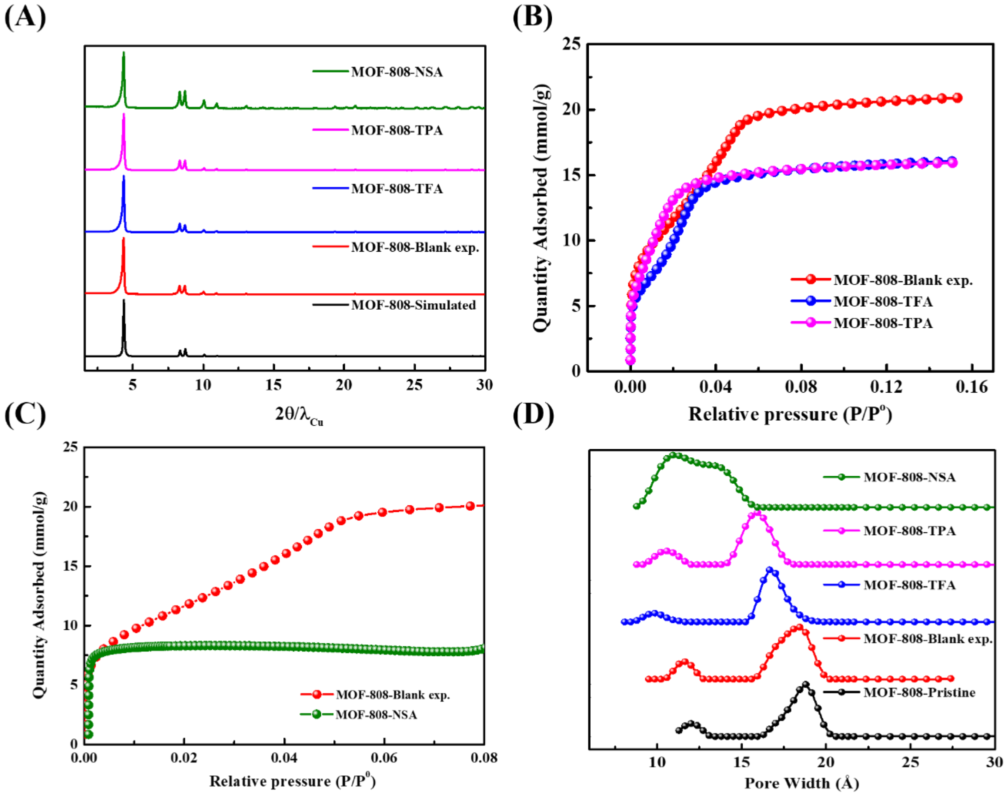

Figure 1: Characterization of MOF-808-PSM. (A) Powder X-ray diffraction; (B, C) N_2 isotherms at 77 K showing only low-pressure range; (D) Pore size distribution simulated by DFT pore size (cylindrical geometry with NLDFT for pillared clay model, $d_V/d_{\log(w)}$ Pore Volume vs pore width).

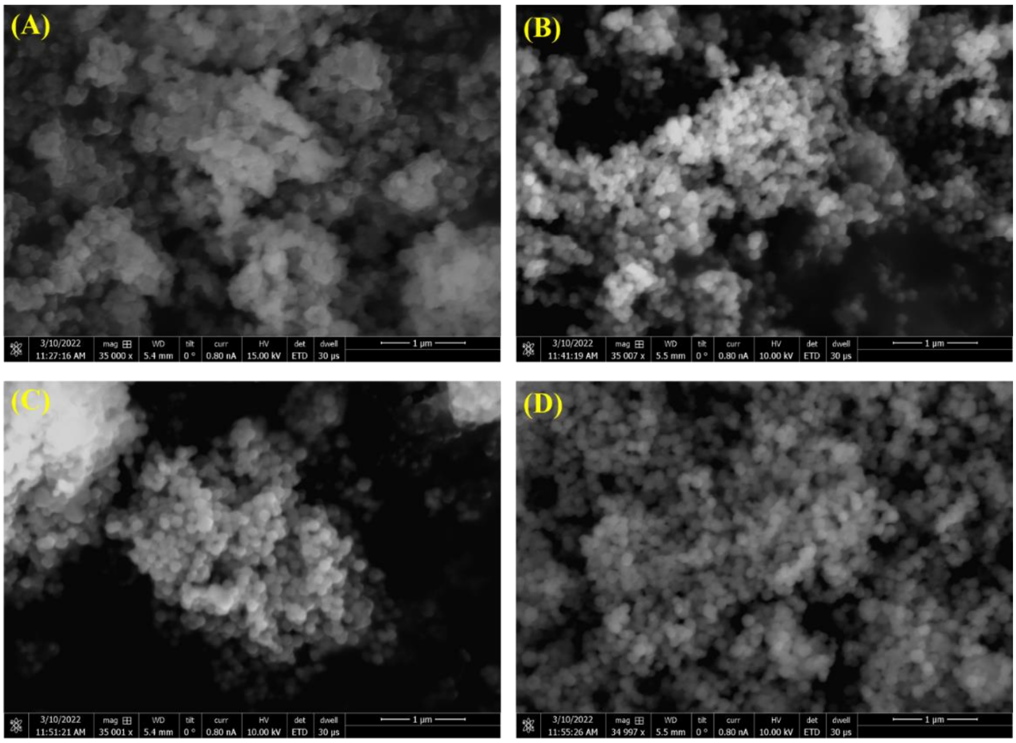

Figure 2: SEM images of MOF-808-Blank exp. (A), MOF-808-TFA (B), MOF-808-TPA (C), MOF-808-NSA (D).

3.2.2 C_2H_6/C_2H_4 adsorption isotherms

In general, for gas separation or storage, adsorption at temperatures much lower than ambient is efficient but expensive. This is why, when possible, adsorption at room temperature is preferred in industry. The loss of efficiency due to a higher adsorption temperature must then be balanced by the use of higher pressures, essentially in the 5-50 bar range. These conditions also correspond to higher densities of the gas and adsorbed phases and then to more compact equipment for the same operating capacity. In research work, the pressure range is sometimes extended up to 150 bar and even above. In contrast with literature reports where the gas isotherms are mainly measured until ambient pressure, here we evaluated the adsorption performance under high pressure, i.e., up to 10 bar. From single component (C_2H_6/C_2H_4) adsorption isotherm measured at 298 K under 9~10 bar, as depicted in Fig. 3, the grafted TFA, TPA and NSA groups in MOF-808 improved the C_2H_6 and C_2H_4 uptake under high pressure, compared with MOF-808-Blank exp. The C_2H_6 uptake amounts of MOF-808-Blank exp/TFA/TPA/NSA were 0.65, 0.70, 0.78, 1.19 mmol g^{-1} at 298 K, 1 bar, 2.96, 3.78, 4.37, 3.32 mmol g^{-1} at 298 K, 9 bar, respectively. Also, a similar trend was observed for C_2H_4 (0.62, 0.75, 0.81, 1.09 mmol g^{-1} at 298 K, 1 bar, 2.38, 3.31, 3.78, 3.38 mmol g^{-1} at 298 K, 9 bar).

To make a comparison with benchmark C_2H_6/C_2H_4 adsorbents, MOF-808-NSA sample exhibited an increase uptake of C_2H_6/C_2H_4 under low pressure (the different uptake between MOF-808-NSA and MOF-808-Blank exp was 0.89 mmol g^{-1} for C_2H_6, 0.86 mmol g^{-1} for C_2H_4, respectively), gradually achieving adsorption saturation with pressure. That result indicated that more phenyl groups together with a small pore size provide more adsorption sites and enhance the C-H···π molecular interactions to achieve high gas uptake and rapid adsorption saturation, although this material has also high amounts of grafted molecules, in comparison with TPA and TFA functionalized materials.

Contrarily, after introduction TFA and TPA molecules, their C_2H_6 and C_2H_4 adsorption isotherm curves almost overlapped well with that of MOF-808-Blank exp before 1 bar. But their uptake continued to increase as a function of pressure (9~10 bars). Similar to naphthalene moiety, -CF_3 groups also offered extra C-H···F hydrogen bonding interactions between C_2H_6/C_2H_4 molecules and the pore walls of MOF-808-TFA/TPA. According to previous work on C_2H_6/C_2H_4 adsorption separation with UiO-66-2CF_3, it was speculated that the grafted TFA/TPA molecules also would lead to a continuing increase of C_2H_6 and C_2H_4 uptake amounts.[23] Tentatively, we hypothesize that before 1 bar, the phenyl groups from trimesic acid should be the main factor to adsorb C_2H_6 and C_2H_4 molecules due to the weak driving force, then the driving force increasing with the pressure, pore space filling effect should become dominant to adsorb more C_2H_6/C_2H_4 molecules.

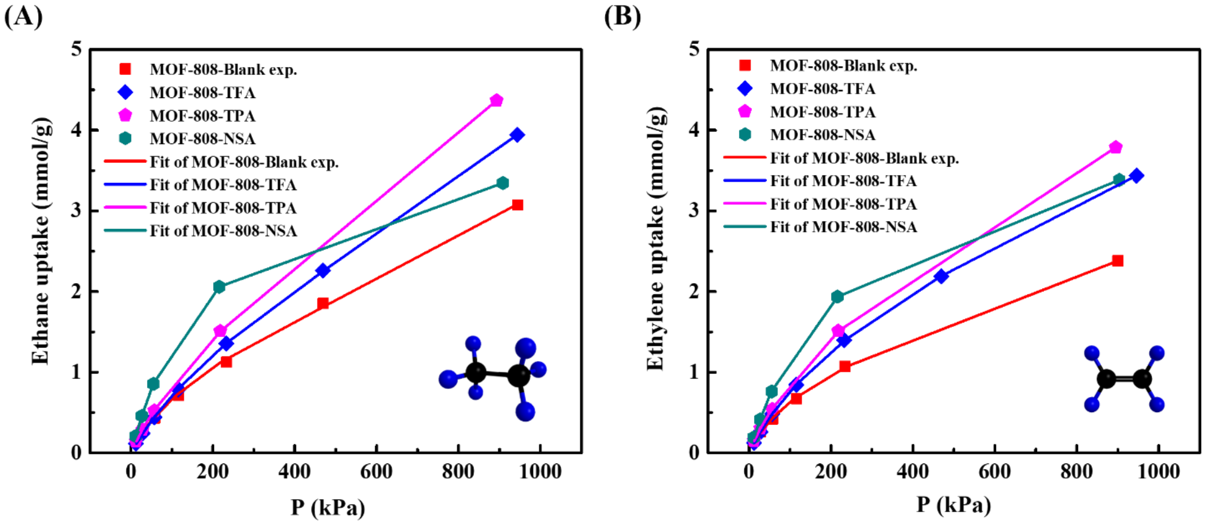

Figure 3: (A) C_2H_6, (B) C_2H_4 single component adsorption isotherm curves and fitting curves of MOF-808-Blank exp/TFA/TPA/NSA under 298 K, 10 bar.

3.2.3 Simulation/calculations about the affinity of C_2H_6/C_2H_4

This part is in progress with our collaborator from Lisbon

3.2.4 Selectivity and working capacity of C_2H_6/C_2H_4 under high pressure

Motivated by the high C_2H_6/C_2H_4 adsorption uptake at high pressure, ideal adsorbed solution theory (IAST) calculated the selectivity of C_2H_6/C_2H_4 for all samples using composition of 50:50 C_2H_6/C_2H_4. Fig. 4A illustrated that the sorption selectivity of C_2H_6/C_2H_4 on MOF-808-Blank exp/TFA/TPA/NSA was estimated to be 1.17, 1.02, 1.05, 1.11 at 298 K, 9 bar, respectively. All the samples still displayed weak C_2H_6-selective adsorption under high pressure. By contrast of the enhancement on C_2H_6/C_2H_4 uptake amounts in MOF-808-TFA/TPA, their C_2H_6/C_2H_4 selectivity indicated that the grafted TFA and TPA molecules on MOF-808 probably provided the almost equivalent C-H···F molecular interactions, even though two extra C-H groups in C_2H_6 molecules. In addition, the small difference between the experimental adsorption isotherms might be due to the limited number of TFA/TPA grafted per Zr_6 oxocluster, where most of the initial formates are still present. For MOF-808-NSA, the selectivity value displayed increased before 175 kPa, thereafter decreased until 10 bar which indicated that there existed the stronger molecular interactions between C_2H_6 and phenyl groups under low pressure, similar pore filling by C_2H_6/C_2H_4 molecules happened as a function of pressure (until 10 bar).

From the regeneration point of view, as above mentioned, many reported adsorbents need moderate vacuum to achieve the full removal of adsorbate which is the very costly and intensive energy-consuming procedure. To avoid or reduce this significant drawback in the PSA cycles, we need to focus on the efficient adsorbent which possesses large uptake gap between atmospheric pressure and high pressure (usually 5-10 times higher than atmospheric pressure). As shown in Fig. 4B, the working capacity of MOF-808-Blank exp/TFA/TPA/NSA were 2.31, 3.08, 3.59, 2.13 mmol g^{-1} for C_2H_6 and 1.76, 2.56, 2.97, 2.29 mmol g^{-1} for C_2H_4 from 1 bar to 9 bar at 298 K, respectively. Significantly, compared with the working capacity of MOF-808-Blank exp and -TFA, one could assume that grafted TPA groups might be associated with shorter contact distances between C_2H_6/C_2H_4 molecules and fluorine atoms when C_2H_6/C_2H_4 molecules enter into the pores, leading to an enhancement of the working capacity but not for selectivity under high pressure. On the contrary MOF-808-NSA exhibited higher C_2H_4 working capacity than C_2H_6 at 298 K, 9 bar, which as above mentioned, naphthalene groups enhance the working capacity for both of gases under high pressure due to the almost equivalent C-H···π affinity.

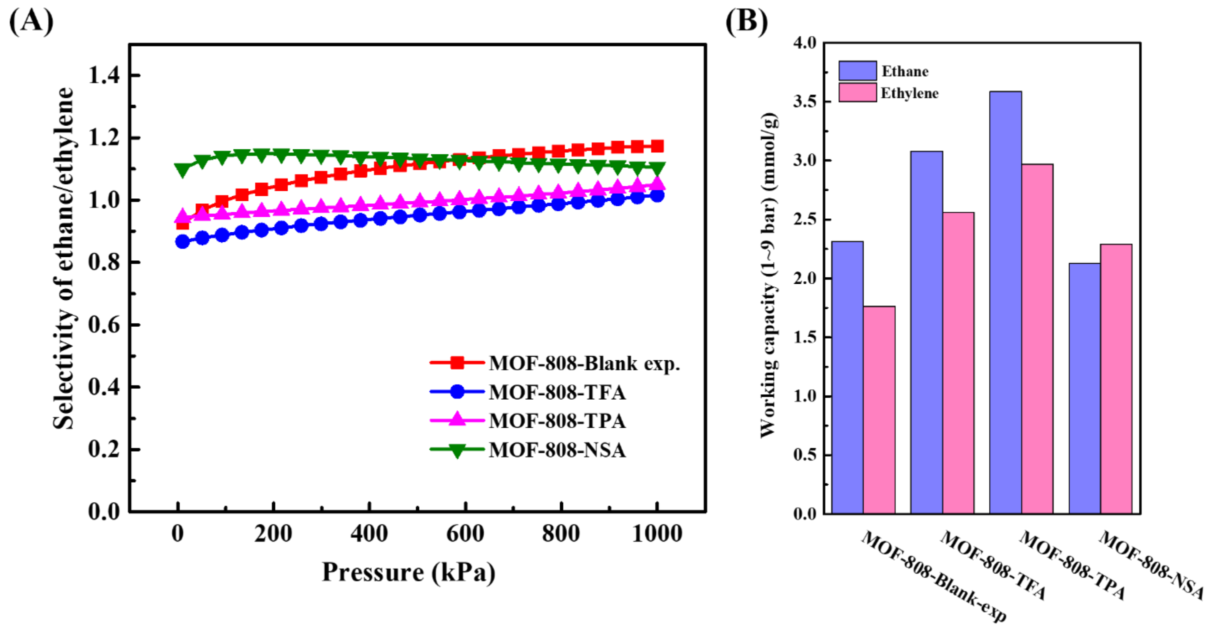

Figure 4: (A) C_2H_6/C_2H_4 (50/50, v/v) IAST selectivity; (B) working capacity (1-9 bar) of MOF-808-Blank exp/TFA/TPA/NSA at 298 K.

3.3 Conclusion

The PSM strategy to graft fluorine-rich functional groups on a MOF-based framework provides a positive influence on the C_2 hydrocarbon separation performance. This work demonstrated that grafting fluorine-rich TFA and TPA on Zr_6 cluster of MOF-808 decreased the pore size systemically, increasing the VdW interactions with C_2H_6 over C_2H_4. Through pure component gas isotherm adsorption, MOF-808-TFA and MOF-808-TPA obtained a higher working capacity at a large range of pressure. It will offer an easy way towards the update of current energy-intensive petrochemical procedures.

3.4 Experimental section

MOF-808(Zr)

Trimesic acid (BTC, 1.49 g) was transferred into a thick-glass jar followed by adding DMF (128 mL). $ZrOCl_2 \cdot 8H_2O$ (2.16 g) was added in the above solution with stirring followed by the addition of formic acid (133 mL). To dissolve the $ZrOCl_2 \cdot 8H_2O$, the stirring kept for 20 mins. Then the jar was sealed and put into the pre-heated oven for 48 hours at 383 K. After cooled down to room temperature, the white crude product was obtained and then collected by centrifugation. Then the product was washed by DMF (1 time) and acetone (2 times), separately to remove the guest molecules from the framework, then dried at 333 K overnight under vacuum condition.

MOF-808(Zr)-Blank exp.

MOF-808 sample (500 mg) was added slowly into DI water (250 mL, 500 mL glass jar), sonicated for 10 mins. Put the glass jar into the per-heated oven for 12 hours at 353 K. After cooling down to room temperature, the product was collected by centrifugation, then the MOF-808-Blank exp. product was washed by DI water (1 time) and acetone (2 times) sequentially and dried at 353 K overnight under vacuum condition.

MOF-808(Zr)-0.1M-TFA (2,2,2-Trifluoroacetic acid)

2,2,2-Trifluoroacetic acid (TFA, 1.9 mL) was dropped slowly into DI water (250 mL, 500 mL glass jar), then MOF-808 sample (500 mg) just obtained was added into above solution, sonicated for 10 mins. Put the glass jar into the pre-heated oven for 12 hours at 353 K. After cooling down to room temperature, the product was collected by centrifugation. Then the product was washed by DI water (1 time) and acetone (2 times), separately to remove the unreacted TFA molecules from the framework, then dried at 60°C overnight under vacuum condition.

MOF-808(Zr)-0.1M-TPA (3,3,3-Trifluoropropionic acid)

3,3,3-Trifluoropropionic acid (TPA, 2.2 mL) was dropped slowly into DI water (250 mL, 500 mL glass jar), the followed the same process as MOF-808-0.1M-TFA.

MOF-808(Zr)-0.1M-NSA (2-Naphthalene-sulfonic acid)

2-Naphthalene-sulfonic acid (NSA, 5.2 g) was dissolved into DI water (250 mL, 500 mL glass jar), the followed the same process as MOF-808-0.1M-TFA

Activation condition for all samples

Before we ran N_2 adsorption and C_2H_6/C_2H_4 adsorption, the samples needed to heat at 393 K for 8 hours under a dynamic vacuum.

Chemicals and instruments

All chemicals were purchased from commercial suppliers and used as obtained without further purification. Powder X-ray diffraction (PXRD) data was recorded on a high-throughput Bruker D8 Advance diffractometer working on transmission mode and equipped with a focusing Göbel mirror producing CuKα radiation ($\lambda = 1.5418$ Å) and a LynxEye detector. Nitrogen porosimetry data were collected on a Micromeritics Tristar/Triflex instrument at 77 K (pre-activating samples at 120°C under vacuum, 5 hours). TGA data were collected on Mettler Toledo TGA/DSC 2, STAR System apparatus with a heating rate of 5°C min^{-1} under the oxygen flow. Mettler Toledo FiveEasyTM Plus pH/mV bench meter. Infrared spectra were measured with a Nicolet iS5 FT-IR ThermoFisher spectrometer. ^{1}H NMR spectra were recorded on a Bruker Avance 300 spectrometer.

Single C_2H_6/C_2H_4 isotherm tests

All the samples were activated under high vacuum (below 10^{-2} Pa) at 473 K overnight, followed by *in situ* activation in the high-pressure adsorption line at 473 K for 30 minutes to account for exposure to ambient air during transfer from overnight activation setup to adsorption cell. All adsorption equilibrium isotherms were measured at 298 K, increasing pressures up to 1000 kPa (10 bar).

3.5 References

(1) Koottungal, L. *Oil and Gas Journal* **2012**, *110*, 85.

(2) Sadrameli, S. *Fuel* **2015**, *140*, 102.

(3) Martins, V. F.; Ribeiro, A. M.; Santos, J. C.; Loureiro, J. M.; Gleichmann, K.; Ferreira, A.; Rodrigues, A. E. *AIChE Journal* **2016**, *62*, 2490.

(4) Worrell, E.; Phylipsen, D.; Einstein, D.; Martin, N. *Energy use and energy intensity of the US chemical industry*, Lawrence Berkeley National Lab.(LBNL), Berkeley, CA (United States), 2000.

(5) Sholl, D. S.; Lively, R. P. *Nature* **2016**, *532*, 435.

(6) Eldridge, R. B. *Industrial & engineering chemistry research* **1993**, *32*, 2208.

(7) Wiessner, F. G. *Gas Separation & Purification* **1988**, *2*, 115.

(8) Wang, Y.; Peh, S. B.; Zhao, D. *Small* **2019**, *15*, 1900058.

(9) Cui, W. G.; Hu, T. L.; Bu, X. H. *Advanced Materials* **2020**, *32*, 1806445.

(10) Mukherjee, S.; Sensharma, D.; Chen, K.-J.; Zaworotko, M. J. *Chemical Communications* **2020**, *56*, 10419.

(11) Lin, J.-B.; Nguyen, T. T.; Vaidhyanathan, R.; Burner, J.; Taylor, J. M.; Durekova, H.; Akhtar, F.; Mah, R. K.; Ghaffari-Nik, O.; Marx, S. *Science* **2021**, *374*, 1464.

(12) Pan, L.; Olson, D. H.; Ciemnolonski, L. R.; Heddy, R.; Li, J. *Angewandte Chemie International Edition* **2006**, *45*, 616.

(13) Hwang, Y. K.; Hong, D. Y.; Chang, J. S.; Jhung, S. H.; Seo, Y. K.; Kim, J.; Vimont, A.; Daturi, M.; Serre, C.; Férey, G. *Angewandte Chemie* **2008**, *120*, 4212.

(14) Bloch, E. D.; Queen, W. L.; Krishna, R.; Zadrozny, J. M.; Brown, C. M.; Long, J. R. *science* **2012**, *335*, 1606.

(15) Yang, S.; Ramirez-Cuesta, A. J.; Newby, R.; Garcia-Sakai, V.; Manuel, P.; Callear, S. K.; Campbell, S. I.; Tang, C. C.; Schröder, M. *Nature chemistry* **2015**, *7*, 121.

(16) Li, B.; Zhang, Y.; Krishna, R.; Yao, K.; Han, Y.; Wu, Z.; Ma, D.; Shi, Z.; Pham, T.; Space, B. *Journal of the American Chemical Society* **2014**, *136*, 8654.

(17) Li, L.; Lin, R.-B.; Krishna, R.; Li, H.; Xiang, S.; Wu, H.; Li, J.; Zhou, W.; Chen, B. *Science* **2018**, *362*, 443.

(18) Lin, R.-B.; Wu, H.; Li, L.; Tang, X.-L.; Li, Z.; Gao, J.; Cui, H.; Zhou, W.; Chen, B. *Journal of the American Chemical Society* **2018**.

(19) Tang, Y.; Wang, S.; Zhou, X.; Wu, Y.; Xian, S.; Li, Z. *Chemical Engineering Science* **2020**, *213*, 115355.

(20) Gu, X.-W.; Wang, J.-X.; Wu, E.; Wu, H.; Zhou, W.; Qian, G.; Chen, B.; Li, B. *Journal of the American Chemical Society* **2022**, *144*, 2614.

(21) Thür, R.; Van Velthoven, N.; Lemmens, V.; Bastin, M.; Smolders, S.; De Vos, D.; Vankelecom, I. F. *ACS applied materials & interfaces* **2019**, *11*, 44792.

(22) Lyu, H.; Chen, O. I.-F.; Hanikel, N.; Hossain, M. I.; Flaig, R. W.; Pei, X.; Amin, A.; Doherty, M. D.; Impastato, R. K.; Glover, T. G. *Journal of the American Chemical Society* **2022**, *144*, 2387.

(23) Pires, J. o.; Fernandes, J.; Dedecker, K.; Gomes, J. R.; Perez-Sanchez, G.; Nouar, F.; Serre, C.; Pinto, M. s. L. *ACS applied materials & interfaces* **2019**, *11*, 27410.

Supporting information

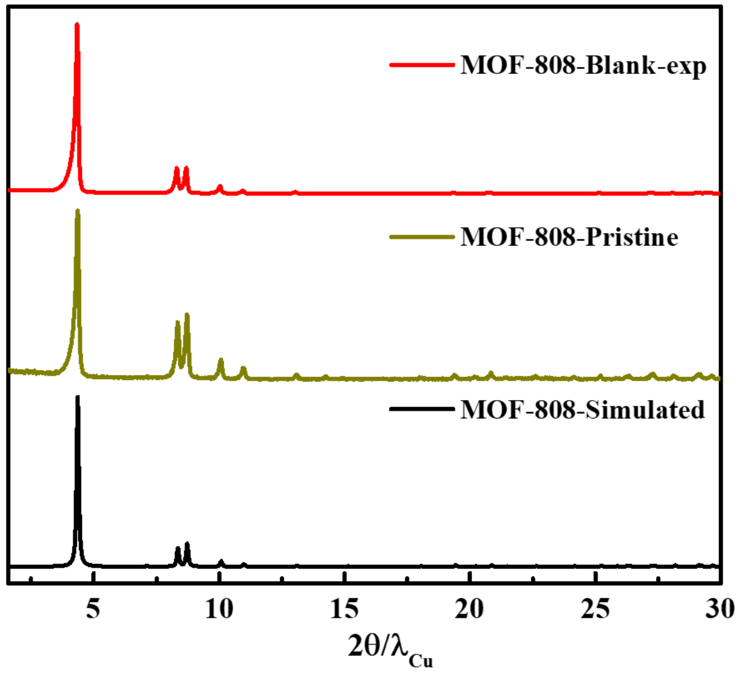

Figure S1: PXRD patterns of MOF-808 and MOF-808-Blank exp.

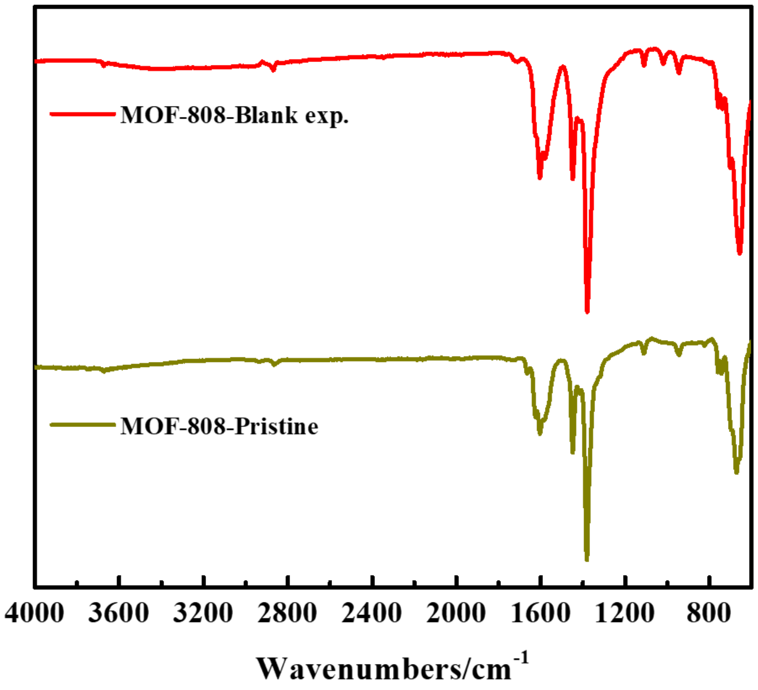

Figure S2: FT-IR spectra of MOF-808 and MOF-808-Blank exp.

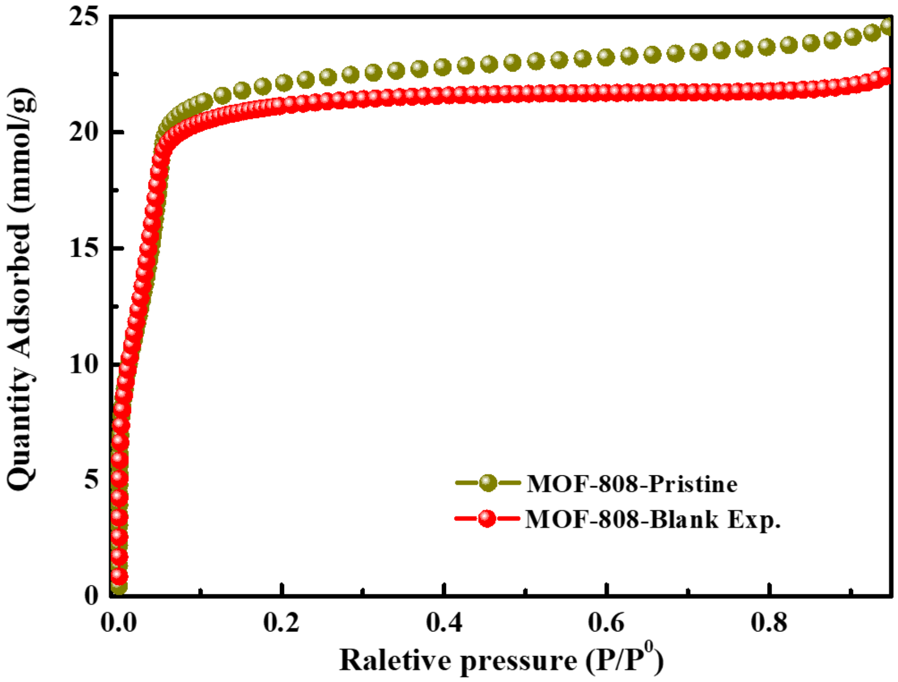

Figure S3: N_2 adsorption isotherms at 77 K of MOF-808-Pristine and MOF-808-Blank exp.

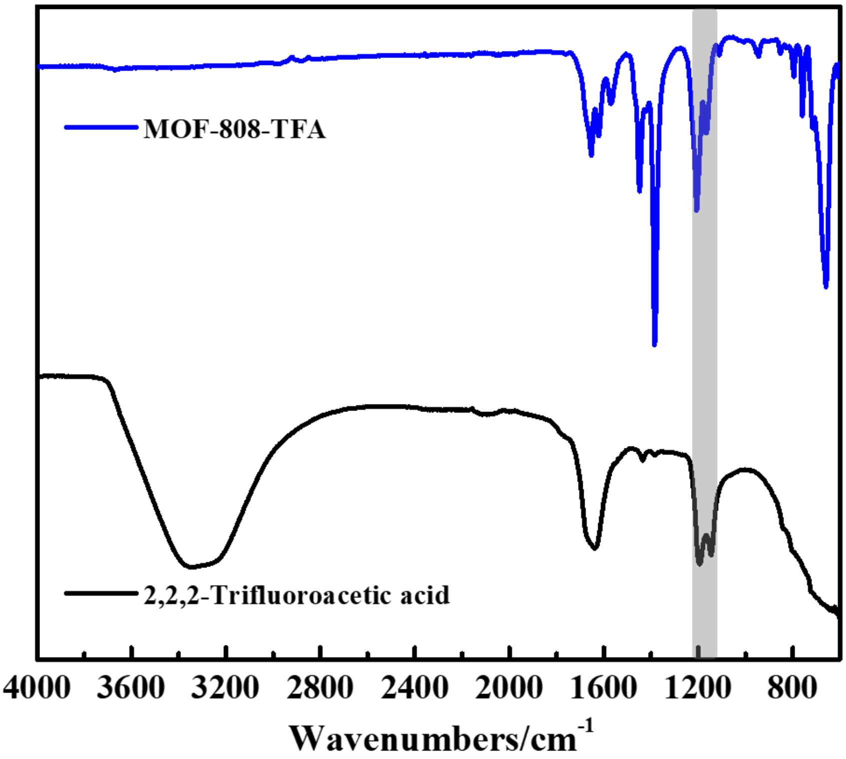

Figure S4: FT-IR spectra of MOF-808-TFA with a comparison of TFA molecule.

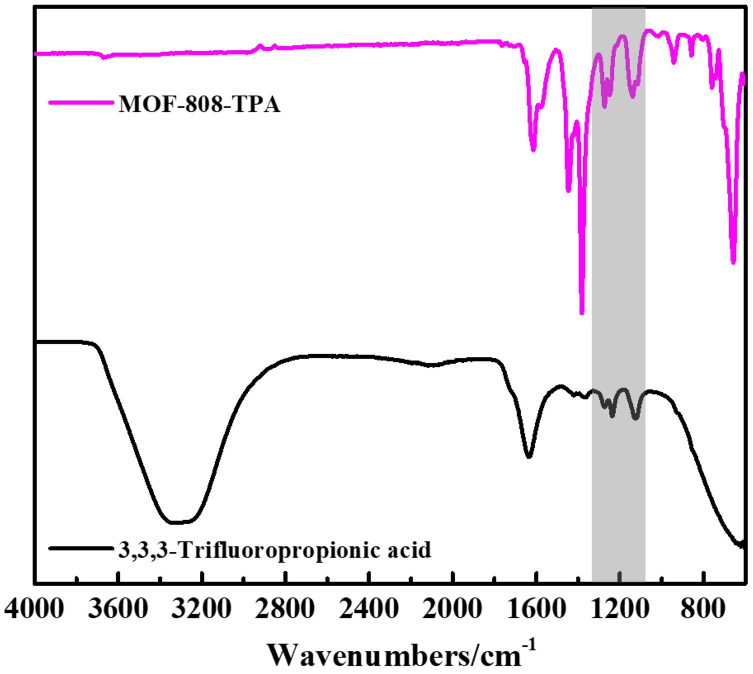

Figure S5: FT-IR spectra of MOF-808-TPA with a comparison of TPA molecule.

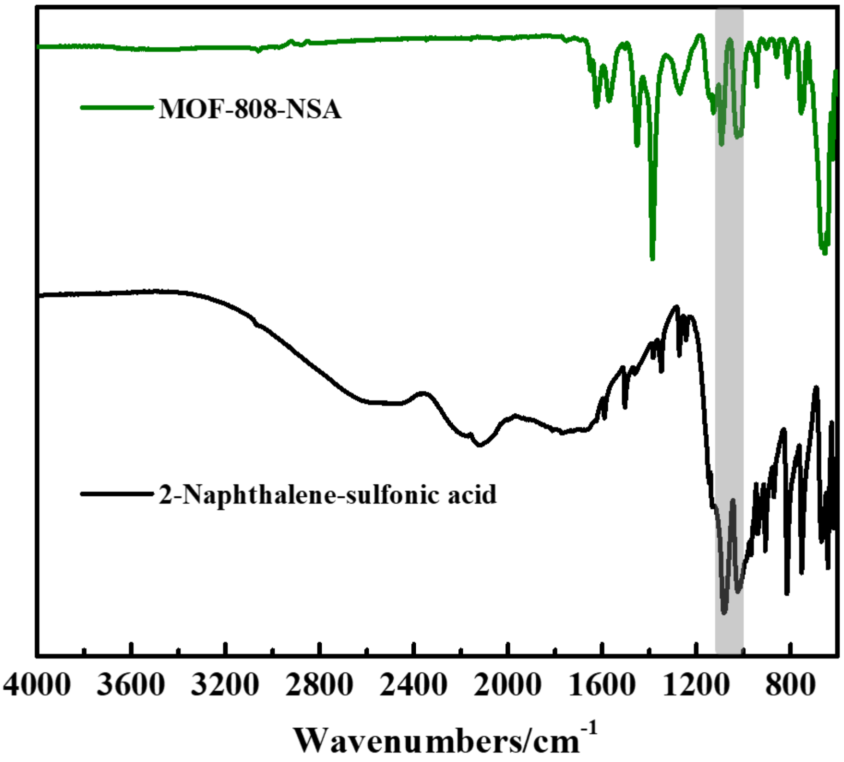

Figure S6: FT-IR spectra of MOF-808-NSA with a comparison of 2-NSA molecule.

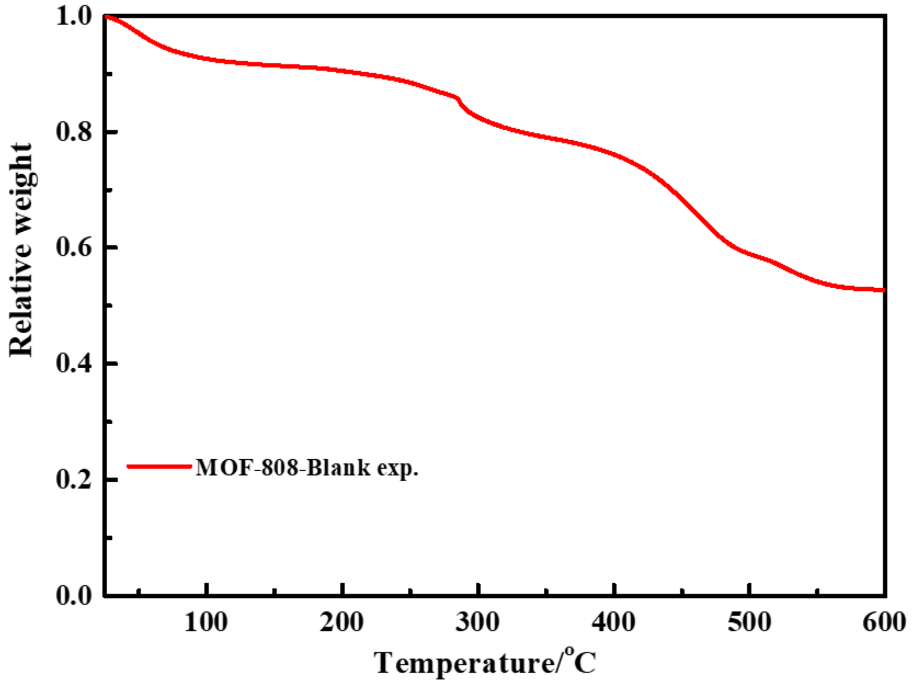

Figure S7: The TGA curves of MOF-808-Blank exp in O_2 condition.

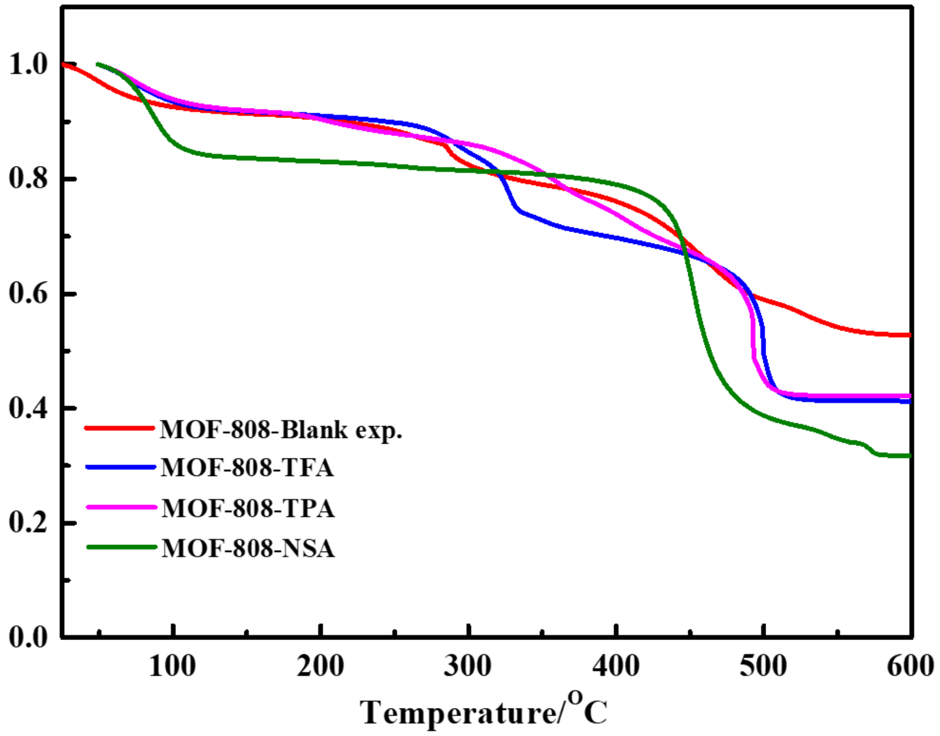

Figure S8: The comparison of TGA results of MOF-808-Blank exp./TFA/TPA/NSA in O_2 condition.

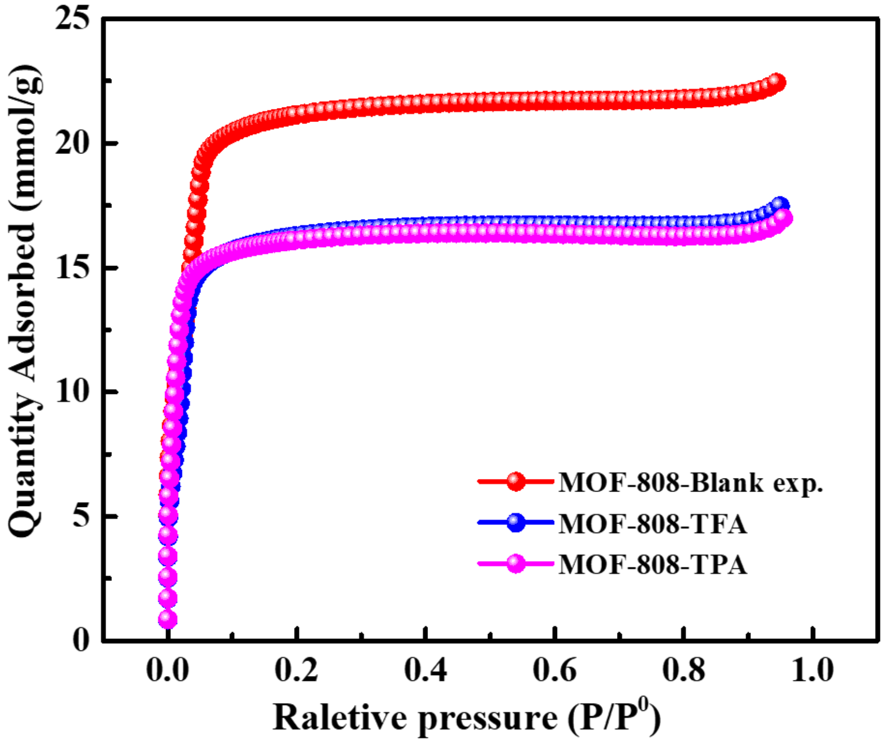

Figure S9: N_2 adsorption isotherms of MOF-808-Blank exp and MOF-808-TFA/TPA at 77 K.

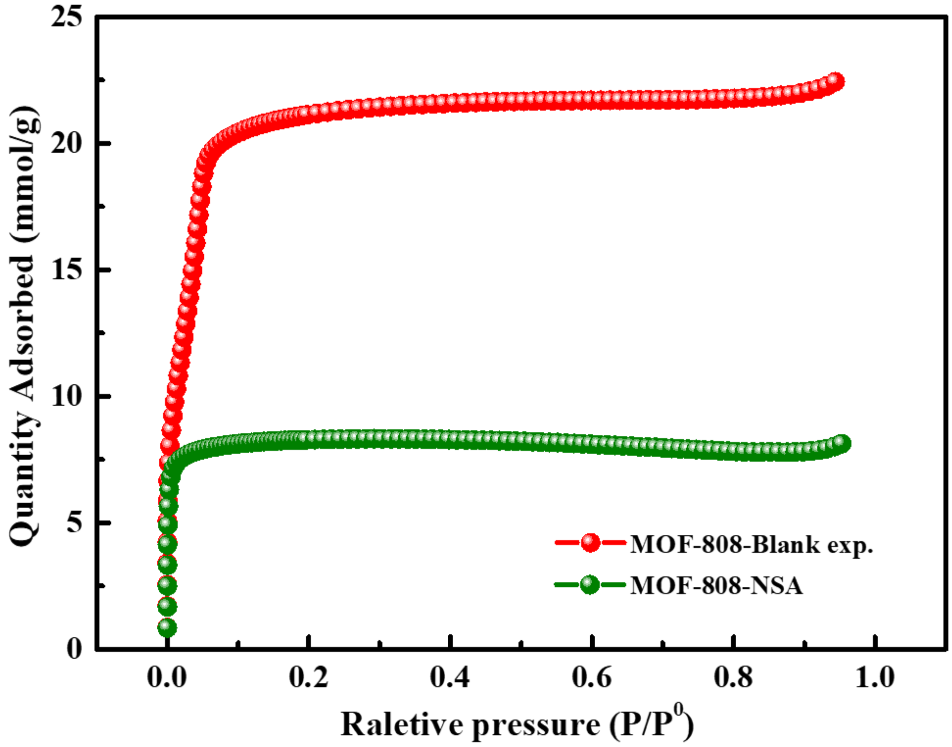

Figure S10: N_2 adsorption isotherms of MOF-808-Blank exp and MOF-808-NSA at 77 K.

Table S1: ^1H liquid phase NMR data of MOF-808-Blank exp/TFA/TPA/NSA by alkaline-digested (KOH/D_2O).

Name	**No. of BTC**	**No. of Formates**	**No. of Grafted molecules**	**Experimental formula**
MOF-808-Blank exp	1.6	2.225	0	$Zr_6O_4(OH)_4(BTC)_{1.6}(HCOO)_{2.2}$
MOF-808-TFA	1.6	1.9	0.32	$Zr_6O_4(OH)_4(BTC)_{1.6}(HCOO)_{1.9}(TFA)_{0.32}$
MOF-808-TPA	1.6	1.66	0.56	$Zr_6O_4(OH)_4(BTC)_{1.6}(HCOO)_{1.66}(TPA)_{0.56}(Cl)_{0.014}$
MOF-808-NSA	1.6	0.896	0.8	$Zr_6O_4(OH)_4(BTC)_{1.6}(HCOO)_{0.896}(NSA)_{0.8}$

Table S2: Summary of high resolution N_2 adsorption isotherms for MOF-808-Blank exp/TFA/TPA/NSA.

Name	**Gas Uptake ($cm^3\ g^{-1}$ STP)**	**Bet Surface Area ($m^2\ g^{-1}$)**	**Pore Volume ($cm^3\ g^{-1}$) @0.2P/P_0**	**Pore Size Distribution /Å**
MOF-808-Blank exp.	476	1850	0.73	11.6 and 18.4
MOF-808-TFA	366	1560	0.56	9.8 and 16.8
MOF-808-TPA	362	1480	0.56	10.5 and 15.8
MOF-808-NSA	185	737	0.28	11.1 and 13.6

Chapter 4

An easy scalable, highly robust microporous Al MOF for post-combustion carbon capture

Table of Contents

Contributions to this work

In this work, I studied the possibility to optimize green synthesis of MIL-120 under mild conditions. The material was characterized using different conventional (PXRD, FT-IR, TGA in O_2, N_2 and CO_2 adsorption at 77 and 298 K, SEM/EDX, ^1H liquid phase NMR) and advanced techniques, such as *in situ* PXRD studies of the activation (dynamic vacuum) and CO_2 loading (with help of Dr. Iurii DOVGALIUK) as well as *in situ* IR spectroscopy for CO_2 adsorption in the presence of water (in collaboration with Prof. Marco DATURI and Dr Nuria GARCÍA MONCADA). Prof. Dr. Guillaume MAURIN and Dr. Dong FAN did the simulation for CO_2 adsorption by DFT and GCMC and analyzed the results. Prof. Dr. Guy DE WEIRELD and Dr. Nicolas HEYMANS measured the CO_2/N_2 breakthrough experiments and analyzed the results. Dr. Shyamapada NANDI measured the water adsorption at 298 K. Dr. Farid NOUAR, Dr. Shyamapada NANDI and Dr. Debanjan CHAKRABORTY adapted the optimized synthesis to 100g-scale batch and shaped the materials by extrusion, wet granulation. Dr. Rosana PINTO and Dr. Farid NOUAR synthesized 6-7 kg material to be shipped to KRICT (Daejon, South Korea) for shaping within the frame of MOF4AIR project. Besides, I have further developed an alternative synthesis protocol using $NaAlO_2$ (an inexpensive Al-precursor) with my intern, Mr. Masheer Ul HAQ, then Dr. Debanjan CHAKRABORTY and Dr. Rosana PINTO adapted the synthesis to a larger scale using a 5 L reactor.

Abstract

Adsorptive separation via scalable, inexpensive adsorbents for post-combustion carbon capture, is now considered among the efficient alternative solutions for carbon mitigation via selective physisorption of CO_2. As the industrial gas streams contain some water vapours, the use of sorbents showing limited detrimental effect of humidity on the working capacity in the operating conditions is considered as a major advantage contributing to lowering the costs and/or accelerating the capture process. Here we report on a robust microporous aluminum tetracarboxylate framework, MIL-120(Al)-AP, (AP refers to ambient pressure synthesis), which possesses relatively high CO_2 uptake (1.9 mmol g^{-1} at 0.1 bar, 298 K) due to the high density of μ_2-OH groups into the framework, gets close to the performances of the benchmark CO_2 physisorbent, CALF-20. This was further supported by the GCMC simulations indicating a great potential of MIL-120(Al)-AP towards carbon capture. Meanwhile, Q_{st} (CO_2) value of MIL-120(Al)-AP (44 kJ mol^{-1}) indicates low energy penalty for full regeneration. Moreover, *in situ* PXRD study revealed a phase transition from monoclinic to triclinic due to partial removal of free water molecules, with *ca.* 40% water molecules still remaining trapped between Al oxo/hydroxo chains, enabling additional hydrogen bonds with CO_2 molecules during adsorption. Due to the high hydrophilic character of MIL-120(Al)-AP, the effect of water during the CO_2 adsorption was investigated via *in situ* infrared spectroscopy. It showed a preferential adsorption of CO_2 over H_2O at the early stage of adsorption, suggesting the potential of MIL-120(Al)-AP to capture CO_2 in presence of water through a fast adsorption/desorption cycle. The low cost of MIL-120(Al) constitutive materials, its environmentally friendly synthesis, easily scalable at the kilogram scale with high yield of this MOF makes it more promising in a view of integration into an industrial scale CO_2 capture process. Its efficient CO_2/N_2 separation ability was finally validated by breakthrough experiments using shaped MOF granules.

4.1 Introduction

Carbon capture and storage (CCS) is envisioned to significantly tackle increasing levels of atmospheric CO_2 achieving the prevention of global warming.[1] Compared with current potential carbon capture technologies, such as direct air capture, pre-combustion capture and oxyfuel combustion, post-combustion capture of flue gas emitted from power plants is considered as a feasible and economically viable process as it might be potentially retrofitted to the existing fleet of coal-fired power stations.[2] So far, aqueous amine solution through a combination of chemical and physical absorption affinity with CO_2 molecule, is the most applicable and mature technology for CO_2 capture in coal-fired power plants.[3,4] However, such well-established large scale carbon capture processes is raising such as the environmentally unfriendly release of toxic pollutants, oxidation of amine group, and the corrosivity of the equipment. This process also requires a high energy consumption for the full-regeneration due to the reversible formation of carbamate or bicarbonate species due to the CO_2 chemisorption. It is estimated for a coal-fired power plants that, 60-80% of total thermal energy and consumption comes from this aqueous amine solution CCS process.[5] Compared with this energy-intensive process, exploration of the non-thermal (or low energy) technology for CO_2 capture is strongly motivated by the tremendous prospects of energy savings. Physisorptive CO_2 capture as an efficient low-heat technology is expected to provide much lower energy consumption for regeneration due to the relatively low adsorption enthalpy compared with the heat of amine (87 kJ mol^{-1}).[6,7]

Porous solid adsorbents especially the cationic zeolites are potential candidates for physisorbents with excellent working capacity and selectivity of CO_2 given their relatively strong affinity of CO_2 over other gases present in the industrial gas stream.[8,9] However, despite their relatively low production cost and high thermally/chemical stability, the detrimental competitive adsorption of water molecules significantly decreases their CO_2 working capacity and selectivity as well as require very high temperature regeneration to desorb free water.[9] Alternatively, amine-functionalized porous materials or porous organic materials inspired by the outstanding CO_2 uptake capacities of aqueous amine solutions are suitable alternative candidates.[10,11] Again, the relatively high energy penalty for the regeneration, long term stability issues and/or challenges in the up-scaling make these classes of solids questionable for real industrial separation processes.[12] Robust metal-organic frameworks (MOFs), built either from high valence metal oxoclusters/chains and poly-carboxylates or phosphonates, or alternatively metal(II) poly-azolates, are also candidates for CO_2 capture. Their high customizability enabling a precise tuning and functionalization of the pore structure, has been intensively investigated for selective gas separation applications.[13-15] Indeed, one can either for instance easily tune their hydrophobicity to mitigate the negative effect of water. For instance, Long et al. have grafted tetraamine chains on the large pores Mg_2(dobpdc) (dobpdc = 4,4′-dioxidobiphenyl-3,3′-dicarboxylate) through post-synthesis modification method, improving the efficiency in CO_2 capture under harsh conditions relevant to natural gas flue emissions.[16] Most notably, the higher thermal stability of the tetraamine-functionalized framework was exploited, enabling a regeneration through a direct steam contact with steam, resulting in a significant energy savings over the conventional methods. Very recently, CALF-20, a microporous robust Zn_2(1,2,4-triazolate)$_2$(oxalate) materials (CALF stands for Calgary Frameworks) has emerged as the new benchmark CO_2 sorbent with physisorptive mechanism for the CO_2 capture from cement flue gas.[17]. Thanks to its moderate (40 kJ mol^{-1}) heat of adsorption, excellent CO_2 capacity in post-combustion conditions (2.66 mmol g^{-1} at 0.15 bar and 298 K), and moderate hydrophilicity, it was exploited, once coated on a rotary bed, for the efficient capture of CO_2 in presence of moisture up to *ca.* 25-30% RH. This MOF was proven to be be scaled-up at the ton-scale. Its production at the hundred tons scale is now ongoing in order to be integrated into larger scale industrial applications. SIFSIX or TIFSIX based MOFs are also considered as potential candidates for the post combustion capture.[18-20] However, their long-term hydrolytic stability is still not well established while their large-scale production is hampered with strong safety issues, due to the potential formation of HF. From the material cost point of view, aluminium based MOFs (Al-MOFs), when relying on cheap commercial polycarboxylic acids, require the use of inexpensive Al metal source and if endowing comparable CO_2 adsorption performance with CALF-20, stand themselves as promising candidates for CO_2 capture. One could highlight additional potential robust MOFs candidates, such as A520 or Al fumarate,[21,22] MIL-91(Ti),[23] MIL-160(Al),[24-26] UTSA-280,[27] which can be obtained easily in kilogram scale product via facile, green and one-pot synthesis procedure and simply manufactured as structured adsorbents, e.g., pellets, beads, monoliths, fibres. However, their CO_2 capacity is significantly lower compared to the benchmark CALF-20.

In this regard, we investigated the performance of other existing microporous Al-based MOFs. We selected the robust microporous aluminum tetracarboxylate framework, MIL-120(Al) because of its excellent CO_2 capture efficiency at relatively low pressure (~1.9 mmol g^{-1} at 0.1 bar at 298 K), comparable to the best amine-free benchmark CO_2 adsorbents. Due its promising performances, we have further explored this MOF through an in-depth joint experimental/computational study to understand the key features driving this performance. In parallel, as this material was initially made under hardly scalable hydrothermal conditions, we developed an alternative eco-friendly ambient-pressure (AP) synthesis procedure suitable for the scale-up of MIL-120(Al)-AP. GCMC simulations showed that the high density of μ_2-OH groups aligned along the 1D narrow channels plays a significant role towards interactions with the CO_2 molecules although the moderate (isosteric) heat of adsorption (Q_{st}) MIL-120(Al)-AP

(44 kJ mol^{-1}) suggesting a relatively low energy cost for adsorbent regeneration. This MOF also possesses very high CO_2/N_2 selectivity of 95 and 122 for the corresponding binary mixture $15CO_2:85N_2$ and $5CO_2:95N_2$ respectively at 0.1 bar and 298 K. Noteworthy, *In situ* PXRD experiments confirm MIL-120(Al)-AP exhibited a phase transition, from monoclinic to triclinic, due to the partial removal of the solvent (water) molecules, as well as a significant amount of free water molecules (*ca.* 40% crystallographic occupancy) still being trapped between Al hydroxo chains, resulting into additional hydrogen bonds with CO_2 molecules during CO_2 adsorption. Additionally, *in situ* infrared spectroscopy (IR) studies have shown that the kinetic of adsorption of CO_2 molecules is much faster than the one of water, suggesting the possibility of a kinetic CO_2/H_2O separation during the CO_2/N_2 separation under humid conditions. Finally, the environment friendly synthesis, high yield, easy processability to the kilogram scale was exploited to produce enough material for shaping prior to breakthrough separation tests for the efficient adsorptive separation of CO_2/N_2 using MIL-120(Al)-AP.

4.2 Results and discussion

4.2.1 Structure and adsorption performance

The single crystal structure of MIL-120(Al) or $Al_4(OH)_8(C_{10}O_8H_2)\ xH_2O$ (x = 4.8~5) was reported more than a decade ago by Loiseau et al., the MOF being made through a hydrothermal route.[28] Its inorganic sub-unit is composed of edge-sharing $AlO_2(OH)_4$ octahedra with oxygen atoms from the carboxylate groups, and the hydroxyl groups forming the common edge resulting in infinite Al hydroxo chains, not very common in Al-MOFs. The ligands, here 1,2,4,5-benzene-tetracarboxylic acid (or BTec), connect these chains through their carboxylates thereby generating a three-dimensional framework that delimit one dimensional (1D) channels (5.4 Å x 4.7 Å along [001]) running alongside the chains (Fig. 1A). More precisely, $AlO_2(OH)_4$ octahedra are linked via double μ_2-OH bridges, generating the infinite trans-cis edge sharing chains of octahedra. Therefore, MIL-120(Al) provides two-fold denser hydroxyl polar groups than other corner-sharing modes commonly present in most Al-MOFs (Fig. 1B). Due to the homogenous arrangement of μ_2-OH groups, we explored this MOF for CO_2 adsorption behaviour. Although the high-pressure CO_2 adsorption isotherm reported in 2009 showed already promising performances in terms of CO_2 uptake, there were neither clear evidence for the CO_2 capacity at low pressure (0.2 bar and < 1 bar) nor any investigation to understand the steep uptake at relatively low pressures. Additionally, this MOF was obtained by hydrothermal synthesis (483 K), this prevented from any scalability. Initially, we first prepared MIL-120(Al) following the reported hydrothermal synthesis, and performed CO_2 adsorption at 298 K. Indeed, the obtained isotherm confirmed, as expected, the promising CO_2 capacity at low pressure (0.2 bar and < 1 bar) (Fig. 1C). Motivated by these findings, it was of importance to obtain this MOF following a simpler, safer way in a view of the large-scale synthesis and further exploitation in large-scale separation processes. After a systematic investigation of the typical synthesis parameters (ratio of metal to ligand, pH, metal sources…) (see Table S1), we could finally obtain MIL-120(Al)-AP as a pure phase, in water at ambient pressure, while keeping a good crystallinity, as confirmed by a large set of complementary characterization from PXRD, FT-IR, TGA, N_2 adsorption at 77 K, pore size distribution, water adsorption and solid-state NMR (see supplementary information for details) (Fig. S1-6). The BET surface area of the MIL-120(Al)-AP was even slightly higher than the one of the hydrothermally made MIL-120(Al) sample. Then pure-component adsorption isotherms of CO_2 and N_2 were carried out at 298 K. As shown in Fig. 1C, the CO_2 uptake in MIL-120(Al)-AP was 1.90 mmol g^{-1} (73.0 $cm^3\ cm^{-3}$, based on the crystallographic density, 1.57 $cm^3\ g^{-1}$), 3.87 mmol g^{-1} (148.8 $cm^3\ cm^{-3}$, STP) at 0.1, 1 bar, respectively, which is comparable to that of the hydrothermal synthesis sample. Additionally, under the same conditions, MIL-120(Al)-AP adsorbed a much lower amount of N_2 (0.04, 0.33 mmol g^{-1} at 0.1, 1 bar, respectively), anticipating a very high CO_2/N_2 selectivity under ambient conditions. The estimation of the CO_2/N_2 selectivity was performed based on the ideal adsorbed solution theory (IAST) (Table S2-4). The CO_2/N_2 selectivity of MIL-120(Al)-AP for the corresponding binary mixture ($15CO_2$:$85N_2$ and $5CO_2$:$95N_2$) was estimated as high as 95 and 122 at 0.1 bar and 298 K, respectively (Fig. 1D). This indicates that MIL-120(Al)-AP has a great potential for the separation of flue gas (5-15% CO_2) emitted from power plants and industrial processes. Meanwhile, coverage-dependent Q_{st} of MIL-120(Al)-AP for CO_2 was determined experimentally from pure component isotherms collected at 288, 298, and 303 K using the Clausius-Clapeyron equation (Fig. S7). The experimental Q_{st} of CO_2 at near-zero coverage is 44 kJ mol^{-1} (Fig. 1E), which is a bit higher than the benchmark CO_2 adsorbent CALF-20 (40 kJ mol^{-1}). The HOA gradually decreased however with the increase of CO_2 loading and it settled down to a moderate value of 38 kJ mol^{-1}. The above results strongly suggest MIL-120(Al)-AP could achieve a good CO_2 capture performance with a high CO_2 working capacity, high CO_2 selectivity over N_2, while still exhibiting a low energy consumption for regeneration. As shown in Fig. 1F, it is noteworthy to mention that at 0.1, 1 bar and 298 K, the CO_2 uptake of MIL-120(Al)-AP is comparable to those of benchmark CO_2 adsorbents (if not higher in some cases), such as MOF-based adsorbents (CALF-20,[17] Mg-MOF-74,[29] USTA-16,[30] ALF,[31] SIFSIX-3-Cu,[32] mmen-Mg_2(dobpdc),[16] SIFSIX-3-Zn,[20] Ni-MOF-74[33]) and several cationic zeolites (NaX[34], ETS-4/10[35]). It should be highlighted here that MIL-120(Al)-AP possesses a high ratio of metal to ligand (4:1), which is (by far) higher than the other MOFs. Since the ligand is the main limiting chemical in MOFs material cost,[36] this shall be highly advantageous for a large-scale industrial synthesis. In fact, if the performances are crucial features for a given application, other aspects including material's cost, sustainability, processability, are also important criteria to take into account, in particular when it is related to a very large-scale application such the CO_2 capture requiring a huge amount of sorbents.

In combination with TGA and variable-temperature PXRD analysis (Fig. S8), as expected, MIL-120(Al)-AP exhibits an excellent thermal stability (up to 400ºC), although some small variation in diffracted Bragg peaks could be observed starting from 100°C, very likely due to a slight structural flexibly induced by solvent removal and/or some bond rearrangement (e.g., OH groups, etc.). Moreover, MIL-120(Al)-AP also showed an exceptional hydrolytic stability, withstanding to boiling water for (at least) 10 days as confirmed by the well-preserved crystallinity and CO_2 capacity, as per the provided PXRD and CO_2 isotherms data, respectively (Fig. S9). This is, to our knowledge, the most hydrothermally stable Al-MOF reported to date. Consequently, this encouraged us to further investigate deeply the CO_2 adsorption behaviour of MIL-120(Al)-AP.

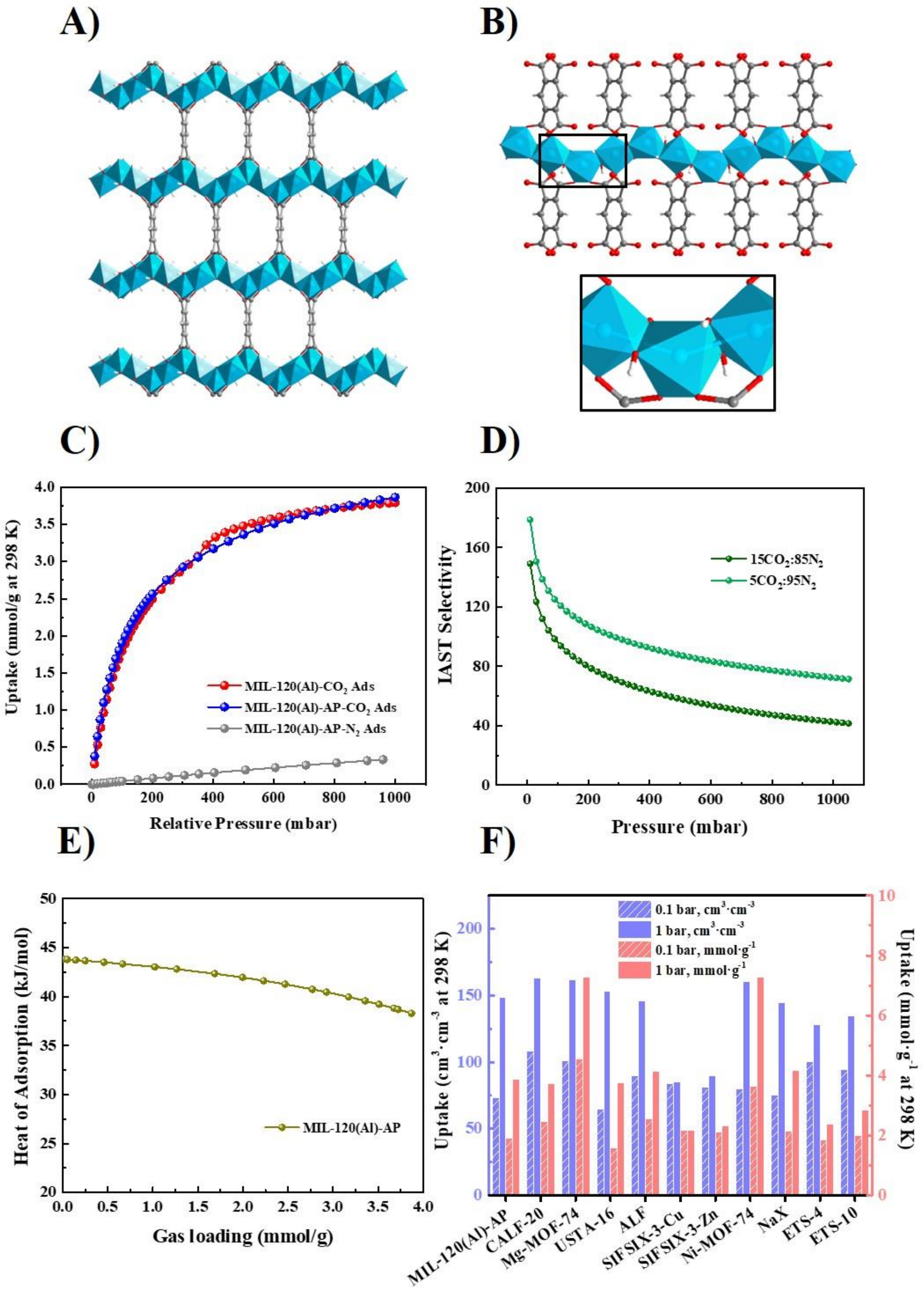

Figure 1: The structure and CO_2 adsorption performance of MIL-120(Al) and MIL-120(Al)-AP. A) 1D channels along [001] direction. B) The coordination type between Al hydroxo chains and BTec ligands with the μ_2-OH groups on $AlO_2(OH)_4$ octahedra. Color code: Al, cyan; C, grey; O, red; $AlO_2(OH)_4$ octahedra, cyan. C) CO_2 and N_2 adsorption isotherms at 298 K. D) IAST selectivity at different compositions. E) The isosteric heat versus CO_2 uptake. F)

Comparison of volumetric and gravimetric CO_2 uptakes at 0.1, 1 bar, 298 K between MIL-120(Al)-AP and benchmark adsorbents including MOFs and zeolites. The volumetric uptake was calculated using the crystallographic density.

4.2.1 *In situ* synchrotron PXRD studies

In comparison with MIL-120(Al), the CO_2 adsorption/desorption isotherms of MIL-120(Al)-AP did not exhibit any hysteresis, which drove us to measure *in situ* PXRD synchrotron experiments for both samples during CO_2 loading. Generally, before CO_2 loading, we should activate the samples by heating under dynamic vacuum conditions, to remove solvent from the pore. Here, variable temperature PXRD data have been collected directly during activation, as shown in Fig 2. After a rapid water removal before 100ºC, MIL-120(Al) could remain in the monoclinic symmetry, meanwhile a *ca.* 33% water occupancy was deduced between the Al hydroxo chains according to the Rietveld refinement of the powder diffraction patterns. Unexpectedly, MIL-120(Al)-AP displayed a phase transition around 80ºC from monoclinic (space group *C*2/*m*) to triclinic (space group *P*-1) phase. According to the crystal structure refinement after cooling, *ca.* 40% water molecules remain occupied between the Al hydroxo chains in MIL-120(Al)-AP. Then the CO_2 loading under different pressures was also studied by *in situ* synchrotron PXRD. As shown in Table 1, through Le Bail matching, the results revealed that MIL-120(Al) exhibited a phase change from monoclinic to triclinic phase in the pressure range from 200 to 400 mbar., but it was not observed in MIL-120(Al)-AP where only triclinic phase remained after activation. This phase transition phenomenon has never been reported in MIL-120(Al), and the clear crystal phase transition in MIL-120(Al)-AP is of importance prior to carry out DFT and GCMC simulations to understand precisely the affinity between CO_2 molecule and the framework. Meanwhile, we observed the CO_2 uptake of MIL-120(Al)-AP decreased slightly when the sample was activated at 150ºC under dynamic vacuum, compared with 50ºC activation (Fig. S1F). This suggested that the residual water molecules provide additional hydrogen bonds with CO_2 molecules, leading to a slightly higher CO_2 uptake at low pressure. More details about the phase transition analysis are included into the supporting information (Fig. S10-15).

A) MIL-120(Al)

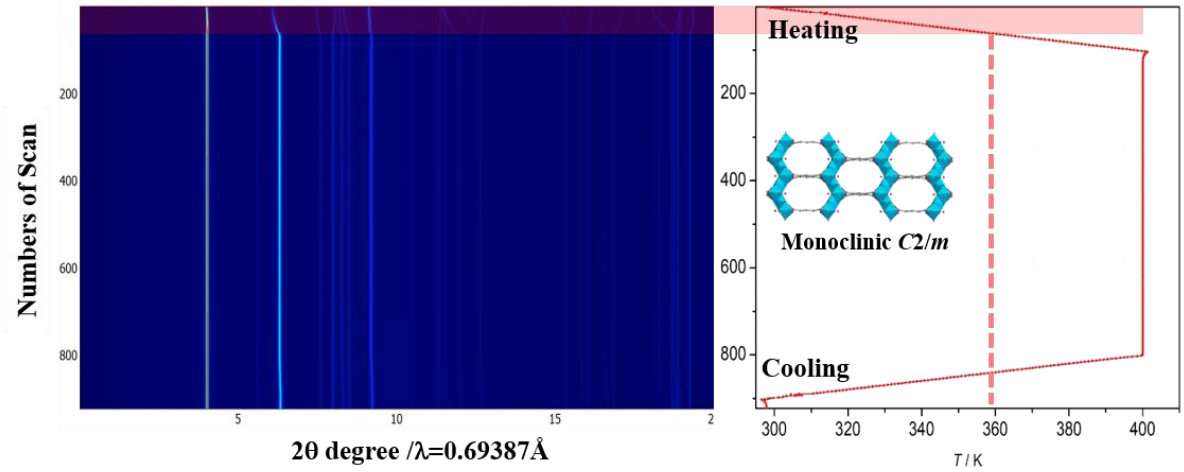

B) MIL-120(Al)-AP

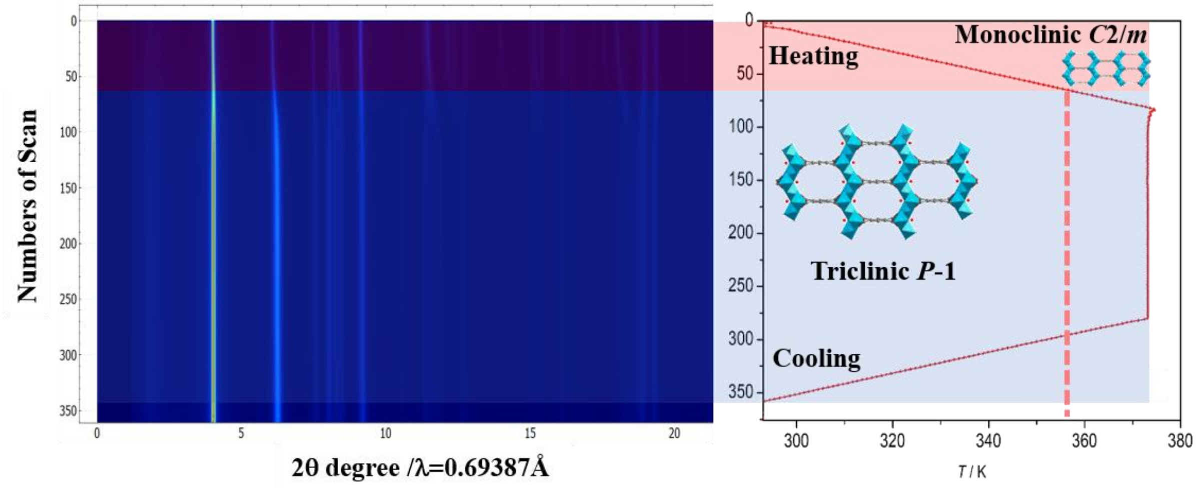

Figure 2: Variable temperature synchrotron PXRD under dynamic vacuum of A) MIL-120(Al) and B) MIL-120(Al)-AP activation. For MIL-120(Al), no phase transition under vacuum and heating activation, the structure remains monoclinic. For MIL-120(Al)-AP, phase transition from monoclinic to triclinic phase during vacuum and heating activation. Color code: Al, cyan; C, grey; O, red; $Al(OH)_4O_2$ octahedral, cyan.

Table 1: The results of phase transition of MIL-120(Al) and MIL-120(Al)-AP during CO_2 loading.

P(CO_2), mbar	MIL-120(Al)	MIL-120(Al)-AP
vac	*C*2/*m* (monoclinic)	*P*-1 (triclinic)
100	*C*2/*m* (monoclinic)	*P*-1 (triclinic)
200	*C*2/*m* (monoclinic)	*P*-1 (triclinic)
300	*C*2/*m* (monoclinic)	*P*-1 (triclinic)
400	*P*-1 (triclinic)	*P*-1 (triclinic)
500	*P*-1 (triclinic)	*P*-1 (triclinic)
1000	*P*-1 (triclinic)	*P*-1 (triclinic)

4.2.2 Computational study and effect of OH groups on the CO_2 interaction

To gain insights into the nature of CO_2 binding and the OH orientation in MIL-120(Al)-AP, we performed atomistic grand canonical Monte Carlo (GCMC) simulations and density functional theory (DFT) calculations. The structure has been optimized by DFT calculation, the unit cell parameters pore size distribution of MIL-120(Al)-AP were excellent agreement between theoretical and experimental results (Table S6). However, as shown in Fig. 3, we could not obtain the same experimental CO_2 adsorption isotherm using different models. For instance, we firstly considered all μ_2-OH groups in the framework provided the affinity to CO_2 molecules in the channel, the simulated CO_2 uptake was significantly higher than the experimental one obtained from single component adsorption isotherms at 298 K. Due to the high density of μ_2-OH groups, then we hypothesized that a reorientation of μ_2-OH groups could occur upon presence/removal of partial water molecules. This reorientation may lead for instance to OH···OH interactions leading to less accessible sites to interact with the CO_2 molecules, thus, decreasing the expected ideal uptake. To clarify that, the structure model of MIL-120(Al) was reoptimized taking into account different scenario. Here the reorientation of OH groups including the OH···OH interactions, named sim_mu_OH model, it exhibited a relatively good agreement with the experimental data, at least up to 0.2-0.25 bar. Besides that, to understand the effect of the residual water in the MIL-120(Al), we created two models (one and two molecules per unit cell, named as mu-OH_1water model and mu_OH_2water model) through the DFT structural simulation, where the localization of one and two water molecules was close to the mu_OH groups. Although the simulated CO_2 uptake still didn't agree with our experimental one, mu_OH_1water model displayed a higher CO_2 uptake than mu_OH_2water model, which revealed the less H_2O per unit cell could enhance significantly the CO_2 uptake at low pressure. The low CO_2 uptake of mu_OH-2water model at 1 bar probably due to the occupancy of water in the pore, decreasing the pore volume of MIL-120(Al). This demonstrated that the orientation and the accessibility of the μ_2-OH groups after the partial removal of H_2O during low temperature activation is crucial to achieve the CO_2 uptake in MIL-120(Al) framework.

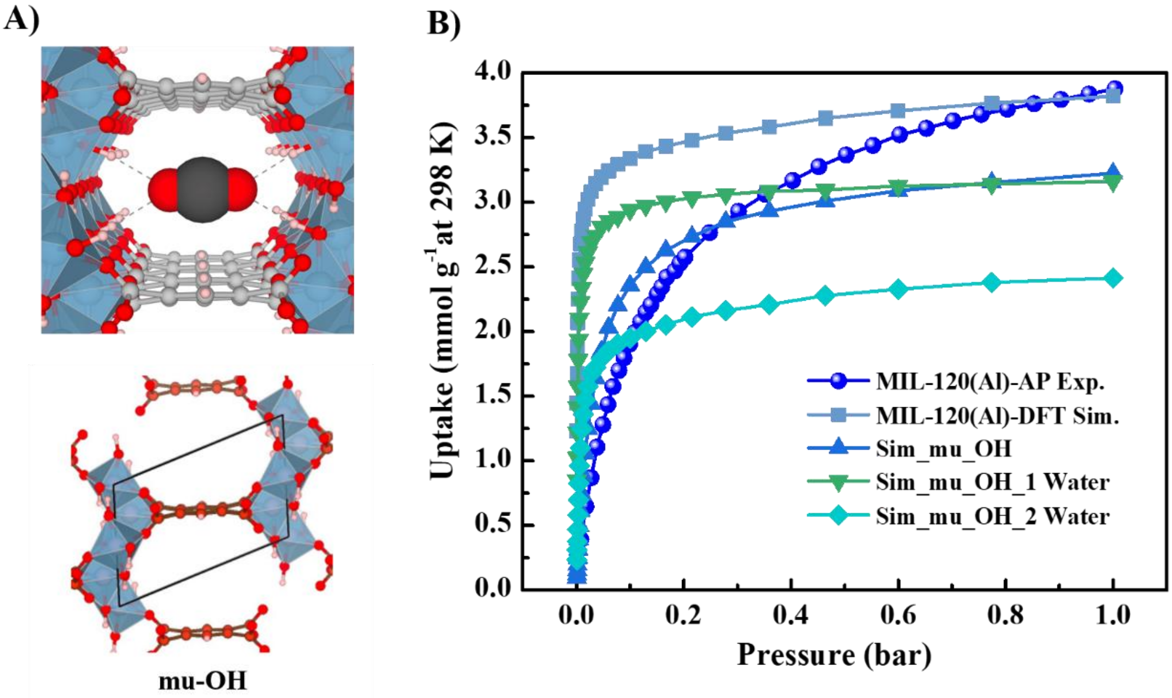

Figure 3: Computational study to understand the interaction of MIL-120(Al) with CO_2 molecules. A) (top) A snapshot for the affinity between OH groups and CO_2 molecule simulated by DFT analysis, (down) the reorientation of OH groups in the framework. B) The comparison of CO_2 adsorption isotherms between the simulated ones by different models and the experimental one at 298 K.

4.2.3 *In situ* IR studies and influence of water on the CO_2 interactions

Similar to the partial water removal from *in situ* PXRD results, an *in situ* infrared (IR) study was carried out by the group of Prof. M. Daturi at LCS Caen. One observes a first rapid water release, after exposure to 8 hours at room temperature in Ar flow, as shown in Fig. S16. To better understand than water release, the sample continued to activate at increasing temperatures (100-300ºC) in the Ar flow. Then combining with Mass Spectroscopy (MS) signal, water release kept at the constant level from 100-200ºC (Fig. S17-18). This means that MIL-120(Al) can be activated under mild conditions. The high density of μ_2-OH group in this material makes MIL-120(Al) highly hydrophilic; this is consistent with the experimental water adsorption isotherm of both MIL-120(Al) and MIL-120(Al)-AP at 298 K (Fig. 4A). Despite this, how water might affect the CO_2 adsorption of MIL-120(Al)-AP under real conditions was still unclear. To investigate the effect of water during CO_2 adsorption, we measured *in situ* IR spectra at room temperature during the CO_2 adsorption of MIL-120(Al)-AP in the presence of 1% H_2O. As shown in Fig. 4B, at the beginning of adsorption process (*ca.* 2 mins), a very fast

CO_2 adsorption (the absorbance peak of CO_2 at 2338 cm^{-1}) is observed; meanwhile there was no H_2O adsorption occurred because the IR band at 3500 $cm^{-1}$of H-bonds kept at a constant value. Then the vibrational band of CO_2 decreased progressively with the slowly increasing of the absorbance of H-bonds, revealing that the water molecules are being replaced by the adsorbed CO_2 from the framework. After 10 mins, a drastic drop of the band of CO_2 molecules and a stable band intensity for the H_2O groups are observed, indicating the adsorbed CO_2 molecules has been replaced by H_2O molecules. This phenomenon has been confirmed by MS signal, as shown in Fig S19, confirming that MIL-120(Al) exhibit a much faster CO_2 adsorption than water molecules. To further clarify the rapid CO_2 adsorption in the presence of water, we measured the CO_2 adsorption in dry or wet Ar flow with different CO_2 concentrations. As depicted in Fig. S20, the presence of H_2O did not decrease the CO_2 uptake compared with the dry conditions. In fact, tiny water in the flow seems even to promote the CO_2 uptake. Furthermore, the uptake of H_2O decreased slowly with increasing CO_2 concentration in the Ar flow, demonstrating that CO_2 can suppress water adsorption to a certain extent. From Fig. S21, the intensity of CO_2 absorbance is proportional to the quantity of adsorbed CO_2 in MIL-120(Al)-AP framework. For instance, the intensity of CO_2 under 30% CO_2 gas flow exhibited the highest absorbance in IR spectra. Combined with the results from MS signal calculation, the presence of H_2O did not decrease CO_2 uptake (dry or wet gas flow), but only occurred at the beginning of adsorption process. After 1 hour, the CO_2 uptake however significantly decreased, showing the saturation of H_2O in time significantly removed most adsorbed CO_2 from the framework.

This preliminary *in situ* IR studies confirms the potential of MIL-120(Al) for the CO_2/N_2 separation even in presence of water (to some extent), despite the hydrophilic behavior revealed by the water isotherms. This calls however for a specific process design taking into account the difference in adsorption kinetics between CO_2 and H_2O as well as regenerate the sorbent, particularly water. This calls in a first step for breakthrough measurements with careful tuning of the stream flow rate and dimension of the column.

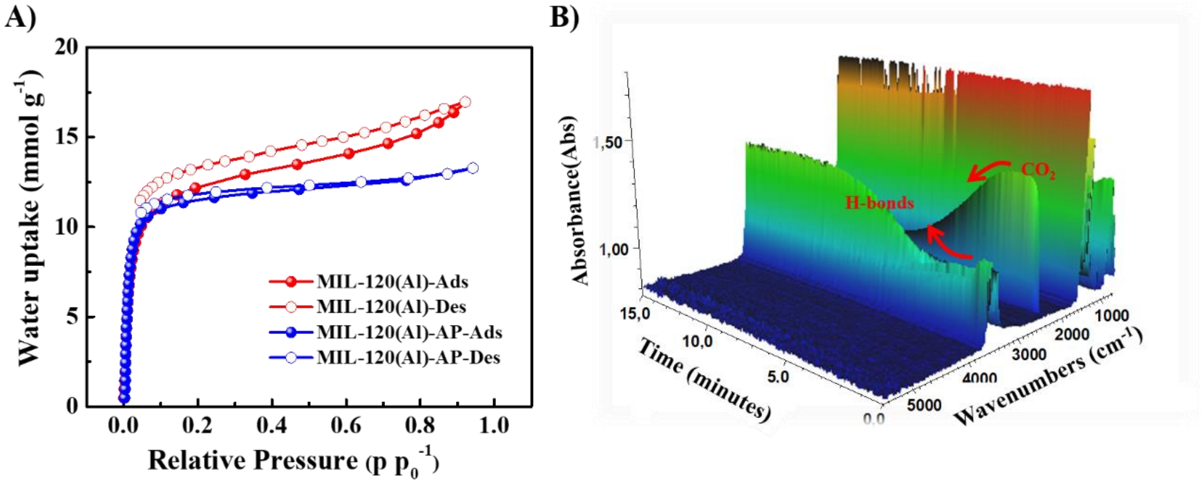

Figure 4: Water adsorption isotherms and *in situ* IR spectra results. A) Comparison of water adsorption at 298 K. B) The IR spectra signal of MIL-120(Al)-AP with time during CO_2 adsorption in the presence of water.

4.2.4 Green scalable synthesis and breakthrough tests

The reusability of MIL-120(Al)-AP solids was investigated upon six consecutive CO_2 adsorption/desorption cycles (Table S7), using different temperatures for the activation. The CO_2 uptake of MIL-120(Al)-AP solids after activating the sample at 25ºC under secondary vacuum during six hours in the first two measurements exhibited slightly higher values compared with the same sample after 50ºC activation, as depicted in Fig. S22. This could be due to the residual traces of water after activation at 25ºC, resulting into slightly higher CO_2 uptakes. After a first activation at 50°C, the CO_2 uptake did however not change much depending on the activation condition, strongly indicating that MIL-120(Al)-AP keeps a good CO_2 uptake repetition due to the dense μ_2-OH groups in the channels. Furthermore, to meet with the industrial separation processes where the sorbents need to be produced at very large scale, first attempts of kg scale synthesis of the MIL-120(Al)-AP solids were carried out (synthesis methods given in SI) based on the optimized AP synthesis method developed in this work. Considering the cost of aluminum precursors ($Al_2(SO_4)_3$ $18H_2O$, $Al(NO_3)_3$ $9H_2O$, $AlCl_3$ $6H_2O$) and their corrosive issue, two other precursors, such as $Al(OH)(CH_3COO)_2$ or $NaAlO_2$ were selected for the synthesis of MIL-120(Al)-AP, see in Table S8. High quality MIL-120(Al)-AP with high yield (>90%) was easily synthesized at kg scale via a green method under ambient pressure. In comparison with small scale synthesis, MIL-120(Al)-AP in large scale synthesis also kept good crystallinity and purity which was confirmed by PXRD patterns, FT-IR spectroscopy, TGA, N_2 adsorption at 77 K, CO_2 adsorption at 298 K, and SEM/EDX results (Fig. 5A and Fig. S23-25). Noteworthy, the kg scale sample exhibited almost the same CO_2 uptake at 0.1 and 1 bar, 298 K. Besides, when $Al(OH)(CH_3COO)_2$ as an aluminum precursor, water is the only solvent in the synthesis procedure, and after washing by warm water, the space-time yield (STY) value was around 30 kg m^{-3} day^{-1}. When using $NaAlO_2$ as an aluminum precursor, it was necessary to add acetic acid as a pH modulator to obtain MIL-120(Al)-AP because of too high alkaline character of the starting $NaAlO_2/H_2O$ solution. The STY value reached around 100 kg m^{-3} day^{-1} due to the higher concentration and the shorter time for washing, which is comparable to the ones of zeolites (50 to 150 kg m^{-3} day^{-1}) or benchmark Al-MOFs such as MIL-160[37] or MOF-303.[38] Meanwhile it is interesting to observed from SEM images (Fig. S26), the particle size of MIL-120(Al)-AP reduced when using $NaAlO_2$ instead of $Al(OH)(CH_3COO)_2$ as metal precursor. That's probably why the impurities such as the unreacted precursors, sodium ions and acetic acid, could be removed rapidly in short washing time, even though the filtration time would take longer since the more production for each batch and smaller particles.

Considering the requirements of the real application, MOFs powders need to be shaped not only (i) avoid the tedious (and possibly risky) manipulation of powder, but also (ii) to minimize the pressure drop and thermal gradient across the adsorption column and ensure an optimal fluid and heat diffusion. Here we have successfully shaped MIL-120(Al)-AP using inorganic binders, namely bentonite and silica. The CO_2 uptakes of the MIL-120(Al)-AP beads obtained with 10% of silica and 10% of bentonite using extrusion/spheronisation techniques were in good agreement with the uptake of the MOF in the powder form (Fig. 5B). Additionally, the MIL-120(Al)-AP beads exhibited a high crushing strength particularly when using bentonite (38.19 N for MIL-120(Al)-AP with 10% bentonite; 8.77 N for MIL-120(Al)-AP with 10% silica) (Fig. S27-28) which is of a high interest for its practical use such as CO_2 capture. The high mechanical strength of beads obtained with bentonite might be due by the chemical nature of bentonite, an aluminum silicate, highly compatible with the one of MIL-120(Al) that exhibits a very high OH/Al ratio suggesting a decoration of the external surface by hydroxyl groups.

Finally, to study the separation performance for CO_2/N_2 (15/85), first dynamic column breakthrough experiments were performed, in collaboration with the group of Prof. Guy De WEIRELD from University of Mons in Belgium, in a packed column filled with activated MIL-120(Al)-AP with 10% silica and MIL-120(Al)-AP with 10% bentonite with a total flow of 1Nl min^{-1}. As depicted in Fig. 5C-D, highly efficient separation of CO_2 from the CO_2/N_2 mixture could be achieved, wherein N_2 gas first eluted through the adsorption bed at very beginning of adsorption process, while CO_2 breakthrough did not occur until reaching the adsorbent saturation of the column, with a pure productivity (0.67 mmol cm^{-3} for MIL-120(Al)-AP with 10% silica; 0.79 mmol cm^{-3} for MIL-120(Al)-AP with 10% bentonite) at the outlet. Additionally, both samples reactivated after humid measurement, performed the same breakthrough results, strongly indicating that this MOF can provide a good repeatability of CO_2 adsorption with full regeneration after exposure to humid atmosphere, although a slight modification of the breakthrough curves can be observed. Overall, since the regeneration was achieved by heating, MIL-120(Al)-AP appears as a suitable adsorbent for TSA carbon capture under real conditions.

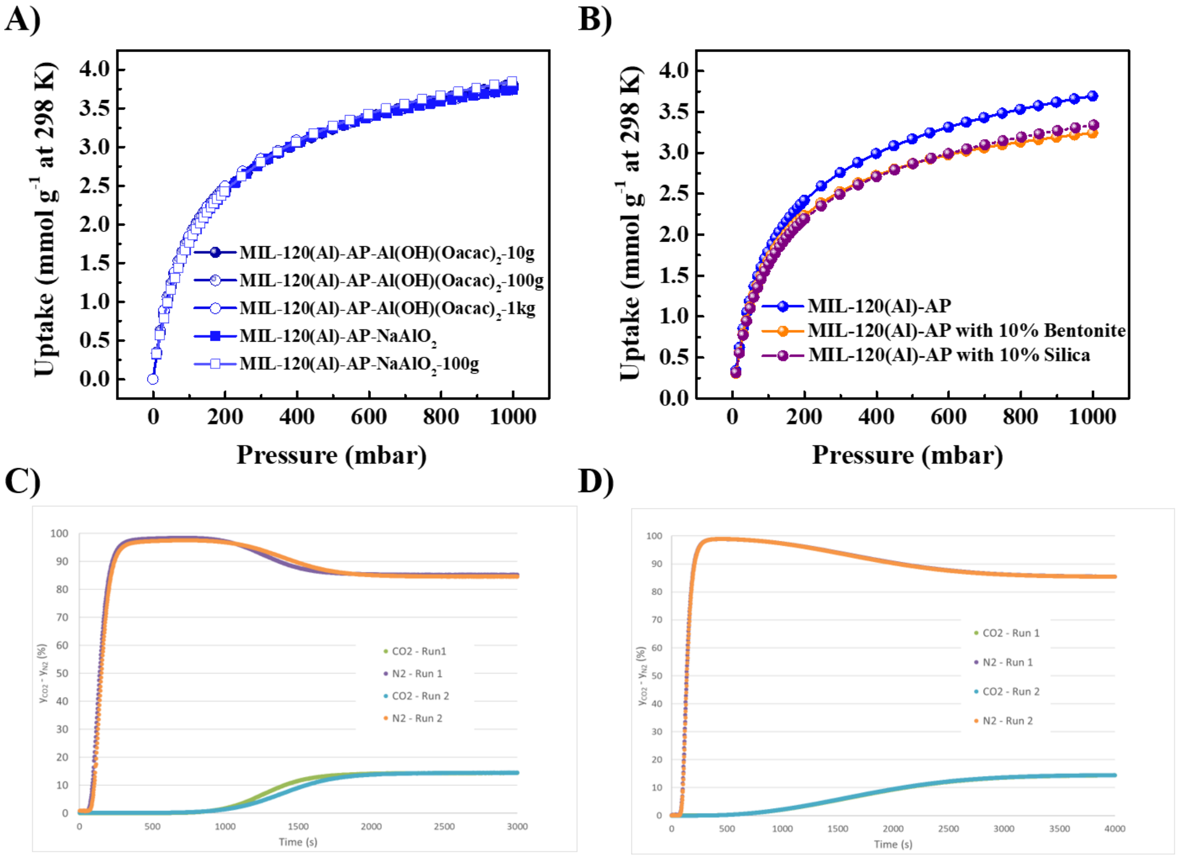

Figure 5: CO_2 adsorption performance and breakthrough measurements of MIL-120(Al)-AP. A) CO_2 adsorption isotherms at 298 K on different scale batch preparations. B) CO_2 adsorption isotherms comparison between pure and structured samples with 10% Bentonite/Silica. C) The breakthrough results of MIL-120(Al)-AP with 10% Si. D) The breakthrough results of MIL-120(Al)-AP with 10% bentonite. The activation condition for both samples was at 50°C for 12 hours under vacuum, run 1 refers to the measurement before humid, run 2 refers to the measurement after humid, same activation procedure was applied after run 1 measurement.

4.3 Conclusion

In this work, a highly promising aluminum-based microporous Al tetracarboxylate MOF, MIL-120, was studied for post-combustion carbon capture. A more friendly economically viable ambient pressure synthesis route was developed leading to the MIL-120(Al)-AP sample, instead of the previously high temperature hydrothermal route. A combination of experimental and computational adsorption results first revealed the high and selective CO_2 uptake of this MOF at low pressure due to the high density of OH groups on the edge sharing Al chains of octahedra. To better understand the affinity between CO_2 molecules and the framework, further simulations are still required, especially in presence of water. The moderate heat of CO_2 adsorption is an asset for a relatively low energy consumption regeneration process. *In situ* PXRD experiments evidenced an irreversible monoclinic to triclinic phase transition phenomenon for the MIL-120(Al)-AP. Through an *in situ* IR set of experiments, the rapid CO_2 adsorption was confirmed, even in the presence of water, indicating MIL-120(Al)-AP can probably be applied for fast adsorption/desorption cycle. Besides, a kg-scale synthesis protocol of MIL-120(Al)-AP with high STY, could be obtained using cheap commercially available precursors via a green ambient pressure route. MIL-120(Al)-AP was shaped with bentonite provided both good sorption performances as well as a very strong mechanic strength. Then the efficient CO_2 adsorption performance of this MOF was confirmed by first dynamic column breakthrough experiments. An ongoing larger scale investigation is being carried out to investigate the kinetics effects in real separation conditions on a VPSA unit, requiring 3 kg of shaped material. Besides, a cost estimation study of MIL-120(Al)-AP solid is in the pipeline.

4.4 References

(1) Mac Dowell, N.; Fennell, P. S.; Shah, N.; Maitland, G. C. The role of CO2 capture and utilization in mitigating climate change. *Nature Climate Change* **2017**, *7*, 243-249.

(2) Samanta, A.; Zhao, A.; Shimizu, G. K.; Sarkar, P.; Gupta, R. Post-combustion CO2 capture using solid sorbents: a review. *Industrial & Engineering Chemistry Research* **2012**, *51*, 1438-1463.

(3) Dutcher, B.; Fan, M.; Russell, A. G. Amine-Based CO2 Capture Technology Development from the Beginning of 2013—A Review. *ACS applied materials & interfaces* **2015**, *7*, 2137-2148.

(4) Wang, M.; Joel, A. S.; Ramshaw, C.; Eimer, D.; Musa, N. M. Process intensification for post-combustion CO2 capture with chemical absorption: A critical review. *Applied Energy* **2015**, *158*, 275-291.

(5) Arakawa, J.; Okuno, S.; Takano, K.; Yamanaka, Y.; Matsuyama, T.; Feron, P.; Cottrell, A.; Cousins, A.; Huang, S.; Davies, R.; Sertori, P. Long Term Evaluation of Advanced PCC System for Coal-fired Power Plant. *Energy Procedia* **2017**, *114*, 1061-1068.

(6) Hou, Q.; Wu, Y.; Zhou, S.; Wei, Y.; Caro, J.; Wang, H. Ultra-tuning of the aperture size in stiffened ZIF-8_Cm frameworks with mixed-linker strategy for enhanced CO2/CH4 separation. *Angewandte Chemie International Edition* **2019**, *58*, 327-331.

(7) Zou, L.; Sun, Y.; Che, S.; Yang, X.; Wang, X.; Bosch, M.; Wang, Q.; Li, H.; Smith, M.; Yuan, S. Porous organic polymers for post-combustion carbon capture. *Advanced materials* **2017**, *29*, 1700229.

(8) Zhou, Y.; Zhang, J.; Wang, L.; Cui, X.; Liu, X.; Wong, S. S.; An, H.; Yan, N.; Xie, J.; Yu, C.; Zhang, P.; Du, Y.; Xi, S.; Zheng, L.; Cao, X.; Wu, Y.; Wang, Y.; Wang, C.; Wen, H.; Chen, L.; Xing, H.; Wang, J. Self-assembled iron-containing mordenite monolith for carbon dioxide sieving. *Science* **2021**, *373*, 315-320.

(9) Datta, S. J.; Khumnoon, C.; Lee, Z. H.; Moon, W. K.; Docao, S.; Nguyen, T. H.; Hwang, I. C.; Moon, D.; Oleynikov, P.; Terasaki, O.; Yoon, K. B. CO2 capture from humid flue gases and humid atmosphere using a microporous coppersilicate. *Science* **2015**, *350*, 302-306.

(10) Qi, G.; Wang, Y.; Estevez, L.; Duan, X.; Anako, N.; Park, A.-H. A.; Li, W.; Jones, C. W.; Giannelis, E. P. High efficiency nanocomposite sorbents for CO2 capture based on amine-functionalized mesoporous capsules. *Energy & Environmental Science* **2011**, *4*, 444-452.

(11) Zeng, Y.; Zou, R.; Zhao, Y. Covalent Organic Frameworks for CO2 Capture. *Advanced Materials* **2016**, *28*, 2855-2873.

(12) Siegelman, R. L.; Kim, E. J.; Long, J. R. Porous materials for carbon dioxide separations. *Nature Materials* **2021**, *20*, 1060-1072.

(13) D'Alessandro, D. M.; Smit, B.; Long, J. R. Carbon dioxide capture: prospects for new materials. *Angewandte Chemie International Edition* **2010**, *49*, 6058-6082.

(14) Zhao, X.; Wang, Y.; Li, D.-S.; Bu, X.; Feng, P. Metal–Organic Frameworks for Separation. *Advanced Materials* **2018**, *30*, 1705189.

(15) Dods, M. N.; Weston, S. C.; Long, J. R. Prospects for Simultaneously Capturing Carbon Dioxide and Harvesting Water from Air. *Advanced Materials* **2022**, *n/a*, 2204277.

(16) Kim, E. J.; Siegelman, R. L.; Jiang, H. Z.; Forse, A. C.; Lee, J.-H.; Martell, J. D.; Milner, P. J.; Falkowski, J. M.; Neaton, J. B.; Reimer, J. A. Cooperative carbon capture and steam regeneration with tetraamine-appended metal–organic frameworks. *Science* **2020**, *369*, 392-396.

(17) Lin, J.-B.; Nguyen, T. T.; Vaidhyanathan, R.; Burner, J.; Taylor, J. M.; Durekova, H.; Akhtar, F.; Mah, R. K.; Ghaffari-Nik, O.; Marx, S. A scalable metal-organic framework as a durable physisorbent for carbon dioxide capture. *Science* **2021**, *374*, 1464-1469.

(18) Mukherjee, S.; Sikdar, N.; O'Nolan, D.; Franz, D. M.; Gascón, V.; Kumar, A.; Kumar, N.; Scott, H. S.; Madden, D. G.; Kruger, P. E. Trace CO2 capture by an ultramicroporous physisorbent with low water affinity. *Science advances* **2019**, *5*, eaax9171.

(19) Ullah, S.; Tan, K.; Sensharma, D.; Kumar, N.; Mukherjee, S.; Bezrukov, A. A.; Li, J.; Zaworotko, M. J.; Thonhauser, T. CO2 Capture by Hybrid Ultramicroporous TIFSIX-3-Ni under Humid Conditions Using Non-Equilibrium Cycling. *Angewandte Chemie* **2022**, e202206613.

(20) Nugent, P.; Belmabkhout, Y.; Burd, S. D.; Cairns, A. J.; Luebke, R.; Forrest, K.; Pham, T.; Ma, S.; Space, B.; Wojtas, L.; Eddaoudi, M.; Zaworotko, M. J. Porous materials with optimal adsorption thermodynamics and kinetics for CO2 separation. *Nature* **2013**, *495*, 80-84.

(21) Gaab, M.; Trukhan, N.; Maurer, S.; Gummaraju, R.; Müller, U. The progression of Al-based metal-organic frameworks – From academic research to industrial production and applications. *Microporous and Mesoporous Materials* **2012**, *157*, 131-136.

(22) Rubio-Martinez, M.; Hadley, T. D.; Batten, M. P.; Constanti-Carey, K.; Barton, T.; Marley, D.; Mönch, A.; Lim, K. S.; Hill, M. R. Scalability of continuous flow production of metal–organic frameworks. *ChemSusChem* **2016**, *9*, 938-941.

(23) Benoit, V.; Pillai, R. S.; Orsi, A.; Normand, P.; Jobic, H.; Nouar, F.; Billemont, P.; Bloch, E.; Bourrelly, S.; Devic, T.; Wright, P. A.; de Weireld, G.; Serre, C.; Maurin, G.;

Llewellyn, P. L. MIL-91(Ti), a small pore metal–organic framework which fulfils several criteria: an upscaled green synthesis, excellent water stability, high CO2 selectivity and fast CO2 transport. *Journal of Materials Chemistry A* **2016**, *4*, 1383-1389.

(24) Permyakova, A.; Skrylnyk, O.; Courbon, E.; Affram, M.; Wang, S.; Lee, U. H.; Valekar, A. H.; Nouar, F.; Mouchaham, G.; Devic, T.; De Weireld, G.; Chang, J.-S.; Steunou, N.; Frère, M.; Serre, C. Synthesis Optimization, Shaping, and Heat Reallocation Evaluation of the Hydrophilic Metal–Organic Framework MIL-160(Al). *ChemSusChem* **2017**, *10*, 1419-1426.

(25) Hastürk, E.; Höfert, S.-P.; Topalli, B.; Schlüsener, C.; Janiak, C. Shaping of MOFs via freeze-casting method with hydrophilic polymers and their effect on textural properties. *Microporous and Mesoporous Materials* **2020**, *295*, 109907.

(26) Gkaniatsou, E.; Chen, C.; Cui, F. S.; Zhu, X.; Sapin, P.; Nouar, F.; Boissière, C.; Markides, C. N.; Hensen, J.; Serre, C. Producing cold from heat with aluminum carboxylate-based metal-organic frameworks. *Cell Reports Physical Science* **2022**, *3*, 100730.

(27) Lin, R.-B.; Li, L.; Zhou, H.-L.; Wu, H.; He, C.; Li, S.; Krishna, R.; Li, J.; Zhou, W.; Chen, B. Molecular sieving of ethylene from ethane using a rigid metal–organic framework. *Nature materials* **2018**, *17*, 1128-1133.

(28) Volkringer, C.; Loiseau, T.; Haouas, M.; Taulelle, F.; Popov, D.; Burghammer, M.; Riekel, C.; Zlotea, C.; Cuevas, F.; Latroche, M. Occurrence of uncommon infinite chains consisting of edge-sharing octahedra in a porous metal organic framework-type aluminum pyromellitate Al4 (OH) 8 [C10O8H2](MIL-120): Synthesis, structure, and gas sorption properties. *Chemistry of Materials* **2009**, *21*, 5783-5791.

(29) Britt, D.; Furukawa, H.; Wang, B.; Glover, T. G.; Yaghi, O. M. Highly efficient separation of carbon dioxide by a metal-organic framework replete with open metal sites. *Proceedings of the National Academy of Sciences* **2009**, *106*, 20637-20640.

(30) Masala, A.; Vitillo, J. G.; Mondino, G.; Grande, C. A.; Blom, R.; Manzoli, M.; Marshall, M.; Bordiga, S. CO2 capture in dry and wet conditions in UTSA-16 metal–organic framework. *ACS applied materials & interfaces* **2017**, *9*, 455-463.

(31) Evans, H. A.; Mullangi, D.; Deng, Z.; Wang, Y.; Peh, S. B.; Wei, F.; Wang, J.; Brown, C. M.; Zhao, D.; Canepa, P. Aluminum formate, Al (HCOO) 3: An earth-abundant, scalable, and highly selective material for CO2 capture. *Science Advances* **2022**, *8*, eade1473.

(32) Shekhah, O.; Belmabkhout, Y.; Chen, Z.; Guillerm, V.; Cairns, A.; Adil, K.; Eddaoudi, M. Made-to-order metal-organic frameworks for trace carbon dioxide removal and air capture. *Nature communications* **2014**, *5*, 1-7.

(33) Chen, C.; Feng, X.; Zhu, Q.; Dong, R.; Yang, R.; Cheng, Y.; He, C. Microwave-Assisted Rapid Synthesis of Well-Shaped MOF-74 (Ni) for CO2 Efficient Capture. *Inorganic chemistry* **2019**, *58*, 2717-2728.

(34) Su, F.; Lu, C. CO2 capture from gas stream by zeolite 13X using a dual-column temperature/vacuum swing adsorption. *Energy & Environmental Science* **2012**, *5*, 9021-9027.

(35) Anson, A.; Lin, C. C. H.; Kuznicki, S. M.; Sawada, J. A. Adsorption of carbon dioxide, ethane, and methane on titanosilicate type molecular sieves. *Chemical Engineering Science* **2009**, *64*, 3683-3687.

(36) Severino, M. I.; Gkaniatsou, E.; Nouar, F.; Pinto, M. L.; Serre, C. MOFs industrialization: a complete assessment of production costs. *Faraday Discussions* **2021**, *231*, 326-341.

(37) Permyakova, A.; Skrylnyk, O.; Courbon, E.; Affram, M.; Wang, S.; Lee, U.-H.; Valekar, A. H.; Nouar, F.; Mouchaham, G.; Devic, T.; De Weireld, G.; Chang, J.-S.; Steunou, N.; Frère, M.; Serre, C. Synthesis Optimization, Shaping, and Heat Reallocation Evaluation of the Hydrophilic Metal–Organic Framework MIL-160(Al). *ChemSusChem* **2017**, *10*, 1419-1426.

(38) Zheng, Z.; Nguyen, H. L.; Hanikel, N.; Li, K. K.-Y.; Zhou, Z.; Ma, T.; Yaghi, O. M. High-yield, green and scalable methods for producing MOF-303 for water harvesting from desert air. *Nature Protocols* **2023**, *18*, 136-156.

Supporting information

Experimental procedures

Chemicals

All chemicals were purchased from commercial suppliers and used as received without further purification. Benzene-tetracarboxylic acid (Acros Organics/thermo), acetic acid (Fisher Scientific), aluminum acetate (thermo), aluminum nitrate nonahydrate (Acros Organics), Sodium aluminate (Fisher Scientific)

Instruments

Powder X-ray Diffraction (PXRD)

High-throughput Bruker D8 Advance diffractometer working on transmission mode and equipped with a focusing Göbel mirror producing CuKα radiation (λ = 1.5418 Å) and a LynxEye detector.

Nitrogen porosimetry

Micromeritics Tristar/ Triflex instrument at 77 K (pre-activating samples at 200°C under vacuum, 5 hours).

Thermogravimetric analyses (TGA)

Mettler Toledo TGA/DSC 2, STAR System apparatus with a heating rate of 5°C min^{-1} under the oxygen flow. Mettler Toledo FiveEasyTM Plus pH / mV bench meter.

Infrared spectra

Nicolet iS5 FTIR ThermoFisher spectrometer.

Temperature dependent PXRD

θ-θ Bruker- D8 Advance diffractometer equipped with a HTK-1200N (Anton Parr) high-temperature chamber and a LYNXEYE XE detector (Cu radiation). PXRD patterns were collected every 25°C from room temperature to 350°C, with *two hours* scan for each temperature.

Laboratory High-resolution X-ray powder diffraction

PANalytical EMPYREAN diffractometer with Cu Kα radiation ($\lambda = 1.5406$ Å) and GaliPIX3D detector. The filled 0.5 mm capillaries were measured in a transmission mode at room temperature. Le Bail profile fitting was carried out using Jana2006.

Scanning transmission microscopy (SEM) and energy dispersive X-ray spectroscopy

FEI Magellan 400 scanning electron microscope, the energy-dispersive X-ray spectroscopy (EDX) analysis allows performing chemical mapping using the "Super-X" systems for EDX analysis that equipped the microscope

Synthesis procedures

Traditional synthesis of MIL-120(Al)

Based on previous reported synthesis procedure, we did a slightly modification to the hydrothermal reaction of MIL-120(Al). To a 23-mL Teflon reactor, 1,2,4,5-benzene-tetracarboxylic acid (1 mmol, 254 mg) was added followed by DI water (10 mL). With stirring, sodium hydroxide (NaOH 8 mmol, 320 mg) was added, meanwhile the suspension solution changed into a clear solution. Then aluminum nitrate ($Al(NO_3)_3·9H_2O$ 4 mmol, 1.5 g) was added slowly into the above solution. Kept stirring for 10 mins, and the reactor was put into a pre-heated oven at 180°C for 24 hours. When the reactor was cooled down to room temperature, the white product was collected by centrifugation (3 mins at 10,000 rpm). The slurry product was washed by water (100 mL) overnight at 45°C in a round bottomed flask. Finally, the sample was collected after drying in air for 2 days.

Synthesis optimization of MIL-120(Al)-AP

10g using aluminum acetate

To a 500-mL round-bottomed flask, DI water (300 mL), BTec (20 mmol, 5.08g), and $Al(OH)(OAc)_2·1.38H_2O$ (80 mmol, 15g) were added with stirring at RT. The mixture was stirred at 80°C for 72 h. After cooling down to RT, the white crude product was collected by filtration or centrifugation (3 mins at 10,000 rpm). The final product was obtained by washing in DI water (200 mL) and filtration. Finally, the sample was collected after drying in air overnight.

100g using aluminum acetate

To a 5 L reactor, DI water (3 L), BTec (0.2 mol, 50.8 g) were added with stirring at RT, then heated up to 100°C, the suspension changed into clear solution. Before started the reaction at 100°C, 200 rpm for 24 hours, $Al(OH)(OAc)_2·1.38H_2O$ (0.67 mol, 125 g) were added with stirring at RT. After cooling down to around 50°C, the white crude product was collected by filtration. Then the crude sample was washed in DI water (6 L) for 18 hours. The sample we obtained finally after filtration and dried in air.

1kg using aluminum acetate

To a 30 L reactor, DI water (9 L), BTec (1.19 mol, 303 g) were added with stirring at RT, then heated up to 100°C, the suspension changed into clear solution. Before started the reaction at

120ºC, 200 rpm for 24 hours, $Al(OH)(OAc)_2 \cdot 1.38H_2O$ (4.79 mol, 885 g) were added with stirring at RT. After cooling down to around 50ºC, the white crude product was collected by filtration, then added 2 L ethanol to speed up the product drying. Due to around 900 g sample we obtained, it's hard to wash all of the sample on one time. For the basic characterizations and CO_2 measurement of large-scale synthesis, here we took 2 g crude product sample, washed two time in DI water at 60ºC overnight. The sample we obtained finally after drying in air overnight.

1g using sodium aluminate

To a 100-mL round-bottomed flask, DI water (15 mL), BTec (1 mmol, 254 g), and $NaAlO_2$ (4 mmol, 328 mg) were added with stirring at RT. Then acetic acid (8 mmol, 0.48 mL) has been added as a modulator. The mixture was stirred at 140ºC for 24 h. After cooling down to RT, the white crude product was collected by filtration or centrifugation (3 mins at 10,000 rpm). The final product was obtained by washing in DI water (200 mL) at 40ºC overnight. Finally, the sample was collected after filtration and dried in air overnight.

100g using sodium aluminate

To a 5 L reactor, DI water (800 mL), BTec (160 mmol, 40.64 g) were added with stirring at RT. Then sodium aluminate (640 mmol, 52.48 g) and acetic acid (73.6 mL) were added slowly into the above suspension. The reflux reaction was carried out for 48 hours. After cooling down to around 50ºC, the white crude product was collected by filtration. The crude sample was washed in DI water (5 L) for 24 hours (3 L for the first time, then 2.5 L for the second time). The sample we obtained finally after filtration and dried in vacuum oven.

Shaping MIL-120(Al)-AP

Shaping of MOFs by extrusion and spheronization technique: The MOFs have been shaped into spheres by a combination of extrusion and spheronization techniques. At first, the sample is mixed with the desired amount of binder in a mortar. After that, a paste has been made from the mixture by judiciously adding suitable solvents until a favorable rheology is obtained. The paste has been extruded using an extrusion apparatus (MULTILAB 806076) through a die with a nozzle diameter of 3 mm. The speed of extrusion has been maintained at 20 rpm until the paste is transformed into pellets. The attained pellets are then fed to the spheronizer and the speed is maintained at 250 rpm for 10 minutes to obtain spheres (diameter around 3 mm). The spheres are dried under vacuum for 12 hours.

Water stability test of MIL-120(Al)-AP

MIL-120(Al)-AP sample (200 mg) was dispersed into 50 mL DI water solution, then kept the stirring under reflux condition for 10 days. White dry sample was collected after centrifugation and drying in air.

Synthesis optimization of MIL-120(Al)-AP in small scale

Al source /mmol	**Btec /mmol**	**Water / mL**	**Acid or base /mmol**	**Starting pH**	**Reflux with setting temperature/ºC**	**Synthesis time /hours**	**Result**
4 $Al(OH)_3$	1.5	15	16 NaOH	>14	140	24	MIL-121
4 $Al(OH)_3$	1.2	15	12 NaOH	>14	140	24	MIL-121
4 $Al(OH)_3$	2	15	-	2	140	24	MIL-121
4 $Al(OH)_3$	1		8 acetic acid		140	24	MIL-121
4 $Al(OH)_3$	1		4 acetic acid		140	24	MIL-121
8 $Al(OH)_3$	2		24 acetic acid		140	13	MIL-121
8 $Al(OH)_3$	2		36 acetic acid		140	13	MIL-121
8 $Al(OH)_3$	2		48 acetic acid		140	13	MIL-121
4 $Al(OH)(acac)_2$	1	15	-	2-3	140	72	MIL-120
16 $Al(OH)(acac)_2$	4	30	-		120	24	MIL-120
8 $Al(OH)(acac)_2$	2	30	-		140	24	MIL-120
8 $Al(OH)(acac)_2$	2	30	-		140	24	MIL-120
8 $Al(OH)(acac)_2$	2	30	-		140	48	MIL-120
8 $Al(OH)(acac)_2$	2	30	-		140	12	MIL-120
8 $Al(OH)(acac)_2$	2	30	-		140	6	MIL-120
8 $Al(OH)(acac)_2$	2	30	-		80	72	MIL-120
8 $Al(OH)(acac)_2$	2	30	-		80	72	MIL-120
2 $Al(OH)(acac)_2$	1	15	-		140	24	MIL-120
2 $Al(OH)(acac)_2$	0.5	15	-		140	24	MIL-120
4 $Al(OH)(acac)_2$	0.5	30	-		140	24	MIL-120
4 $NaAlO_2$	1	15	-		140	72	Amorphous
4 $NaAlO_2$	1	15	8 acetic acid	3-4	140	24	MIL-120
4 $NaAlO_2$	1	15	4 acetic acid	3-4	140	24	MIL-120

Table S1: the all trials about the optimizations synthesis of MIL-120(Al)-AP. Noted: $M(Al(OH)(acac)_2) = 162$ g/mol; $M(Al(OH)_3) = 78$ g/mol; $M(NaAlO_2) = 82$ g/mol; $M(BTec) = 254$ g/mol

Comparison between MIL-120(Al) and MIL-120(Al)-AP

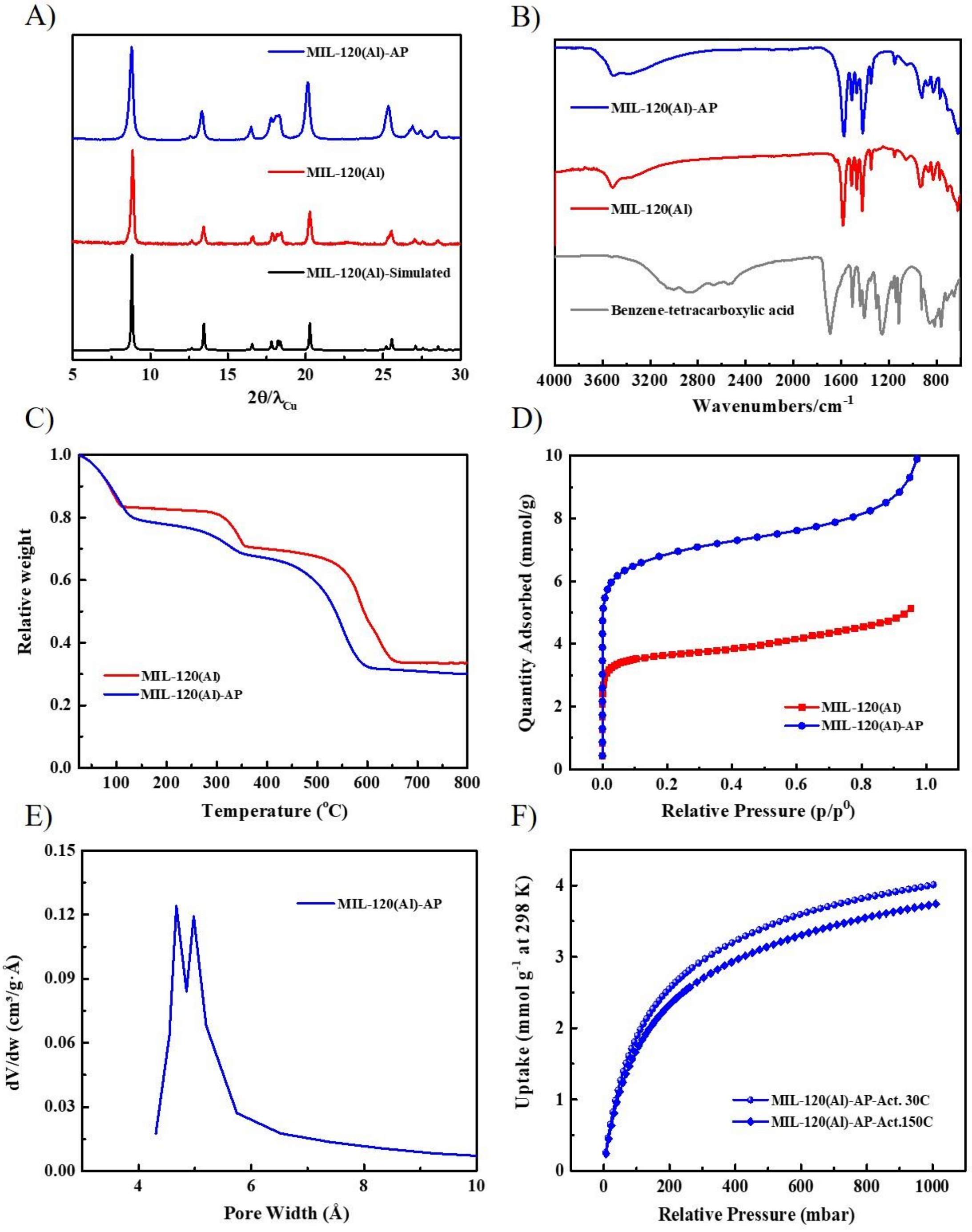

Figure S1: The comparison of MIL-120(Al) and MIL-120(Al)-AP: A) PXRD patterns. It displayed the same phase of MIL-120(Al) could be obtained successfully using modified synthesis method. B) FT-IR spectroscopy. it demonstrated that no free carboxylic acid groups in MIL-120(Al)-AP from the C=O stretch vibration at 1705 cm^{-1}, and large vibration (around 3514 cm^{-1}) belongs to hydroxyl group could be observed in MIL-120(Al) and MIL-120(Al)-AP structures. C) TGA in O_2 (5°C min^{-1}). According to the TGA curve before 150°C, MIL-120(Al)-AP sample contained around 3.7% higher water than MIL-120(Al) sample during free water release stage, which was consistent with 3.8% lower weight of MIL-120(Al)-AP sample at the end of measurement. D) N_2 adsorption at 77 K. the N_2 uptake of MIL-120(Al) at 77 K was consistent with the previous reported one in 2009. For MIL-120(Al)-AP sample, the N_2 uptake at 77 K could be almost double higher using proper washing procedure. E) Pore size distribution of MIL-120(Al)-AP simulated by Horvath-Kawazoe model. F) CO_2 adsorption isotherms at 298 K after 30°C and 150°C activation.

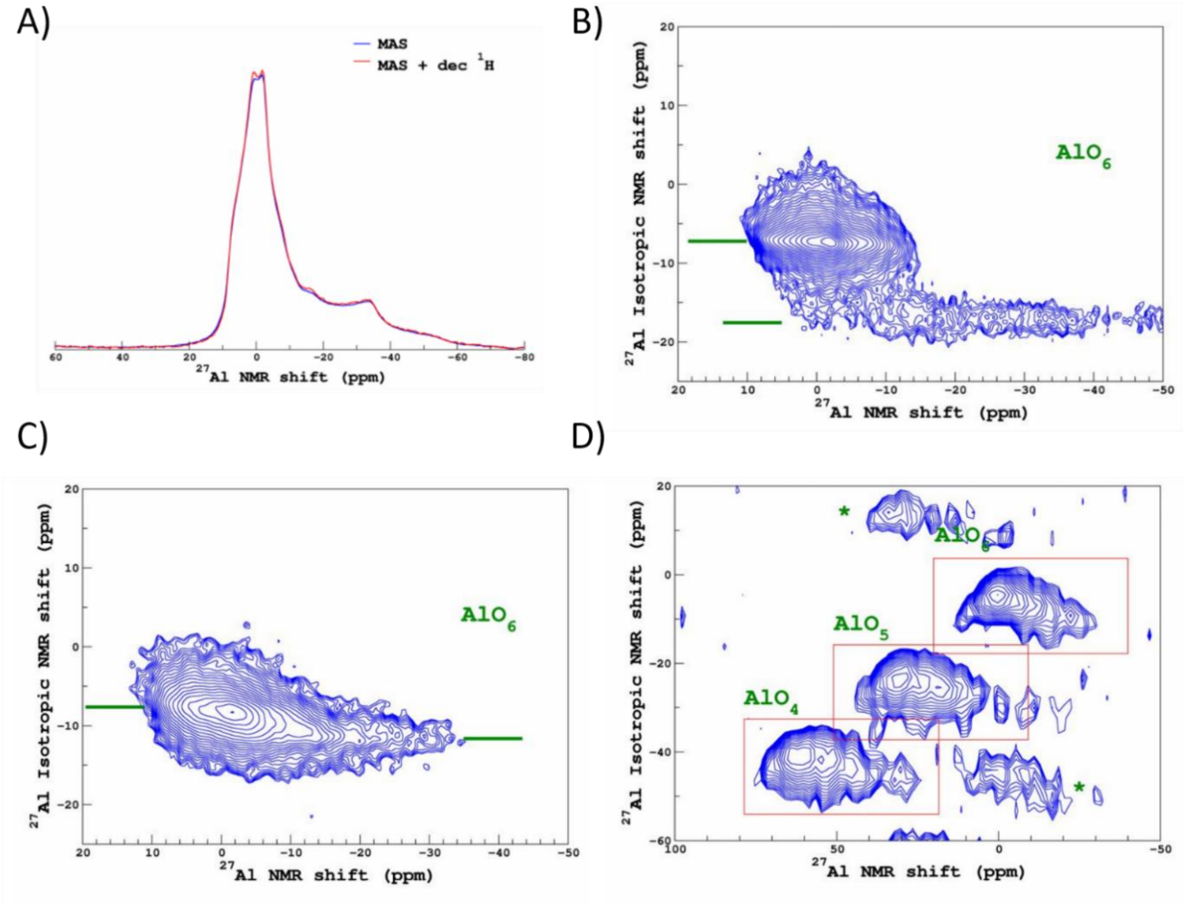

Figure S2: ^{27}Al MAS NMR results of MIL-120(Al)-AP under different conditions. A and B) ^{27}Al MAS NMR shift of MIL-120(Al)-AP, showing the same experimental spectrum. C) The heating conditions were at 120°C for 4 hours. D) The heating conditions were at 430°C for 4 hours.

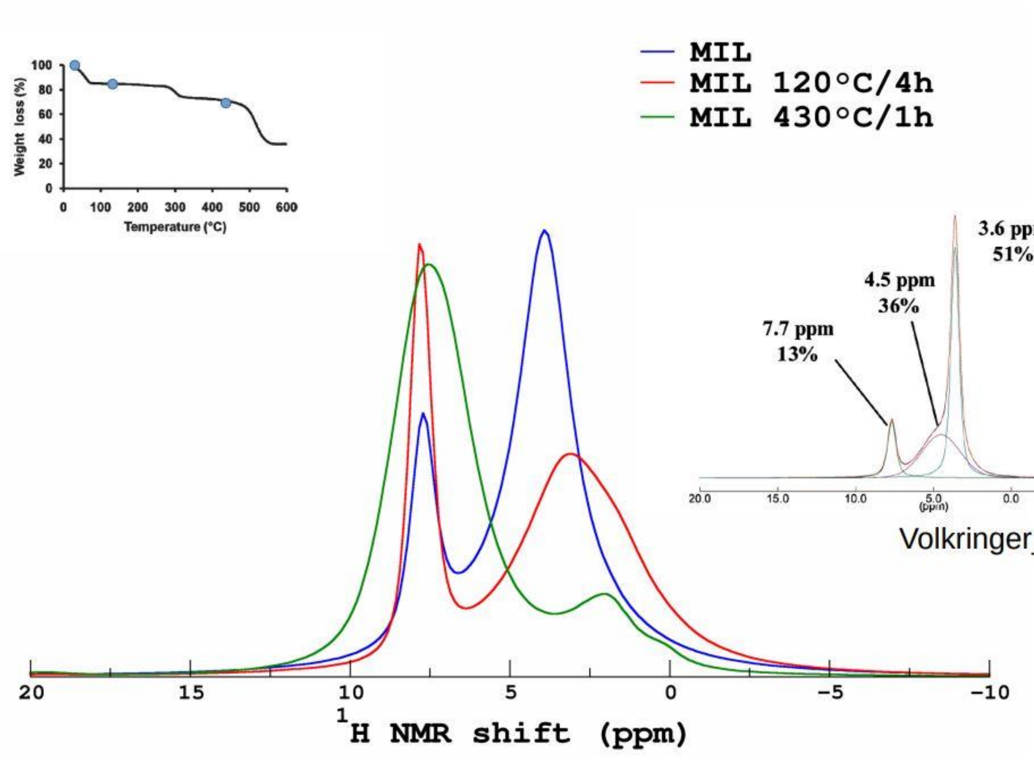

Figure S3: ^{1}H MAS NMR of MIL-120(Al)-AP.

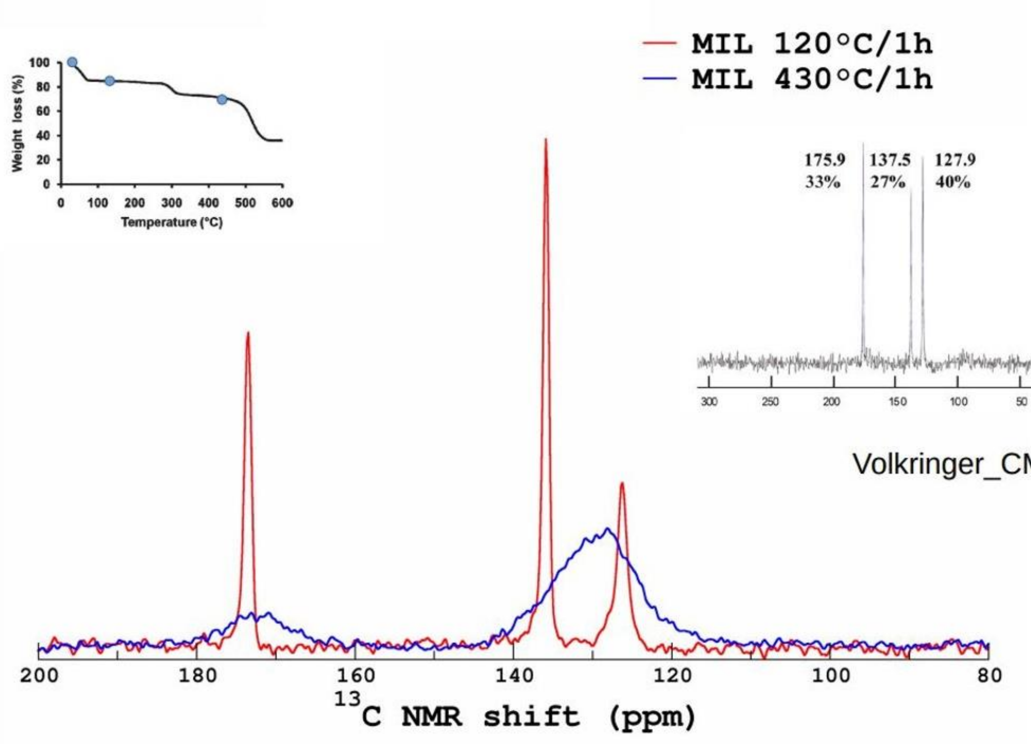

Figure S4: ^{13}C MAS NMR of MIL-120(Al)-AP.

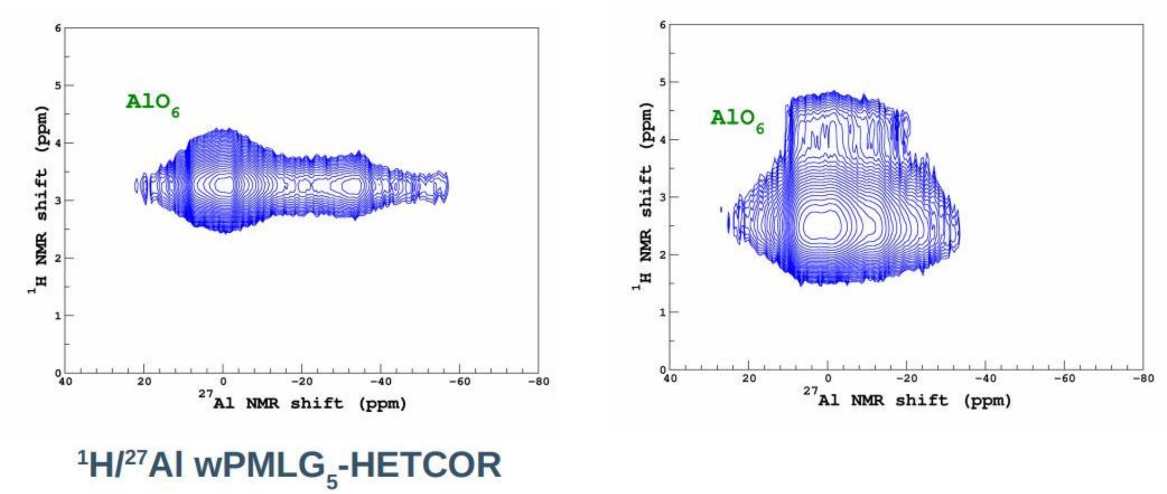

Figure S5: ^{1}H/^{27}Al MAS NMR of MIL-120(Al)-AP.

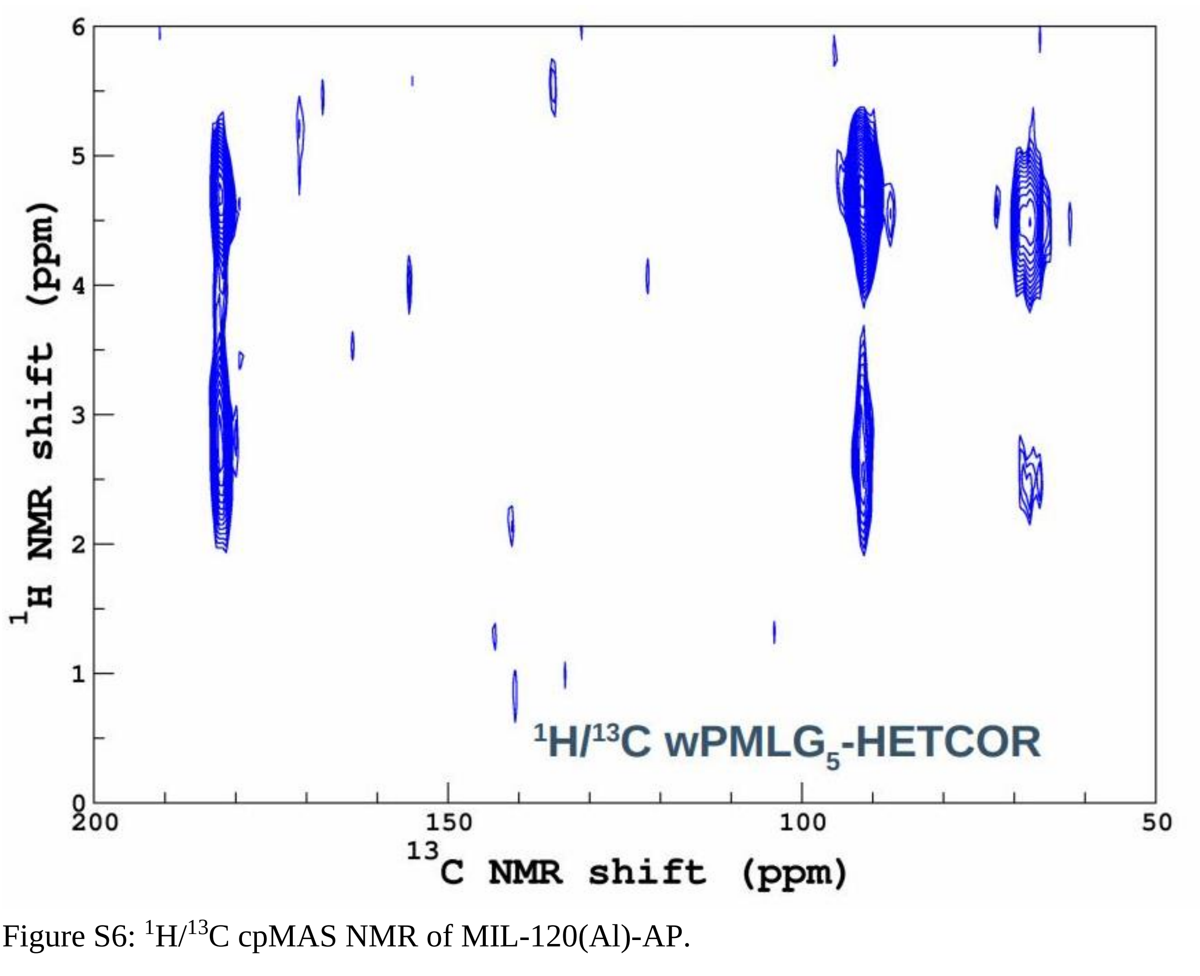

Figure S6: ^{1}H/^{13}C cpMAS NMR of MIL-120(Al)-AP.

Fitting CO_2 adsorption of MIL-120(Al)-AP

Langmuir fits:

In most cases the isotherms were fit to the Single-Site Langmuir (SSL) equation. The isotherms were fit by solving the Langmuir equation using the solver function in Microsoft Excel following a similar protocol to Keller et al (Saleh, M.; Lee, H. M.; Kemp, K. C.; Kim, K. S. *ACS Appl. Mater. Interfaces* **2014**, *6*, 7325.). Utilizing this routine circumvents some of the problems associated with favoring either high- or low-pressure regions when linearizing the Langmuir equation and offers a balanced approach.

Single-Site Langmuir (SSL)

$$q_i = q_m \frac{k_i}{1 + k_i P} P$$

Dual-Site Langmuir (DSL)

$$q_i = q_{m,1} \frac{K_1}{1 + K_1 P} P + q_{m,2} \frac{K_2}{1 + K_2 P} P$$

Virial analysis:

The CO_2 & N_2 adsorption data for the polymers were measured from 0-1 bar at 288, 298 and 303 K and were fitted by the following virial equation.

*ln(P) = ln(Va)+(A0+A1*Va +A2*Va^2 …+ A6*Va^6)/T+(B0+B1*Va)*

Where P is pressure, Va is amount adsorbed, T is temperature, and A0, A1, A2 …, A4 and B0, B1 are temperature independent empirical parameters.

Table S2: Fitted Virial parameters for CO_2.

Parameters	**MIL-120(Al)-AP**
A0	
A1	
A2	
A3	
A4	
B0	
B1	

Table S3: Fitted Virial parameters for N_2.

Parameters	**MIL-120(Al)-AP**
A0	
A1	
B0	

B1	

Ideal Adsorption Solution Theory (IAST):

IAST calculations were employed as described by Prausnitz et al (Myers, A. L.; Prausnitz, J. M. *AIChE J.* **1965**, *11*, 121.). The equation that is involved in selectivity calculations has been given below.

$$S_{1,2} = \frac{q_1/q_2}{p_1/p_2}$$

IAST fitting parameters:

Table S4: Fitted IAST parameters for CO_2/N_2 ($15CO_2:85N_2$ composition) selectivity for MIL-120(Al)-AP at 298 K.

Constants	**Gas A**	**Gas B**
	298 K	**298 K**
qA1	4.643024581	3.98711562
qA2	0	0
kA1	0.01390145	0.00010159
kA2	0	0
nA1	0.846475646	0.99322407
nA2	0	0
HA1/B1	0.064544776	0.00040505
HA2/B2	0	0

Table S5: Fitted IAST parameters for CO_2/N_2 ($5CO_2:95N_2$ composition) selectivity for MIL-120(Al)-AP at 298 K.

Constants	**Gas A**	**Gas B**
	298 K	**298 K**
qA1	4.643024581	3.98711562
qA2	0	0
kA1	0.01390145	0.00010159
kA2	0	0
nA1	0.846475646	0.99322407
nA2	0	0
HA1/B1	0.064544776	0.00040505
HA2/B2	0	0

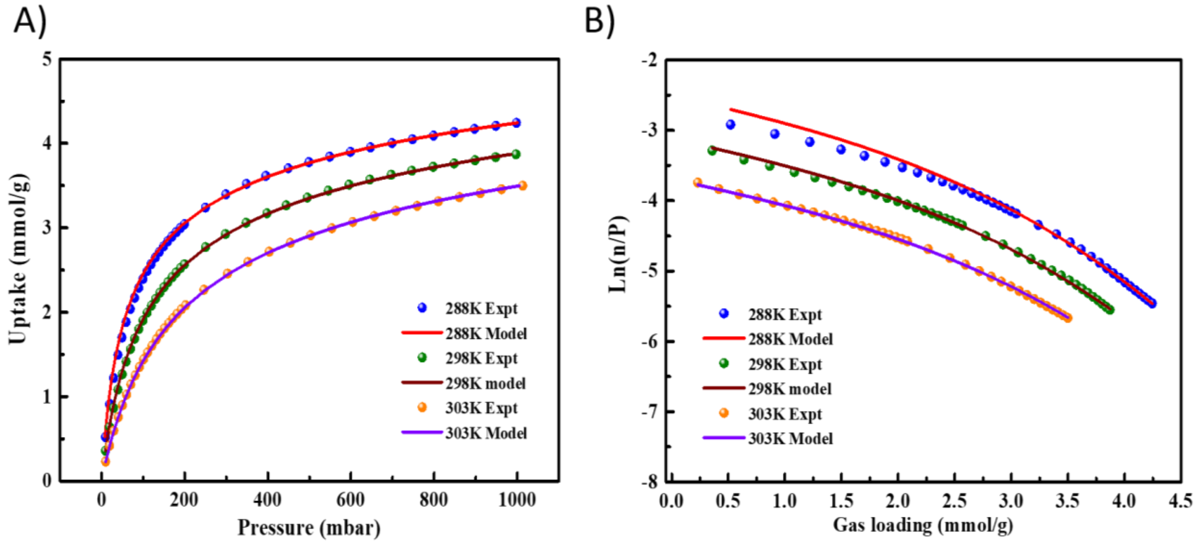

Figure S7: Virial plots for CO_2 adsorption for MIL-120(Al)-AP. A) Comparison of experimental CO_2 isotherms with the isotherms calculated from virial model at three different temperatures, 288 K, 298 K, and 303 K. B) Virial plots for CO_2 adsorption at three different temperatures, 288 K, 298 K, and 303 K.

Stability of MIL-120(Al)-AP

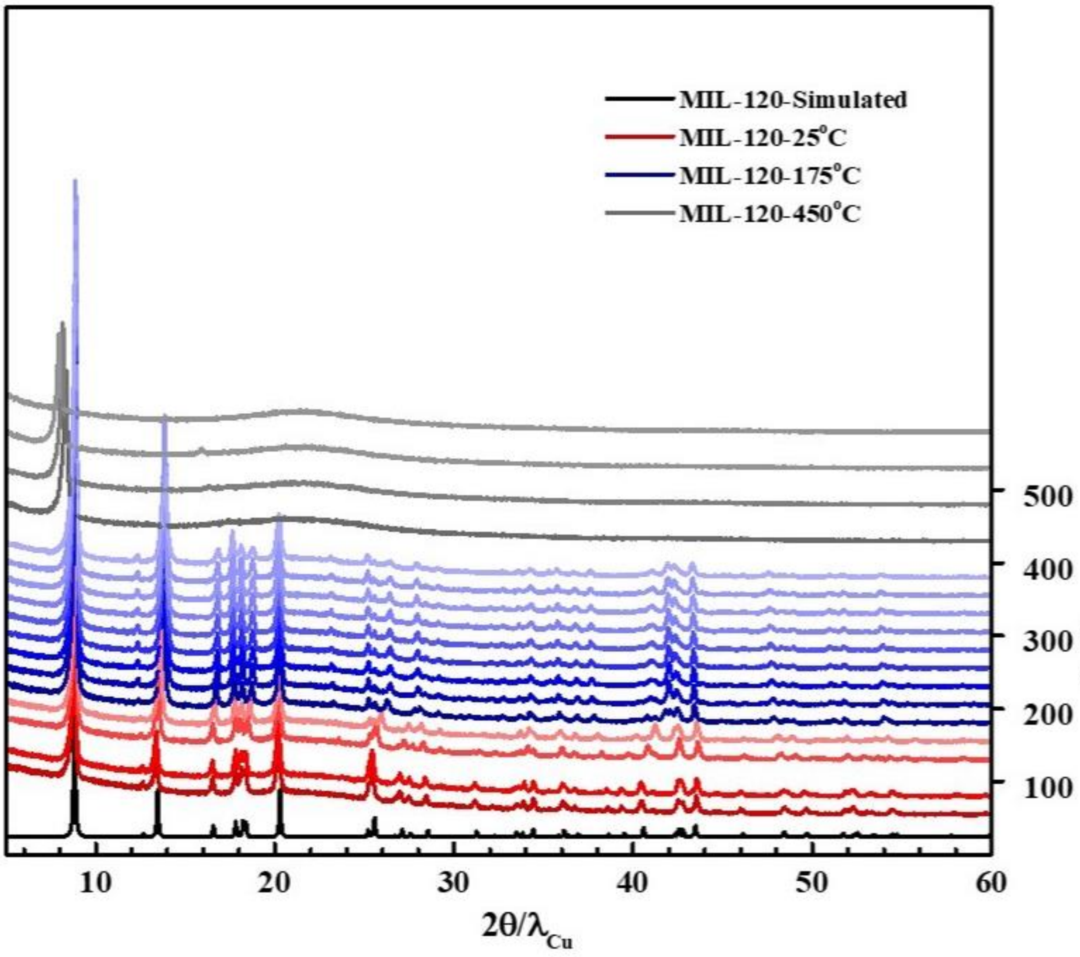

Figure S8: VT-PXRD of MIL-120(Al), here MIL-120(Al) had been used for thermal stability test due to the same topology as MIL-120(Al)-AP.

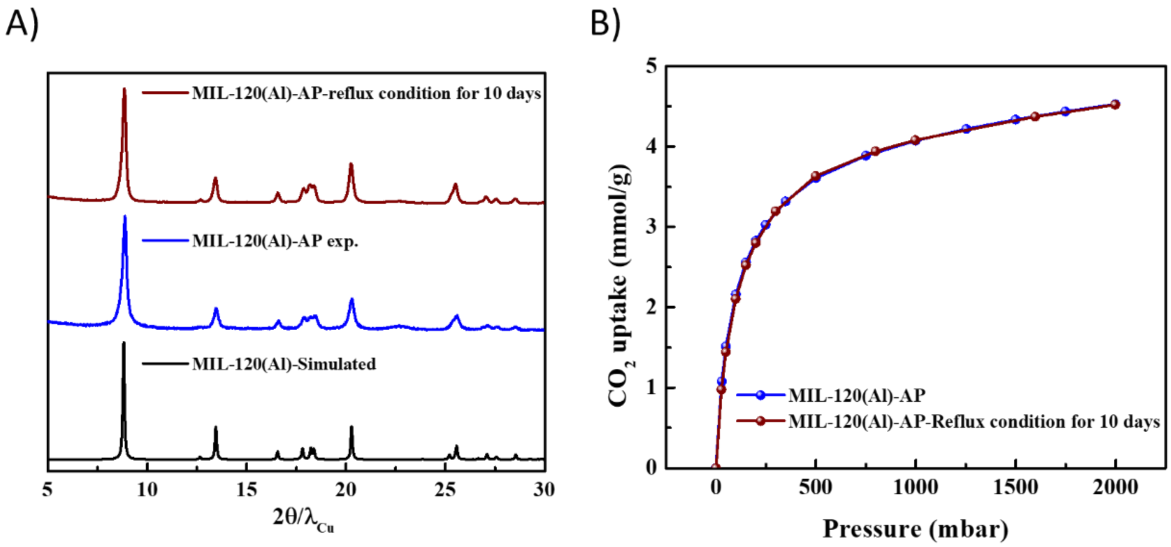

Figure S9: The water stability of MIL-120(Al)-AP. A) PXRD patterns showing the high crystallinity could be kept after 10 days water reflux. B) CO_2 adsorption isotherm showing CO_2 uptake after 10 days' water reflux was highly consistent with that of the pristine MIL-120(Al)-AP sample.

In situ PXRD experiments

in situ PXRD of MIL-120(Al)

Activation

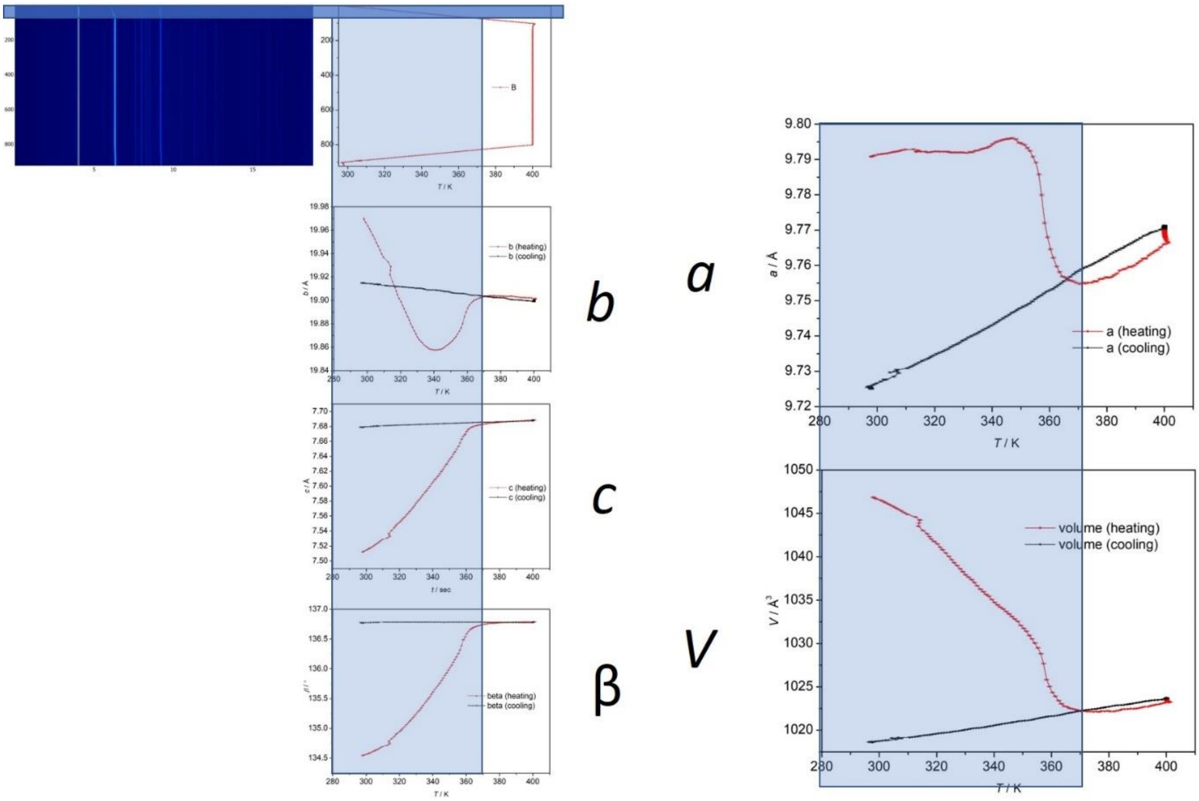

Figure S10: Variable temperature synchrotron PXRD of MIL-120(Al) activation parameter changes. The changes of the position of the peaks mostly are due to the increase of β angle.

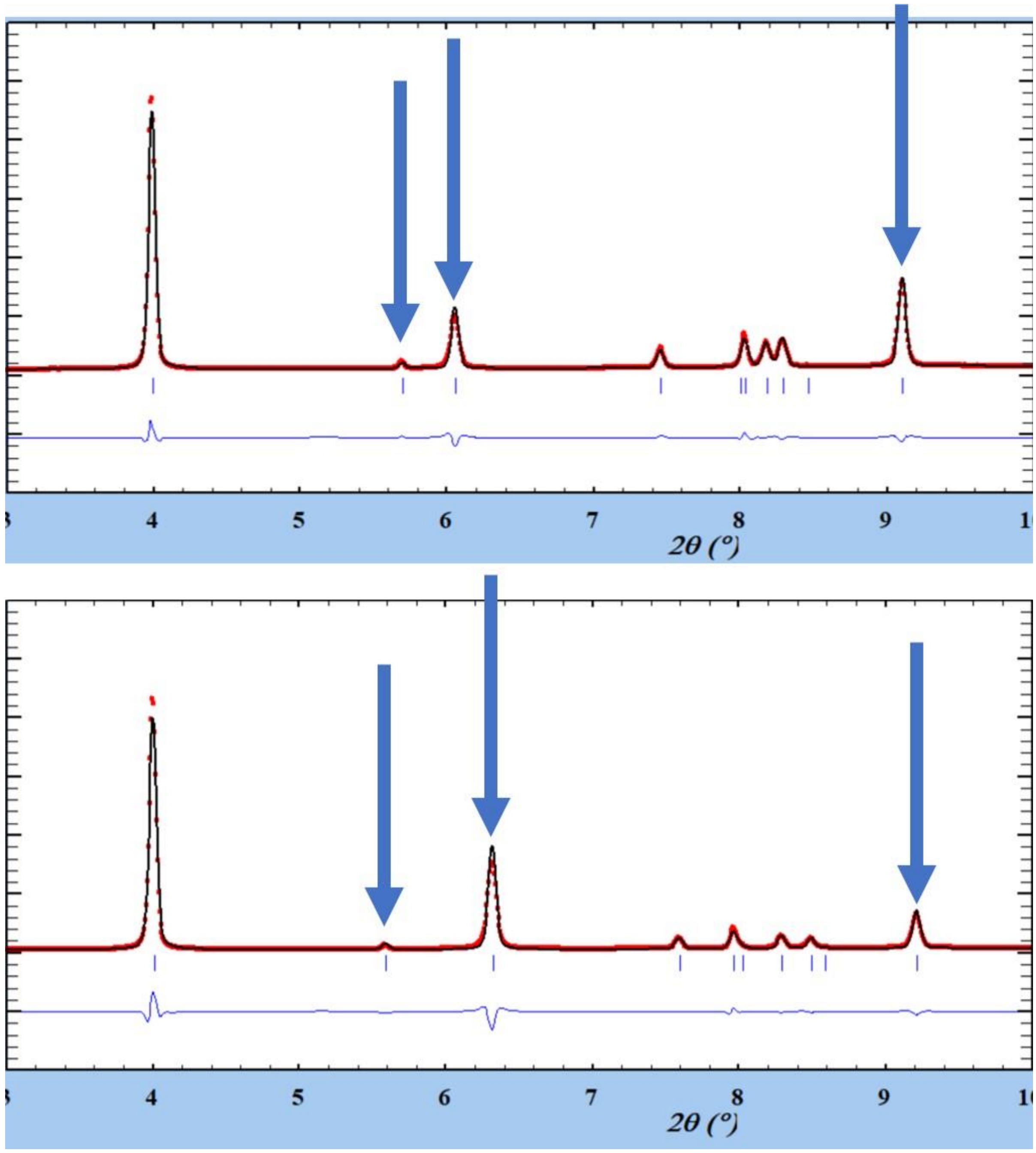

Figure S11: No change from the peaks of MIL-120(Al) before and after activation.

.

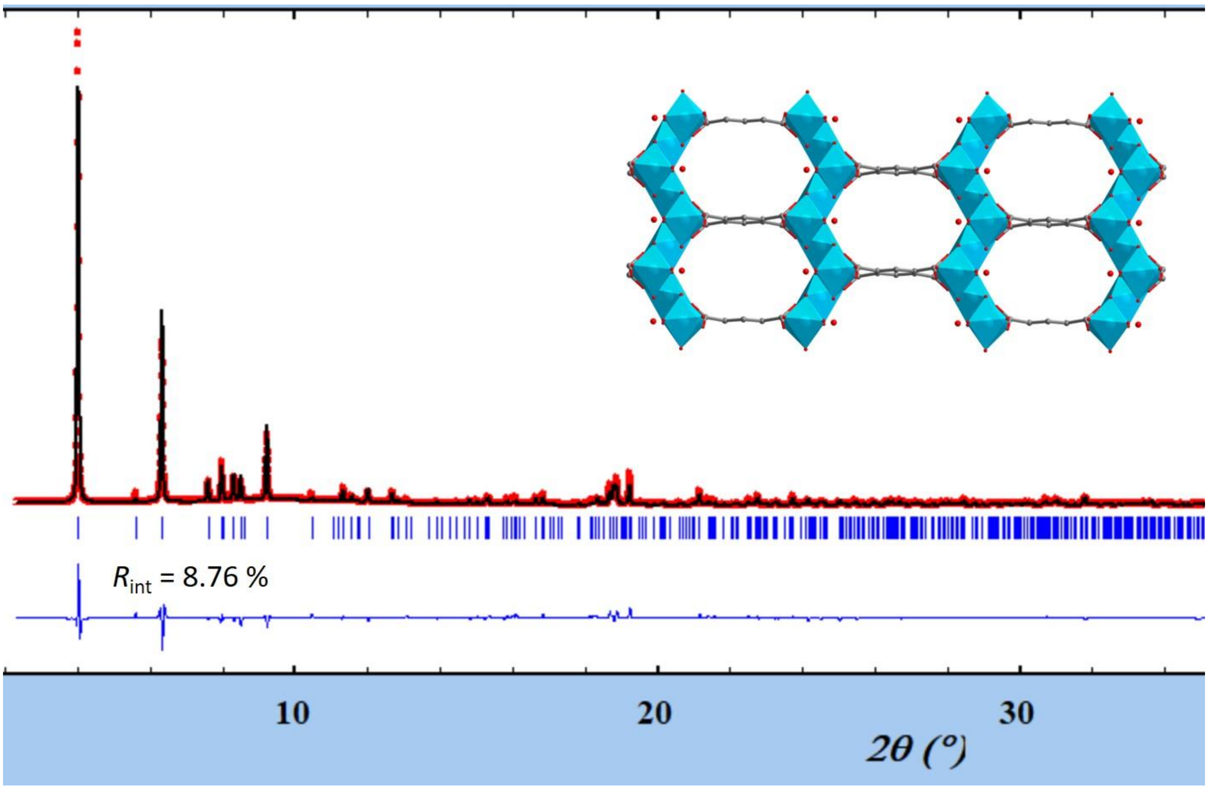

Figure S12: PXRD refinement and the structure of MIL-120(Al) after activation-peaks refinement.

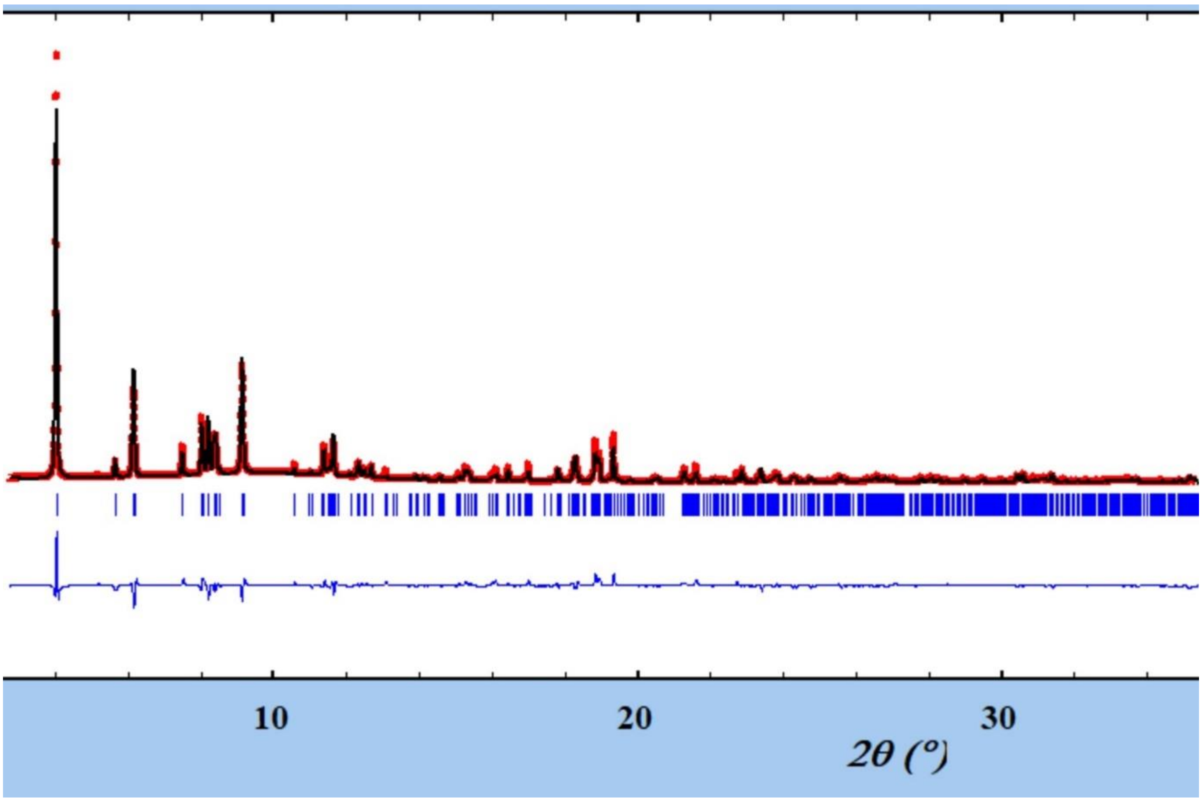

Figure S13: PXRD refinement of MIL-120(Al) CO_2 ads at 4 bar 298 K.

In situ PXRD of MIL-120(Al)-AP

Activation

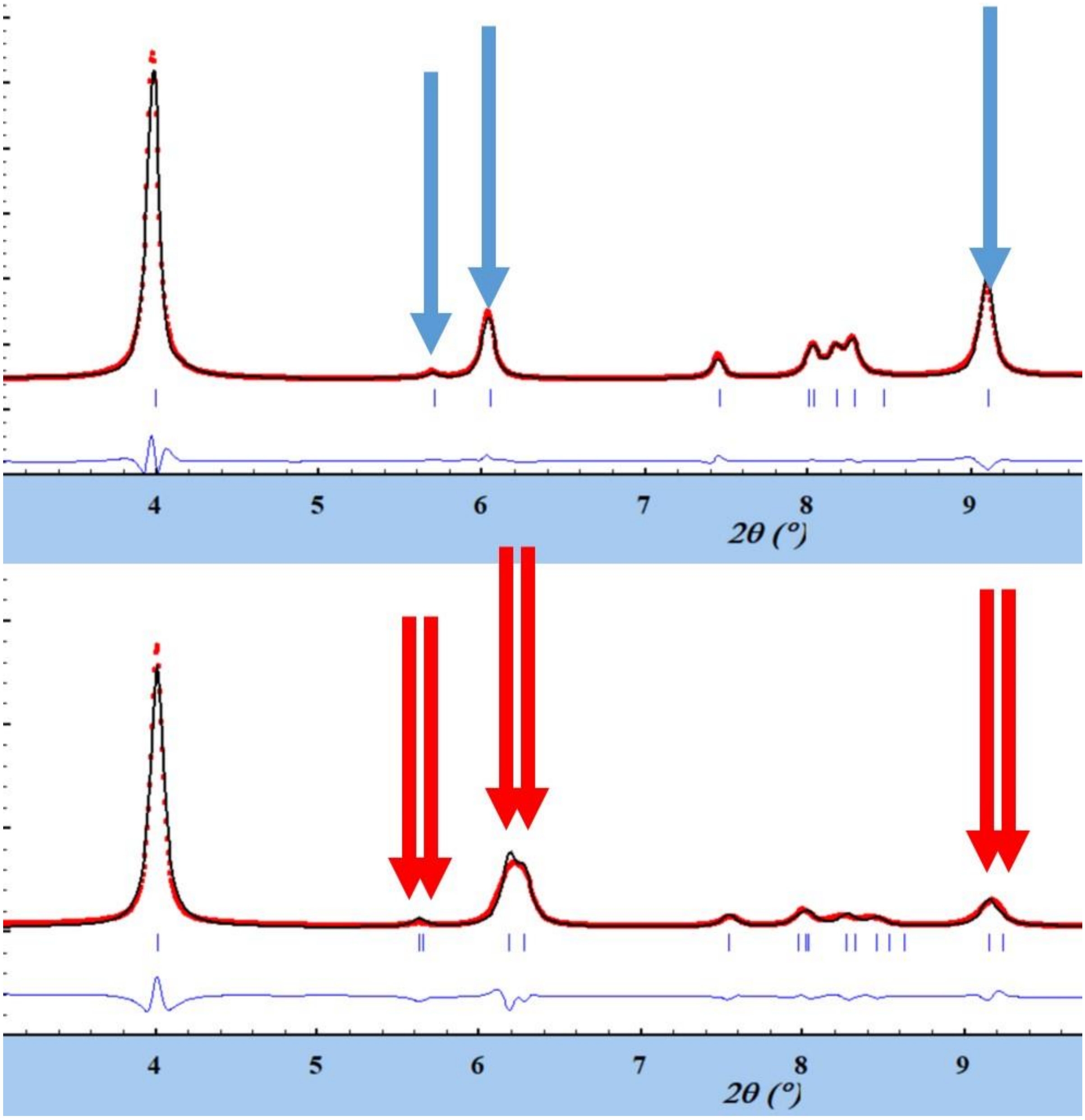

Figure S14: The peaks change of MIL-120(Al)-AP before and after activation.

CO_2 adsorption

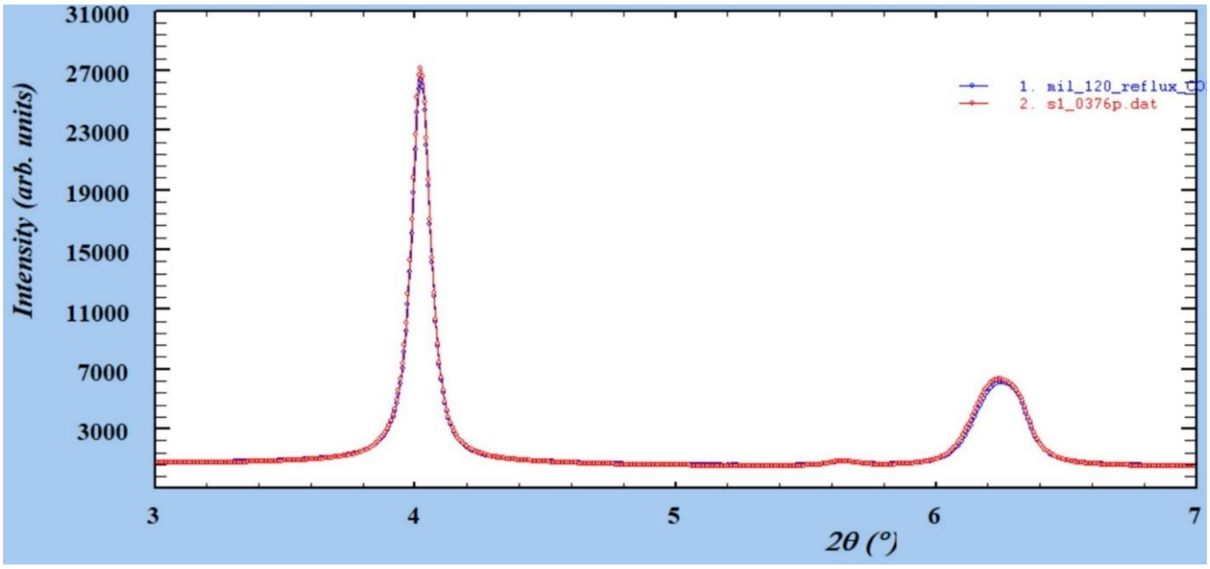

Figure S15: PXRD refinement of MIL-120(Al)-AP CO_2 ads at 1.5 bar 298 K.

Simulation and modeling

	a	***b***	***c***	***α***	***β***	***γ***	**V**
Exp. [with H_2O]	6.9770	7.4687	11.1296	107.809	106.376	95.443	519.25
DFT [with H_2O]	6.9328	7.4974	11.1727	107.816	106.060	96.489	518.75
DFT [without H_2O]	7.0990	7.4997	11.1064	107.611	106.441	96.301	528.07

Table S6: Comparison of theoretically calculated and experimentally tested lattice parameters of MIL-120(Al).

In situ IR experiments

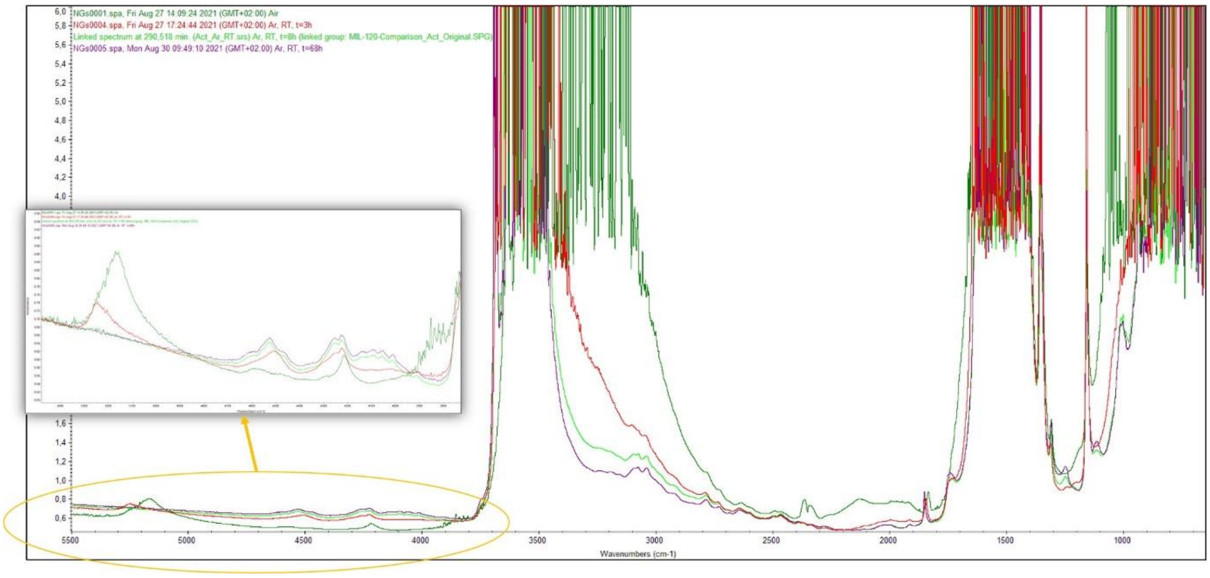

Figure S16: The IR spectra during room temperature activation (up to 68 hours) in Ar flow (25 mL min^{-1}). From the result, at 8 h under flow the water (5170 cm^{-1}) was completely removed.

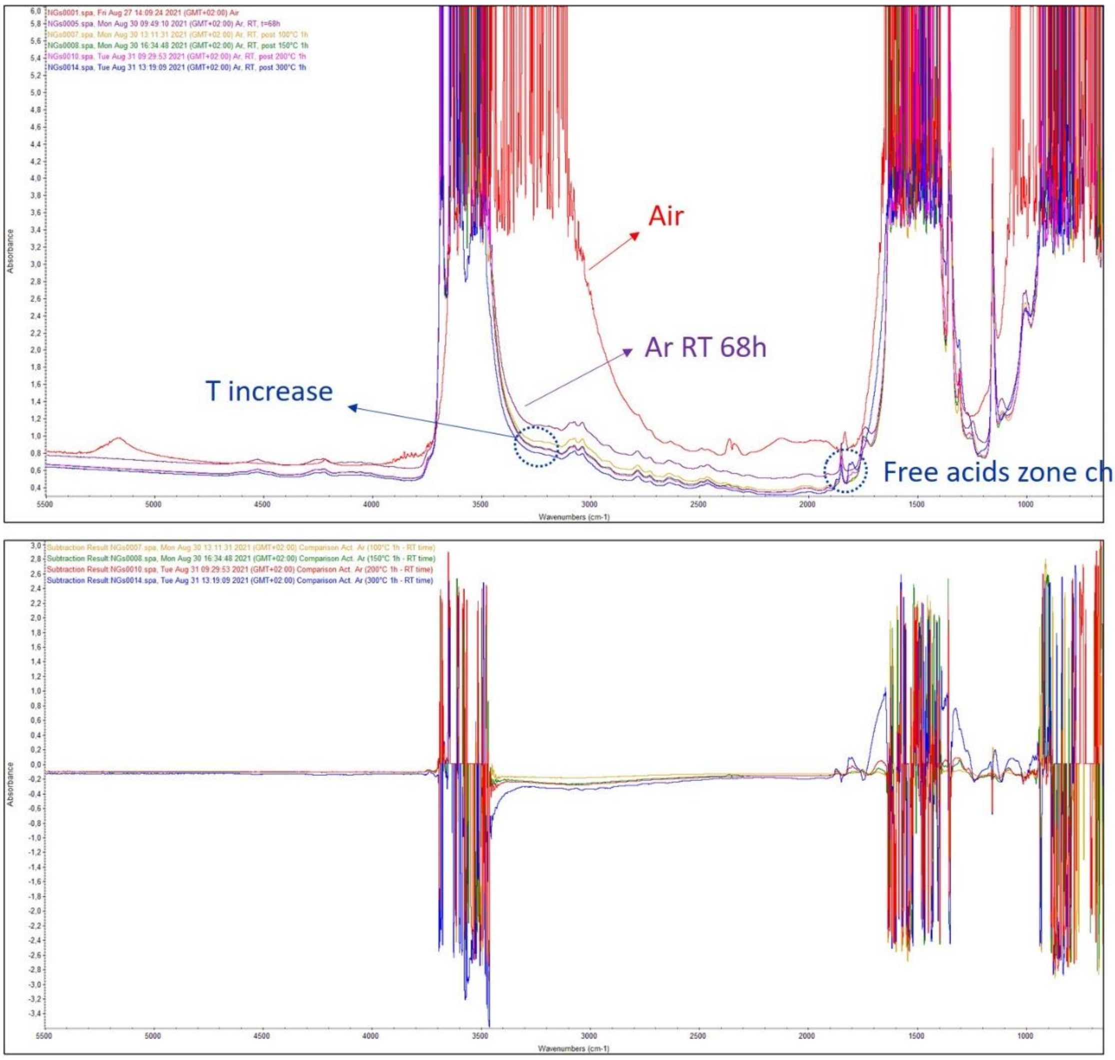

Figure S17: The IR spectra of MIL-120(Al)-AP at different temperatures (50-100-150-200-300°C) in Ar flow (25 mL min^{-1}), after 68 hours activation in Ar flow.

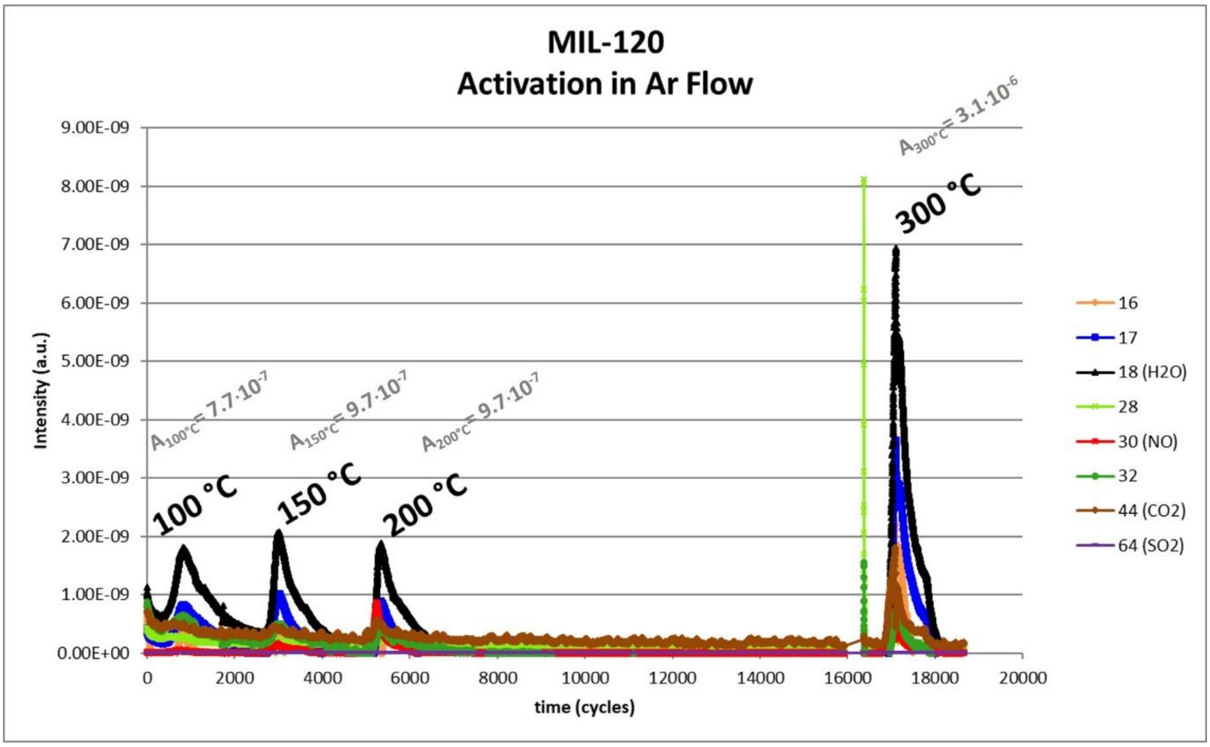

Figure S18: The MS results of MIL-120(Al)-AP at different temperatures, after 68 hours activation in Ar flow. It depicted that H_2O can be removed at 100°C in 1 h. Then, only free acid was removed at each temperature. Finally, a significant structural degradation starts at 300°C.

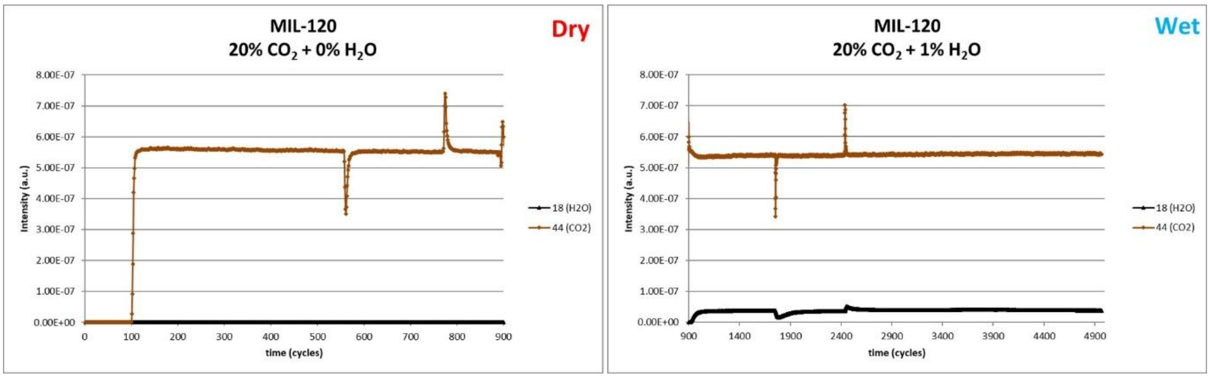

Figure S19: The MS signal during CO_2 ads/desorption (Dry & Wet) in Ar flow. The dry CO_2 consisted of 20% in Ar flow at RT; the wet CO_2 consisted of 20% CO_2, 1% H_2O in the Ar flow at RT.

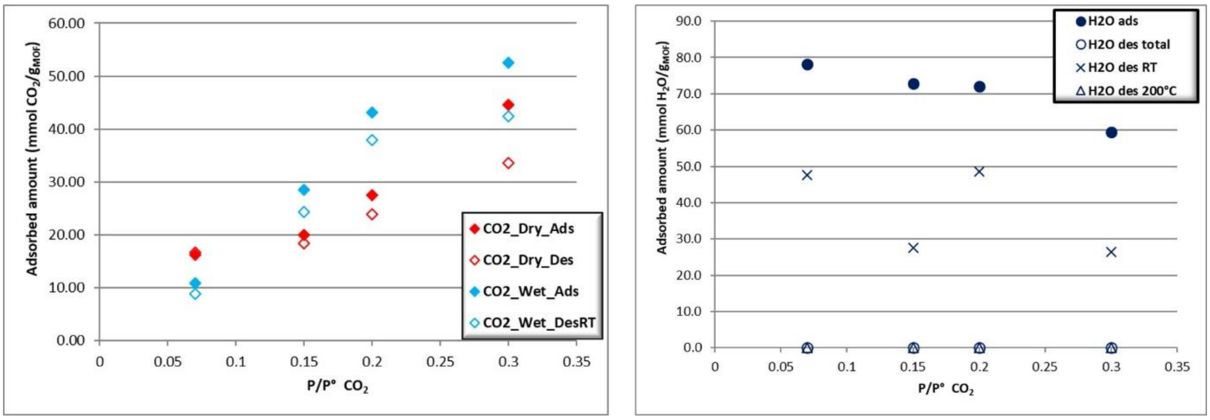

Figure S20: The quantified CO_2 uptake and H_2O uptake calculated by MS signal. Dry CO_2: 7, 15, 20 and 30% CO_2 in Ar flow at RT; Wet CO_2: 7, 15, 20 and 30% CO_2 + 1% H_2O in Ar flow at RT.

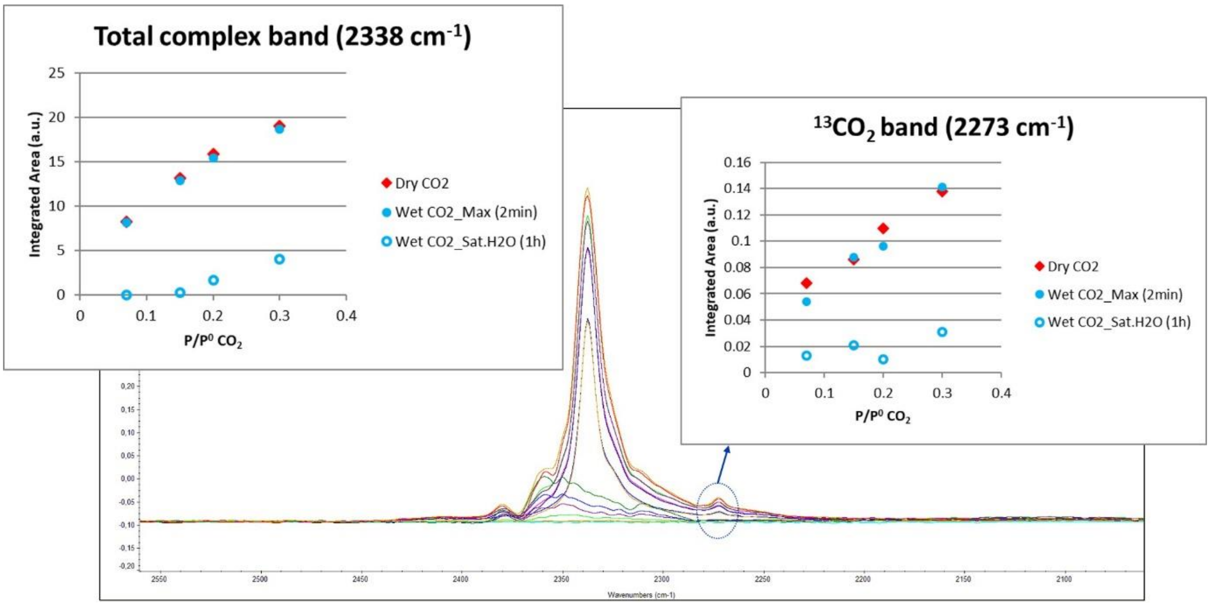

Figure S21: The IR spectra and the CO_2 uptake calculated by MS signal during CO_2 ads/desorption (Dry & Wet) in Ar flow. Dry CO_2: 7, 15, 20 and 30% CO_2 in Ar flow at RT; Wet CO_2: 7, 15, 20 and 30% CO_2 + 1% H_2O in Ar flow at RT.

Cyclability of MIL-120(Al)-AP

	Before exposure to air			After exposure to air		
Act. temp	1st activation at 25°C	2nd activation at 25°C	3rd activation at 50°C	1st activation at 25°C after exposure to air	2nd activation at 25°C after exposure to air	2nd activation at 50°C after exposure to air
Act. Time (hour)	6	6	6	6	6	6
Sample weight/mg	78.54	78.44	78.02	78.50	78.48	78.00
CO_2 uptake/(mmol/g) at 0.15 bar	2.55	2.52	2.26	2.32	2.30	2.26

Table S7: Six times CO_2 adsorption measurements of MIL-120(Al)-AP.

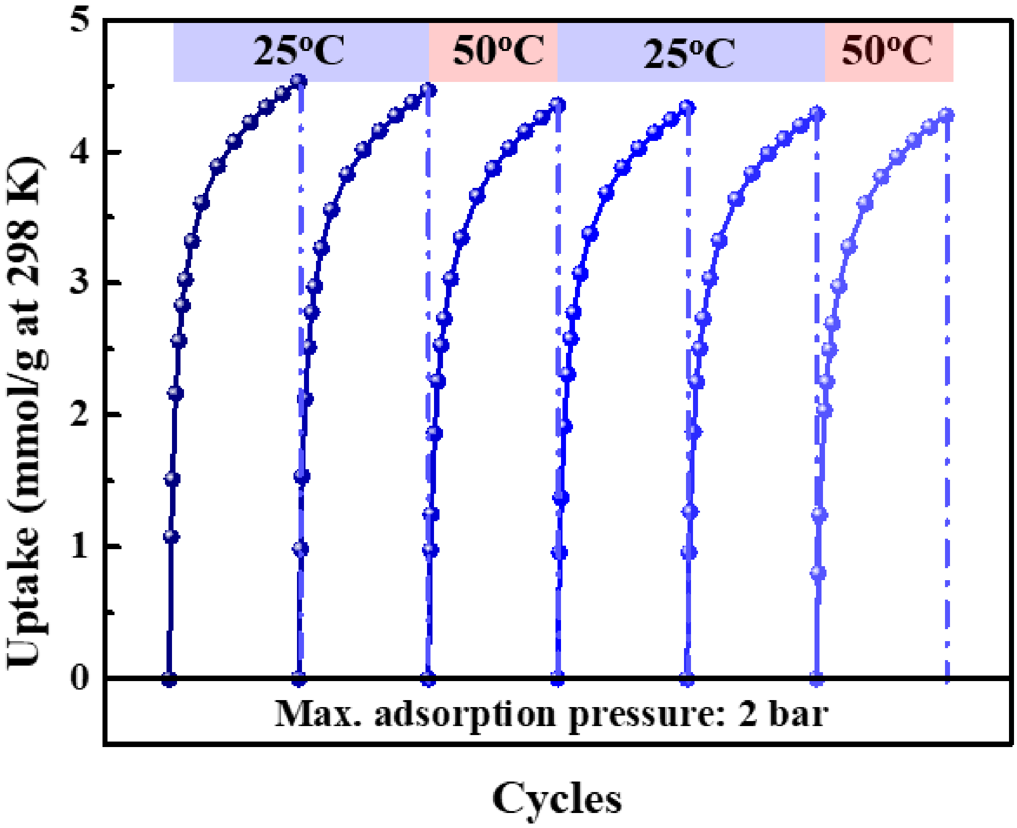

Fig S22: Six times CO_2 adsorption measurements of MIL-120(Al)-AP.

Synthesis optimization of MIL-120(Al)-AP in large-scale

Aluminum precursor	Quantity/kg	Price/euro
$NaAlO_2$	2.5	81.8
$Al_2(SO_4)_3\ xH_2O$	2.5	119
$Al(OH)_3$	2.5	156
$Al(OH)(C_2H_3O_2)_2$	2.5	214
$Al_2(SO_4)_3\ 18H_2O$	2.5	263
$Al(NO_3)_3\ 9H_2O$	2.5	294
$AlCl_3\ 6H_2O$	2.5	298

Table S8: The price of different aluminium precursors from Sigma supplier.

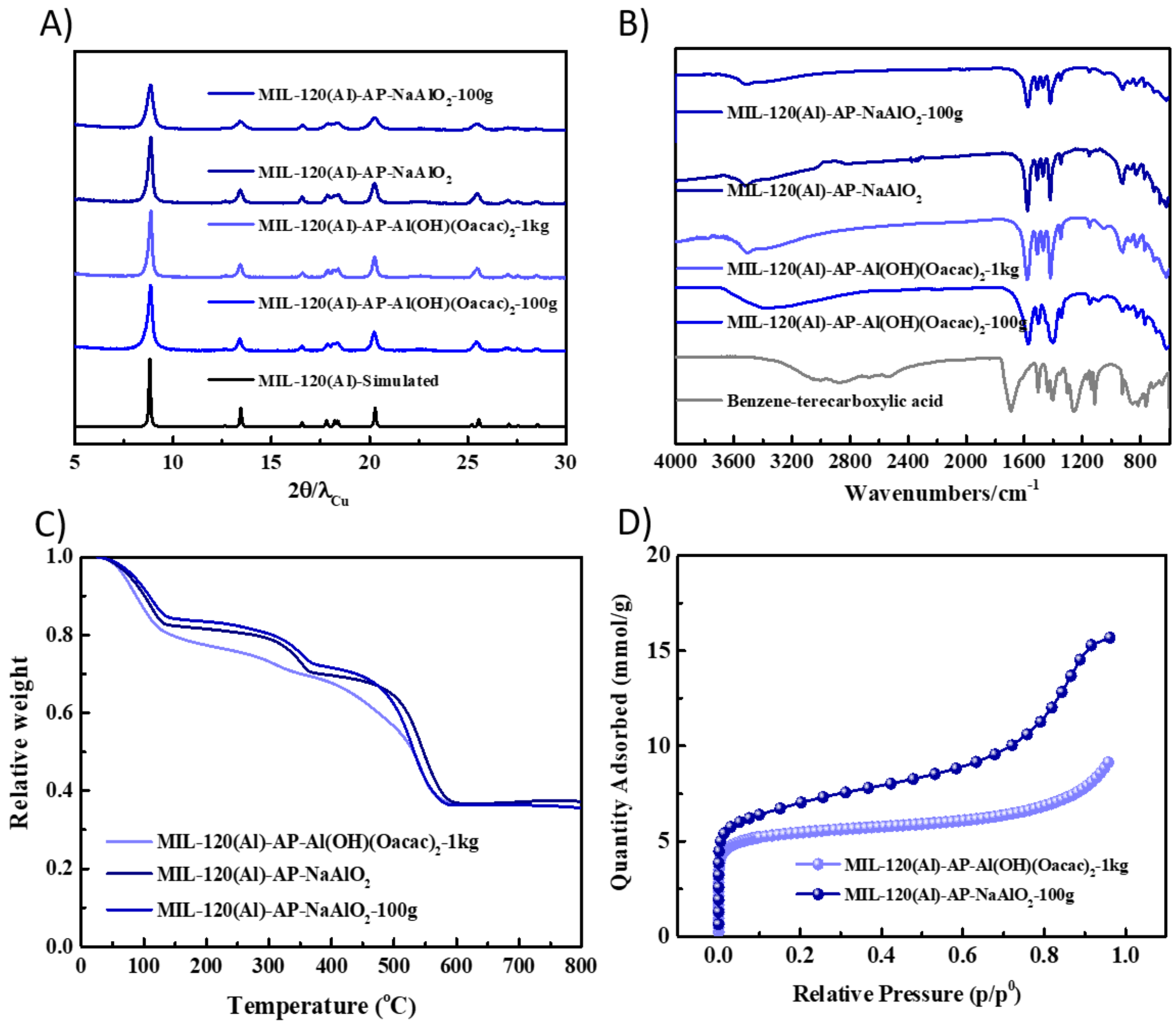

Figure S23: The characterizations of the different synthesis scale of MIL-120(Al)-AP. A) PXRD patterns showing pure MIL-120(Al)-AP phase could be obtained. B) FT-IR spectra showing there were no free carboxylic group in the different MIL-120(Al)-AP samples. C) TGA results showing the similar composition in the comparison with MIL-120(Al)-AP. D) N_2 adsorption isotherms showing the similar BET surface area (471 m^2 g^{-1} for MIL-120(AP)-Al(OH)(CH_3COO)$_2$-1kg; and 527 m^2 g^{-1} for MIL-120(AP)-NaAlO$_2$-100g), this difference was probably caused from the different activation conditions under vacuum.

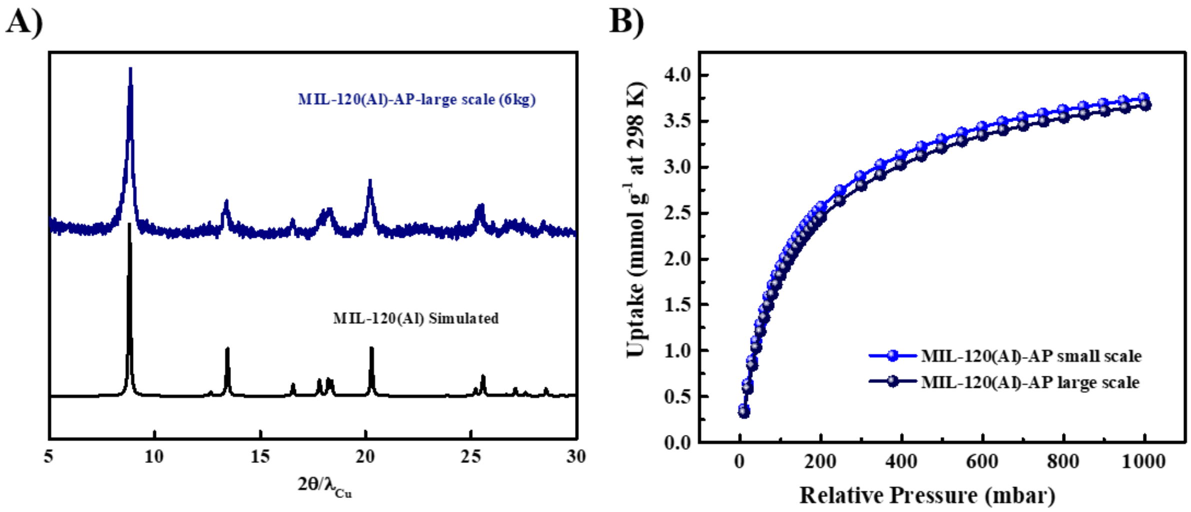

Figure S24: The characterizations of MIL-120(Al)-AP for 6 kg large-scale synthesis using Al(OH)($CH_3COO)_2$. A) PXRD patterns showing pure MIL-120(Al)-AP phase could be obtained. B) CO_2 uptake at 298 K, compared with the small-scale synthesis.

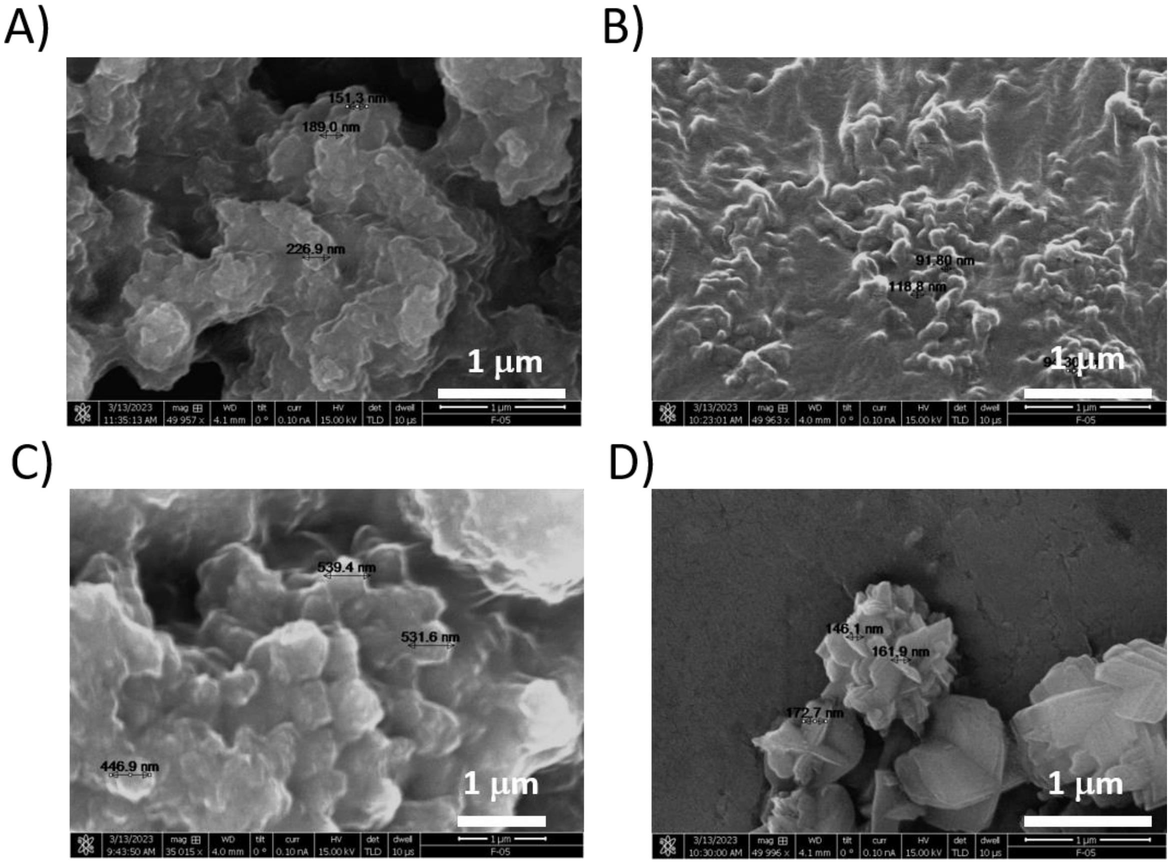

Figure S25: SEM images of the different synthesis scale of MIL-120(Al)-AP. A) Small scale synthesis using Al(OH)($CH_3COO)_2$ showing the particle size was around 200 nm. B) Small scale synthesis using $NaAlO_2$ showing the particle size was around 100 nm. C) Large scale synthesis using Al(OH)($CH_3COO)_2$ showing the particle size was around 500 nm. D) Large scale synthesis using $NaAlO_2$ showing the particle size was around 150 nm.

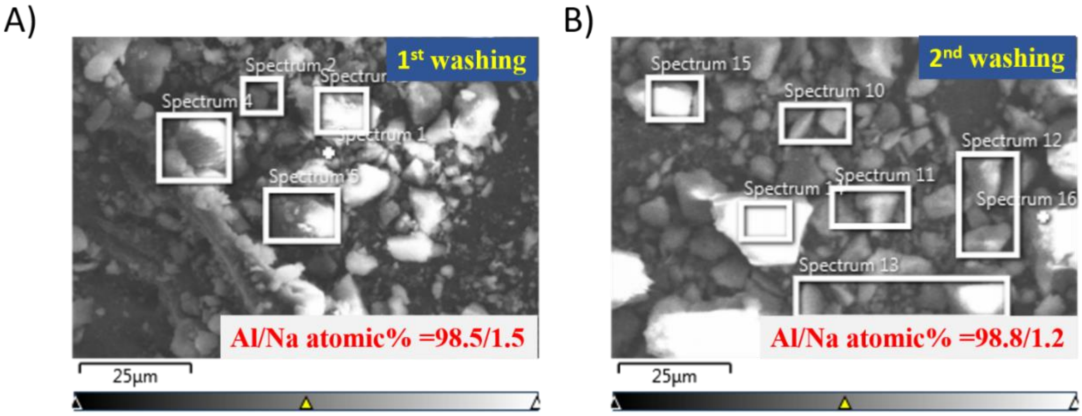

Figure S26: EDX results of sodium element in the MIL-120(Al)-AP-100g scale. A) First time washing, B) Second time washing in water at 60°C for 24 hours, showing there existed around 1.5 percentage of sodium element in the sample.

Shaping of MIL-120(Al)-AP

Shaping MIL-120(Al)-AP with 10% bentonite (MIL-120(Al)-AP with 10% Silica)

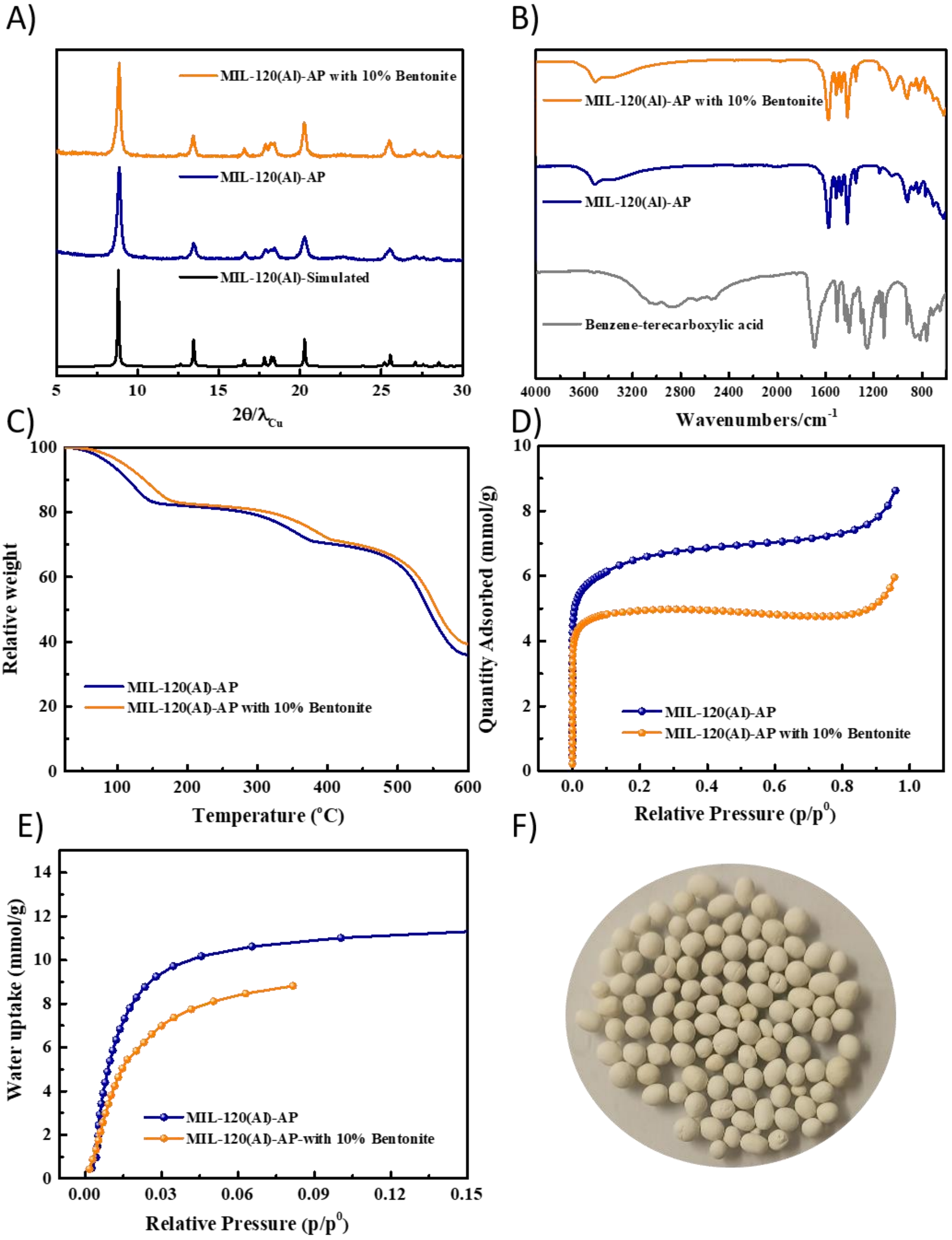

Figure S27: The comparison of the MIL-120(Al)-AP and MIL-120(Al)-AP with 10% Bentonite. A) PXRD patterns. B) FT-IR spectra. C) TGA in O_2. D) N_2 adsorption isotherms at 77 K. E) Water adsorption isotherms at 298 K, F) The photo of the MIL-120(Al)-AP beads with 3-5 mm diameter.

Shaping MIL-120(Al)-AP with 10% Silica

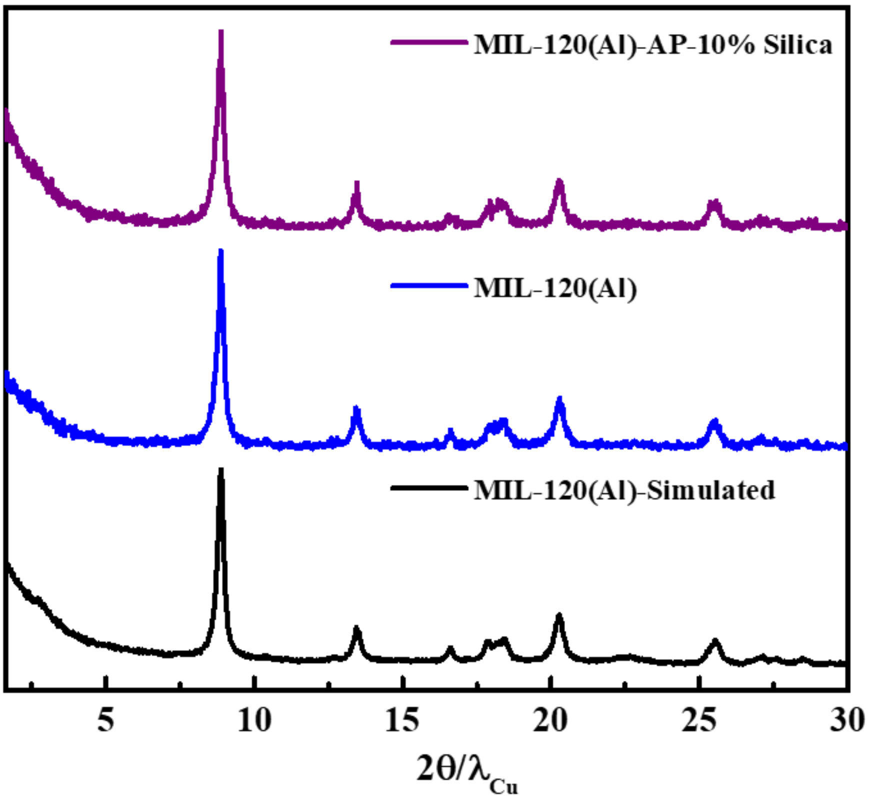

Figure S28: The comparison PXRD patterns of the MIL-120(Al)-AP and MIL-120(Al)-AP with 10% Silica.

Chapter 5

A novel titanium metal-organic framework platform for photocatalytic hydrogen evolution

Table of Contents

Contributions to this work

In this work, I synthesized this novel Ti-MOF by solvothermal reactions, then characterized by PXRD, FT-IR, TGA in O_2, N_2 adsorption at 77 K, CO_2 adsorption at 298 K, SEM/EDX, ^1H liquid NMR. To enhance its water stability, I synthesized this Ti-MOF with Cr doping by one-pot synthesis. Dr. Asma MANSOURI, Dr. Iurii DOVGALIUK, Dr. Philippe BOULLAY, and Dr. Gilles PATRIARCHE solved the structure by continuous rotation electron diffraction and other complementary techniques such as low dose HRTEM and synchrotron PDF analysis. Celia M. RUEDA-NAVARRO, Prof. Dr. Sergio NAVALÓN, Prof. Dr. Hermenegildo GARCIA measured the photocatalytic tests. Prof. Dr. Guillaume MAURIN and Dr. Dong FAN did the simulation for photocatalytic performance by DFT and analyzed the results.

Abstract

Compared with dense titanium dioxide, constructing porous titanium-based metal-organic frameworks (Ti-MOFs) is an effective way towards the enhancement of the photocatalytic performance through more accessible active sites and rapid diffusion of substrates and products. In this regard, Ti-MOFs have attracted much attention as being considered photocatalyst candidates due to their high porosity and tunability in terms of chemical composition and pore engineering. However, Ti-MOFs remain still scarce because of the complexity of titanium chemistry in solution rendering any attempt of rational design highly challenging, despite recent progresses. Here, we present a new microporous Ti-MOFs, labeled MIP-209(Ti) (MIP stands for Materials from Institute of Porous Materials of Paris) constructed by a nitro terephthalate ligand and $Ti_{12}O_{15}$ oxo-clusters, as revealed by continuous rotation electron diffraction method (cRED). Indeed, MIP-209(Ti) can be obtained using various terephthalate (1,4-BDC^{2-}) derivatives such as NO_2-BDC, 2Cl-BDC using an eco-friendly solvent, suggesting the ability of Ti_{12}-MOFs for isostructural chemistry. Alternatively, it is also possible to tune the composition of its Ti-oxo-cluster, similarly to MIP-177(Ti)_LT bearing the same Ti sub-unit. For instance, 5% Cr^{3+} doping in MIP-209(Ti) could favorably enhance the water stability, and maintained good crystallinity after soaking in water for at least 7 days. Motivated by the enhanced water stability and unique Ti-MOFs properties, photocatalytic hydrogen evolution from water splitting reaction (HER) have been measured. Interestingly, MIP-209(Ti-Cr)-NO_2 displayed a significant hydrogen production rate with good reusability and stability under simulated solar light irradiation. It showed fourfold enhanced hydrogen production in HER in presence of methanol (5812 µmol of H_2/gcat, in 5 hours), in comparison with the benchmark MOF IEF-11 (1391 of H_2/gcat in 5 hours). Besides that, without the addition of a noble metal co-catalyst, MIP-209(Ti-Cr)-NO_2 exhibited threefold enhanced hydrogen production (681 µmol of H_2/gcat in 5 hours) in OWS reaction under simulated solar light irradiation, in comparison with IEF-11 (220 µmol of H_2/gcat in 5 hours). This work represents a leap forward for the synthesis progress of Ti-MOFs and its practical photocatalytic applications.

5.1 Introduction

Titanium dioxide (TiO_2) has demonstrated significant potential as an inorganic semiconducting photocatalyst due to its environmentally friendly, earth-abundant and remarkable stable properties.[1,2] However, the enhancement of its photocatalytic performance is still strongly desired via efficient exploitation of visible light, high adsorption capacity of reactants, and simplification in separating from the suspension.[3-6] Compared with particulate TiO_2, construction of long-range order Ti-O moieties into stable titanium-based MOFs (Ti-MOFs), shall not only promote improved the accessibility to the active sites with rapid diffusion rate of reactants and products, but also allow to expand the photocatalytic reaction to the visible range via the rational design of inorganic/organic moieties.[7-10] If the early work has reported only Ti-phosphonate based MOFs with a limited porosity,[11-13] since 2009, highly porous crystalline Ti-carboxylate based MOFs built by the strong coordination bonding connections of various organic linkers and titanium-based inorganic building units have emerged and their properties were assessed for various photocatalytic reactions such as overall water splitting,[14,15] CO_2 reduction,[16] hydrogen evolution[17], and pollutant degradation.[18,19] Nevertheless, only scarce examples were reported on Ti-MOFs for overall water spitting (i.e., producing H_2 and O_2 in a stoichiometric amount)[20-22] or half reactions (i.e., proton reduction and water oxidation)[23-26] under visible-light irradiation. Meanwhile, the rational design of new high porous crystalline Ti-MOFs remains still not mature because of the high degree of complexity of titanium chemistry in solution.[7] For instance, while more than 100,000 of different MOF structures were reported so far, less than three dozens of Ti-MOFs structures obtained via one-step synthesis and bimetallic Ti-MOFs have been described to date.[8,27-30] Several challenges on Ti-MOFs stem from the synthesis procedure, the structural determination and sometimes the chemical stability issues of Ti-MOFs, especially under practical photocatalytic test conditions.

The challenges of producing new Ti-MOFs are mainly related to high reactivity of Ti^{4+} species in the presence of water leading to uncontrolled precipitation of metal oxide/hydroxides. The use of air-stable or hydrophobic Ti precursor, e.g., $Ti(iPrO)_4$, $TiOSO_4$, $TiO(OAcac)_2$ or even pre-formed Ti-oxoclusters is required to avoid uncontrolled titanium hydrolysis during the Ti-MOFs synthesis.[31] Additionally, several attempts to reach a more rational approach have been recently proposed such as using inhibitors to better control the trade-off of M-O bond association and disassociation rate, but the synthesis methods of Ti-MOFs are still driven by serendipity as evidenced by the large diversity of inorganic building units (IBU) that range from discrete Ti octahedra to infinite Ti-oxo-chains, with almost a different IBU per type of ligand.[7] Recently, some of us have reported several new Ti-MOFs obtained under acidic conditions which offers new opportunities to extend the Ti-MOFs library.[32-34] In comparison with the more discrete IBUs obtained when using pure organic solvents (DMF, alcohols), it appears that higher nuclearity IBUs (Ti_{12}, Zr_{12}) clusters have been obtained under pure acid solvothermal conditions (formic or acetic acids) leading to the highly porous robust MIP-177(Ti)_LT, MIP-206(Zr) frameworks.[32,35] Additionally, providing the same topology with different functional or expanded ligands in backbone Ti-MOFs leading to isostructural platform might provide a rational way to tune the physical/chemical properties, such as porosity, bandgap, hydrophilicity, etc.[36] However, such an approach was successfully applied with a very limited number of Ti-MOFs (MIL-125(Ti)-NH_2,[37] ZSTU-1/2/3,[23] UCFMOF-1/2/3/4,[38] MOF-901/2[39]) were successfully obtained via a direct route. Another possibility is to rely on the multivariate approach to tune the properties of a given MOF (MTV-MOFs), in order to endow the pores with a new level of complexity to fine-tune the pore environment and resulting properties.[35,40] Recently this method has been applied for several Ti-MOFs such as MIP-207,[33] MIP-208,[34] cMUV-11[41] enhancing the porosity and their performance.

The second important challenge of Ti-MOFs development lies in their crystal structure determination. Very often poorly crystalline samples are obtained, precluding from their structure solution. To date only a few Ti-MOFs structures (e.g., DGIST-1,[42] cMUV-11[41] and PCN-22[43]) have been solved from single crystal data so far. In general, only powders are obtained (e.g., MIP-177(Ti)_LT/HT,[32] ACM-1,[44] ICGM-1[26]) requiring the use of high resolution powder X-ray diffraction (PXRD), combining direct structure solution (e.g., charge flipping) and refinement (the Rietveld method), and in most cases complemented by density functional theory (DFT) calculations. In some cases it required the use of electron diffraction (ED) that enables rapid data collection time (minutes or less), low dose measurement and high accuracy by integrating reflection intensity.[45-47] MOF nanocrystals should however be slightly resistant to electron beam exposure and in the case of Ti-MOFs was successfully applied with COK-47[48] and IEF-11[21], for instance.

The usual good chemical stability of Ti-MOFs is an asset to enhance the photocatalytic lifetime and photocatalyst reusability in real conditions. The ligand decorations with some hydrophobic fluorine-containing and/or (long-chain) alkyl substituents linkers can also increase their hydrophobicity, affiliating the diffusion of water molecules from reaction-generated product.[49,50] Another post-synthetic strategy consists of grafting hydrophobic moieties on the secondary building blocks of Ti-MOFs providing great potential on gas separation and catalysis applications.[51] According to recent work, the connections on Ti-oxo clusters or Ti-oxo chains in the frameworks performed a positive correlation with the chemical stability such as MIP-177(Ti)_LT[32] (12-connected Ti_{12}-oxocluster), ZSTU-1/2/3[23] (Ti_6O_9 nanowire), MIP-208[34] (cis-connected corner-sharing oxochains) which maintained a good crystallinity in water even under acidic conditions. Furthermore, the radiolytic stability under light irradiation is of interest for photocatalytic applications; noteworthy, the bare IEF-11 could also keep the constant photocatalytic activity for at least 10 days.[21]

Herein we present a new microporous Ti-MOF, labeled MIP-209(Ti), constructed from a nitro terephthalate derivative ligand and $Ti_{12}O_{15}$ oxoclusters with the general formula $Ti_{12}O_{15}(NO_2$-1,4-BDC$)_6$(acetate$)_3$. As revealed by continuous rotation electron diffraction method (cRED), the structure of MIP-209(Ti)-NO_2 crystalizes in a hexagonal space group $P6_3/mmc$ with unit cell parameters of a = 22.3854 Å, c = 16.5906 Å and V= 7199.83 $Å^3$. Indeed, MIP-209(Ti) is obtained along solvothermal conditions in pure acetic acid. Alternatively, it was also possible to tune the composition of its Ti_{12}-oxocluster, similarly to MIP-177(Ti)_LT, to reach higher chemical stability. For instance, substitution of Ti^{4+} by 5% Cr^{3+} doping could favorably enhance the water stability, where crystallinity and porosity were maintained after soaking the solid in water for at least 7 days. Given the enhanced water stability and unique physical properties on MIP-209(Ti-Cr)-NO_2, photocatalytic hydrogen evolution from overall water splitting (OWS) reaction has been evaluated under simulated sunlight irradiation. MIP-209(Ti-Cr)-NO_2 displayed a significantly high hydrogen production rate with good reusability and stability in presence of methanol as scavenger under simulated sunlight irradiation, which exhibited fourfold (5812 µmol of H_2/gcat in 5 hours) enhanced hydrogen production, compared with the benchmark MOF IEF-11 (1391 µmol of H_2/gcat in 5 hour). Besides that, MIP-209(Ti-Cr)-NO_2 without any noble metal exhibits threefold enhanced hydrogen production (681 µmol of H_2/gcat in 5 hours) in OWS reaction under simulated solar light irradiation, in comparison with IEF-11 (220 µmol of H_2/gcat in 5 hours).

5.2 Results

5.2.1 Synthesis and structure solution

MIP-209(Ti)-NO_2 was prepared through a one-step green solvothermal reaction by mixing titanium (IV) isopropoxide, 2-nitro-terephthalic acid in acetic acid. The mixture was heated at 150ºC for *ca.* 30 hours before being filtered at room temperature. The solid was then washed in warm (60°C) ethanol, filtered and air-dried to yield MIP-209(Ti)-NO_2 (0.5 g, 23% yield based on ligand) as off-white microcrystalline powder. Powder X-ray diffraction (PXRD) patterns and scanning electron microscopy (SEM) (Fig. S1-2) images, has shown the gradual crystallization of MIP-209(Ti)-NO_2 with optimal formation after 30 hours synthesis in the described conditions. The high thermal stability (>300ºC) was confirmed by variable temperature PXRD and thermogravimetric analysis (TGA) in O_2, (Fig. S3-4). Nitrogen porosimetry data collected at 77 K gave a Brunauer-Emmett-Teller (BET) area of 830(10) $m^2 g^{-1}$ and a free pore volume of 0.31(7) $cm^3 g^{-1}$ (Fig. S5). It is to be noted that the color change occurred when the powder was activated at different temperatures under vacuum condition (Fig. S6), which might result from a partial conversion of -NO_2 to -NH_2. Besides, MIP-209(Ti)-NO_2 was further characterized by Fourier transform infrared spectroscopy (FT-IR) showing that there is still residual trace of free carboxylic group from the tiny absorbance band of C=O between 1715-1750 cm^{-1} (Fig. S7). CO_2 and water sorption were also measured at 298 K. The near-liner CO_2 adsorption demonstrated there existed no efficient CO_2 confinement within the micropores, and the S-shaped water adsorption isotherms showed MIP-209(Ti)-NO_2 exhibits a relatively slight hydrophobic behavior which may be accounted to the methyl group of acetates moieties (Fig. S8-9).

As initial attempts to solve the structure from high resolution PXRD did not lead to a satisfying structure solution, consequence of the presence of nanoparticles of 100-350 nm in length and 25-100 nm in width according to SEM, we first investigated the local arrangement of the titanium atoms by high-energy synchrotron X-rays pair distribution function (PDF) analysis. Firstly, we compared the local organization with the one of MIP-177(Ti)_LT, which bears $Ti_{12}O_{15}$ clusters, after collecting suitable X-ray data in the same conditions prior to the PDF analysis of both MOFs. The two functions overlap well in the short-range distances (below 6.15 Å) (Fig. 1A), indicating that the IBU of the new MOF is indeed made of $Ti_{12}O_{15}$ clusters. In a second step, we tentatively solved the structure of MIP-209(Ti)-NO_2 by continuous rotation electron diffraction (cRED). A dataset with good enough quality was collected on an isolated nanocrystal via cRED, which used the 2D ED patterns to reconstruct the 3D reciprocal space (Fig. 1B). The rotation range, resolution and completeness are specified in Table S1. The 3D electron density map gives well-identified atomic positions for the $Ti_{12}O_{15}$ oxoclusters and the nitro-terephthalate ligands. Therefore, the whole framework of MIP-209(Ti)-NO_2 was derived from the structure solution step using the charge flipping method with atomic scattering factors for electrons (Fig. 1C). The obtained model was kinematically refined against the cRED data. Calculating difference Fourier maps after each set of refinement cycles enables the localization of some of the missing atoms such as bridging oxygen atoms in the $Ti_{12}O_{15}$ oxoclusters and the nitrogen atom of the ligand's NO_2 groups. For the latter, the occupancy was refined and then fixed to 1/2, indicating that the NO_2 is disordered in two opposite ortho positions on the aromatic ring (Fig. S10). The atomic displacement parameters (ADP) of all atoms were refined isotropically, they were restrained to similar values for the Ti, C, O and N atoms independently. As expected for 3D ED data (due to dynamical scattering effects), the R-factors converge to high values (wR(obs) = 24.2%; wR(all) = 44.3%), but are relatively good values for kinematically treated electron diffraction data. As depicted in Fig. 1D, the structure of MIP-209(Ti)-NO_2 was finally validated, in combination with Rietveld refinement from the laboratory high-resolution PXRD data and the simulated pattern from the final ED model. The model from PXRD refinement contains some solvent molecules in the pores, which are shown as the residual electron density in Fig.1C. It is interesting to note that, the use of PDF analysis proved itself as an excellent method to further help the establishment of the ED model, providing precise and local information on the short inter-atomic distances in the inorganic Ti oxocluster.

As shown in Fig. 2A, the $Ti_{12}O_{15}$ oxoclusters in MIP-209(Ti)-NO_2 are connected to 12 terephthalate groups (gray color) bridging with neighboring Ti_{12}-oxoclusters and coordinate three acetate moieties (green color). Viewing the structure, a small cage (purple color) is consisted by five $Ti_{12}O_{15}$ cluster and 12 BDC-NO_2 ligands, all disordered NO_2 groups point to the center of the small cage. Besides, the methyl groups of the residual acetate moieties on the belt of $Ti_{12}O_{15}$ cluster results in the relatively slight hydrophobicity of MIP-209(Ti)-NO_2 framework. The main difference between the structures of MIP-177(Ti)_LT and MIP-209(Ti)-NO_2 lies on the linear and zig-zag shaped connectivity between adjacent $Ti_{12}O_{15}$ oxocluster SBUs bridging two terephthalate ligands (Fig. 2B), which results in a 3D structure with 1D nano-sized hexagonal channels along the *c* axis (Fig. 2C).

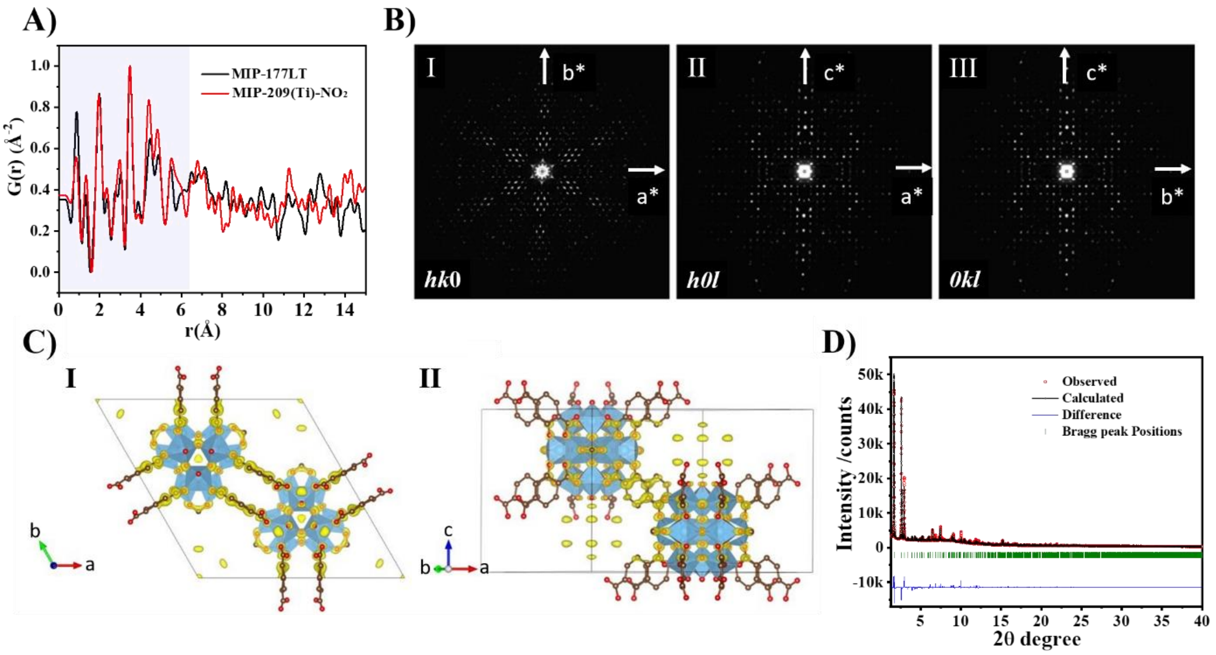

Figure 1: Structural determination of MIP-209(Ti)-NO_2. A) Synchrotron X-ray PDF data of MIP-209(Ti)-NO_2 and MIP-177(Ti)_LT. The constituents of MIP-177(Ti)_LT, $Ti_{12}O_{15}$ oxocluster has the maximum Ti-Ti distance (6.15 Å) in the oxocluster (the purple region); B) 2D slices of the 3D reciprocal space (I) *hk*0, (II) *h*0*l* and (III) 0*kl* obtained from the cRED dataset; C) I) view along [001] and II) view along an axis perpendicular to [001] of the Fourier potential map of MIP-209(Ti)-NO_2 and overlaid atomic model. Color code: Ti is shown in blue, C in brown and O in red. Atoms shown are those assigned first in structure solution by charge flipping; D) The crystal structure refinement by the Rietveld method from the laboratory high-resolution PXRD pattern (Cu Kα radiation $\lambda = 1.5406$ Å).

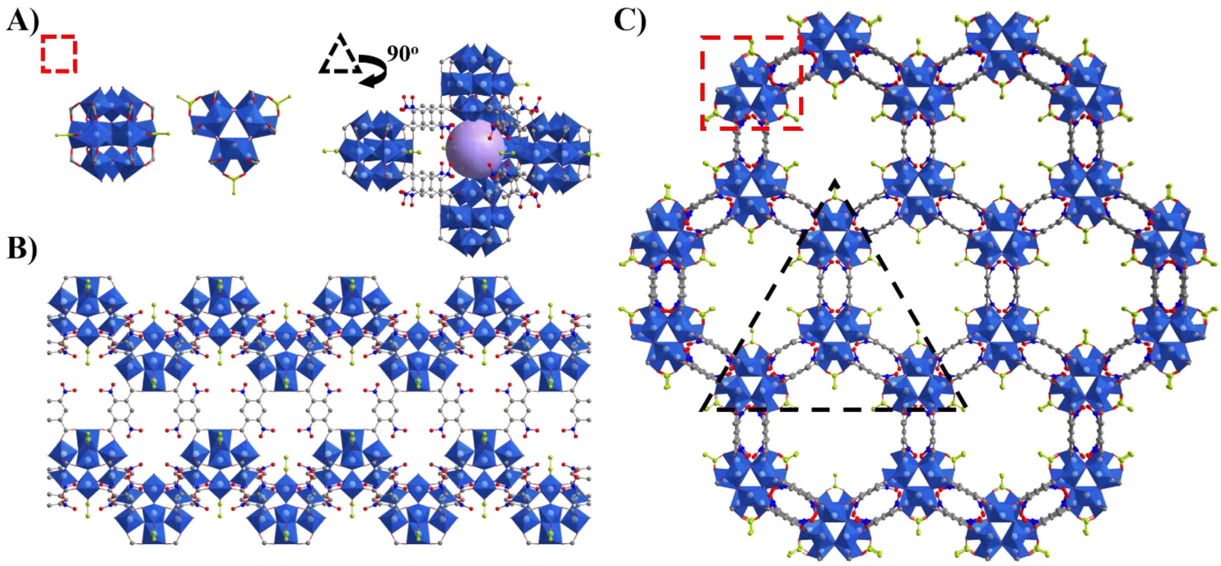

Figure 2: The crystal structure of MIP-209(Ti)-NO_2. A) $Ti_{12}O_{15}$ oxocluster IBU in red square frame and the small cage (purple) in black triangle frame; B) Zig-zag connectivity between $Ti_{12}O_{15}$ oxoclusters and BDC-NO_2 ligands; C) 3D structure viewed along the c axis with nano-sized hexagonal channels. (The figures showed the BDC-NO_2 with 2 nitro on 2 ortho positions.)

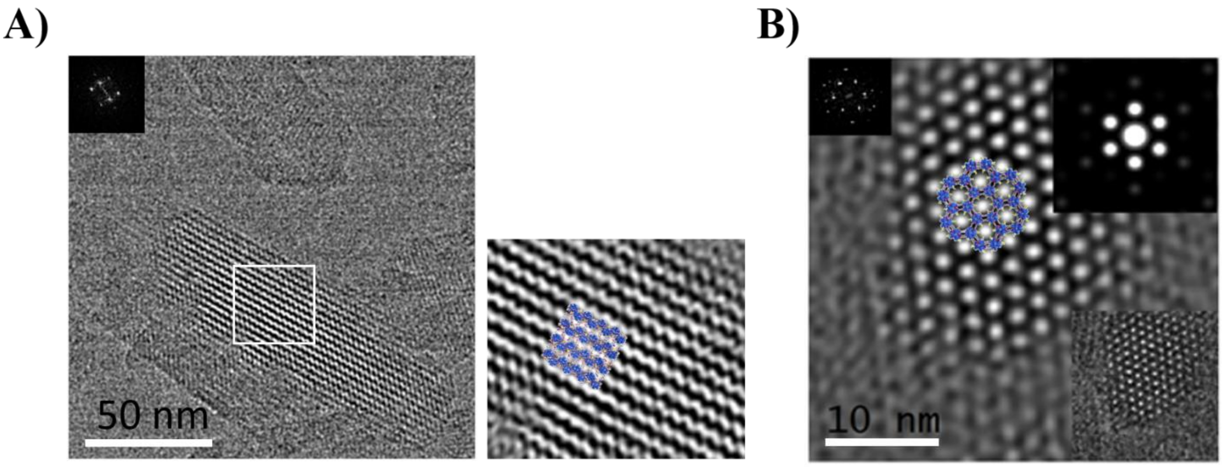

Figure 3: The filtered HRTEM images of MIP-209(Ti)-NO_2. A) The [100] plane, displayed the zig-zag $Ti_{12}O_{15}$ oxoclusters. B) The [001] plane displayed the 1D hexagonal channel. The images were overlapped well by the structural model from [100] and [001] plane.

Imaging the particles of the MOF using low-dose conditions was employed to further confirm the ED model obtained as well (Fig. S11-12, Table S2). Compared to the structural model along a certain crystallographic orientation, the high-resolution images of the surface of a particle oriented in this same orientation enable a first qualitative validation of the structure. Indeed, HRTEM images allowed us to visualize the $Ti_{12}O_{15}$ oxoclusters adopting the same zig-zag arrangements observed at the surface of a [100] axis particle (Fig. 3A). Similarly, the hexagonal-symmetry channels along the [001] axis can be observed as bright discs at the surface of a [001] axis particle (Fig. 3B). Moreover, from the several particles found along the [001] axis, the visualization channels enable the measurement of their diameters using a profile line along the row of bright spots on the images (Fig. S13). The average diameter measured is 1.1 nm which corroborates with the value found from the nitrogen adsorption isotherm at 77 K. The second quantitative information is the unit cell parameters determination. For a hexagonal crystal system, the small deviations (%) observed for a and c (Table S3), demonstrates the unit cell parameters calculated from low-dose HRTEM, refinement of the powder diffraction data (Rietveld method) and electron diffraction data, are all in very good agreements.

Interestingly, as a preliminary attempt, following slightly similar synthetic conditions (Synthetic details are given in the Supporting Information) the use of 2,5-dicholrotherephthalic acid yielded the isostructural phase MIP-209(Ti)-2Cl as revealed from the PXRD patterns (Fig. S14). Although a similar pore size is estimated from DFT pore size calculations, the experimental N_2 uptake at 77 K is significantly lower than expected (Fig. S15-16), likely to be due to residual impurities such as TiO_2, calling for further synthesis optimization. If all other attempts to produce similar structures using other functionalized 1,4-BDC ligands did not result in crystalline solids, MIP-209(Ti) represents however a very scare example of isostructural Ti-MOF platform achieved using functional terephthalate ligands.

When analyzing the differences in terms of IBU for Ti-MOFs (Table S4), it is clear that any attempt to correlate relate them with differences in terms of synthesis conditions is still highly challenging. Ti carboxylate based MOFs are constructed either from Ti_3 to Ti_{12} oxoclusters or infinite chains of corner-sharing of Ti octahedra or more complex Ti_6 chains. When it turns to Ti_8 or Ti_{12} IBUs, the resulting MOFs are obtained in pure acid solvent solvothermal conditions while these IBUs combine carboxylates from the ligands and bridging or chelating formates or acetates. In the case of TiO chains or Ti_6O_9 nanowire chains based MOFs, these are obtained in pure organic solvents solvothermal conditions (DMF, DEF, alcohols) without any formic or acetic acid that might compete for the chelation of the Ti species. In the case of lower nuclearity Ti clusters based MOFs such as Ti_3 or Ti_7, these have been obtained using mixtures of organic solvent and acids as modulators. This is still not enough to establish a rational. However, until recently any new Ti carboxylate MOF exhibited a new IBU,[7] but the very recent appearance of several Ti-MOFs bearing the same IBU (Ti_{12} clusters, Ti_6 chains) suggests the existence of chemical keys that have still to be deciphered in order to develop rational design strategies of Ti-MOFs.

5.2.2 Modification of the inorganic moiety

The chemical (as well as photochemical) stability of MIP-209(Ti)-NO_2 was evaluated in view of its potential applications such as in photocatalysis. After exposing the solid (20 mg/mL) in different solvents for 24 h/7 days (Table S5), PXRD patterns revealed however a significant decrease in crystallinity (e.g., particle size decrease) and/or possible structural degradation (Fig. 4A, red curves, Fig. S17, 7D and 7Ds stands for 7 days without and with stirring, respectively). The FT-IR spectral analyses showed the generation of free carboxylic ligands when soaked into warm water or strong acids (Fig. S18). Nitrogen porosity measurements (N_2 at 77 K) (Fig. 4B, red curves, Fig. S19) revealed a 14-19% decrease of uptake compared with MIP-209(Ti)-NO_2 before treatment. To overcome this lack of chemical stability, we decided to dope the MOF. The doping strategy with transition metal elements on the inorganic $Ti_{12}O_{15}$ cluster moiety has been rarely reported[32,52], nevertheless, the low water exchange constants of Cr^{3+} ions is a promising transition metal candidate to enhance the water stability of MIP-209(Ti)[53,54]. This, together with the proven ability of metal ions substitution onto the Ti_{12}-oxocluster of MIP-177(Ti)_LT,[32] lead us to investigate the doping of the Ti-MOF through the direct synthesis relying on diverse chromium metal precursors like $Cr(NO_3)_3$, $CrCl_3$, while tuning the order of addition of each chemical, and other reaction conditions. Here a Cr-doped MIP-209(Ti)-NO_2 sample, named as MIP-209(Ti-Cr)-NO_2, was obtained by one-pot synthesis procedure and analysed by several characterization methods (Fig. S20-22). A 5 at% Cr doped MIP-209(Ti-Cr)-NO_2 could be obtained showed with a very good reproducibility as shown by PXRD analysis. The sample purity was further assessed through a combination of advanced characterizations, namely HRTEM mapping and energy-dispersed X-ray spectroscopy (EDX) (Fig. S23-25). Unfortunately, the MIP-209(Ti-Cr)-NO_2 sample existed around 6 wt% titanium oxide impurity, as estimated from TGA. Note that this oxide impurity exhibited about one order of magnitude less Cr element (0.5 at%) compared to the doped MOF as shown from HRTEM mapping.

The good water stability of MIP-209(Ti-Cr)-NO_2 was demonstrated under different conditions (Table S5-6). In contrast with MIP-209(Ti)-NO_2, MIP-209(Ti-Cr)-NO_2 displayed relatively higher water tolerance and kept the high porosity after the same condition treatment. As observed by PXRD analysis (Fig. 4A, green curves), the peak intensity was kept indicating confirming the positive role of the Cr doping. Nitrogen-porosimetry measurements further confirmed the increase of stability. The BET area and free pore volume of MIP-209(Ti-Cr)-NO_2 after 7days water treatment at room temperature (Table S7) was even slightly higher than pristine MIP-209(Ti)-NO_2 and MIP-209(Ti-Cr)-NO_2. The slight (positive) deviation is probably ascribed to the removal of free residual ligand or acetates after soaking the MOF for such a long period of time. To better understand this, a series of characterizations, including FT-IR, TGA, ^{1}H nuclear magnetic resonance, and SEM/EDX energy-dispersed X-ray spectroscopy (Fig. S26-33), confirmed this hypothesis with the release of ligands and acetates from MIP-209(Ti-Cr)-NO_2 during this water treatment, respectively, as shown in Fig. S34, leading to an increase of the pore volume and surface area. Motivated by the enhanced water stability and the tuning of the photo-related chemical and physical properties of MIP-209(Ti-Cr)-NO_2, photocatalytic hydrogen evolution in water was investigated.

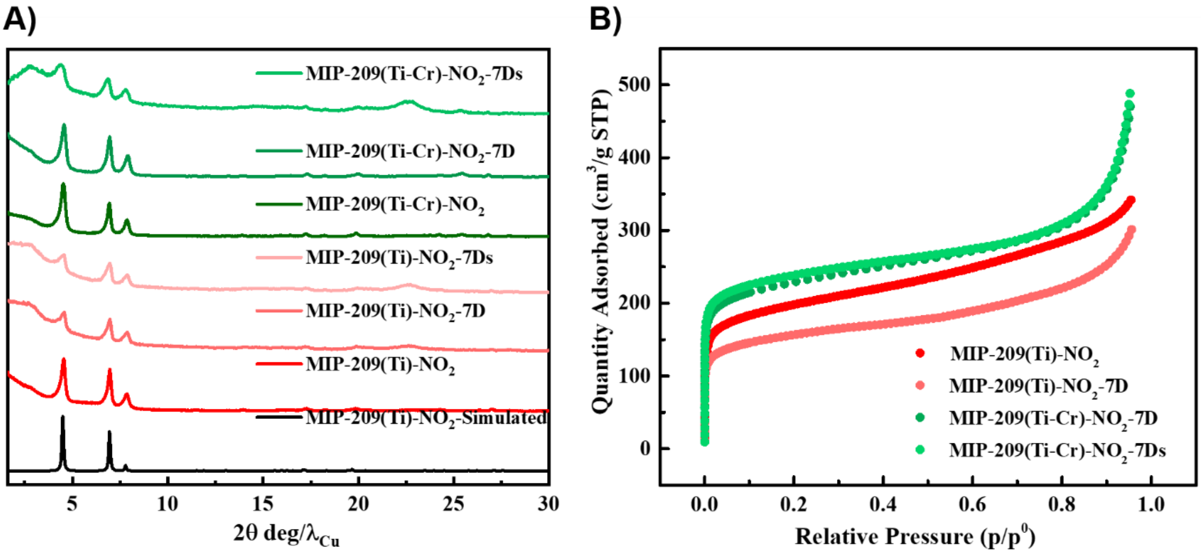

Figure 4: Water stability test results of MIP-209(Ti)-NO_2 and MIP-209(Ti-Cr)-NO_2. A) PXRD patterns and B) nitrogen adsorption isotherms before and after water treatment with or without stirring conditions. (The hump at 22.5 degree observed from PXRD patterns comes from the hold paper sample holder)

5.2.3 Photocatalytic hydrogen evolution

Regarding the photocatalytic activity, one important information that indicates which are the photos absorbed by the material is the UV-vis absorption spectra. These absorption spectra of MIP-209(Ti)-NO_2 and MIP-209(Ti-Cr)-NO_2 recorded in the diffuse reflectance mode were presented in Fig. S35. The optical band gaps of MIP-209(Ti)-NO_2 and MIP-209(Ti-Cr)-NO_2 were simulated to be 3.46 and 3.34 eV by Tauc plots, respectively (Fig. S36). This result indicated that Cr doping strategy could slightly narrow the band gap of MIP-209(Ti)-NO_2, thus increasing the light trapping ability. The composition and oxidation state of the elements in the materials have been confirmed by X-ray photoelectron spectroscopy (XPS), as shown in Fig. S37-38. The C1s spectrum shows the characteristic signals of the nitro-terephthalate ligand, characterized by C-N (287 eV). Note here that the high C=O energy value (288 eV) might correspond to some remaining acetate moieties from the synthesis. The O1s spectrum exhibits a main band at about 531.8 eV, characteristic of the oxygen atoms presents in the carboxylate or nitro groups. The N 1s spectrum is characteristic of the C-N (399.3 eV) and N-O (405.2 eV) of the nitro group present in the MIP-209(Ti). The Ti2p spectrum shows two bands attributable to the $Ti2p^{1/2}$ (458.4 eV) and $Ti2p^{3/2}$ bands (464.1 eV), characteristic of the Ti^{4+} ions present in the $Ti_{12}O_{15}$ oxocluster. The Cr2p is attributable to the presence of Cr^{3+} and Cr^{4+} ions in the SBU, as revealed by the $Cr2p^{3/2}$ (577.14 eV). Furthermore, the valence band energy maximum of MIP-209(Ti)-NO_2 and MIP-209(Ti-Cr)-NO_2 was estimated by XPS from the intersection of a linear fit to the linear portion of the electron emission edge and the background (Fig. S39A-B). The obtained value corresponds to the valence band maximum energy versus the Fermi level (E^f_υ). The valence band position vs the NHE (E_υ^{NHE}) can be obtained from the following equation: $E_\upsilon^{NHE} = E^f_\upsilon + \phi_{sp} - 4.44$, where ϕ_{sp} is the work function of the spectrometer with the value 4.244 eV. From this $E\upsilon^{NHE}$ value and the band gap, the conduction band energy minimum (E_c^{NHE}) can be determined. As shown in Fig. S39C, both can meet the thermodynamic prerequisites to be used as photocatalysts for the OWS. Especially, MIP-209(Ti-Cr)-NO_2 exhibits a slightly lower band gap and more positive lowest unoccupied crystal orbital (LUCO) value in comparison with MIP-209(Ti)-NO_2. Because Cr doping strategy on Ti-MOF can replace the Ti atoms in the lattice with oxygen vacancy compensation, distribute homogeneously in the framework of TiO_2 crystals, and may make the n-type TiO_2 less n-type or more p-type due to the resultant formation of oxygen vacancies, resulting in absorption of visible light, decrease of the intensity of Photoluminescence (PL) emission and prolonged lifetime of photo-generated charge carriers.

Motivated by aforementioned properties of MIP-209(Ti) materials, the photocatalytic hydrogen evolution reaction (HER) and overall water splitting (OWS) experiments were carried out under simulated sunlight irradiation at 20°C. To make a clear comparison with MIP-209(Ti) materials, pure anatase solid was firstly used as photocatalyst for HER in the presence of methanol as a scavenger due to tiny of anatase impurity existed in MIP-209(Ti-Cr)-NO_2 sample. We subsequently evaluated the activity of MIP-209(Ti)-NO_2, and MIP-209(Ti-Cr)-NO_2 for HER under the same conditions, as shown in Fig. 5A. Although MIP-209(Ti)-NO_2 showed significant activity in both HER (*ca.* 4750 μmol H_2/gcat in 5 hours) and OWS (*ca.* 325 μmol H_2/gcat in 5 hours) reactions, the real active species are unclear once MOF loses its crystallinity. Interestingly, MIP-209(Ti-Cr)-NO_2 also exhibited a significant hydrogen production (5812 μmol H_2/gcat), which exhibited fourfold enhanced hydrogen production, in comparison with the current promising IEF-11 framework (1391 μmol H_2/gcat) in 5 hours (studies conducted under similar experimental conditions). Even though pure anatase was active for HER (2609 μmol H_2/gcat), we believe the major activity is attributed to MIP-209 (Ti-Cr)-NO_2 for this reaction, because the quantity of anatase impurity in that sample was only around 6 wt%. However, one cannot exclude any synergetic effect of interfaced TiO_2/MIP-

209(Ti-Cr). In OWS reactions (water, without methanol as a scavenger), MIP-209(Ti-Cr)-NO_2 without precious metal nanoparticles exhibits high hydrogen production (681 µmol H_2/gcat) under simulated solar light irradiation (Fig. 5B). In addition, compared with MOF-derived photocatalysts with precious metal, MIP-209(Ti) photocatalysts, may significantly decrease the overall cost of the catalyst. Noteworthy, MIP-209(Ti-Cr)-NO_2 after 3 times use for HER tests kept a better crystallinity (Fig. S40A), in comparison with MIP-209(Ti)-NO_2. Additionally, if MIP-209(Ti)-NO_2 became totally amorphous solid after the OWS test, MIP-209(Ti-Cr)-NO_2 still displayed some crystallinity, although low (Fig. S40B), in agreement with the promotion effect of Cr doping on the stability. The ongoing research is to better understand not only the chemical keys to better control the chemistry of Ti-MOFs but also to better assess the effect of TiO_x on the photocatalytic activity by performing additional tests on MIP-209(Ti-Cr)-NO_2 with different degrees of Ti oxide impurity and by trying to prepare the pure Cr-doped TiO_2 for the comparison.

To clarify the versatility of MIP-209(Ti) as the second Ti_{12} oxocluster based framework, transition metal doping strategy, isostructural property and photocatalytic hydrogen production tests have been investigated carefully, motivated by the excellent photo-responsive performance of MIP-177(Ti)_LT[32,55].

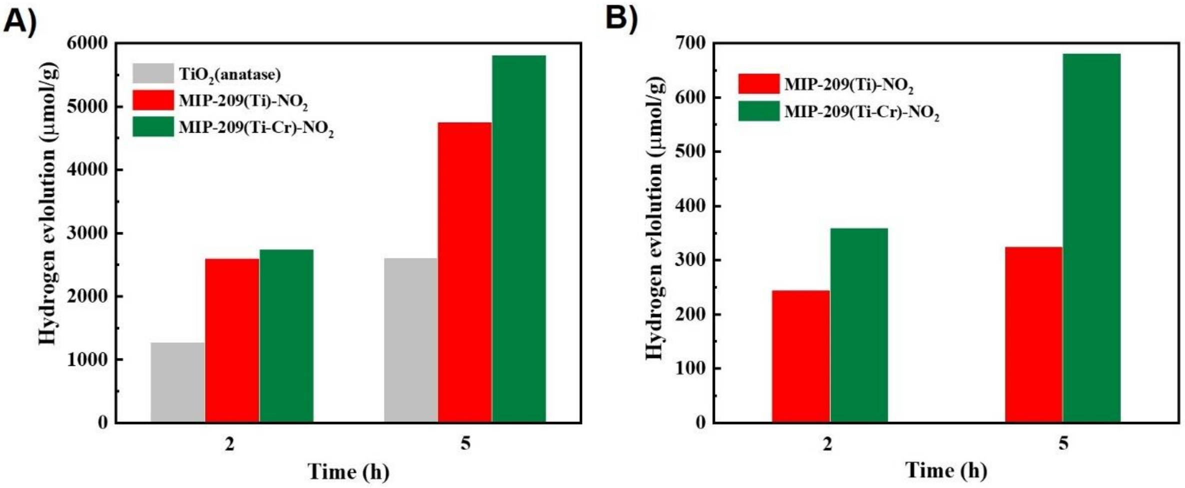

Figure 5: Photocatalytic performance of MIP-209(Ti)-NO_2 and MIP-209(Ti-Cr)-NO_2. (A) Photocatalytic HER in the presence of methanol under simulated sunlight irradiation, in comparison with anatase. (B) Photocatalytic overall water splitting under simulated sunlight irradiation.

5.2.4 Simulation or mechanism of photocatalytic reaction

The photocatalytic mechanism is being studied with our collaborator (Prof. G. MAURIN).

5.3 Conclusion

A novel isostructural Ti-MOF, MIP-209(Ti), bearing $Ti_{12}O_{15}$ oxoclusters and terephthalate derivatives, has been obtained via a green solvothermal synthesis route. Through a combination of the synchrotron PDF analysis, cRED technique, and HRTEM, the structure of MIP-209(Ti) was successfully determined and refined using high-resolution PXRD. Due to the tunability of the inorganic building unit, Cr element was doped uniformly in the framework which enhanced the water stability for the potential photocatalytic hydrogen production in water. We observed that this material demonstrated a significantly high hydrogen production rate with relatively good reusability and stability in HER and OWS reactions under simulated sunlight irradiation. This work represents another leap forward in the rational design of porous functional Ti-MOFs, and their related photo-responsive applications.

5.4 References

(1) Wang, Q.; Domen, K. Particulate Photocatalysts for Light-Driven Water Splitting: Mechanisms, Challenges, and Design Strategies. *Chemical Reviews* **2020**, *120*, 919-985.

(2) Chen, S.; Takata, T.; Domen, K. Particulate photocatalysts for overall water splitting. *Nature Reviews Materials* **2017**, *2*, 17050.

(3) Tao, X.; Zhao, Y.; Wang, S.; Li, C.; Li, R. Recent advances and perspectives for solar-driven water splitting using particulate photocatalysts. *Chemical Society Reviews* **2022**, *51*, 3561-3608.

(4) Rahman, M. Z.; Edvinsson, T.; Gascon, J. Hole utilization in solar hydrogen production. *Nature Reviews Chemistry* **2022**, *6*, 243-258.

(5) Jaryal, R.; Kumar, R.; Khullar, S. Mixed metal-metal organic frameworks (MM-MOFs) and their use as efficient photocatalysts for hydrogen evolution from water splitting reactions. *Coordination Chemistry Reviews* **2022**, *464*, 214542.

(6) Chen, X.; Liu, L.; Yu, P. Y.; Mao, S. S. Increasing Solar Absorption for Photocatalysis with Black Hydrogenated Titanium Dioxide Nanocrystals. *Science* **2011**, *331*, 746-750.

(7) Assi, H.; Mouchaham, G.; Steunou, N.; Devic, T.; Serre, C. Titanium coordination compounds: from discrete metal complexes to metal–organic frameworks. *Chemical Society Reviews* **2017**, *46*, 3431-3452.

(8) Li, L.; Wang, X.-S.; Liu, T.-F.; Ye, J. Titanium-Based MOF Materials: From Crystal Engineering to Photocatalysis. *Small Methods* **2020**, *4*, 2000486.

(9) Yan, Y.; Li, C.; Wu, Y.; Gao, J.; Zhang, Q. From isolated Ti-oxo clusters to infinite Ti-oxo chains and sheets: recent advances in photoactive Ti-based MOFs. *Journal of Materials Chemistry A* **2020**, *8*, 15245-15270.

(10) Kolobov, N.; Goesten, M. G.; Gascon, J. Metal–Organic Frameworks: Molecules or Semiconductors in Photocatalysis? *Angewandte Chemie International Edition* **2021**, *60*, 26038-26052.

(11) Serre, C.; Férey, G. Hybrid Open Frameworks. 8. Hydrothermal Synthesis, Crystal Structure, and Thermal Behavior of the First Three-Dimensional Titanium(IV) Diphosphonate with an Open Structure: Ti3O2(H2O)2(O3P−(CH2)−PO3)2·(H2O)2, or MIL-22. *Inorganic chemistry* **1999**, *38*, 5370-5373.

(12) Serre, C.; Férey, G. Hydrothermal Synthesis and Structure Determination from Powder Data of New Three-Dimensional Titanium(IV) Diphosphonates Ti(O3P−(CH2)n−PO3) or MIL-25n (n = 2, 3). *Inorganic chemistry* **2001**, *40*, 5350-5353.

(13) Serre, C.; Groves, J. A.; Lightfoot, P.; Slawin, A. M. Z.; Wright, P. A.; Stock, N.; Bein, T.; Haouas, M.; Taulelle, F.; Férey, G. Synthesis, Structure and Properties of Related Microporous N,N‘-Piperazinebismethylenephosphonates of Aluminum and Titanium. *Chemistry of Materials* **2006**, *18*, 1451-1457.

(14) Meyer, K.; Ranocchiari, M.; van Bokhoven, J. A. Metal organic frameworks for photo-catalytic water splitting. *Energy & Environmental Science* **2015**, *8*, 1923-1937.

(15) Nguyen, H. L. Metal–organic frameworks for photocatalytic water splitting. *Solar RRL* **2021**, *5*, 2100198.

(16) Li, R.; Zhang, W.; Zhou, K. Metal–organic-framework-based catalysts for photoreduction of CO2. *Advanced Materials* **2018**, *30*, 1705512.

(17) Lu, L.; Wu, B.; Shi, W.; Cheng, P. Metal–organic framework-derived heterojunctions as nanocatalysts for photocatalytic hydrogen production. *Inorganic Chemistry Frontiers* **2019**, *6*, 3456-3467.

(18) McNamara, N. D.; Neumann, G. T.; Masko, E. T.; Urban, J. A.; Hicks, J. C. Catalytic performance and stability of (V) MIL-47 and (Ti) MIL-125 in the oxidative desulfurization of heterocyclic aromatic sulfur compounds. *Journal of catalysis* **2013**, *305*, 217-226.

(19) Wang, H.; Yuan, X.; Wu, Y.; Zeng, G.; Chen, X.; Leng, L.; Li, H. Synthesis and applications of novel graphitic carbon nitride/metal-organic frameworks mesoporous photocatalyst for dyes removal. *Applied Catalysis B: Environmental* **2015**, *174*, 445-454.

(20) Remiro-Buenamanana, S.; Cabrero-Antonino, M.; Martinez-Guanter, M.; Alvaro, M.; Navalon, S.; Garcia, H. Influence of co-catalysts on the photocatalytic activity of MIL-125 (Ti)-NH2 in the overall water splitting. *Applied Catalysis B: Environmental* **2019**, *254*, 677-684.

(21) Salcedo-Abraira, P.; Babaryk, A. A.; Montero-Lanzuela, E.; Contreras-Almengor, O. R.; Cabrero-Antonino, M.; Grape, E. S.; Willhammar, T.; Navalón, S.; Elkäim, E.; García, H. A Novel Porous Ti-Squarate as Efficient Photocatalyst in the Overall Water Splitting Reaction under Simulated Sunlight Irradiation. *Advanced Materials* **2021**, *33*, 2106627.

(22) An, Y.; Xu, B.; Liu, Y.; Wang, Z.; Wang, P.; Dai, Y.; Qin, X.; Zhang, X.; Huang, B. Photocatalytic Overall Water Splitting over MIL-125 (Ti) upon CoPi and Pt Co-catalyst Deposition. *ChemistryOpen* **2017**, *6*, 701-705.

(23) Li, C.; Xu, H.; Gao, J.; Du, W.; Shangguan, L.; Zhang, X.; Lin, R.-B.; Wu, H.; Zhou, W.; Liu, X. Tunable titanium metal–organic frameworks with infinite 1D Ti–O rods for efficient visible-light-driven photocatalytic H 2 evolution. *Journal of Materials Chemistry A* **2019**, *7*, 11928-11933.

(24) Song, Y.; Li, Z.; Zhu, Y.; Feng, X.; Chen, J. S.; Kaufmann, M.; Wang, C.; Lin, W. Titanium hydroxide secondary building units in metal–organic frameworks catalyze hydrogen evolution under visible light. *Journal of the American Chemical Society* **2019**, *141*, 12219-12223.

(25) Wang, X.; Zhang, X.; Zhou, W.; Liu, L.; Ye, J.; Wang, D. An ultrathin porphyrin-based metal-organic framework for efficient photocatalytic hydrogen evolution under visible light. *Nano Energy* **2019**, *62*, 250-258.

(26) Kolobov, N.; Zaki, A.; Świrk, K.; Maity, P.; Garzon-Tovar, L.; Angeli, G. K.; Dikhtiarenko, A.; Delahay, G.; Trikalitis, P. N.; Emwas, A.-H. Understanding Photocatalytic Activity Dependence on Node Topology in Ti-Based Metal–Organic Frameworks. *ACS Materials Letters* **2023**, *5*, 1481-1487.

(27) Freund, R.; Zaremba, O.; Arnauts, G.; Ameloot, R.; Skorupskii, G.; Dincă, M.; Bavykina, A.; Gascon, J.; Ejsmont, A.; Goscianska, J. The current status of MOF and COF applications. *Angewandte Chemie International Edition* **2021**, *60*, 23975-24001.

(28) Melillo, A.; Cabrero-Antonino, M.; Navalon, S.; Alvaro, M.; Ferrer, B.; Garcia, H. Enhancing visible-light photocatalytic activity for overall water splitting in UiO-66 by controlling metal node composition. *Applied Catalysis B: Environmental* **2020**, *278*, 119345.

(29) Yuan, S.; Qin, J.-S.; Xu, H.-Q.; Su, J.; Rossi, D.; Chen, Y.; Zhang, L.; Lollar, C.; Wang, Q.; Jiang, H.-L. [Ti8Zr2O12 (COO) 16] Cluster: an ideal inorganic building unit for photoactive metal–organic frameworks. *ACS central science* **2018**, *4*, 105-111.

(30) Hong, K.; Chun, H. Unprecedented and highly symmetric (6, 8)-connected topology in a porous metal–organic framework through a Zn–Ti heterometallic approach. *Chemical Communications* **2013**, *49*, 10953-10955.

(31) Fang, W.-H.; Zhang, L.; Zhang, J. Synthetic strategies, diverse structures and tuneable properties of polyoxo-titanium clusters. *Chemical Society Reviews* **2018**, *47*, 404-421.

(32) Wang, S.; Kitao, T.; Guillou, N.; Wahiduzzaman, M.; Martineau-Corcos, C.; Nouar, F.; Tissot, A.; Binet, L.; Ramsahye, N.; Devautour-Vinot, S. A phase transformable ultrastable titanium-carboxylate framework for photoconduction. *Nature communications* **2018**, *9*, 1-9.

(33) Wang, S.; Reinsch, H.; Heymans, N.; Wahiduzzaman, M.; Martineau-Corcos, C.; De Weireld, G.; Maurin, G.; Serre, C. Toward a rational design of titanium metal-organic frameworks. *Matter* **2020**, *2*, 440-450.

(34) Wang, S.; Cabrero-Antonino, M.; Navalón, S.; Cao, C.-c.; Tissot, A.; Dovgaliuk, I.; Marrot, J.; Martineau-Corcos, C.; Yu, L.; Wang, H. A robust titanium isophthalate metal-organic framework for visible-light photocatalytic CO2 methanation. *Chem* **2020**, *6*, 3409-3427.

(35) Wang, S.; Chen, L.; Wahiduzzaman, M.; Tissot, A.; Zhou, L.; Ibarra, I. A.; Gutiérrez-Alejandre, A.; Lee, J. S.; Chang, J.-S.; Liu, Z. A mesoporous zirconium-isophthalate multifunctional platform. *Matter* **2021**, *4*, 182-194.

(36) Zlotea, C.; Phanon, D.; Mazaj, M.; Heurtaux, D.; Guillerm, V.; Serre, C.; Horcajada, P.; Devic, T.; Magnier, E.; Cuevas, F. Effect of NH 2 and CF 3 functionalization on the hydrogen sorption properties of MOFs. *Dalton transactions* **2011**, *40*, 4879-4881.

(37) Fu, Y.; Sun, D.; Chen, Y.; Huang, R.; Ding, Z.; Fu, X.; Li, Z. An amine-functionalized titanium metal–organic framework photocatalyst with visible-light-induced activity for CO2 reduction. *Angewandte Chemie International Edition* **2012**, *51*, 3364-3367.

(38) Bryant, J. T.; Logan, M. W.; Chen, Z.; Djokic, M.; Cairnie, D. R.; Vazquez-Molina, D. A.; Nijamudheen, A.; Langlois, K. R.; Markley, M. J.; Pombar, G. Synergistic Steric and Electronic Effects on the Photoredox Catalysis by a Multivariate Library of Titania Metal–Organic Frameworks. *Journal of the American Chemical Society* **2023**, *145*, 4589-4600.

(39) Nguyen, H. L.; Vu, T. T.; Le, D.; Doan, T. L.; Nguyen, V. Q.; Phan, N. T. A titanium–organic framework: engineering of the band-gap energy for photocatalytic property enhancement. *ACS Catalysis* **2017**, *7*, 338-342.

(40) Deng, H.; Doonan, C. J.; Furukawa, H.; Ferreira, R. B.; Towne, J.; Knobler, C. B.; Wang, B.; Yaghi, O. M. Multiple functional groups of varying ratios in metal-organic frameworks. *Science* **2010**, *327*, 846-850.

(41) Lerma-Berlanga, B.; Castells-Gil, J.; Ganivet, C. R.; Almora-Barrios, N.; González-Platas, J.; Fabelo, O.; Padial, N. M.; Martí-Gastaldo, C. Permanent Porosity in Hydroxamate Titanium–Organic Polyhedra. *Journal of the American Chemical Society* **2021**, *143*, 21195-21199.

(42) Keum, Y.; Park, S.; Chen, Y. P.; Park, J. Titanium-Carboxylate Metal-Organic Framework Based on an Unprecedented Ti-Oxo Chain Cluster. *Angewandte Chemie* **2018**, *130*, 15068-15072.

(43) Yuan, S.; Liu, T.-F.; Feng, D.; Tian, J.; Wang, K.; Qin, J.; Zhang, Q.; Chen, Y.-P.; Bosch, M.; Zou, L. A single crystalline porphyrinic titanium metal–organic framework. *Chemical science* **2015**, *6*, 3926-3930.

(44) Cadiau, A.; Kolobov, N.; Srinivasan, S.; Goesten, M. G.; Haspel, H.; Bavykina, A. V.; Tchalala, M. R.; Maity, P.; Goryachev, A.; Poryvaev, A. S. A titanium metal–organic framework with visible-light-responsive photocatalytic activity. *Angewandte Chemie* **2020**, *132*, 13570-13574.

(45) Dorset, D. L.; Hauptman, H. A. Direct phase determination for quasi-kinematical electron diffraction intensity data from organic microcrystals. *Ultramicroscopy* **1976**, *1*, 195-201.

(46) Dorset, D. L. Electron crystallography–accomplishments and challenges. *Acta Crystallographica Section A: Foundations of Crystallography* **1998**, *54*, 750-757.

(47) Yang, T.; Willhammar, T.; Xu, H.; Zou, X.; Huang, Z. Single-crystal structure determination of nanosized metal–organic frameworks by three-dimensional electron diffraction. *Nature Protocols* **2022**, 1-25.

(48) Smolders, S.; Willhammar, T.; Krajnc, A.; Sentosun, K.; Wharmby, M. T.; Lomachenko, K. A.; Bals, S.; Mali, G.; Roeffaers, M. B.; De Vos, D. E. A Titanium (IV)-Based Metal–Organic Framework Featuring Defect-Rich Ti-O Sheets as an Oxidative Desulfurization Catalyst. *Angewandte Chemie* **2019**, *131*, 9258-9263.

(49) Isaka, Y.; Kawase, Y.; Kuwahara, Y.; Mori, K.; Yamashita, H. Two-phase system utilizing hydrophobic metal–organic frameworks (MOFs) for photocatalytic synthesis of hydrogen peroxide. *Angewandte Chemie* **2019**, *131*, 5456-5460.

(50) Yang, Y.; Huang, W.; Guo, Z.; Zhang, S.; Wu, F.; Huang, J.; Yang, H.; Zhou, Y.; Xu, W.; Gu, S. Robust fluorine-free colorful superhydrophobic PDMS/NH2-MIL-125 (Ti)@ cotton fabrics for improved ultraviolet resistance and efficient oil–water separation. *Cellulose* **2019**, *26*, 9335-9348.

(51) Kawase, Y.; Isaka, Y.; Kuwahara, Y.; Mori, K.; Yamashita, H. Ti cluster-alkylated hydrophobic MOFs for photocatalytic production of hydrogen peroxide in two-phase systems. *Chemical Communications* **2019**, *55*, 6743-6746.

(52) Murillo, B.; Zornoza, B.; de la Iglesia, O.; Wang, S.; Serre, C.; Téllez, C.; Coronas, J. Tin-Carboxylate MOFs for Sugar Transformation into Methyl Lactate. *European Journal of Inorganic Chemistry* **2019**, *2019*, 2624-2629.

(53) Bosch, M.; Zhang, M.; Zhou, H.-C. Increasing the stability of metal-organic frameworks. *Adv. Chem* **2014**, *2014*, 1155.

(54) An, Y.; Liu, Y.; Wang, Z.; Wang, P.; Zheng, Z.; Dai, Y.; Qin, X.; Zhang, X.; Whangbo, M.-H.; Huang, B. Stabilizing the titanium-based metal organic frameworks in water by metal

cations with empty or partially-filled d orbitals. *Journal of colloid and interface science* **2019**, *533*, 9-12.

(55) García-Baldoví, A.; Del Angel, R.; Mouchaham, G.; Liu, S.; Fan, D.; Maurin, G.; Navalón, S.; Serre, C.; Garcia, H. Active site imprinting on Ti oxocluster metal–organic frameworks for photocatalytic hydrogen release from formic acid. *Energy & Environmental Science* **2023**.

Supporting Information

Experimental procedures

Chemicals

All chemicals were purchased from commercial suppliers and used as received without further purification. 2-nitro-terephthalic acid (Fluochem), dichloride-terephthalic acid (Fluochem), acetic acid (Acros), ethanol (Fisher Scientific), $Cr(NO_3)_3 \cdot 9H_2O$ and $Ti(iPrO)_4$ (Alfa Aesar).

Instruments

1) Conventional Powder X-ray Diffraction (PXRD) analysis

High-throughput Bruker D8 Advance diffractometer was used for the phase analysis working on transmission mode and equipped with a focusing Göbel mirror producing CuKα radiation (λ = 1.5418 Å) and a LynxEye detector.

2) Nitrogen porosimetry

Micromeritics Tristar/ Triflex instrument at 77 K (pre-activating samples at 200°C under vacuum, 8 hours).

3) Thermogravimetric analyses (TGA)

Mettler Toledo TGA/DSC 2, STAR System apparatus with a heating rate of 5°C min^{-1} under the oxygen flow. Mettler Toledo FiveEasyTM Plus pH / mV bench meter.

4) Infrared spectra

Nicolet iS5 FTIR ThermoFisher spectrometer.

5) Temperature dependent PXRD

PANalytical EMPYREAN diffractometer equipped with a HTK-1200N (Anton Paar) high-temperature chamber and Galipix detector (CuKα radiation). PXRD patterns were collected every 25°C from room temperature to 350°C, with two hours scan for each temperature.

6) Laboratory High-resolution X-ray powder diffraction

PANalytical EMPYREAN diffractometer with Cu Kα1 radiation (λ = 1.5406 Å) and GaliPIX3D detector. The filled 0.5 mm capillaries were measured in a transmission mode at room temperature. The crystal structure model of MIP-209(Ti) from the ED was refined using the Rietveld method with the inclusion of the water guest molecules in Fullprof software [**Physica B 192 (1993) 55-69**]. The water positions were determined by the direct space method in FOX [**J. Appl. Cryst. (2002). 35, 734−743**]

7) Scanning transmission microscopy (SEM) and energy dispersive X-ray spectroscopy

FEI Magellan 400 scanning electron microscope, the energy-dispersive X-ray spectroscopy (EDX) analysis allows performing chemical mapping using the "Super-X" systems for EDX analysis that equipped the microscope

8) Pair distribution function (PDF) analysis

The PDF data were collected at the CRISTAL beamline at the synchrotron SOLEIL using 21.3 keV (0.581502 Å) X-rays, equipped with a Mythen detector. The powder XRD data were converted to PDFs using the program PDFgetX3 [**Billinge, J. Applied Crystallography 2013, 46, 560**]. The samples were finely ground and sealed in 0.5 mm(inner)-diameter capillaries. The background (empty capillary) and the two samples were measured to a Q_{max} of 18.65 Å-1. The same experimental conditions were used for the measurements of both MOFs, MIP-209(Ti)-NO_2 and MIP-177(Ti)_LT. The set of parameters (background scale factor: 1.5; parameter controlling the degree of data-correction polynomial: 0.9; $Q_{maxinst}$: 18.64; Q_{min}-Q_{max}: 0.1-18.64; r_{min}-r_{max}: 0-40) were used to generate the pair distribution functions G(r).

9) High-resolution scanning transmission microscopy

High-resolution scanning transmission microscopy images (HRSTEM) were acquired on a FEI Titan Themis microscope 200 (Palaiseau, France) corrected for spherical aberrations on the probe, operating at 200 kV, equipped with a Ceta 16M hybrid camera from ThermoFischer Scientific capable of working under low-dose conditions. The HRSTEM images are obtained under a low probe current of around 40 to 50 pA, to reduce the sample damage. For the grid preparation, a solution is prepared by stirring 10 mg in 1 mL of ethanol, and then a drop of the solution is deposited on a 200-mesh copper grid covered with a pure carbon membrane.

10) Continuous rotation electron diffraction (cRED) and low-dose high resolution transmission electron microscopy (TEM)

10.1) Continuous rotation electron diffraction (cRED) data collection

The continuous rotation electron diffraction (cRED) data has been collected using the continuous rotation electron diffraction method (cRED), in collaboration with Philippe Boullay from CRISMAT laboratory (UMR 6508 - ENSICAEN), through the "METSA" French network (FR CNRS 3507) on the platform IRMA (CRISMAT - Caen).

The data was collected on a JEOL JEM2100-LaB6 TEM operated at 200 kV, equipped with 2 cameras, an ASI Medipix3 detector (ASI = Amsterdam Scientific Instruments) and a GATAN RIO16 camera. A series of 2D electron diffraction patterns are acquired while continuously rotating the crystal (cRED method) using a tomography holder (+/- 70°). The diameter of the parallel beam was set to 300 nm obtained by inserting a 10 µm condenser aperture. For some particularly sensitive MOFs, before data collection, the sample was cooled down to lower temperatures in the TEM using a Gatan Elsa™ cryo-transfer holder, to reduce the electron beam damage. Crystal tracking is achieved by defocusing every nth ED frame, to know if the crystal has moved out of the illumination area, or if other neighboring crystals are also diffracting during the continuous sample rotation.

The data collection was performed using Instamatic program or the Digital Micrograph script, InsteaDMatic, from Gatan Inc. The software PETS2 is used for data processing. The structure was solved using SUPERFLIP program (charge flipping method) and refined using JANA2006 or JANA2020 using electron scattering factors [**Palatinus, Z. Kristallographie-Crystalline Materials 2014, 229, 345.**]. Isolated crystals on the grid are selected to collect datasets as fast as possible, using an extremely low electron dose rate to reduce beam damage. The datasets with the best combination of resolution and completeness are processed and merged into a single dataset in JANA2006.

10.2) Low-dose high resolution transmission electron microscopy (TEM)

Low-dose HRTEM data were collected on the FEI Titan 80-300 E-TEM microscope equipped with the Gatan K2 direct-detection electron counting camera (DDEC), operated at 300 kV. We used an electron dose rate between 7 to 15 $e^-/Å^2$ s. The exposure time of each image is 1 s and the data collection was performed at room temperature. No automated procedure, including zone axis alignment and data processing, was used. The “HRTEM filter” (D. R. G Mitchell, v4.0, Nov 2019) was used to apply a Wiener filter, followed by the Average Background Subtraction Filter (ABSF) to enhance the image quality and eliminate any artefacts caused by the Wiener filter. For clarity, when only the filtered HRTEM image in shown in the main section, the raw image can be found in Annex.

10.3) Grid preparation

The precise control of the density of the sample on the grid is an important step. For HRTEM, the particle distribution should be homogeneous and form a thin layer rather than thick aggregates. The density should be high enough to maximize the probability of finding particles oriented in different directions. Grids with suitable densities were prepared by diluting 10 mg of the MOF in 1 mL ethanol. The solutions are magnetically stirred until the solution’s color is homogeneous, and 1-3 drops were deposited on a 200 mesh copper grid covered with a pure carbon membrane and left to air-dry at room temperature.

The particles on the grid tend to form aggregates, especially for MIL-209(Ti) small particles, where finding isolated particles on the grid was particularly challenging. Therefore, the density should be adjusted by carefully inspecting the grid under a light microscope after each deposited drop until a satisfying dispersion is achieved.

Synthetic procedures

Synthesis of MIP-209(Ti)-NO_2

To a 23-mL Teflon reactor, 2-Nitro-terephthalic acid (1.25 g) was added followed by the addition of acetic acid (5 mL). The suspension solution was stirred at room temperature for 20 mins before $Ti(iPrO)_4$ (0.59 mL) was rapidly added once. After stirring for 10 min, the reaction was put into a pre-heated oven at 150°C for 30 h. When the reactor was cooled down to room temperature, light yellow product was collected by centrifugation (3 mins at 10,000 rpm), then washed in pure ethanol at 50°C overnight, finally dried under vacuum condition at room temperature.

Ex situ synthesis of MIP-209(Ti)-NO_2

To a 23-mL Teflon reactor, 2-Nitro-terephthalic acid (1.25 g) was added followed by the addition of acetic acid (5 mL). The suspension solution was stirred at room temperature for 20 mins before Ti(iPrO)$_4$ (0.59 mL) was rapidly added once. After stirring for 10 min, the reaction was put into a pre-heated oven at 150°C for 5, 10, 15, 20, 25, 30 h. When the reactor was cooled down to room temperature, the product was collected by centrifugation (3mins at 10,000rpm), then washed in pure ethanol, finally dried in air at room temperature.

Synthesis of MIP-209(Ti)-2Cl

To a 23-mL Teflon reactor, dichloride-terephthalic acid (0.48 g) was added followed by the addition of acetic acid (5 mL). The suspension solution was stirred at room temperature for 20 mins before Ti(iPrO)$_4$ (0.1 mL) was rapidly added once. After stirring for 10 min, the reaction was put into a pre-heated oven at 180°C for 72 hours. When the reactor was cooled down to room temperature, light yellow product was collected by centrifugation (3 mins at 10,000 rpm), then washed in pure ethanol at 50°C overnight, finally dried under vacuum condition at room temperature.

One-pot synthesis of MIP-209(Ti-Cr)-NO$_2$

To a 23 mL Teflon reactor, 2-nitro-terephthalic acid (1.25 g) was added followed by the addition of acetic acid (5 mL). The mixture was stirred at room temperature for 5 mins before adding $Cr(NO_3)_3 \cdot 9H_2O$ (40 mg). Then Ti(iPrO)$_4$ (0.56 mL) was rapidly added. After 10 mins stirring, the reaction was put into a pre-heated oven at 180°C for 48 h. When the reactor was cooled down to room temperature, dark brown product was collected by centrifugation (3 mins at 10,000 rpm), then washed in pure ethanol at 50°C overnight, finally dried under vacuum condition at room temperature.

Stability test

All the stability tests were performed using the same procedure. The powder sample was suspended into different solvent as listed in the supplementary table 4 and 5.

Supplementary figures

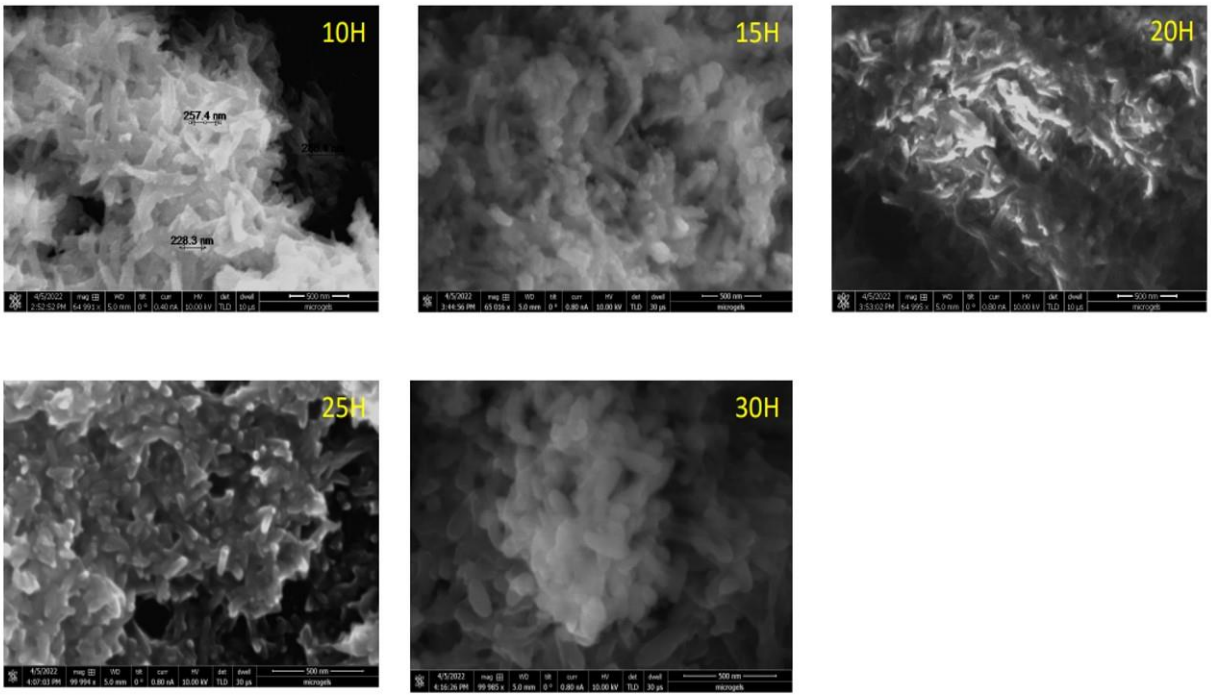

Figure S1 SEM images of *ex situ* MIP-209(Ti)-NO_2 synthesis.

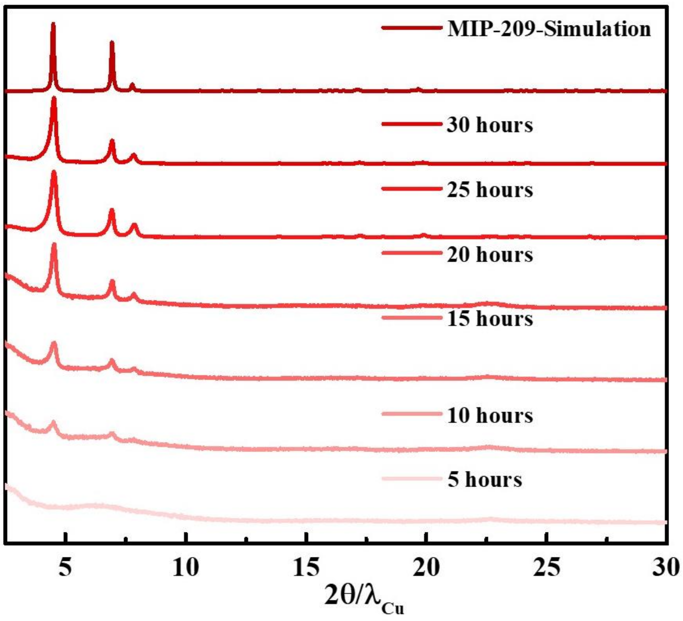

Figure S2 PXRD patterns of *ex situ* MIP-209(Ti)-NO_2 synthesis.

From above two figures, it is observed that the nano rods formed at first 10 hours with around 200 nm size. Then the particle size became more homogenous and the size didn't display any changes with the elongated synthesis time. According to the synthesis time of MIP-209(Ti)-NO_2, the SEM images were consistent very well with the crystallinity we measured by PXRD.

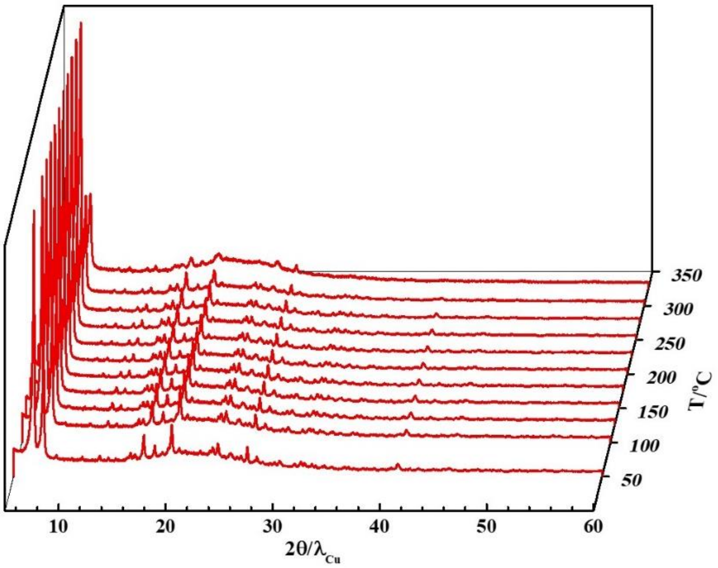

Figure S3 Variable temperature PXRD patterns of MIP-209(Ti)-NO_2.

From above figure, PXRD patterns do not show notable changes below 300°C, indicating that the removal of solvent molecules in MIP-209(Ti)-NO_2 framework occurs without structural changes. After 300°C, TiO_2 forms gradually with the decomposition of MIP-209(Ti)-NO_2 framework.

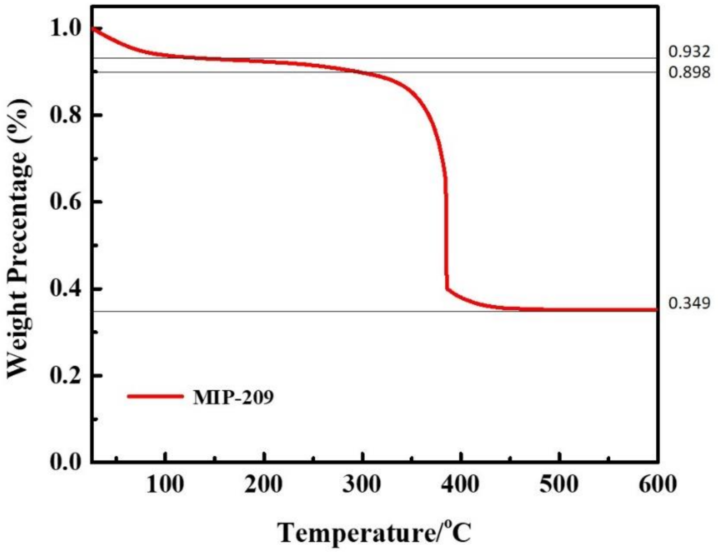

Figure S4 TGA curves in O_2 of MIP-209(Ti)-NO_2.

From above figure, the weight loss of free solvent, acetate group, and ligand in MIP-209(Ti)-NO_2 could be calculated, respectively. Based on the tentative formula of MIP-209(Ti)-NO_2, $Ti_{12}O_{15}[1,4\text{-BDC-}NO_2]_6[CH_3COO]_3$ with coordinated $6H_2O$, the theoretical TiO_2 % is 39.9%, here the experimental value of TiO_2 % is 38.9%, suggesting the result has an agreement with the value from MIP-209(Ti)-NO_2 tentative formula. The tiny difference probably is caused by the coordinated H_2O molecules we expected here. In fact, acetate group also can coordinate with Ti at the up and bottom of $Ti_{12}O_{15}$ cluster.

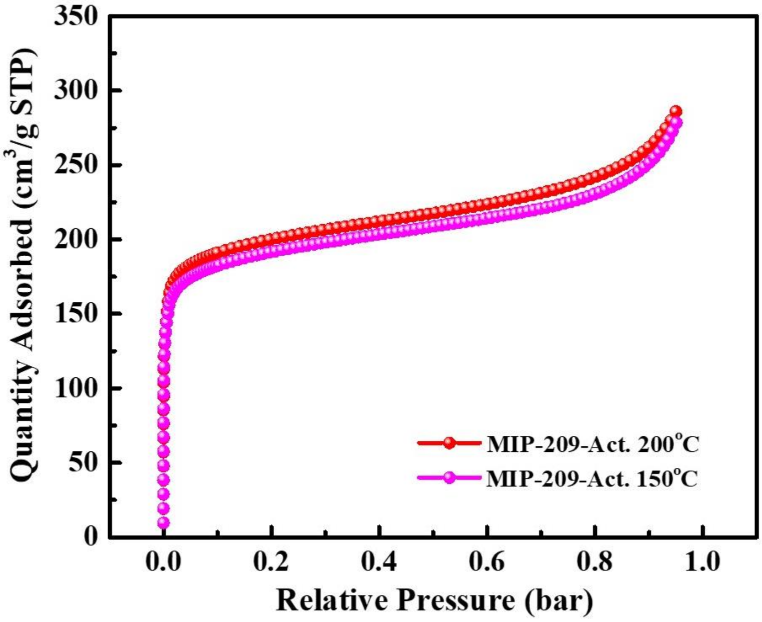

Figure S5 Nitrogen sorption isotherms of MIP-209(Ti)-NO_2 at 77 K.

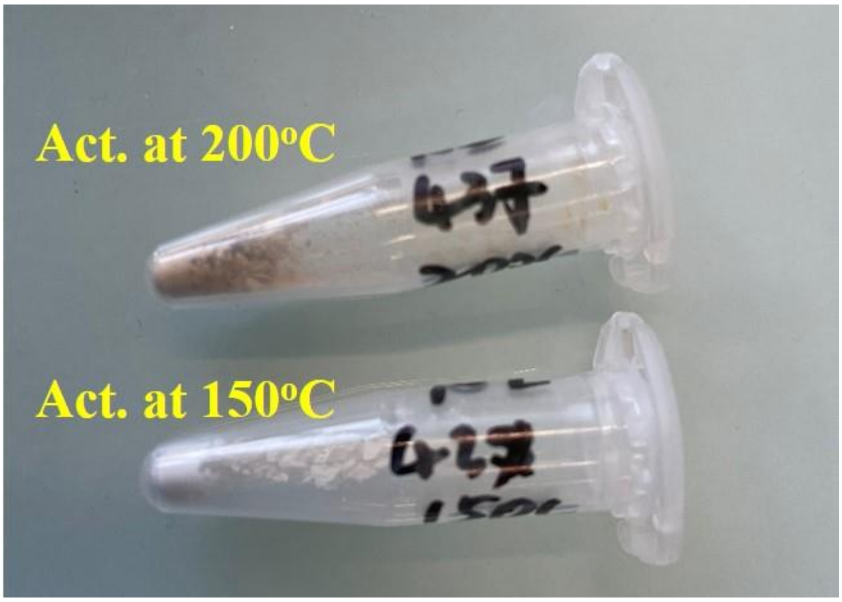

Figure S6 The color change of MIP-209(Ti)-NO_2 when activated at 150°C and 200°C under vacuum condition.

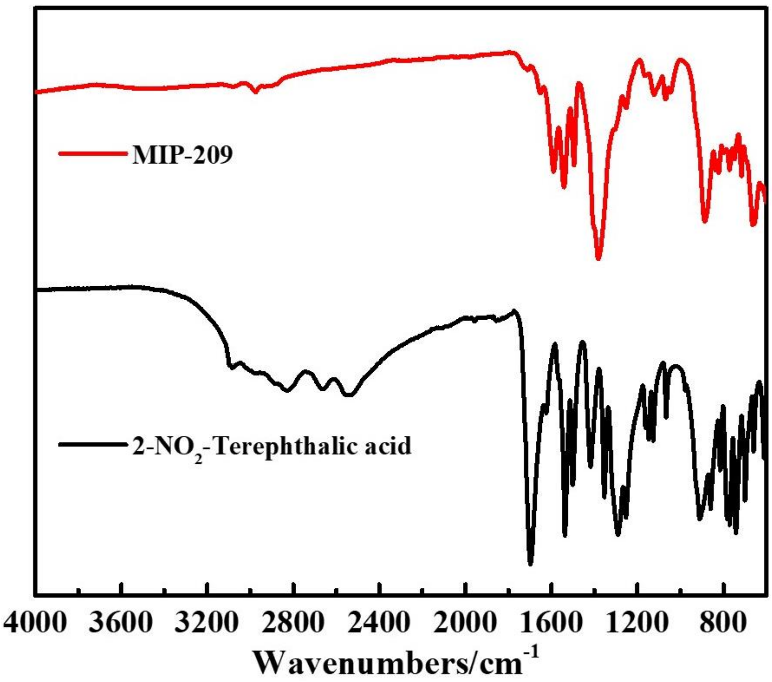

Figure S7 FT-IR spectra of MIP-209(Ti)-NO$_2$.

From above figure, compared to nitro-terephthalate group, the peak at 1696 cm^{-1} in MIP-209(Ti)-NO$_2$ solids belongs to C=O stretching vibration, which could be caused by the defects of MIP-209(Ti)-NO$_2$ formed during the synthesis.

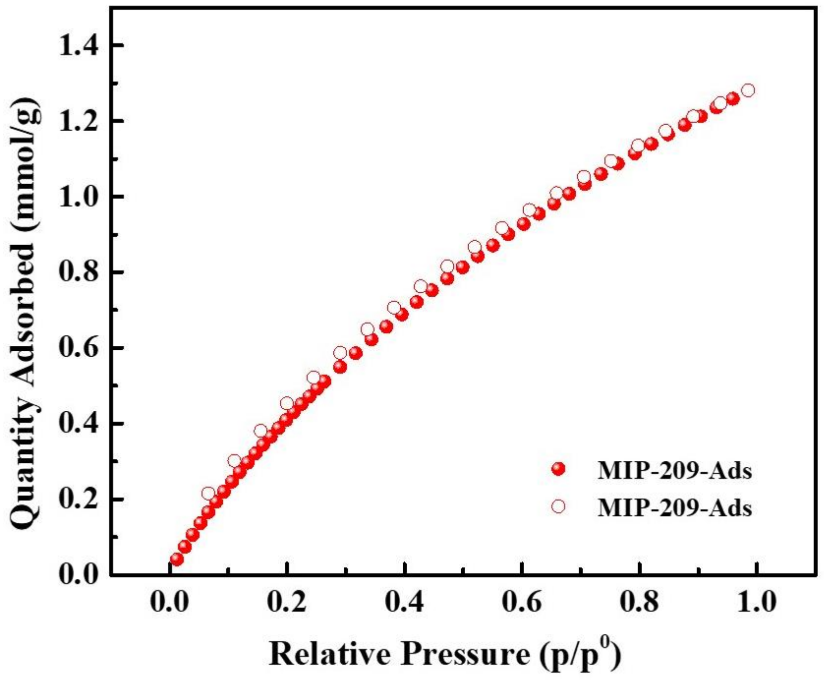

Figure S8 Carbon dioxides sorption isotherms of MIP-209(Ti)-NO$_2$ at 298 K.

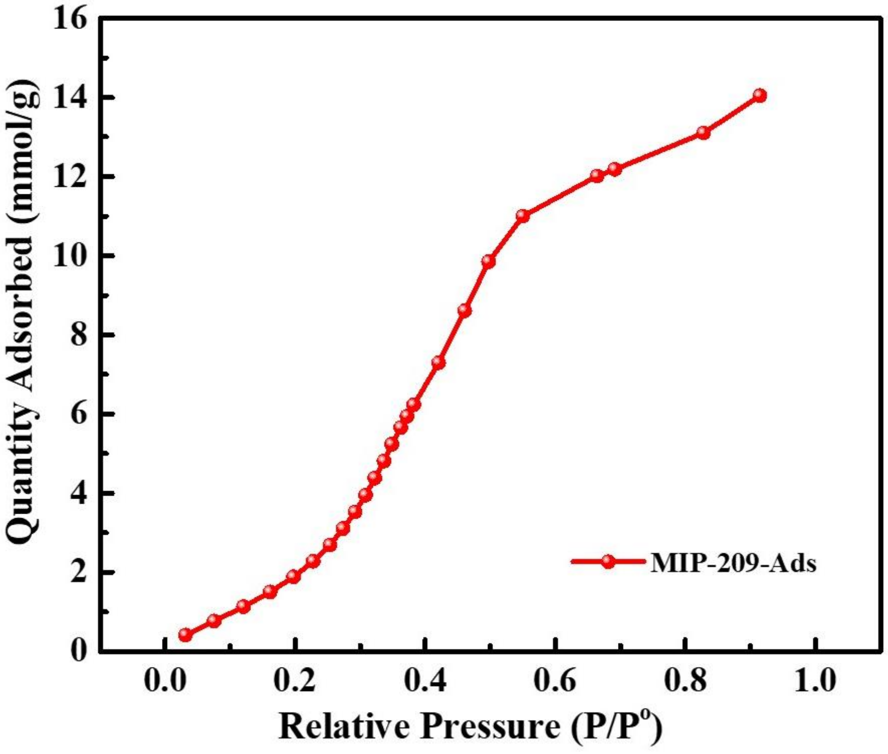

Figure S9 Water sorption isotherms of MIP-209(Ti)-NO$_2$ at 298 K.

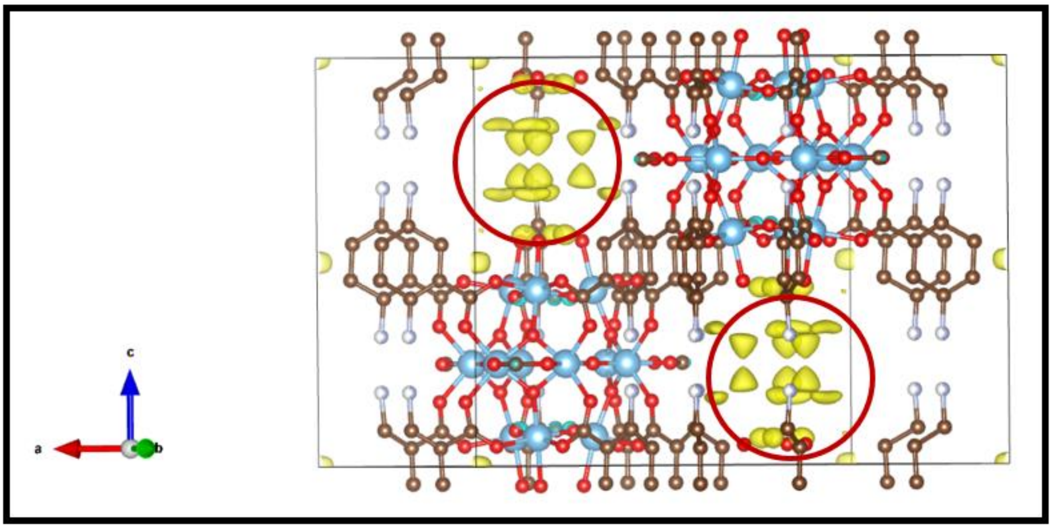

Figure S10 Difference Fourier map for MIP-209(Ti)-NO_2 after a set of refinement cycles. The nitrogen atom with 1/2 occupancy is identified. The red circles indicate the residual density in the pores.

The presence of residual density in the pores is not interpreted here as it does not considerably affect the reliability factors. It could be attributed to solvent molecules from the synthesis (disordered water and acetic acid molecules).

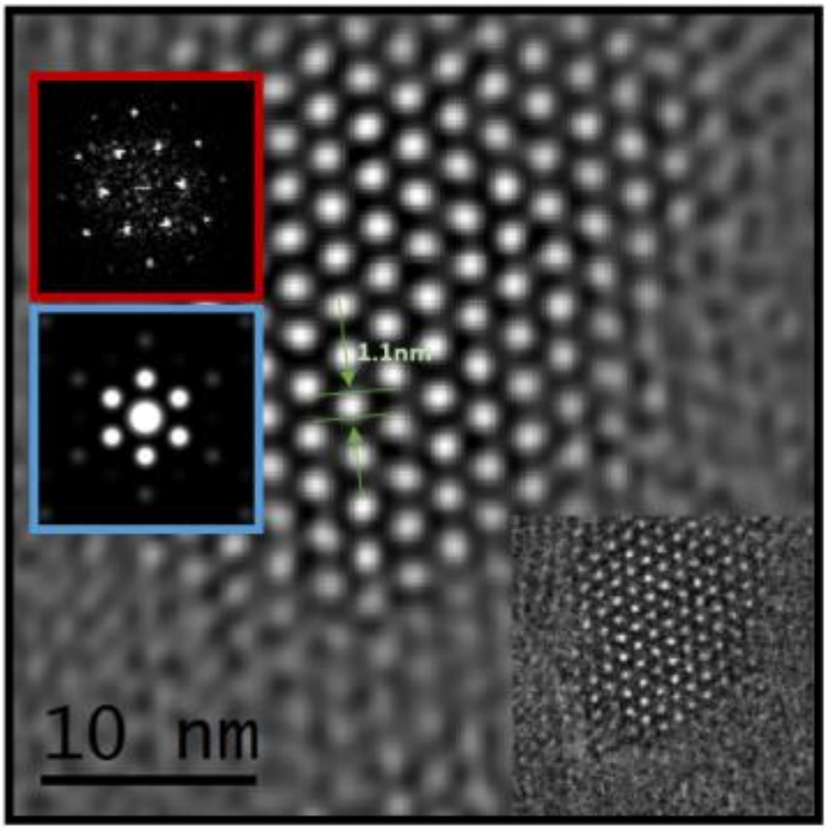

Figure S11 Filtered low-dose HRTEM image of MIP-209(Ti)-NO_2 along [001]. The insets are the FFT (red), the simulated electron diffraction pattern (blue) and the raw HRTEM image. The diameter of the channels is shown by the green arrows.

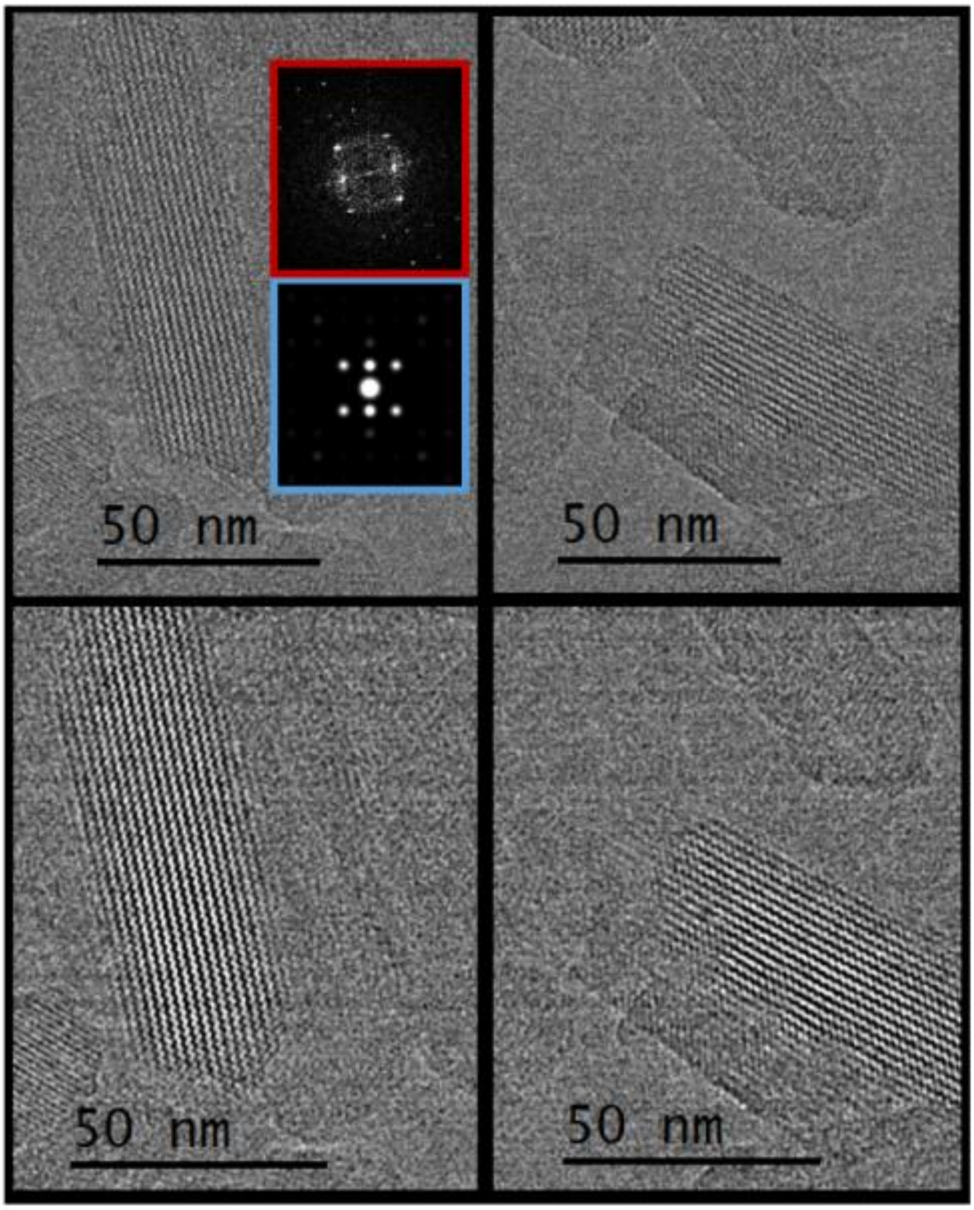

Figure S12 Raw (top) and filtered (bottom) low-dose HRTEM images of MIP-209(Ti)-NO_2 along [100]. The insets are the FFT (red) and the simulated electron diffraction pattern (blue).

The orientations of the particles presented are determined by low-dose HRTEM. The values extracted from the experimental FFTs are consistent well with the simulated ED patterns.

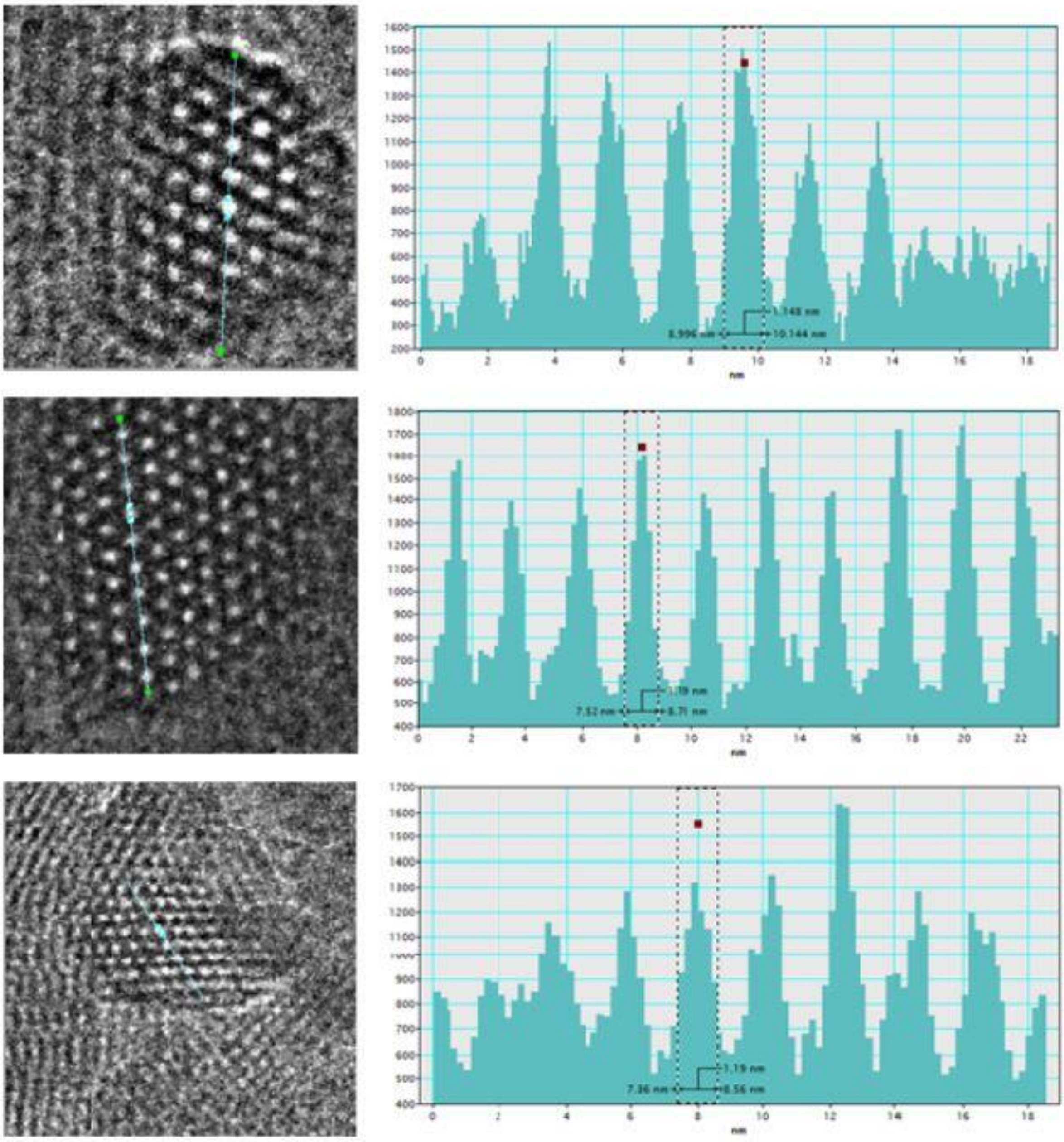

Figure S13 Three raw HRTEM images of particles of MIP-209(Ti)-NO_2 oriented along the [001] axis. The diameter of the channels calculated from the profile line along the particle is around 1.1 nm.

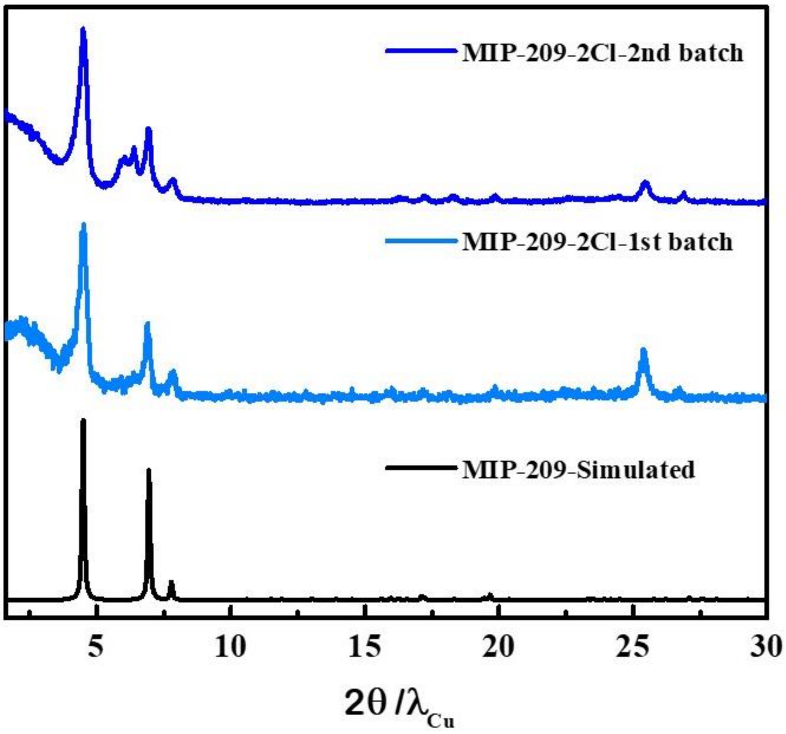

Figure S14 PXRD patterns of MIP-209(Ti)-2Cl with two different batches.

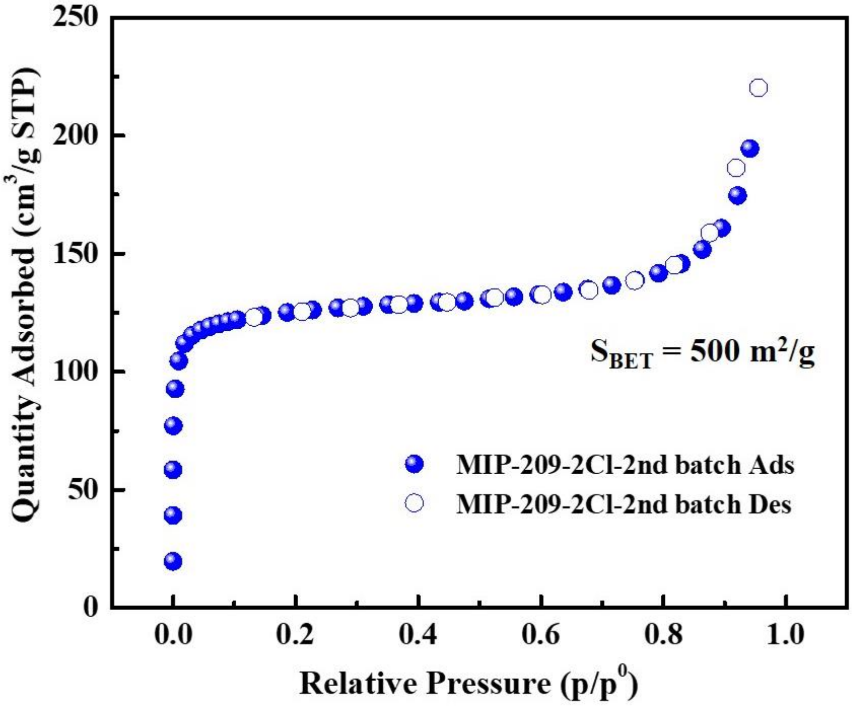

Figure S15 Nitrogen sorption isotherm of MIP-209(Ti)-2Cl at 77 K.

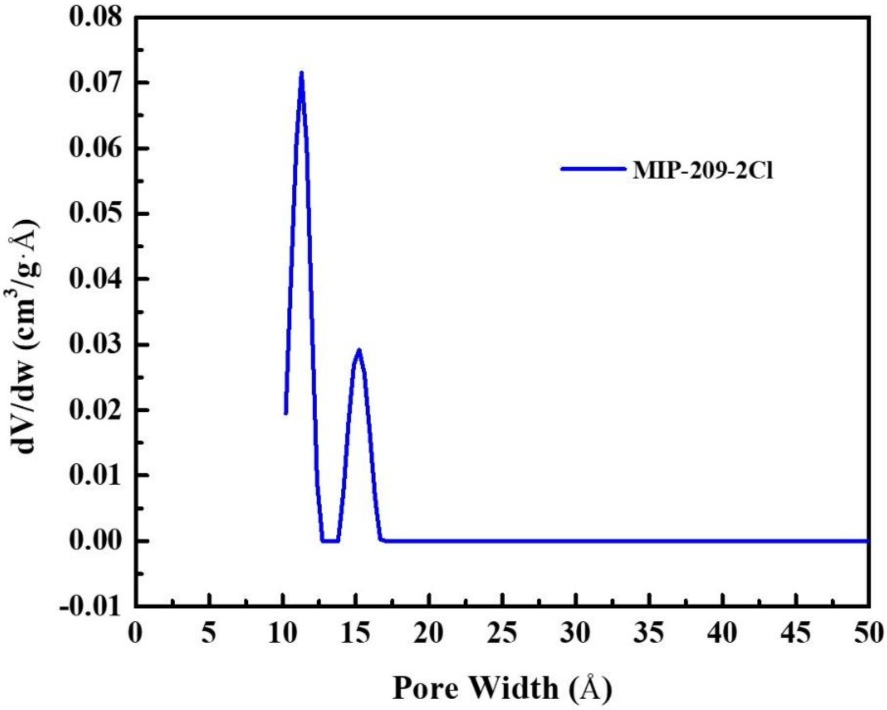

Figure S16 Pore size distribution of MIP-209(Ti)-2Cl calculated by DFT pore size with NLDFT for pillared clay model (the experimental pore size is 1.13 and 1.53 nm).

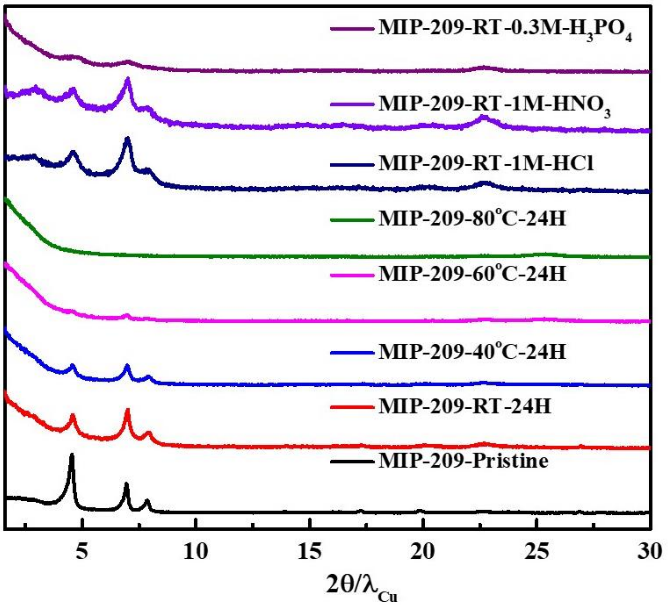

Figure S17 PXRD patterns of MIP-209(Ti)-NO_2 after chemical treatment in various conditions.

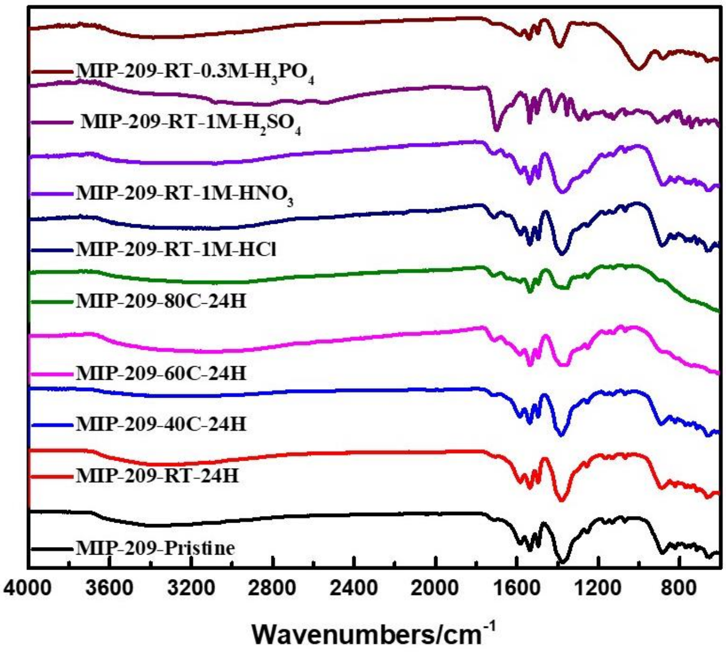

Figure S18 FT-IR results of MIP-209(Ti)-NO_2 after chemical treatment in various conditions.

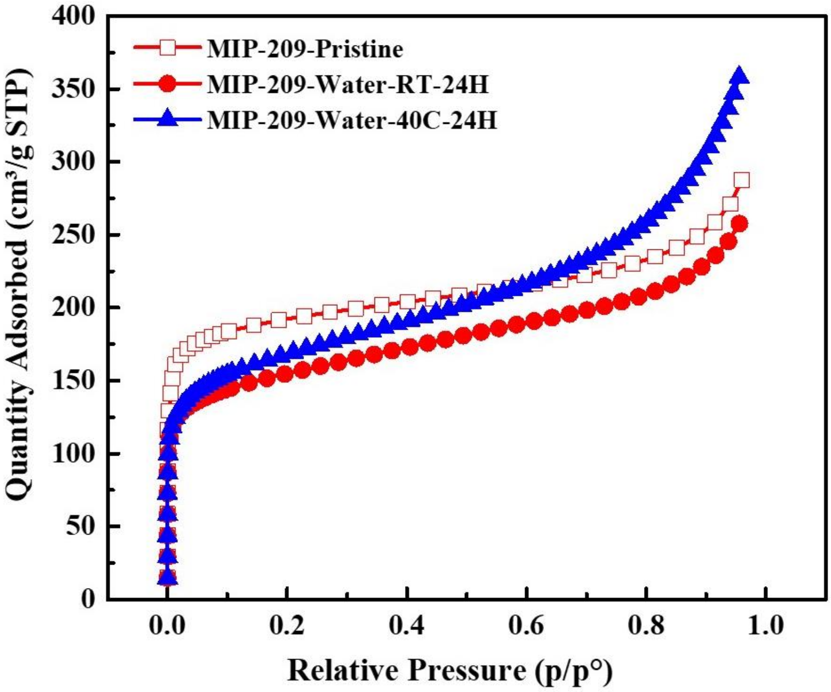

Figure S19 N_2 adsorption isotherms of MIP-209(Ti)-NO_2 after water treatment in different conditions.

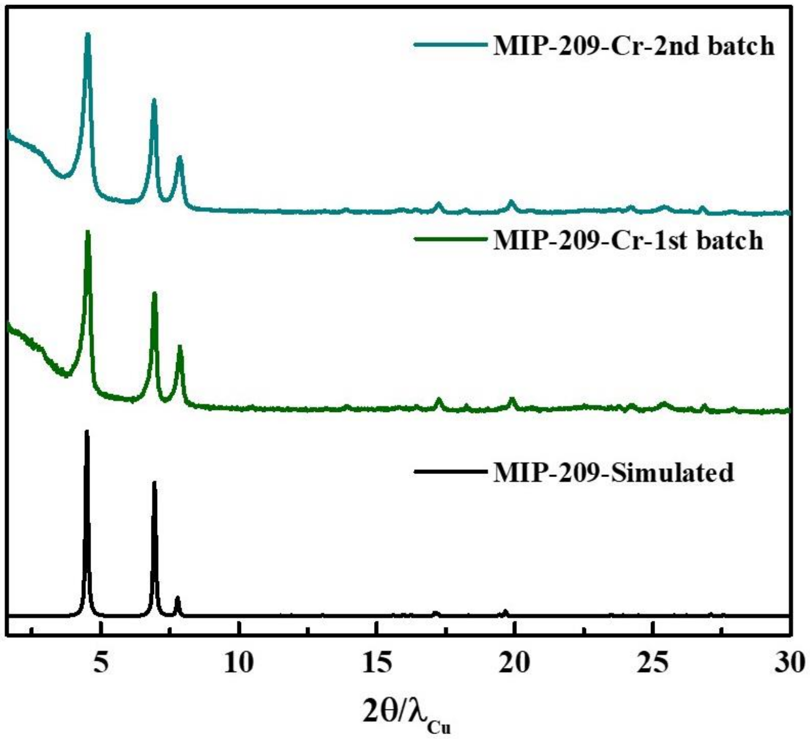

Figure S20 PXRD patterns of MIP-209(Ti-Cr)-NO_2.

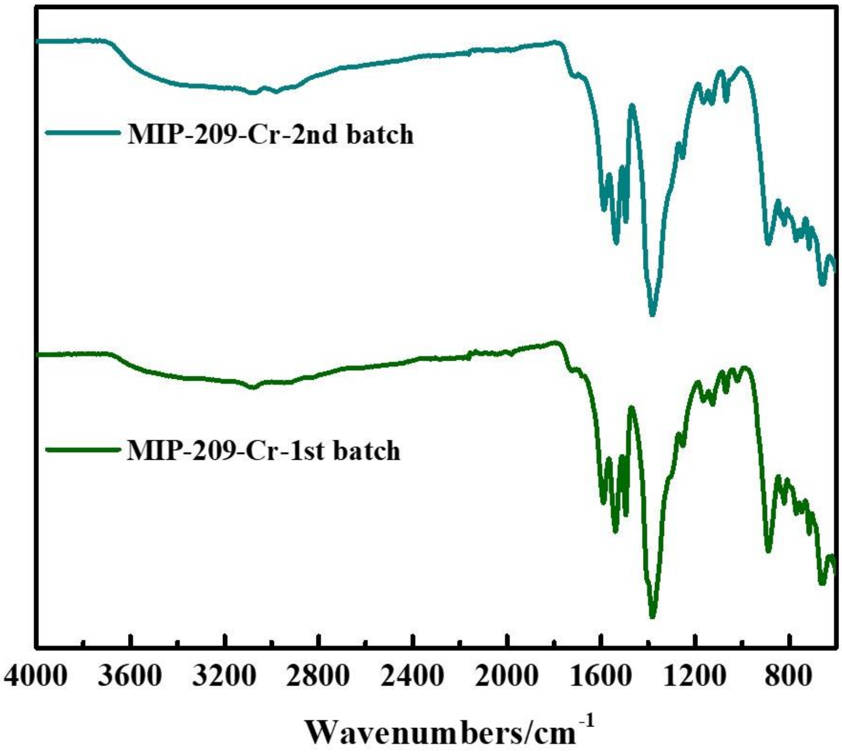

Figure S21 FT-IR spectra of MIP-209(Ti-Cr)-NO_2.

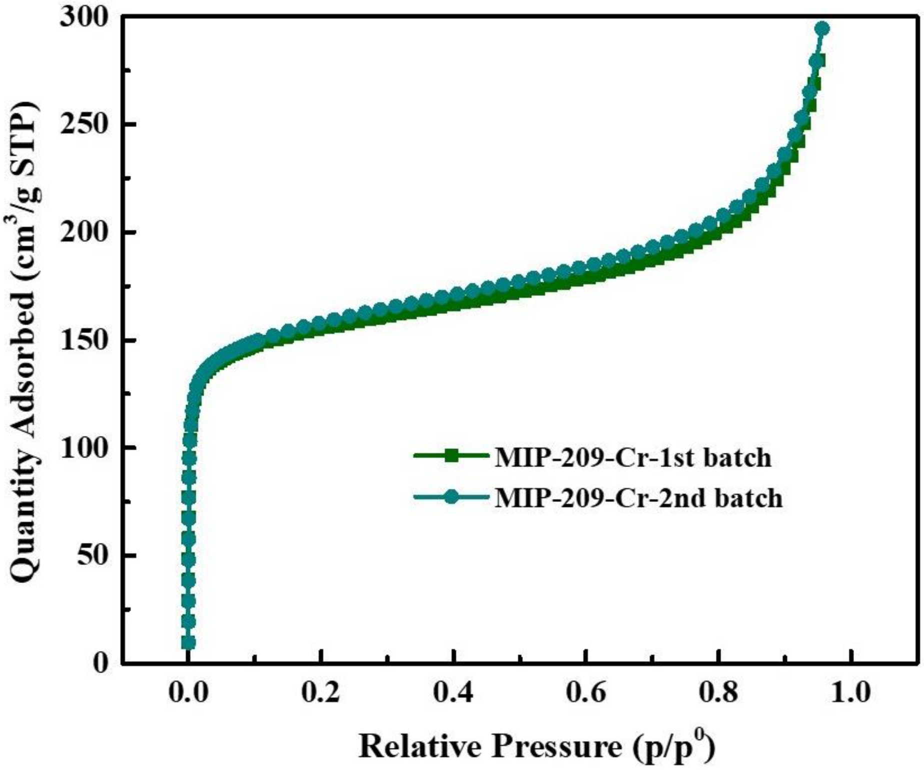

Figure S22 Nitrogen sorption isotherms at 77 K of MIP-209(Ti-Cr)-NO_2.

The pore size distribution (PSD) by Horvath-Kawazoe model reveals MIP-209(Ti-Cr)-NO_2 with relatively low N_2 uptake at 77 K (148 cm^3 g^{-1} STP), displayed a slightly smaller pore diameter compared to as-synthesized MIP-209 (183 cm^3 g^{-1} STP), which happened in different batches. We speculated that the channel has been filled by extra acetate groups leading to the block of the channel.

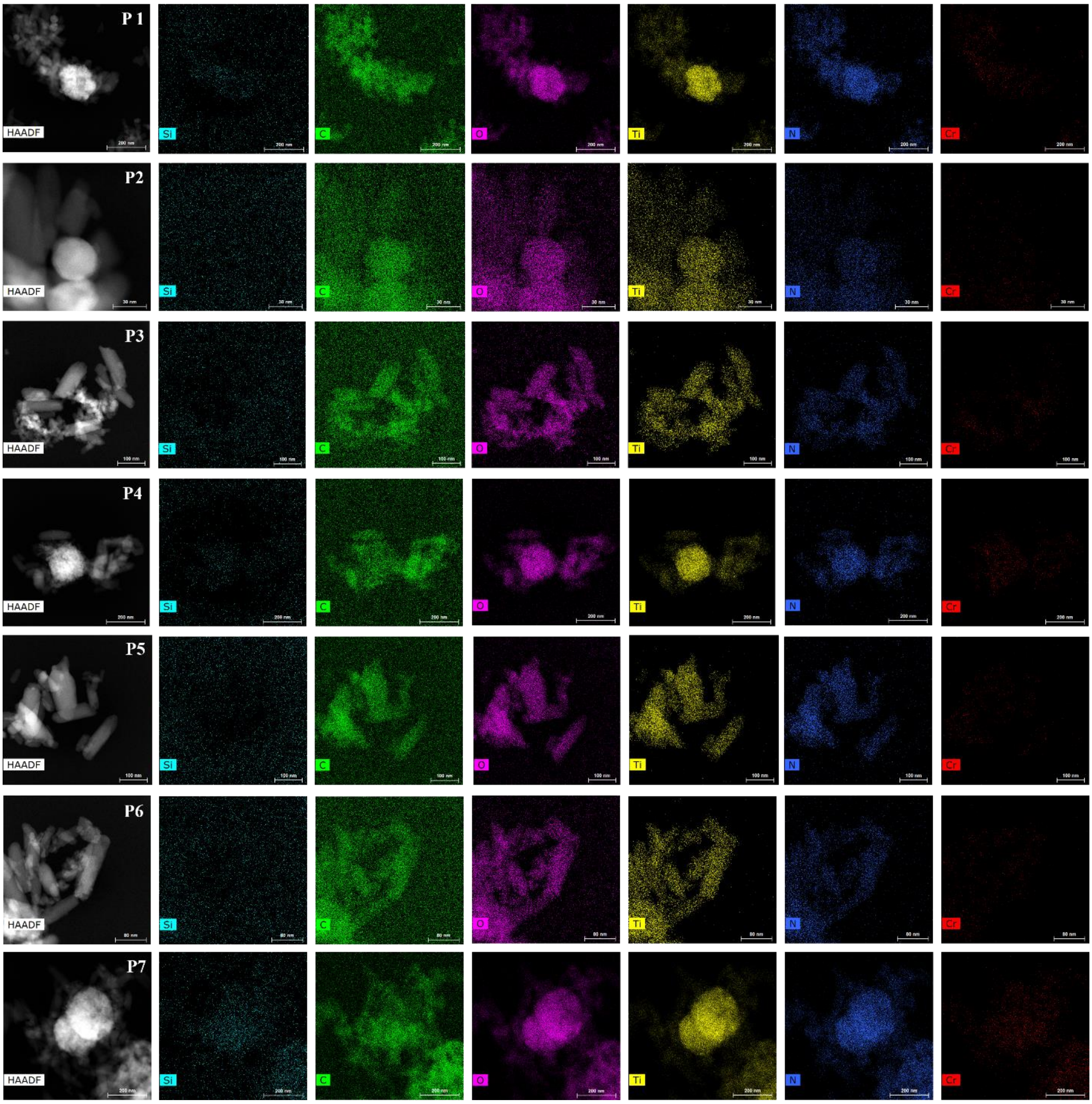

Figure S23 Elements mapping results by HRTEM of MIP-209(Ti-Cr)-NO_2.

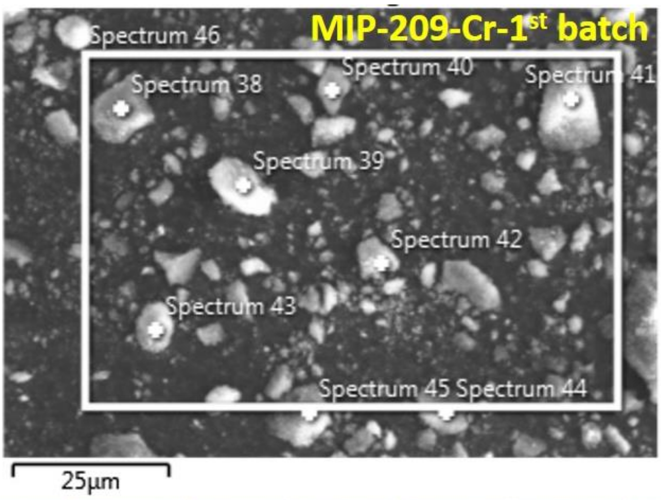

Spectrum Label	Spectrum 38	Spectrum 39	Spectrum 40	Spectrum 41	Spectrum 42	Spectrum 43	Spectrum 44	Spectrum 45	Spectrum 46
Ti	94.69	95.08	93.02	94.65	94.63	93.54	94.56	96.92	96.11
Cr	5.31	4.92	6.98	5.35	5.37	6.46	5.44	3.08	3.89
Total	100	100	100	100	100	100	100	100	100

Figure S24 Energy-dispersed X-ray spectroscopy result of MIP-209(Ti-Cr)-NO_2-1st batch.

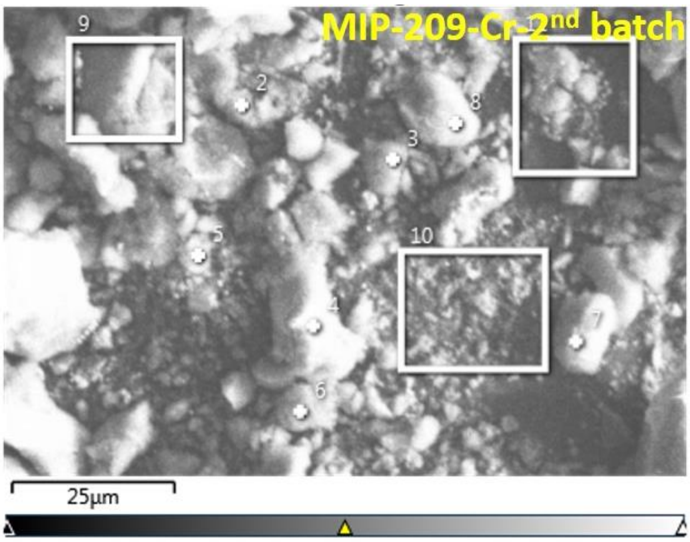

Spectrum Label	Spectrum 2	Spectrum 3	Spectrum 4	Spectrum 5	Spectrum 6	Spectrum 7	Spectrum 8	Spectrum 9	Spectrum 10	Spectrum 11
Ti	90.9	95.9	95.2	93.4	90.6	93.0	95.0	94.8	96.2	95.1
Cr	9.1	4.1	4.8	6.6	9.4	7	5	5.2	3.8	4.9
Total	100	100	100	100	100	100	100	100	100	100

Figure S25 Energy-dispersed X-ray spectroscopy result of MIP-209(Ti-Cr)-NO_2-2nd batch.

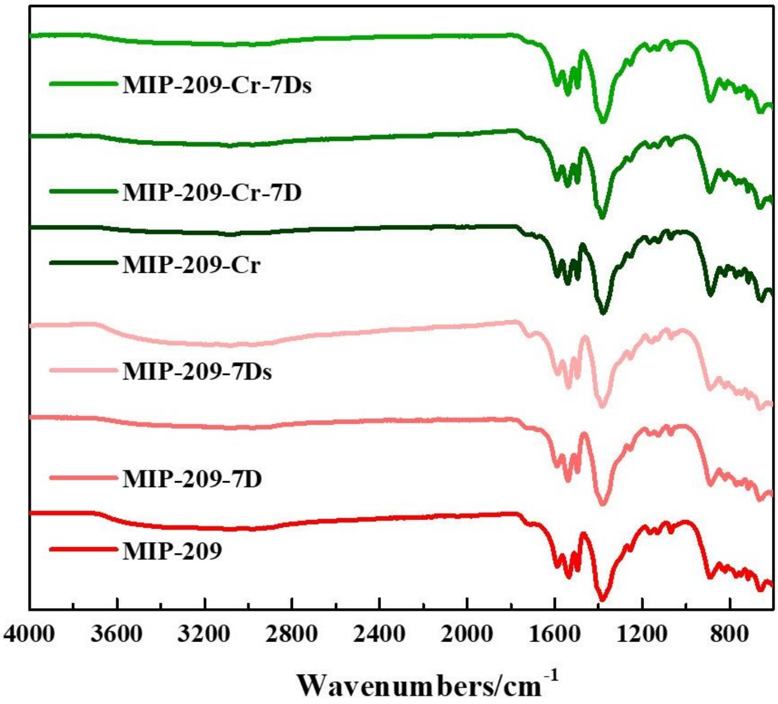

Figure S26 FT-IR results of MIP-209(Ti)-NO$_2$ and MIP-209(Ti-Cr)-NO$_2$ samples after water treatment.

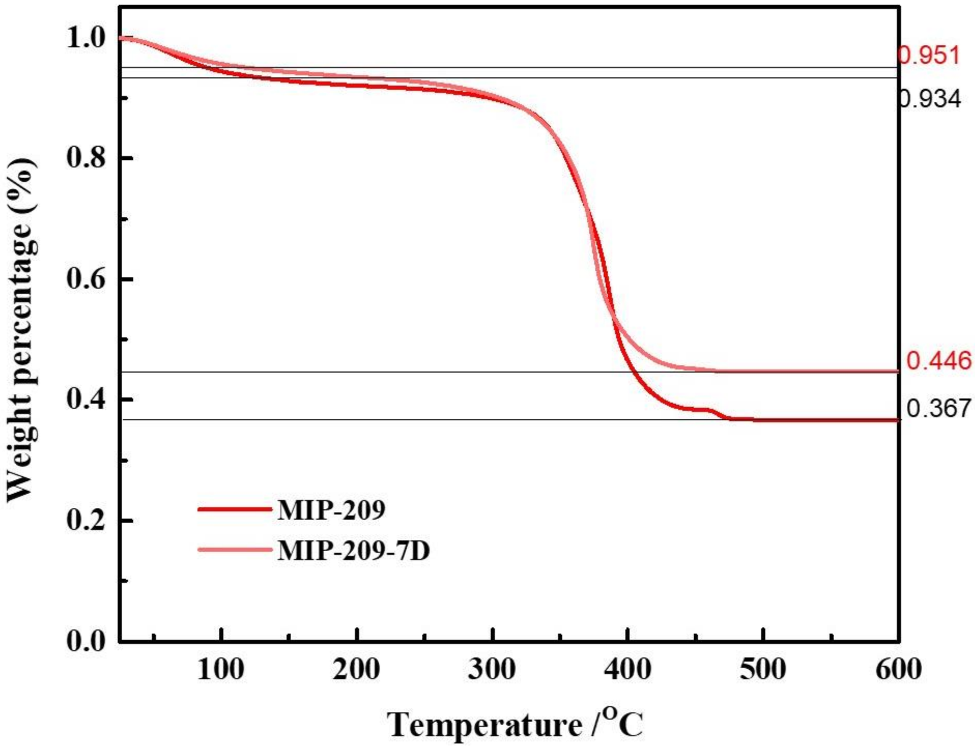

Figure S27 TGA curves in O$_2$ of MIP-209(Ti)-NO$_2$ samples after water treatment.

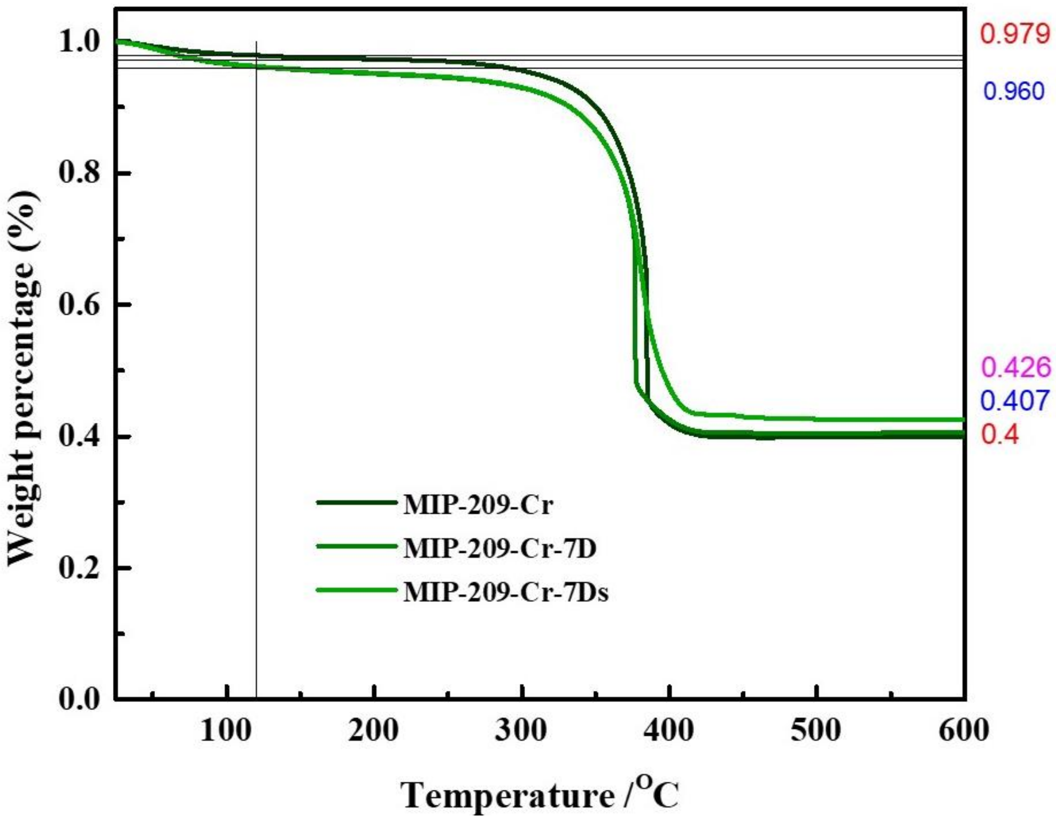

Figure S28 TGA curves in O_2 of MIP-209(Ti-Cr)-NO_2 samples after water treatment.

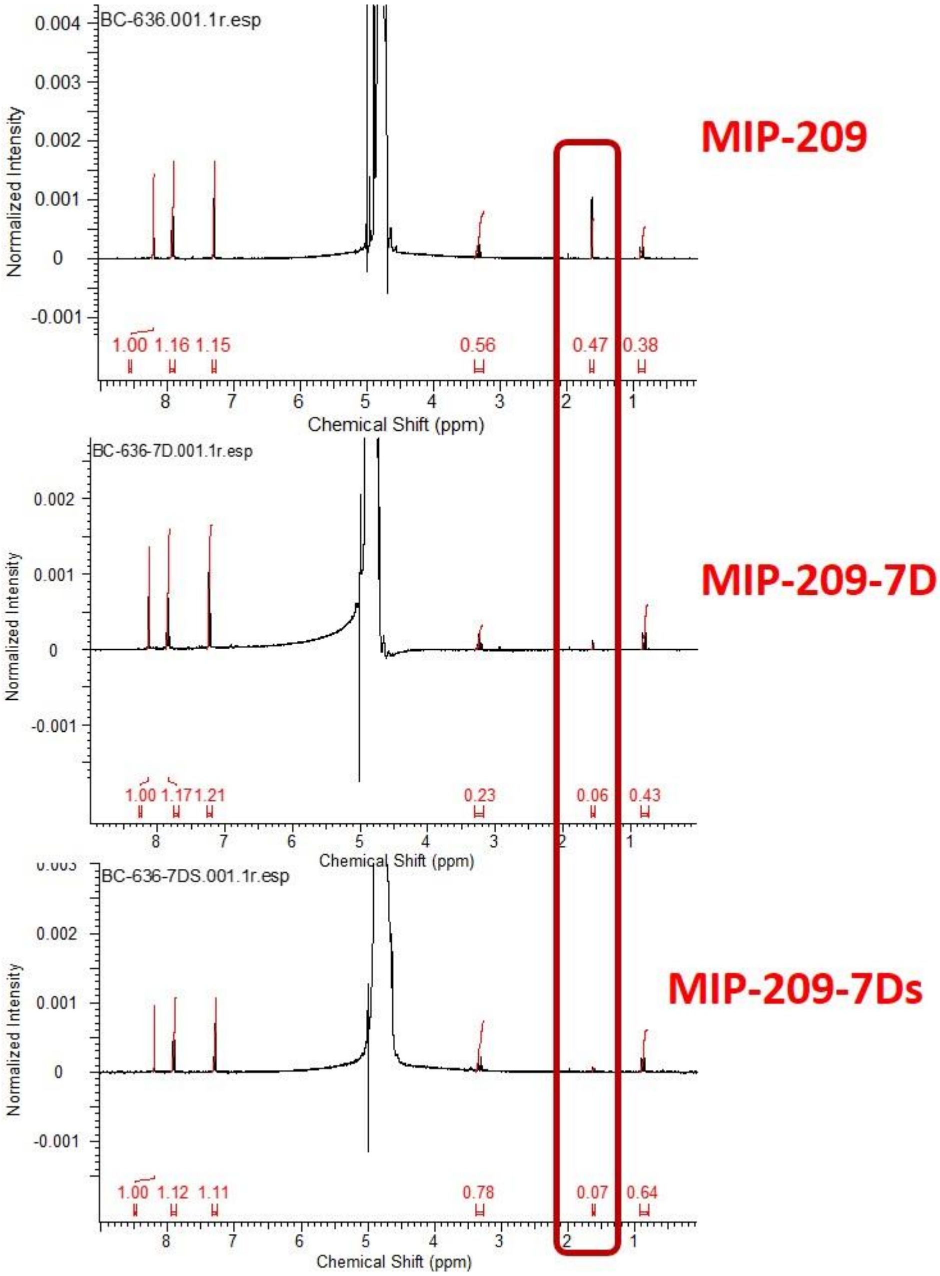

Figure S29 ^{1}H NMR results of MIP-209(Ti)-NO_2 samples after water treatment.

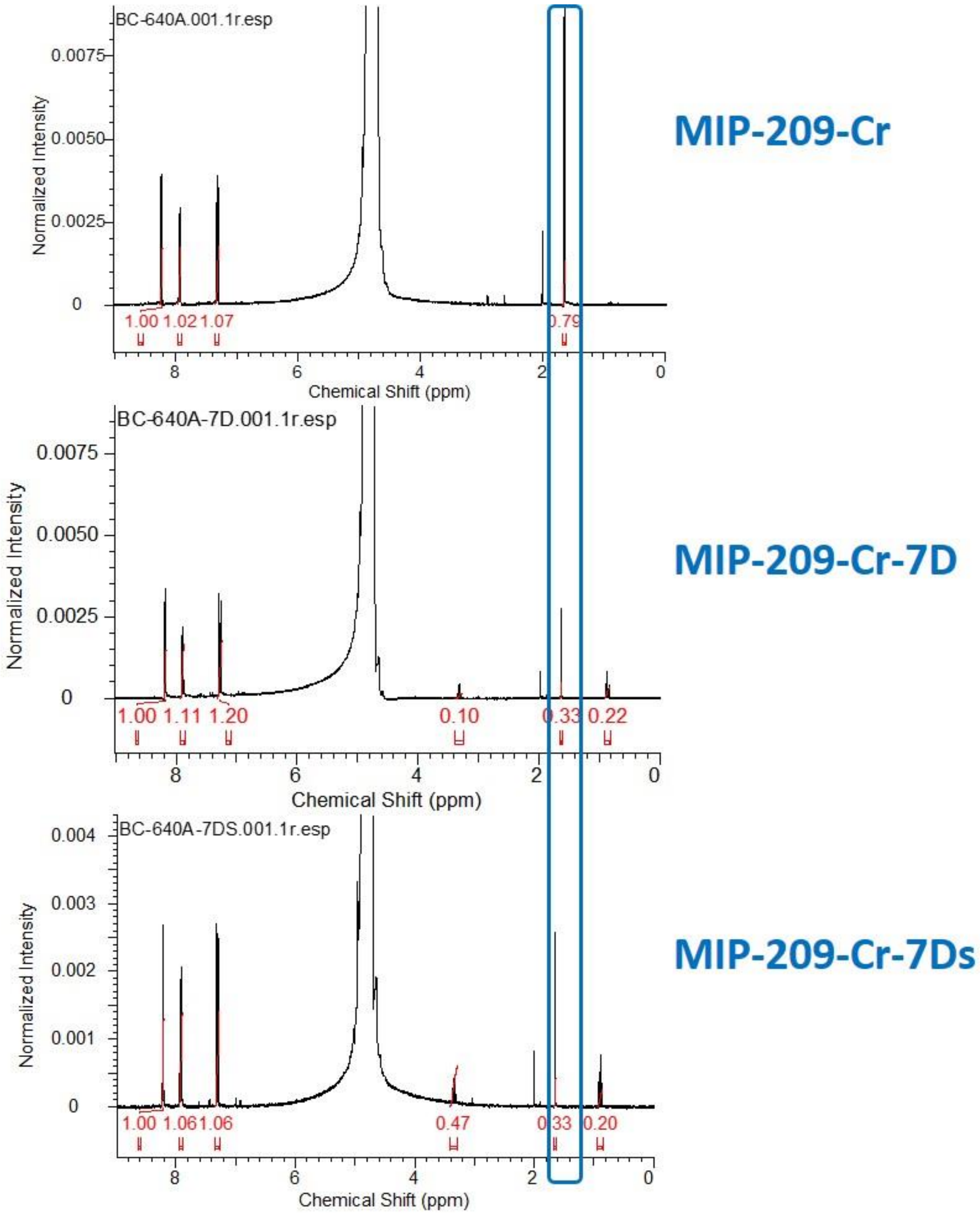

Figure S30 ^{1}H NMR results of MIP-209(Ti-Cr)-NO_2 samples after water treatment.

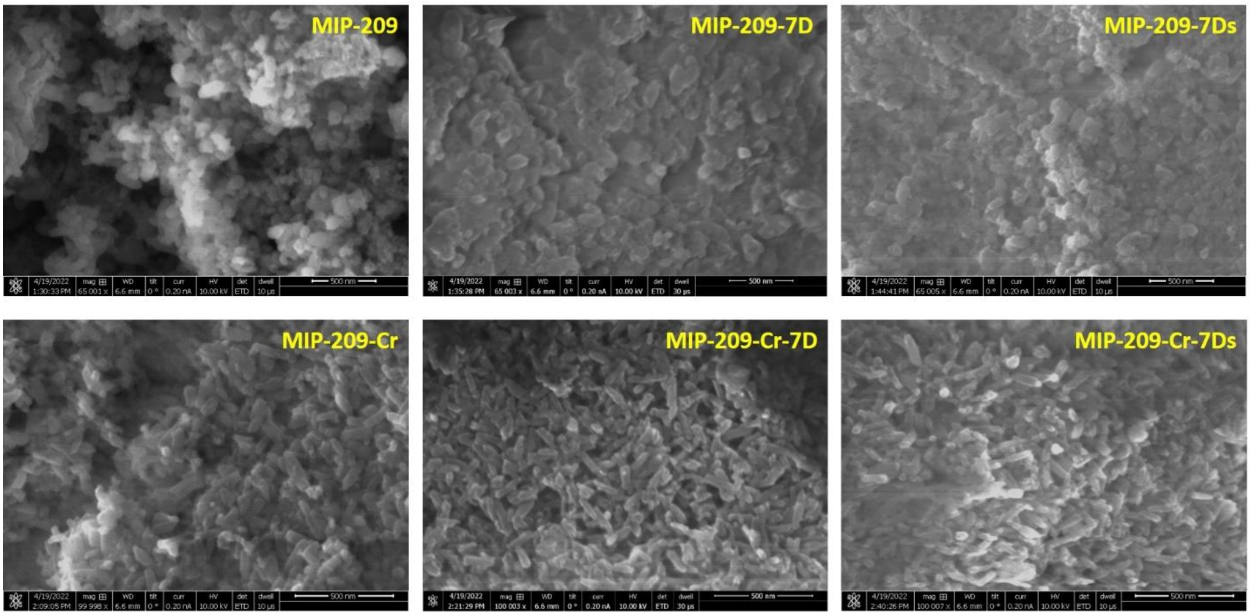

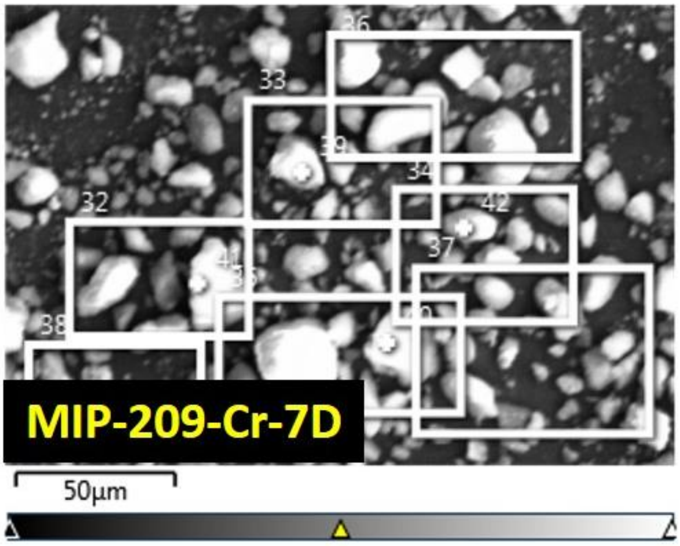

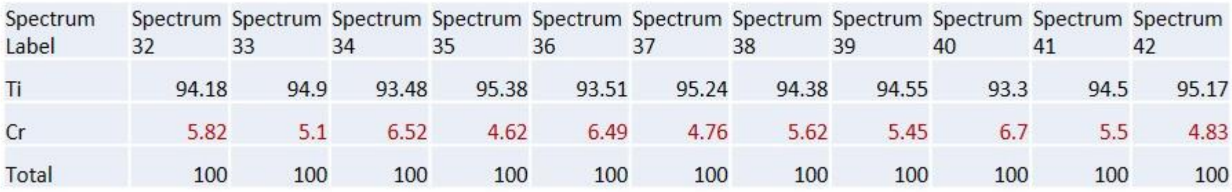

Spectrum Label	Spectrum 32	Spectrum 33	Spectrum 34	Spectrum 35	Spectrum 36	Spectrum 37	Spectrum 38	Spectrum 39	Spectrum 40	Spectrum 41	Spectrum 42
Ti	94.18	94.9	93.48	95.38	93.51	95.24	94.38	94.55	93.3	94.5	95.17
Cr	5.82	5.1	6.52	4.62	6.49	4.76	5.62	5.45	6.7	5.5	4.83
Total	100	100	100	100	100	100	100	100	100	100	100

Figure S31 SEM images of MIP-209(Ti)-NO_2 and MIP-209(Ti-Cr)-NO_2 samples after water treatment.

Figure S32 EDX results of MIP-209(Ti-Cr)-NO_2 -7D sample.

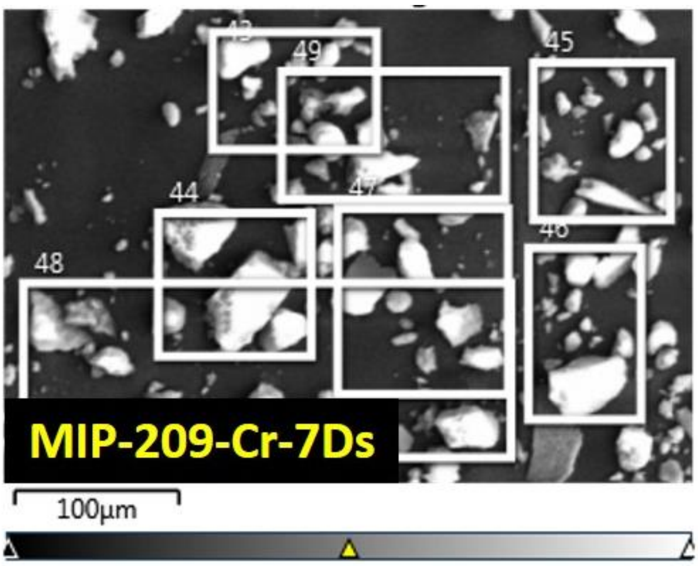

Spectrum Label	Spectrum 43	Spectrum 44	Spectrum 45	Spectrum 46	Spectrum 47	Spectrum 48	Spectrum 49
Ti	94.14	95.41	94.01	95.18	94.62	95.56	94.32
Cr	5.86	4.59	5.99	4.82	5.38	4.44	5.68
Total	100	100	100	100	100	100	100

Figure S33 EDX results of MIP-209(Ti-Cr)-NO_2 -7Ds sample.

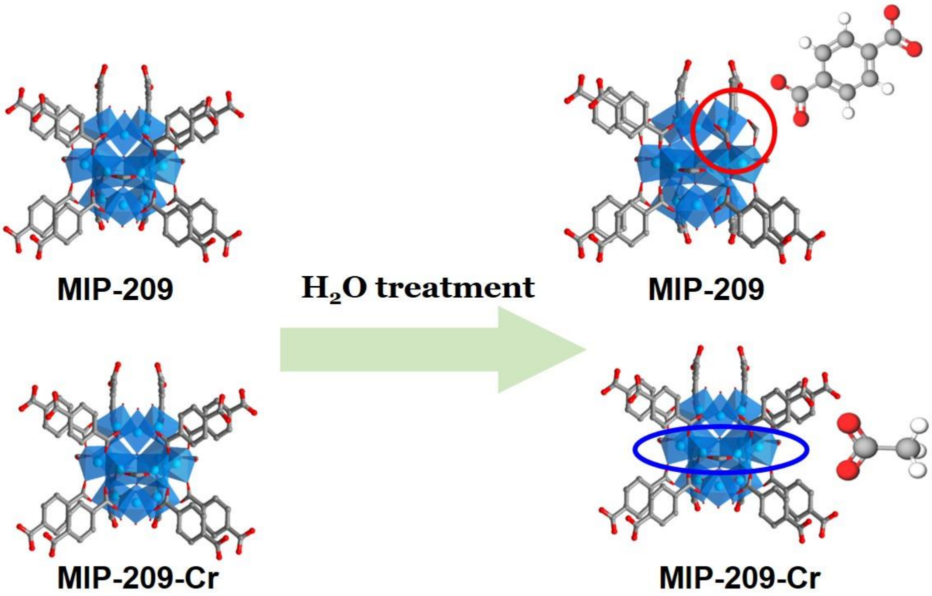

Figure S34 Hypothesis about MIP-209(Ti)-NO_2 and MIP-209(Ti-Cr)-NO_2 after water treatment based on $Ti_{12}O_{15}$ Cluster.

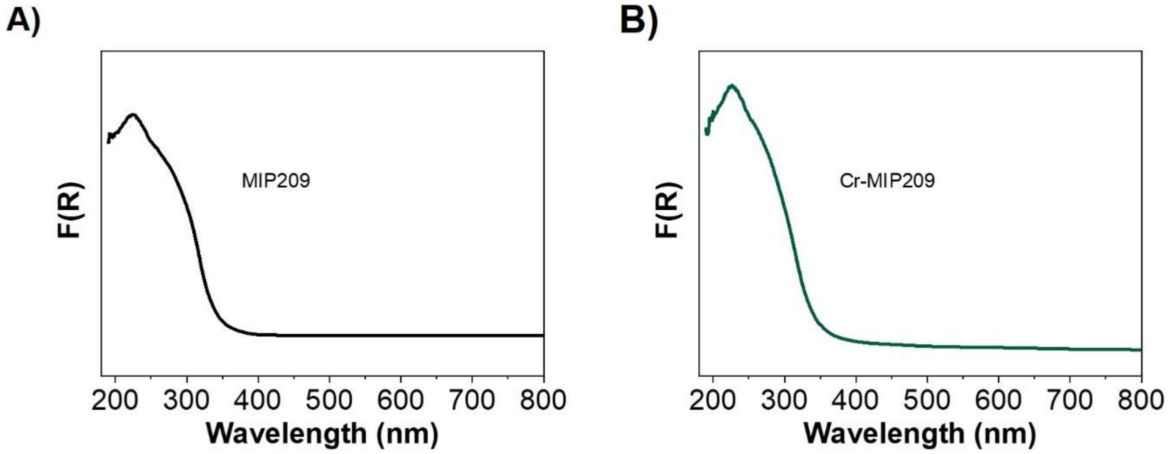

Figure S35 UV-vis DRS spectra of A) MIP-209(Ti)-NO_2 and B) MIP-209(Ti-Cr)-NO_2.

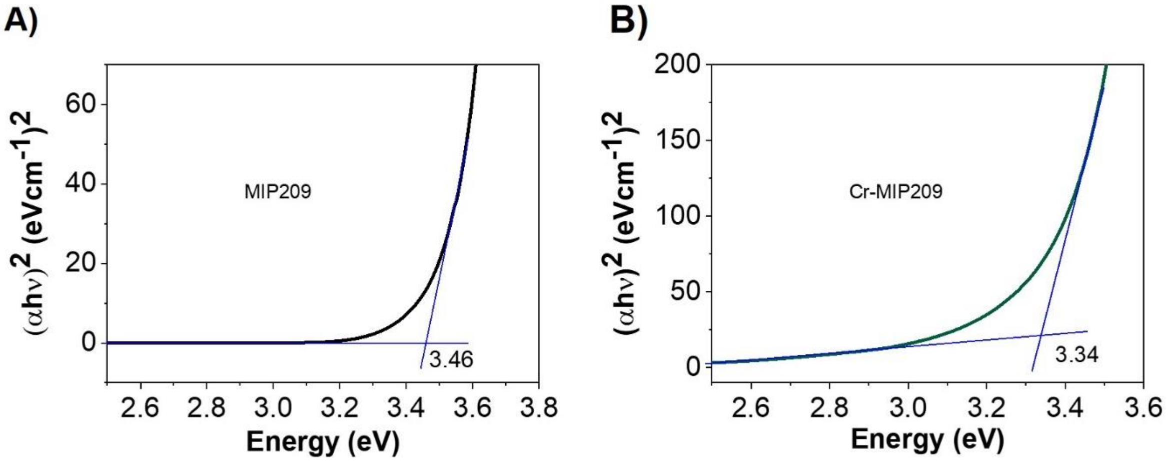

Figure S36 Tauc plots of A) MIP-209(Ti)-NO_2 and B) MIP-209(Ti-Cr)-NO_2. The estimated band gap value is shown in each graph.

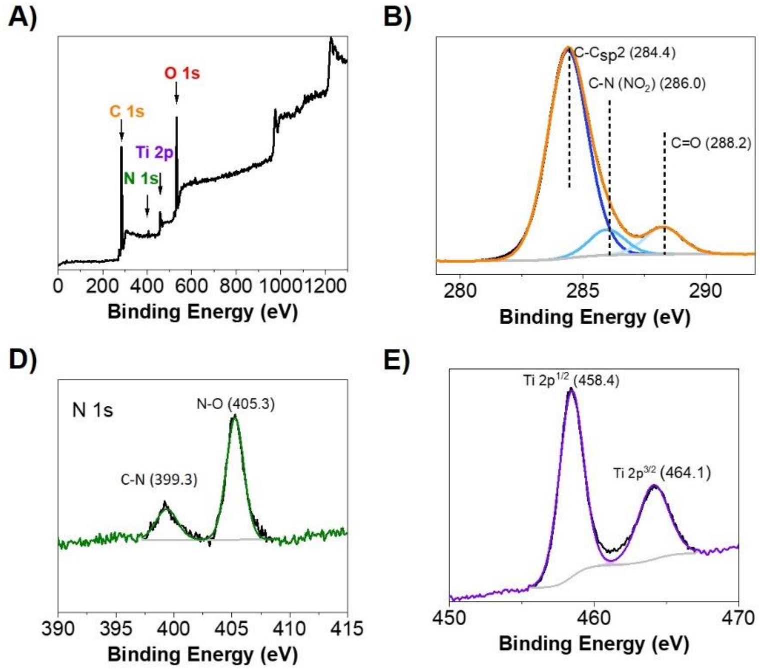

Figure S37 XPS spectra (A) of MIP-209(Ti)-NO$_2$, and the best deconvolution for the C 1s (B), O 1s (C), N1s (D), Ti 2p (E).

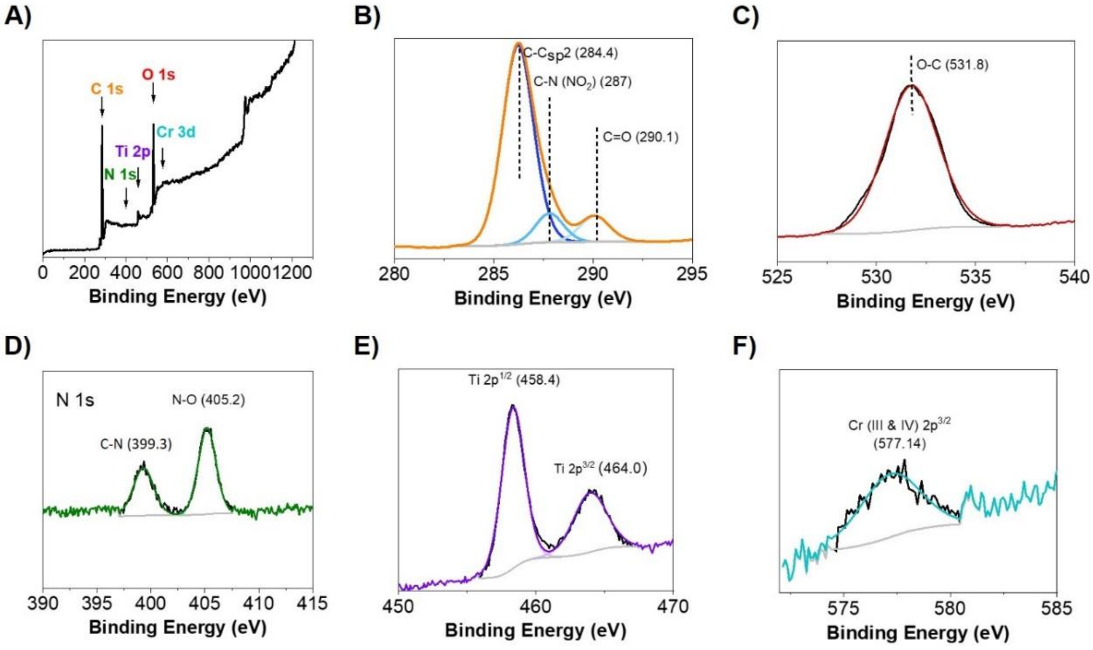

Figure S38 XPS spectra (A) of MIP-209(Ti-Cr)-NO$_2$, and the best deconvolution for the C 1s (B), O 1s (C), N1s (D), Ti 2p (E), Cr 2p (F).

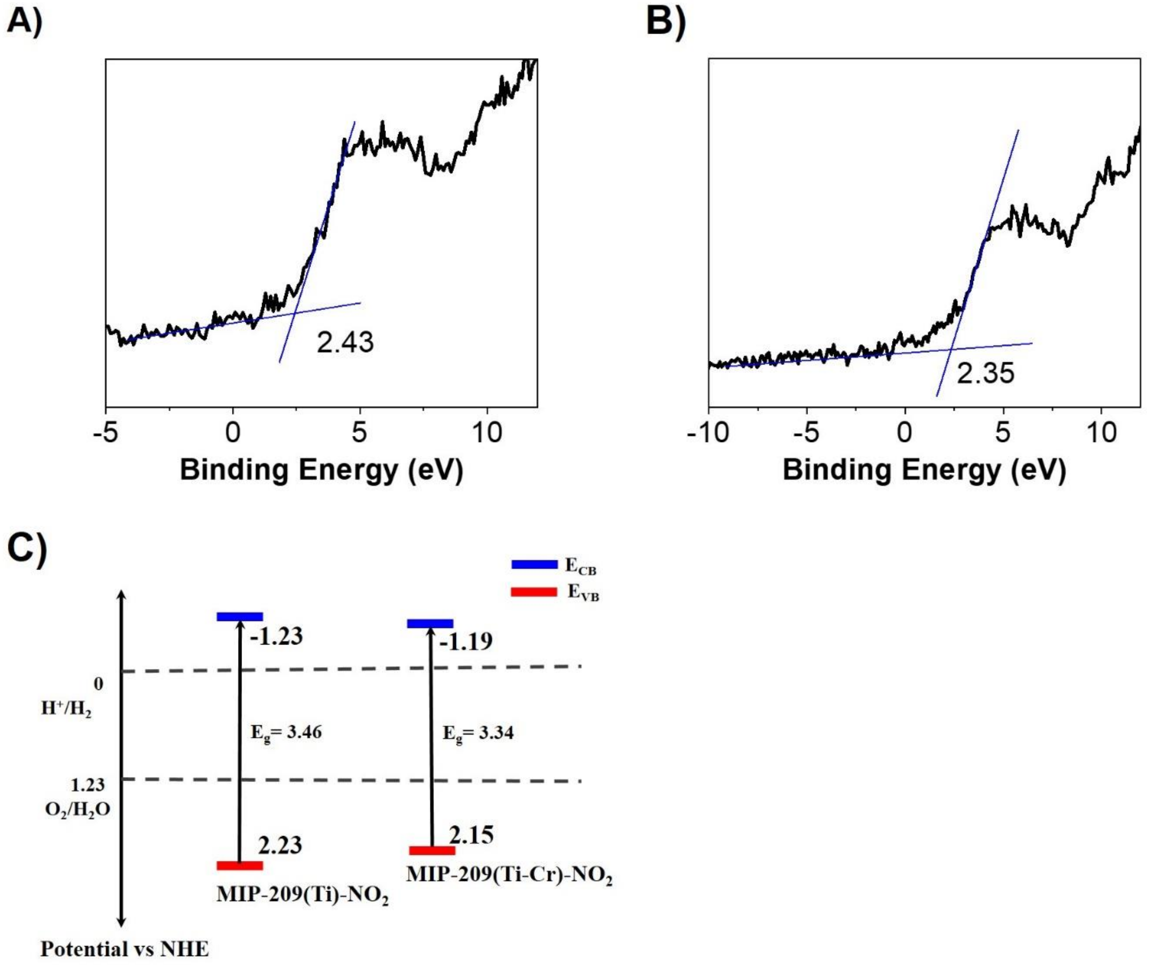

Figure S39 XPS intensity onset from where the valence band potential value was estimated for A) MIP-209(Ti)-NO_2 and B) MIP-209(Ti-Cr)-NO_2 (C) Energy band diagram and the positions of reduction potentials of H^+ to H_2 and O_2 to H_2O in the vacuum level (Valence band: VB; Conduction band: CB).

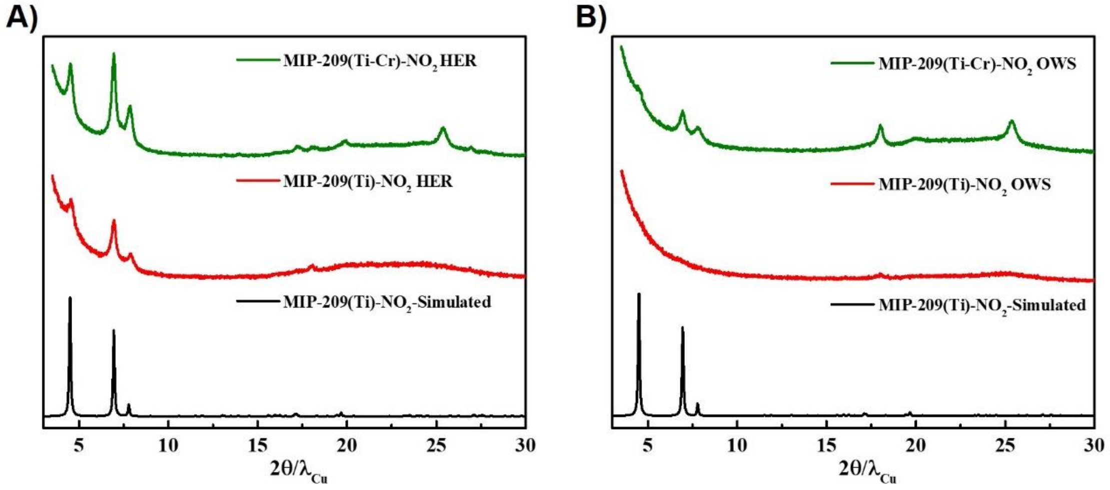

Figure S40 PXRD patterns of MIP-209(Ti)-NO_2 and MIP-209(Ti-Cr)-NO_2 after photocatalytic HER (A) and OWS (B) tests.

Supplementary tables

	Dataset used
Rotation range (°)	50.76
Tilting rate (° s^{-1})	0.58
Collection time (s)	87.939
Resolution (Å)	1.111
Completeness (%)	85.5

Table S1 Parameters of the selected cRED dataset.

Chemical Formula	$C_{4.25}\ N_{0.5}\ O_{4.25}\ Ti_1$
Formula weight	173.9
Crystal system, space group	Hexagonal, $P6_3/mmc$
a, c (Å)	22.3854, 16.5906
V (Å^3)	7199.83
Z	24
Radiation type	Electrons $\lambda = 0.02508$ Å
Diffractometer	JEOL COM, F200
No. of measured, independent and observed [$I > 3\sigma(I)$] reflections	5681, 877, 643
R_{int}	0.287
θ_{max} (°)	0.7
R[F2 > 2σ(F2)], wR(F2), S	0.242, 0.443, 10.17
No. of reflections	877
No. of parameters	51
$\Delta\rho_{max}$, $\Delta\rho_{min}$ (e^{-}Å^{-3})	0.64, – 0.47

Table S2 Data collection and kinematical structure refinement details.

Parameter	HRTEM(Å)	DV(%)	HRPXRD(Å)	DV(%)	ED model(Å)
a	22.03	1.59	22.4603(3)	0.75	22.3854
c	16.60	0.06	16.8687(4)	1.69	16.5906

Table S3 Unit cell parameters a and c calculated from the LD-HRTEM images and from the Lebail profile matching compared to the values of the ED structural model. HR-PXRD, ED = Electron diffraction. DV = Percentage deviation.

Ti-MOFs	**Ti oxocluster**	**ligand**	**Ti precursor**	**organic solvent**	**acid**	**Temperature /C**	**Photo-acitivity**	**ref.**
FIR-120	Ti(IV) ion	H_4DOBPDC	Ti(i-OPr)$_4$	1,4-dioxane	acetic acid	160	NO_2 sensing	J. Mater. Chem. A, 2023,11, 965-971
MUV-11	Ti(IV) ion	Benzene-1,4-dihydroxamic Acid	Ti(i-OPr)$_4$	DMF	acetic acid	120	Hydrogen production, Sacrificial agent: TEOA (triethanolamine) or CH_3CN: TEA: H_2O (TEA, trie- thylamine)	J. Am. Chem. Soc. 2019, 141, 13124−13133
MIL-167 (Alternative synthesis)	Ti(IV) ion	2,5-dihydroxyterephthalate	Ti(i-OPr)$_4$	diethylamine	acetic acid	120	HER from water and triethylamine	Inorg. Chem. 2016, 55, 15, 7192-7199
MIL-167-169	Ti(IV) ion	2,5-dihydroxyterephthalate	Ti(i-OPr)$_4$//Ti_4O_4(ox)$_7$(pipH$_2$)$_3$ 2H_2O	DEF-Methanol//DEF-catechol//catechol-water	-	180/180/150	HER from water and triethylamine	Inorg. Chem. 2016, 55, 15, 7192-7199
NTU-9	Ti(salicylate)$_3$]$_2$ ions	2,5-dihydroxyterephthalate	Ti(i-OPr)$_4$	-	acetic acid	120	Degradation of rhodamine B (RB)	Chem. Commun., 2014,50, 3786-3788
MOF-217	Ti(C_2O_2)$_3$	TDHT	Ti(i-OPr)$_4$	DMF-Methanol-amylamine	-	180	Proton conductivity	Chem. Sci.,2020, 11,3978–3985
COK-47s	TiO_6 layer	BPDC	Cp_2Ti(IV)Cl_2	(DMF)-propylene carbonate	acetic acid	185	DBT oxidation	Angew.Chem. 2019, 131,9258 –9263
COK-47L	TiO_6 layer	BPDC	Cp_2Ti(IV)Cl_2	DMF	Formic acid	150	DBT oxidation	Angew.Chem. 2019, 131,9258 –9263
IEF-11	TiO_5 and TiO_6	3,4-dihydroxycyclobut-3-ene-1,2-	Ti(OBu)$_4$/Ti(i-OPr)$_4$	isopropanol	acetic acid	120	Overall water splitting	Adv. Mater. 2021, 2106627

	polyhedra	dionate,						2106627
MUV-10-Ca/Mn	$Ti(IV)_2Ca(II)_2$	1,3,5-BTC	$Ti(i\text{-}OPr)_4$	DMF	acetic acid	120	Photocatalysts for H_2 generation in water: methanol	Angew. Chem. 2018, 130, 1 - 6
MUV-12	$Ti(IV)_3Ca(II)_3$	BTB	$CaCl_2/Ti(i\text{-}OPr)_4$	DMF	acetic acid	120	The formation of cyclic carbonates by the cycloaddition of CO_2 to epoxides	Angew.Chem. Int. Ed. 2021, 60,11868 – 11873
MIL-100(Ti)	Ti_3O	1,3,5-BTC	$Ti_6O_6(4\text{-}tbbz)_6(OiPr)_6$	acetonitrile-tetrahydrofuran	acetic acid	160	Photocatalytic H_2 production in a mixture of H_2O: MeOH (4 : 1, v/v%)	Chem. Sci.,2019, 10,4313–4321
MIL-101-Ti	$Ti_3O(OEt)$	1,4-BDC	$TiCl_3$	DMF-Ethanol	-	120		Inorg. Chem. 2015, 54, 20, 10096–10104.
$Ti_3(BPDC)$-Ir/Ru	$Ti_3(OH)_2$	BPDC	$Ti_6O_6(OiPr)_6(abz)_6$	DMF	acetic acid	120	HER with 1,3-dimethyl-2-phenyl-2,3-dihydro-1H-benzo[d]imidazole (BIH) as the sacrificial agent	J. Am. Chem. Soc. 2019, 141, 12219−12223 Chem. Sci.,2019, 10,2193–2198
COK-69	$Ti(IV)_3O$	Trans-1,4-cyclohexane-dicarboxylate	$Cp_2Ti(IV)Cl_2$	DMF	acetic acid	110	Photoreduction	Angew.Chem.Int. Ed. 2015, 54,13912 – 13917.
MOF-901	$Ti_6O_6(OCH_3)_6$	Benzene-1,4-dialdehyde	$Ti(i\text{-}OPr)_4$	Methanol	-	125	Photocatalyzed polymerization of methyl methacrylate (MMA) under visible light irradiation.	J. Am. Chem. Soc. 2016, 138, 13, 4330–4333
MOF-901/902	$Ti_6O_6(AB)_6$	1,4-Beneze dialdehyde/4,4’-Biphenyldicarboxaldehyde	$Ti(i\text{-}OPr)_4$	Methanol	-	140	Polymerization reaction of methylmethacrylate under visible light	ACS Catal. 2017, 7, 1, 338–342
DGIST-1	$Ti_6O_6(OiPr)_6(t\text{-}BA)_6$	TCPP	$Ti_6O_6(OiPr)_6(t\text{-}BA)_6$	DEF	benzoic acid	150	Selective oxidation of benzyl alcohol to benzaldehyde	Angew. Chem. Int. Ed. 2018, 57,

								14852.
PCN-22	Ti_7O_6	tetra-kis(4-carboxyphenyl)porphyrin)	$Ti_6O_6(OiPr)_6(abz)_6$	DEF	benzoic acid	150	Benzyl alcohol oxidation reaction	Chem. Sci.,2015, 6,3926.
MIL-125(Ti)	Ti_8O_8	1,4-BDC	$Ti(i\text{-}OPr)_4$	DMF-Methanol	-	150	Oxidation of alcohols	J. Am. Chem. Soc. 2009, 131, 10857–10859.
MIL-125(Ti)-NH_2	Ti_8O_8	1,4-BDC-NH_2	$Ti(i\text{-}OPr)_4$	DMF-Methanol		150	Reduction of CO_2	Angew. Chem. Int. Ed.2012,51, 3364 –3367.
MIP-207	Ti_8O_8	1,3,5-BTC	Ti_8AF	acetic anhydride	acetic acid	180	CO_2/N_2 separation	https://doi.org/10.1016/j.matt.2019.11.002
FIR-125-126	Ti_8O_8	4,4′-oxydibenzoic acid (H_2odb)	$Ti(i\text{-}OPr)_4$, Cp_2TiCl_2, $Ti_6(O)_6(i\text{-}OPr)_6$(4-aminobenzoate)$_6$, $Ti_6O_4(OEt)_4(i\text{-}OPr)_4(C_6H_5CO_2)_8$, $Ti_8O_8(C_6H_5CO_2)_{16}$, $Ti_8O_8((C(CH_3)_3CO_2)_{16})$	DMF-CH_3CN	acetic acid	160	Photocatalytic reduction of CO_2 to CO and H_2	ACS Materials Lett. 2021, 3, 64−68
MIP-177(Ti)_LT	$Ti_{12}O_{15}$	Methanediphenyl-3,3′,5,5′-tetra-carboxylic acid	$Ti(i\text{-}OPr)_4$	-	formic acid	120	Hydrogen production/ wound healing	Nat Commun 9, 1660 (2018)/Angew.Chem.Int.Ed.2020,59,5135 –5143/ACS Sustainable Chem. Eng. 2019, 7, 6, 5776–

								5783/Energy Environ. Sci., 2023,16, 167-177
TiTBP	Ti oxochains	5,10,15,20-tetra(p-benzoato)porphyrin (TBP) ligands	$TiCl_4·2THF$	DMF	acetic acid	120	Generating four distinct ROSs	J. Am. Chem. Soc. 2019, 141, 4204−4208
MIP-208	Ti oxochains	NH_2-IPA	Ti(i-OPr)$_4$	acetic anhydride	acetic acid	120	CO_2 Methanation	https://doi.org/10.1016/j.chempr.2020.10.017
ACM-1/Pt	Ti oxochains	H_4TBAPy	Ti(i-OPr)$_4$	DEF-chlorobenzene	propionic acid	150	HER in CH_3CN and H_2O	Angew. Chem. 2020, 132, 13570 – 13574
MIP-177(Ti)_HT	Ti_6O_9 nanowire	Methanediphenyl-3,3′,5,5′-tetra-carboxylic acid	-	-	-	280	Photoconductivity	Nat Commun 9, 1660 (2018).
ZSTU-1/2/3	Ti_6O_9 nanowire	TCA/BTB/BTCA	Ti(i-OPr)$_4$	DMF	-	180	Photocatalytic H_2 evolution in a TEOA/CH_3CN/H_2O system	J. Mater. Chem. A,2019, 7,11928–11933
UCFMOF-n	Ti_6O_9 nanowire	BPDC/TPDC/QPDC/DAQP	$Ti_8O_8(tBuCO_2)_{16}$	DMF	-	120/150	BzOH photocatalyzed oxidation	J. Am. Chem. Soc. 2023, 145, 8, 4589–4600
ICGM-1	Ti_6O_9 nanowire	1,4-BDC-NH_2	Ti(i-OPr)$_4$	2-propanol/imidazole	-	150	Photocatalytic activity in HER	ACS Materials Lett. 2023, 5, 1481−1487

Table S4 The list of the current reported Ti-MOFs.

No.	Quantity/ mg	Solvent	Volume/ml	concentration	Temperature/°C	Time/h
MIP-209-1	40	water	2		RT	24
MIP-209-2	40	water	2		40	24
MIP-209-3	40	water	2		60	24
MIP-209-4	40	water	2		80	24
MIP-209-5	40	HCl	2	1M/0.167ml	RT	24
MIP-209-6	40	HNO_3	2	1M/0.126ml	RT	24
MIP-209-7	40	H_2SO_4	2	1M/0.113ml	RT	24
MIP-209-8	40	H_3PO_4	2	0.3M/57mg	RT	24

Table S5 The details of chemical stability tests for MIP-209(Ti)-NO_2.

No.	Quantity/mg	Solvent	Volume/ml	Temperature/C	Time/day	Stirring
MIP-209-7D	50	water	2	RT	7	No
MIP-209-BC-7Ds	50	water	2	RT	7	Yes
MIP-209-Cr-7D	50	water	2	RT	7	No
MIP-209-Cr-7Ds	50	water	2	RT	7	Yes

Table S6 The details of water stability tests for MIP-209(Ti)-NO_2 and MIP-209(Ti-Cr)-NO_2.

No.	BET surface area (m^2/g, STP)	Pore volume (cm^3/g)
MIP-209-7D	578	0.225
MIP-209-BC-7Ds	-	-
MIP-209-Cr-7D	857	0.333
MIP-209-Cr-7Ds	900	0.348

Table S7 The BET surface area and pore volume results of MIP-209(Ti)-NO_2 and MIP-209(Ti-Cr)-NO_2 after water treatment.

General conclusion and perspectives

This thesis focuses on crystalline MOF-based materials in energy and environmental applications.

The main objectives of the thesis were:

1) The enhancement of the C_2H_6-selective adsorption performance over C_2H_4 under high pressure conditions through several MOF-based materials bearing rich-benzene;

2) The improvement on C_2H_6 and C_2H_4 working capacity through post-synthetic modifications on the backbone of MOF-based material;

3) The synthesis optimization and fundamental characterizations of an efficient CO_2 adsorbent, and

4) The synthesis of a new Ti-MOFs, its structure determination, and the study of its photocatalytic hydrogen evolution.

Following an introduction to C_2H_6-selective adsorption in C_2 hydrocarbons using MOF-based materials in chapter 1, chapter 2 presented several MOF-based materials (Al/Fe/Zr-1,4-NDC (naphthalene-1,4-dicarboxylic acid), Al-2,6-NDC-OP/CP (naphthalene-2,6-dicarboxylic acid, OP = open pore, CP = close pore with rich aromatic moieties which exhibited C_2H_6-selective adsorption behaviours under high pressure conditions. Through pure-component gas adsorption experiments, the results revealed that the increased C-H···π interactions between C_2H_6 molecule and these moieties enhanced the space confinement of C_2H_6 in C_2H_6/C_2H_4 binary mixture. According to their single component thermodynamic adsorption performance, Al-2,6-NDC-OP exhibited the best C_2H_6-selective performance with high C_2H_6 selectivity and working capacity under high pressure. Unfortunately, the preliminary dynamic column breakthrough experiments didn't confirm so far the C_2H_6-selective adsorption as suggested from near-ambient pressure single component isotherms. Additionally, from practical application point of view, Al-2,6-NDC-OP was shaped (i.e., extrusion followed by spheronisation) with 3% PVB binder (PVB stands for polyvinyl butyral) prior to breakthrough measurements. The obtained beads (*ca.* 2 mm diameter) exhibited good mechanical strength (*ca.* 11 N) with preserved porosity. Additional studies are still in progress for further understandings. Secondly, chapter 3 pointed out another strategy which enhanced C_2H_6 and

C_2H_4 uptake by post-synthetic modification on MOF-based material backbone using monocarboxylic acid bearing more fluorinated or aromatic moieties to enhance the VdW interaction with C_2H_6 molecules. As a proof of concept, grafting fluorinated functional group on the framework allowed to significantly improve the C_2 hydrocarbons working capacity of MOF-808 under high pressure through pure component gas isotherm adsorption. Compared with the bare MOF-808, MOF-808-TFA and MOF-808-TPA showed 133%, 155% increase in C_2H_6 working capacity at 298 K, between 1-9 bar, respectively. While the selectivity of C_2H_6/C_2H_4 was higher than bare MOF-808 until 4 bars, unfortunately, MOF-808-NSA bearing more benzene rings could enhance the uptake for both of gases, particularly C_2H_4 under high pressure conditions due to their equivalent C-H···π affinity. This work is currently being complemented by computational studies to shed light on the interaction in play and confirm our hypothesis.

Subsequently, chapter 4 demonstrated a potential of MIL-120(Al)-AP (refers to AP via ambient pressure synthesis) for CO_2 capture. Due to the high density of μ_2-OH groups and their availabilities for the interactions with CO_2, this MIL-120(Al)AP exhibited high CO_2 uptake, which was further supported by the GCMC simulations. Meanwhile a less energy cost for the regeneration is required due to the low isosteric heat of CO_2 adsorption (Q_{st}) MIL-120(Al)-AP (44 kJ mol^{-1}). *In situ* PXRD study confirms a phase transition from monoclinic to triclinic due to partial removal of the guest water molecules. In the presence of water vapor, rapid adsorption of CO_2 molecules in this material could be apparently observed through *in situ* IR measurement which indicates the importance of the materials potential ability to capture CO_2 in presence of water. The synthesis of MIL-120(Al)-AP with environment friendly, cheap scalability to the kg-scale, high yield, easy processability has been optimized. The efficient adsorptive separation of CO_2/N_2 of the structured MIL-120(Al)-AP was validated by breakthrough experiments. The ongoing research in collaboration with Prof. G De WEIRELD is to investigate the kinetics effects in real separation conditions on a VPSA unit, requiring 3 kg of shaped material.

In complement to energy-efficient gas separation strategies, the work described in chapter 5 slot into another strategy to address energy-efficiency issues dealing with producing clean energy vectors via renewable resources. Indeed, it discussed a new Ti-MOFs photocatalytical active for the production of H_2. Starting from the synthesis of new microporous Ti-MOFs, MIP-209(Ti), constructed by terephthalate derivatives ligands and $Ti_{12}O_{15}$ oxo-cluster, as revealed by continuous rotation electron diffraction method (cRED). Interestingly, MIP-209(Ti) can be obtained using various terephthalate (1,4-BDC) derivatives such as NO_2- and 2Cl-1,4-BDC, in an eco-friendly solvent, indicating the useful ability on Ti-MOF isostructural chemistry. Alternatively, it is also possible to tune the composition of its Ti-oxo-cluster, similarly to MIP-177(Ti)_LT. For instance, 5% Cr^{3+} doping can favorably enhance the water stability, and maintained good crystallinity after soaking in water for at least 7 days. Motivated by the enhanced water stability and unique Ti-MOFs properties, photocatalytic hydrogen evolution from water splitting reaction under simulated sunlight irradiation have been measured. MIP-209(Ti-Cr)-NO_2 displayed a very high hydrogen production rate with good reusability and stability in presence of methanol as scavenger under simulated sunlight irradiation, which exhibited fourfold enhanced hydrogen production, in comparison with the benchmark IEF-11 framework.

Overall, the main objectives of this thesis are met, and whilst there are still some future works that need to be completed. This work will provide a promising effect on energy and environment application using MOF-based materials. And the synthesis of new useful MOFs will never stop, more efficient and amazing structures will be obtained in the coming future.

Perspectives

Robust MOFs as platforms have been attracted more interest on environmental and renewable energy applications. Using MOF-based adsorbents to mitigate some of the environmental issues from the utilization of fossil fuel nowadays, in my thesis, we dealt with two challenging separation processes: i) C_2 hydrocarbons adsorption separation under high pressure; ii) CO_2 capture from diluted emission under practical condition, which could reap great global benefits if improved. However, in the C_2 hydrocarbon separation parts, several points of MOF-based adsorbents candidates still need to be further investigated, such as: 1) the systematic investigation on the different percentage replacement of formate group in MOF-808-TPA via the synthesis optimization; 2) the measurement of the diffusion rate difference of C_2H_6 and C_2H_4 under high pressure through dynamic breakthrough tests; 3) the affinity between gas molecules and the wall of the frameworks under high pressure could be explained through computational simulation or modeling; 4) the structuration of powder using different binders via extrusion and wet granulation.

Despite the highly promising performance of MIL-120(Al)-AP has been descripted in details in CO_2 capture part, several challenges still exist. From fundamental scientific investigation, due to the hydrophilic behaviour of MIL-120(Al)-AP, designing less hydrophilic MIL-120(Al)-AP will be a great added-value to the features of the MOFs. This could be achieved via several strategies. Once can for instance tune the chemical composition of the MOFs using mixed high-valence metal and/or hydrophobic derivative ligands strategy. This will very likely allow to avoid the competitive adsorption between CO_2 and water molecules providing high CO_2-selectivity in presence of vapour or under realistic chemical mixtures. Another strategy could lay in the use of hydrophobic binders as moisture repellant to make “water-proof” shaped objects. First encouraging results in this direction could be obtained so far. From a large-scale carbon capture application point of view, increasing the STY value by the optimization of the washing process can let it be one comparable CO_2 adsorbent like CALF-20. In addition, the durable stability as one of essential factors for practical application needs to be evaluated through a long-term CO_2 adsorption test.

The water stability is one of crucial limitations on Ti-MOFs, which could hinder its reusability on the photocatalytic applications. The photocatalytic activity of Ti-MOFs under the visible light is still need to be improved. MIP-209 platform could be indeed very promising in a sense, it has demonstrated its ability (i) to yield isostructures, so one can tune the bandgap using suitable ligands, and (ii) to tune the chemical composition of the Ti_{12} through transition metal doping. Thus, one can tune the stability and the redox activity, charge migration, etc. Although MIP-209(Ti-Cr)-NO_2 exhibited an enhanced water stability, it is still not enough to meet the harsh conditions of the HER and OWS applications. Here several feasible investigations for MIP-209 to achieve a higher photocatalytic performance: 1) decreasing the effect of water by phosphate or sulfate grafting on Ti_{12} oxocluster; 2) ligand partial substitution (NH_2, SO_3H-based ligands) to improve the visible light harvesting; 3) the improvement of the number of photocatalytic active sites through acidic solution treatment for instance, washing out some of the anon-bridging acetate groups; 4) design MOF-based composite combining with either actives particles (i.e., co-catalysts, charge promotors) and/or photosensitizers (such as metal oxides, carbon quantum dots, etc.) to enhance further the light-harvesting and/or to avoid fast recombination phenomenon of electron and hole leading to low photocatalytic efficiency.

Through these fundamental scientific studies, robust MOFs based platforms could be one of potential materials suitable to participate to the massive efforts needed for mitigating the negative effect of CO_2 and to and foster further the efficient utilization of clean energy. Hopefully, this thesis can provide several useful ideas towards clean energy society.

Annex-1

Résumé

Limiter les processus énergivores actuels dans les industries lourdes (par exemple, la pétrochimie, les usines de ciment, etc.) et atténuer les problèmes environnementaux grâce à l'utilisation de sources d'énergie propres et durables ont récemment attiré beaucoup d'attention en raison du dérèglement climatique critique, accompagné d'un nombre accru de risques pour les êtres humains, les économies et les écosystèmes. Par exemple, la séparation/purification par distillation cryogénique, l'une des procédures les plus énergivores dans les installations industrielles pétrochimiques actuelles, représente 10 à 15 % de la consommation mondiale d'énergie. De plus, l'utilisation en particulier des combustibles fossiles, accentue davantage les nombreux problèmes environnementaux , tels que le réchauffement climatique et la pollution de l'air. Par conséquent, un investissement politique, économique et technologique mondial rapide sera nécessaire pour relever ce défi collossale et permettre à limiter la progression du dérèglement climatique. Les avancées dans le domaine des matériaux devrait pouvoir contribuer de manière significative à ces efforts en fournissant des alternatives très performantes pour des processus de séparation/purification efficaces et/ou une conversion hautement sélective de sources durables en énergie propre, avec les coûts énergétiques les plus faibles possible.

Parmi les différents candidats potentiels, les solides poreux hybrides, ou les MOFs (Metal-Organic Frameworks) commencent à montrer des résultats très prometteurs dans ce domaine. Les MOFs sont des solides hybrides cristallins poreux, pouvant être conçus de manière rationnelle grâce à l'assemblage des unités de construction inorganiques (IBUs) multiples avec des chaînons organiques divers, formant ainsi des structures ordonnées et poreuses bi- ou tridimensionnelles. Leurs structures polyvalentes, en termes de compositions chimiques et de caractéristiques géométriques, leur confèrent de nombreux avantages et un fort potentiel dans diverses applications liées à l'énergie, à l'environnement et à la santé.

L'éthylène (C_2H_4) est l'une des matières premières essentielles pour la fabrication de plastiques tels que le polyéthylène dans le monde entier. À ce jour, la production d'environ 200 millions de tonnes de C_2H_4 principalement à partir du craquage du mélange éthane (C_2H_6) nécessite environ 0,3 % de la consommation mondiale d'énergie, ce qui souligne clairement que sa séparation par distillation cryogénique classique est énergivore, même s'il s'agit d'un processus hautement intégré sur le plan thermique dans l'industrie pétrochimique. En alternative à cette distillation énergivore, la séparation par adsorption utilisant des adsorbants poreux dans des conditions modérées s'est avérée être une procédure efficace pour les mélanges de gaz dans l'industrie pétrochimique en aval. Cette séparation par adsorption présente l'avantage de pouvoir être réalisée en un temps opérationnel relativement court grâce à une régénération/cyclage rapide, ainsi que la possibilité d'offrir des technologies relativement flexibles et facilement adaptables. À cet égard, l'utilisation d'adsorbants à base de MOFs comportant des sites métalliques ouverts (OMS), tels que Ag(I), Cu(I) et Fe(II), s'est révélée très efficace. La présence de ces OMS bien agencés dans un espace confiné permet une interaction relativement forte ($Q_{st} > 60$ kJ mol^{-1}) avec le nuage électronique π des molécules de C_2H_4, ce qui permet une adsorption sélective du C_2H_4 par rapport au C_2H_6 dans des conditions ambiantes. Toutefois, le Q_{st} relativement élevé peut nécessiter un processus de régénération énergivore en cas d'affinité prononcée entre l'adsorbant et l'adsorbat, nécessitant un vide et/ou un chauffage plus élevés. Par conséquent, un adsorbant à base de MOFs optimal offrant une sélectivité élevée du C_2H_6 par rapport au C_2H_4 avec des interactions relativement modérées est un des paramètres clés pour concevoir des solutions d'adsorption économiquement et énergétiquement viables pour les processus de séparation efficace du C_2H_6/C_2H_4. De plus, compte tenu de la plage de pression industrielle pratique, lorsque l'opération est réalisée sous une pression relativement élevée, la production de C_2H_4 avec une pureté élevée pourrait être améliorée en raison d'une plus grande quantité de C_2H_6 pouvant être retenue dans la colonne à lit fixe de l'adsorbant.

D'un point de vue plus large, le CO_2 est un autre aspect de la production/consommation mondiale d'énergie, étant donné que la grande majorité dépend encore des ressources fossiles. Étant la principale cause du réchauffement climatique, la concentration de CO_2 dans l'atmosphère a considérablement augmenté au cours des dernières décennies, en raison de la croissance de la demande mondiale d'électricité et de chaleur, ainsi que des émissions accrues de CO_2, atteignant 36,3 gigatonnes (Gt) de CO_2 en 2021. Jusqu'à ce que notre dépendance aux ressources fossiles diminue de manière significative, la seule solution possible pour réduire la quantité de CO_2 dans l'atmosphère est de le capturer (soit à la source, soit de l’atmosphère) et de le stocker. Jusqu'à présent, les solutions aqueuses d'amines, grâce à une combinaison d'absorption chimique et physique avec la molécule de CO_2, constituent la technologie de référence pour la capture du CO_2 dans les centrales thermiques au charbon. Cependant, ce procédé de capture bien établi à grande échelle présente certains inconvénients/limitations sur le plan environnemental, tels que le rejet de polluants toxiques, l'oxydation du groupe amine et la corrosivité de l'équipement. Ce processus nécessite également une consommation d'énergie élevée pour une régénération complète en raison de la formation réversible d'espèces carbonates ou bicarbonates. Par conséquent, poussé par une technologie non thermique et respectueuse de l'environnement, l'utilisation d'adsorbants poreux efficaces pour la capture physisorptive de CO_2 à partir des gaz de combustion des centrales électriques (10 à 15% de CO_2) est désespérément nécessaire pour réduire les émissions de CO_2, éviter la pollution de l'air et atténuer le réchauffement climatique mondial actuel. Les adsorbants à base de MOFs sont également des candidats potentiels pour la capture de CO_2 grâce à leur excellente capacité de sorption et leur sélectivité de CO_2 relativement forte par rapport aux autres gaz présents dans les rejets provenant de combustion des centrales électriques. A titre d’exemple, un MOF prometteur à base de cations de zinc, le CALF-20 (CALF pour CALgary Frameworks), a démontré une, à l’échelle de pilote industriel, une capture sélective du CO_2 dans des conditions de forte humidité, alors que sa synthèse à grande échelle a atteint le niveau de plusieurs tonnes. Comme décrit ci-dessus, étant donné que l'utilisation de combustibles fossiles est à l'origine de l'accumulation importante de CO_2, il est urgent de rechercher des ressources durables ayant une empreinte carbone faible et un impact environnemental réduit. L'énergie hydrogène est considérée comme une alternative idéale en raison de ses caractéristiques telles que ses sources variées, sa valeur calorifique élevée lors de la combustion et son absence de carbone. Jusqu'à présent, les processus électrocatalytiques sont les technologies les plus avancées utilisées pour la production d'hydrogène. De plus, la production d'H_2 à partir de sources renouvelables telles que l'énergie solaire, par le biais, par exemple, de la réaction de conversion photocatalytique de l'eau (HER) et du craquage total de l'eau (OWS), suscite beaucoup d'attention ces dernières années. Bien que cela ne s'oppose pas aux processus photoélectrocatalytiques, qui reposent sur la seule source de lumière solaire, permettant ainsi de simplifier le processus et de réduire considérablement les coûts ainsi que les obstacles liés aux infrastructures lourdes requises par les processus électrochimiques, la photocatalyse constitue donc une bonne alternative à envisager pour les stations d'H_2 dans des emplacements éloignés pour une production d'énergie décentralisée de petite à moyenne échelle. Le photocatalyseur à base de titane (c.-à-d. TiO_2) est une technologie très respectueuse de l'environnement, utilisant l'eau comme matière première et l'énergie solaire inépuisable comme force motrice. Lorsqu'il s'agit du photocatalyseur à base de TiO_2, il est fortement nécessaire d'améliorer sa performance photocatalytique en exploitant efficacement la lumière visible, en augmentant la capacité d'adsorption des réactifs et en simplifiant la séparation de la suspension. Ainsi, la construction de composés/clusters de Ti-oxo/hydroxo ordonnésdans les MOFs à base de titane (Ti-MOFs) stables pourrait permettre non seulement l'amélioration des sites actifs plus accessibles et de la vitesse de diffusion rapide des réactifs et produits, mais aussi l'amélioration des conditions de réaction photocatalytique sous UV et/ou lumière visible grâce à la conception rationnelle de moitiés inorganiques/organiques. Cependant, la conception et la synthèse des Ti-MOFs en sont encore à un stade préliminaire en raison de la complexité de la chimie du titane en solution, rendant toute tentative de conception rationnelle encore difficile, malgré les progrès récents réalisés.

Cette thèse porte sur les matériaux hybrides cristallins poreux de type MOFs pour des applications dans le domaine de l’énergie et/ou de l’environnement.

Les principaux objectifs de la thèse sont les suivants :

1) Amélioration de la performance d'adsorption sélective à haute pression du C_2H_6 par rapport au C_2H_4 à partir de MOFs à base d’espaceurs aromatiques;

2) Amélioration de la capacité de travail du C_2H_6 et du C_2H_4 par la modification post-synthèse du squelette de MOFs;

3) Optimisation de la synthèse et étude des propriétés d’adsorption d’un MOF microporeux à base d’Aluminium pour la capture du CO_2;

4) Synthèse et caractérisation d'un nouveau MOF au titane et l'étude de ses propriétés photocatalytiques pour la production d'hydrogène.

Dans le premier chapitre, nous avons présenté de manière générale les applications des cadres métallo-organiques (MOFs) dans la séparation des alcanes à chaîne courte et la capture de CO_2, ainsi que les exemples et stratégies clés utilisés jusqu'à présent dans ces deux cas. La première partie aborde la séparation sélective de C_2H_6 à l'aide d'adsorbants basés sur les MOFs, en se basant sur différents mécanismes d'adsorption, et discute de plusieurs exemples de séparation sélective C_2H_6/C_2H_4 à haute pression. La deuxième partie présente brièvement quatre stratégies de conception visant à améliorer les performances de capture de CO_2 des adsorbants basés sur les MOFs, et les explique en détail à l'aide de plusieurs exemples de référence.

Dans le deuxième chapitre, en tant que première stratégie pour obtenir des adsorbants sélectifs pour C_2H_6, nous avons étudié les performances de candidats MOFs poreux dotés de groupes aromatiques riches en présence de hautes pressions. Les résultats montrent que dans ces structures (Al/Fe/Zr-1,4-NDC [acide naphtalène-1,4-dicarboxylique], Al-2,6-NDC-OP/CP [acide naphtalène-2,6-dicarboxylique avec pores ouverts/fermés]), les interactions améliorées C-H···π entre les molécules de C_2H_6 et ces groupes fonctionnels augmentent la sélectivité d'adsorption de C_2H_6 par rapport au mélange binaire C_2H_6/C_2H_4. Les expériences d'adsorption de gaz en composant pur montrent que les interactions C-H···π renforcées entre les molécules de C_2H_6 et ces groupes fonctionnels confèrent à C_2H_6 une contrainte spatiale accrue dans ces matériaux adsorbants candidats. Parmi ces matériaux, Al-2,6-NDC-OP présente les meilleures performances de sélectivité pour C_2H_6, avec une sélectivité élevée et une capacité de travail à haute pression. Malheureusement, des expériences préliminaires de percé de colonne dynamique n'ont pas confirmé la sélectivité d'adsorption de C_2H_6 estimée à partir des isothermes de sorption monocomposant obtenues à des pressions proches de la pression atmosphérique. De plus, du point de vue de l'application pratique, des particules d'Al-2,6-NDC-OP de 2 mm de diamètre ont été préparées en utilisant un liant organique, le PVB (PVB représente un polyvinylbutyral) à 3%, présentant une bonne résistance mécanique (environ 11 N) et maintenant la porosité. D'autres recherches sont en cours pour approfondir nos connaissances.

Le troisième chapitre concerne la deuxième stratégie utilisée pour renforcer les interactions van der Waals entre les molécules de C_2H_6 et de C_2H_4. Cette stratégie implique la conception d'un groupe fonctionnel organique dans les MOFs ou la modification ultérieure des unités de construction inorganiques. Nous avons choisi le MOF-808 comme structure d'armature car il contient six groupes formiate (HCOO-) situés aux sites de la bande de cluster d'oxygène du Zr_6. Cela nous permet de remplacer partiellement ou totalement ces groupes formiate par des acides contenant des groupes fonctionnels fluorés ou phényle par une modification post-synthétique (PSM). Nous présentons ici les MOF-808-R (R = acide trifluoroacétique (TFA), acide trifluoropropanoïque (TPA), acide 2-naphtalènesulfonique (NSA)), qui offrent un environnement poreux riche en fluor ou en phényle, réduisent la taille des pores et créent des points de contact plus denses entre les atomes d'hydrogène du fluor ou du phényle et les alcanes C_2. Par rapport au MOF-808, le MOF-808-R présente une affinité plus forte pour les alcanes C_2, améliorant ainsi la capacité de travail des alcanes C_2 sur toute la gamme de pression, de la pression ambiante aux hautes pressions. En raison des interactions moléculaires accrues entre le MOF-808-TFA/TPA et les alcanes C_2, l'amélioration de la capacité de travail du C_2H_6 (de 1 à 9 bar) est supérieure de 133% et 155% à celle du MOF-808. Le mécanisme hypothétique de l'adsorption sélective de l'éthane peut être illustré par le schéma 1.

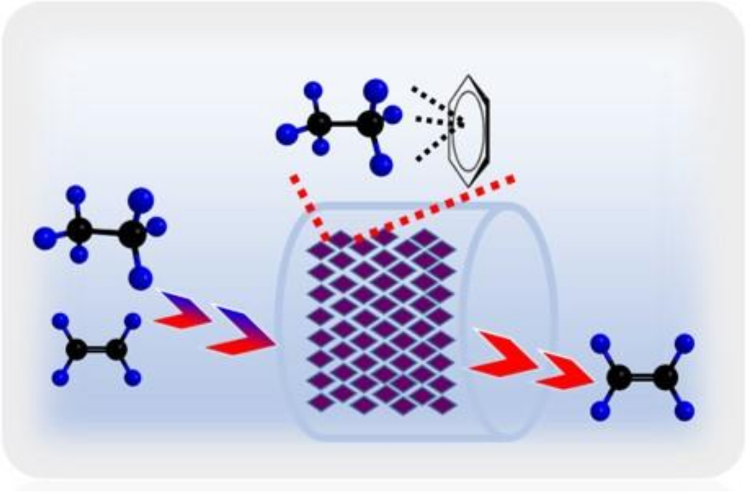

Schéma 1: Illustration de l'adsorption sélective de l'éthane par rapport à l'éthylène en utilisant un adsorbant à base de MOFs sous haute pression. Ici, il montre l'interaction relativement forte

entre les molécules d'éthane et la fonction benzène dans la structure.

Dans le quatrième chapitre, nous avons démontré le potentiel du MIL-120(Al)-AP (MIL-120(Al)-AP synthétisé à pression ambiante) pour la capture du CO_2. Il présente une capacité d'adsorption élevée de CO_2 grâce à la densité élevée du groupe μ_2-OH et à leur disponibilité pour les interactions avec le CO_2, ce qui est confirmé par les simulations GCMC. La chaleur isostérique d'adsorption du CO_2 (Q_{st}) du MIL-120(Al)-AP (44 kJ mol^{-1}) indique un coût énergétique relativement faible pour la régénération de l'adsorbant. L'étude de diffraction des rayons X sur poudre (PXRD) *in situ* confirme une transition de phase de monoclinique à triclinique due à l'élimination partielle des molécules d'eau invitées. Comparée à l'adsorption lente de H_2O, une adsorption cinétique rapide des molécules de CO_2 a été observée grâce à des études spectroscopiques infrarouges (IR) *in situ*, ce qui indique indirectement que ce MOF présente une cinétique plus favorable pour la sorption de CO_2 par rapport à l'eau, et pourrait donc être un processus idéal pour la séparation CO_2/N_2 en présence de H_2O. La synthèse du MIL-120(Al)-AP, réalisée de manière respectueuse de l'environnement (c'est-à-dire dans l'eau à pression ambiante) en utilisant des matériaux de départ peu coûteux, a d'abord été optimisée à l'échelle du gramme, puis a été mise à l'échelle avec succès à l'échelle du kilogramme. La séparation adsorptive efficace CO_2/N_2 du MIL-120(Al)-AP structuré a été validée par des expériences de rupture de colonne. Les recherches en cours, en collaboration avec le professeur G De WEIRELD, visent à étudier les effets cinétiques dans des conditions réelles de séparation sur une unité VPSA nécessitant 3 kg de matériau façonné. Le mécanisme de capture du CO_2 utilisant Al-MOF a été illustré dans le schéma 2.

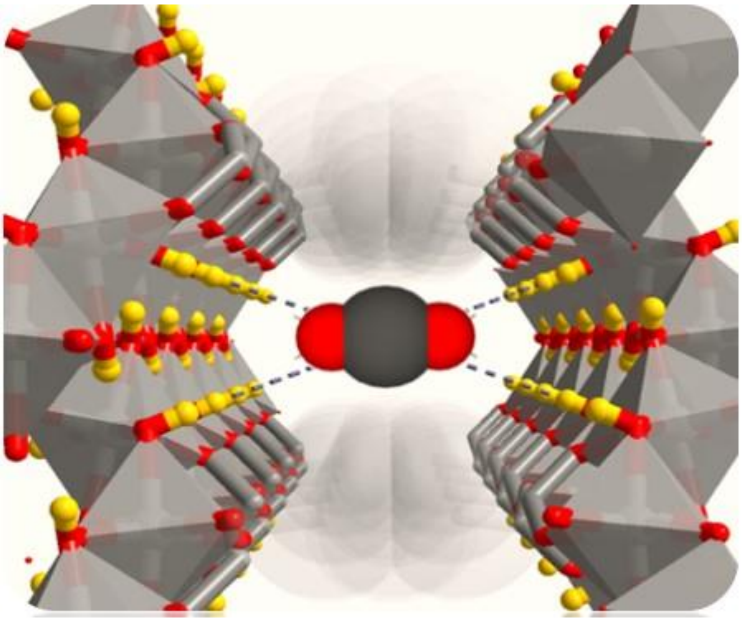

Schéma 2 : Capture efficace du CO_2 utilisant un adsorbant à base de MOF-Al porteur d'une haute densité de groupes OH. Ici, il est montré les interactions de liaison hydrogène à haute densité permettant la confinement des molécules de CO_2 dans la structure.

Dans le cinquième et dernier chapitre, nous avons présenté une nouvelle série de Ti-MOF microporeux, dénomée MIP-209(Ti) (MIP signifie Matériaux de l'Institut des Matériaux Poreux de Paris), construits à partir de ligands dérivés du téréphtalate et de clusters oxo $Ti_{12}O_{15}$ avec la formule $Ti_{12}O_{15}(NO_2\text{-}1{,}4\text{-}BDC)_6(\text{acétate})_3$, telle que révélée par la méthode de diffraction électronique en rotation continue (cRED), cristallisée dans le groupe d'espace hexagonal $P6_3/mmc$ avec les paramètres de maille a = 22,3854 Å, c = 16,5906 Å et V = 7199,83 $Å^3$. En effet, le MIP-209(Ti) peut être obtenu en utilisant différents dérivés de téréphtalate (1,4-BDC) tels que NO_2- et 2Cl-1,4-BDC, dans un solvant respectueux de l'environnement (c'est-à-dire l'acide acétique). Alternativement, il était également possible de régler la composition de son cluster oxo Ti, de manière similaire au MIP-177(Ti)_LT. Par exemple, un dopage de 5% de Cr^{3+} pourrait améliorer favorablement la stabilité à l'eau et maintenir une bonne cristallinité après trempage dans l'eau pendant au moins 7 jours. Motivés par la stabilité accrue à l'eau et les propriétés uniques des Ti-MOF, nous avons mesuré l'évolution photocatalytique de l'hydrogène par réaction de division de l'eau. Le MIP-209(Ti-Cr)-NO_2 a présenté un taux de production d'hydrogène très élevé avec une bonne réutilisabilité et stabilité en présence de méthanol comme sorbant sous irradiation solaire simulée, ce qui a induit une production d'hydrogène augmentée par un facteur de quatre par rapport au cadre IEF-11 de référence. Le mécanisme de production d'hydrogène par photocatalyse utilisant les Ti-MOFs comme plateforme efficace a été représenté dans le schéma 3.

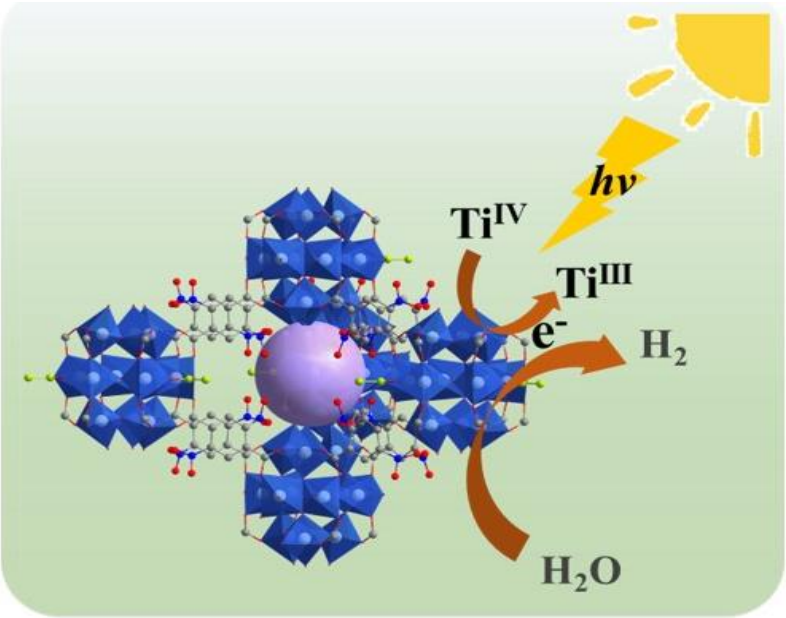

Schéma 3 : Illustration de la production photocatalytique d'hydrogène à partir de l'eau utilisant le nouveau Ti-MOF. Ici, il montre la structure du nouveau Ti-MOF et le mécanisme photocatalytique de production d'hydrogène à partir de l'eau sous illumination solaire simulée.

Dans ma thèse, nous avons étudié l'utilisation de MOFs robustes pour la séparation des hydrocarbures C_2 et la capture du CO_2. Ces MOFs robustes présentent un grand intérêt pour les applications environnementales et les énergies renouvelables. Nous avons utilisé des adsorbants à base de MOFs pour atténuer certains problèmes environnementaux liés à l'utilisation des combustibles fossiles. Dans la partie consacrée à la séparation des hydrocarbures C_2, plusieurs points concernant les candidats adsorbants à base de MOFs doivent être investigués, tels que l'optimisation de la synthèse pour remplacer le groupe formate dans le MOF-808-TPA, la mesure de la différence de taux de diffusion du C_2H_6 et du C_2H_4 sous haute pression, l'affinité entre les molécules de gaz et la structure des MOFs sous haute pression, et la structuration de la poudre à l'aide de différents liants par extrusion et granulation humide. Malgré les performances prometteuses du MIL-120(Al)-AP dans la capture du CO_2, plusieurs défis subsistent. Il serait intéressant de concevoir un MIL-120(Al)-AP moins hydrophile pour améliorer ses caractéristiques. Cela pourrait être réalisé en ajustant la composition chimique des MOFs en utilisant des métaux de valence élevée mixtes et/ou des ligands dérivés hydrophobes. Une autre stratégie consisterait à utiliser des liants hydrophobes pour rendre les objets résistants à l'eau. Des résultats encourageants ont été obtenus dans cette direction. Sur le plan de l'application de la capture du carbone à grande échelle, l'optimisation du processus de lavage peut augmenter la vitesse de production spécifique (STY) et rendre le MIL-120(Al)-AP comparable à un adsorbant de CO_2 tel que le CALF-20. De plus, la stabilité durable, un facteur essentiel pour une application pratique, doit être évaluée par le biais d'un test de capture du CO_2 à long terme.

La stabilité dans l'eau est une limitation cruciale des MOFs à base de Ti, ce qui limite leur réutilisation dans les applications photocatalytiques. L'activité photocatalytique des MOFs à base de Ti sous la lumière visible doit encore être améliorée. La plateforme MIP-209(Ti) présente un grand potentiel, car elle permet (i) de produire des isostructures en ajustant la bande interdite à l'aide de ligands appropriés et (ii) de régler la composition chimique du Ti_{12} grâce au dopage de métaux de transition. Ainsi, il est possible de régler la stabilité, l'activité redox, la migration de charge, etc. Bien que le MIP-209(Ti-Cr)-NO_2 présente une stabilité dans l'eau améliorée, elle n'est pas encore suffisante pour répondre aux conditions difficiles des applications HER et OWS. Plusieurs investigations réalisables pour améliorer les performances photocatalytiques du MIP-209(Ti) sont proposées, notamment la réduction de l'effet de l'eau par greffage de phosphate ou de sulfate sur les oxoclusters de Ti_{12}, la substitution partielle des ligands (basés sur NH_2, SO_3H) pour améliorer la capture de la lumière visible, l'amélioration du nombre de sites actifs photocatalytiques par traitement à l'aide d'une solution acide, et la conception de composites à base de MOFs combinant des particules actives (co-catalyseurs, promoteurs de charge) et/ou des photosensibilisateurs (tels que les oxydes métalliques, les nanoparticules de carbone (quantum dots), etc.) pour améliorer encore la capture de la lumière et éviter les phénomènes de recombinations rapides d'électrons et de trous conduisant à une faible efficacité photocatalytique.

Grâce à ces études scientifiques fondamentales, les plates-formes à base de MOFs robustes pourraient être des matériaux potentiels pour participer aux efforts massifs nécessaires pour atténuer les effets négatifs du CO_2 et favoriser une utilisation plus efficace des énergies propres. J'espère que cette thèse contribuera à l'avancement vers une société d'énergie propre.

RÉSUMÉ

Les solides poreux hybrides (ou MOFs) suscitent un intérêt croissant grâce à leurs applications potentielles en lien avec l'environnement et l’énergie. Cette thèse de doctorat s’est focalisée dans un premier temps sur l’exploration du potentiel d’adsorbants de type MOFs pour deux procédés de séparation très énergivores. Cela a concerné tout d'abord une stratégie consistant à favoriser les interactions dispersives pour améliorer l'adsorption sélective de l'éthane sur l'éthylène à haute pression. Ainsi, plusieurs adsorbants robustes à base d'Al- ou de Zr, riches en groupement aromatiques et en fluor, ont été synthétisés soit par voie directe, soit par modification post-synthèse. Ensuite, le potentiel d'un MOF microporeux, le MIL-120(Al) (MIL pour Matériaux de l'Institut Lavoisier), pour la capture du CO_2 en postcombustion a été démontré par une étude approfondie combinant des mesures d’adsorption, des caractérisations in situ (e.g., diffraction RX, Infra-rouge) et des calculs théoriques. La synthèse de ce MOF a été ensuite optimisée selon une procédure éco-compatible puis mise à l’échelle du kilogramme. Enfin, un nouveau MOF au titane, dénommé MIP-209(Ti) (MIP pour Matériaux de l’Institut des Matériaux Poreux de Paris), a été découvert et sa structure résolue à l’aide de la diffraction électronique. Ce MOF a ensuite été dopé avec 5% de Cr et s'est avéré être un photocatalyseur prometteur pour la production de H_2 par photolyse de l’eau, avec et sans présence d’agent sacrificiel, sous lumière solaire simulée.

MOTS CLÉS

Solides poreux hybrides, MOFs, séparation des gaz, capture du CO_2, catalyse

ABSTRACT

Metal-Organic Frameworks (MOFs) have been attracting an increasing interest for their potential applications related to environmental and renewable energy challenges. In this regard, this PhD thesis has first explored the use of MOFs to tackle two challenging energy demanding separation processes. First, a strategy consisting on fostering the dispersive interactions to enhance the ethane selective adsorption over ethylene under high pressure was studied. Thus, several phenyl-rich and fluorine-rich robust Al- or Zr-MOF-based adsorbents have been synthesized either through one-pot synthesis or post-synthetic modification. Then, the post-combustion CO_2 capture properties of an Al-MOF, the MIL-120(Al) (MIL stands for Materials from Institut Lavoisier), was demonstrated through an in-depth investigation involving advanced adsorption analysis, in situ characterizations (e.g., x-ray diffraction, infra-red spectroscopy…) and computational studies. Besides, the synthesis of this MOF was integrally optimized through a cost-effective eco-friendly procedure and scaled-up to the kg scale. Finally, a novel Ti-MOF, denoted MIP-209(Ti) (MIP stands for Materials from Porous Institute of Paris) was discovered and its structure solved from electron diffraction techniques. Markedly, MIP-209(Ti) doped with 5 at% of Cr was proven to be efficient photocatalyst for the H_2 production through hydrogen evolution and overall water splitting reactions under simulated solar light.

KEYWORDS

Metal-organic frameworks (MOFs), gas separation, CO_2 capture, catalysis